Ludwig-Maximilians-Universität
München

High-Power Few-Cycle Pulse Generation Towards the Gigawatt Frontier

Sebastian Gröbmeyer

München 2022

High-Power Few-Cycle Pulse Generation Towards the Gigawatt Frontier

Dissertation
der Fakultät für Physik
der Ludwig-Maximilians-Universität
München

vorgelegt von
Sebastian Gröbmeyer
aus München

München, den 21.12.2021

Erstgutachter: Prof. Dr. Ferenc Krausz
Zweitgutachter: Prof. Dr. Franz X. Kärtner
Tag der mündlichen Prüfung: 17.03.2022

Zusammenfassung

Das Aufkommen hochpräziser Spektroskopiemethoden, insbesondere im extremen Ultraviolett (XUV) und im mittleren Infrarot, hat eine Vielzahl von Möglichkeiten eröffnet, unser Verständnis physikalischer und biomedizinischer Zusammenhänge grundlegend zu erweitern. Dabei deckt der XUV-Bereich eine große Anzahl elektronischer Übergänge in Atomen und Molekülen ab, während das mittlere Infrarot zahlreiche fundamentale Schwingungs- und Rotationsmoden verschiedenster biologisch relevanter Moleküle enthält.

Unabhängig vom Spektralbereich sind viele dieser neuartigen Spektroskopieverfahren gleichermaßen auf die Verfügbarkeit von breitbandiger Strahlung mit einem kontrollierten Feldverlauf und einer hohen Brillanz angewiesen. Da es in den oben genannten Wellenlängenbereichen keine geeigneten Laserverstärkungsmedien gibt, wird derartige Strahlung üblicherweise durch die nichtlineare Frequenzkonversion von hochintensiven Femtosekunden-Laserimpulsen im Spektralbereich des nahen Infrarot erzeugt, wie sie beispielsweise von Dünnscheibenoszillatoren generiert werden. Diese Impulse haben jedoch im Allgemeinen eine Dauer von Hunderten von Femtosekunden — zu lang, um die gewünschte hohe Spitzenleistung und breite spektrale Abdeckung für eine effektive nichtlineare Frequenzumwandlung bereitstellen zu können. Außerdem variiert ihre elektrische Wellenform von Impuls zu Impuls nach dem Zufallsprinzip, was ihre Anwendung für beispielsweise die Frequenzkammspektroskopie behindert.

Diese Arbeit beschreibt experimentelle Entwicklungen von Methoden zur weiteren Komprimierung der Impulsdauer sowie zur aktiven Stabilisierung des elektrischen Feldverlaufs von hochintensiven Dünnscheibenoszillatoren. Es wird gezeigt, dass dispersionskontrollierte Herriott-Multipasszellen ein effizientes Mittel zur Erweiterung der spektralen Bandbreite von Laserpulsen darstellen, wobei im Gegensatz zu vielen anderen Techniken nahezu keine Verschlechterung der räumlichen Strahlqualität auftritt.

Erstmalig wurde die durch einen Dünnscheibenlaser getriebene spektrale Verbreiterung in einer Herriott-Zelle im negativen Dispersionsregime durchgeführt. Die spektrale Verbreiterung erreichte dabei höhere Verbreiterungsfaktoren, als sie jemals zuvor mit einem auf Multipass-Zellen basierenden Verbreiterungsschema mit einem einzigen nichtlinearen Medium erzielt wurden. Darüber hinaus wurde auch die spektrale Verbreiterung im positiven Dispersionsregime untersucht. Das Hintereinanderschalten zweier Herriott-Zellen ermöglichte die Erzeugung von 15.6 fs kurzen Impulsen mit einer zuvor unerreichten Spitzenleistung von 463 MW — ein Rekord für ein System, das ohne weitere Verstärkerstufen direkt von einem Laseroszillator getrieben wird.

Die weitere zeitliche Kompression am Ausgang dieses zweistufigen Systems wurde mit dem Ansatz eines verteilten Quasi-Wellenleiters gelöst. Diese Technik ermöglicht die unabhängige Anpassung von Nichtlinearität und Dispersion, was für die Impulskompression in

Richtung einer Dauer von wenigen optischen Zyklen unerlässlich ist. Mit einer Impulsdauer von lediglich 10.8 fs bei einer Spitzen- und Durchschnittsleistung von 0.64 GW und 101 W markieren die erzeugten Laserimpulse den Beginn einer neuen Ära von verstärkerfreien Dünnscheibenlasersystemen im Gigawattbereich.

Des Weiteren wurden die beschriebenen Laserimpulse dafür genutzt, um mittels Differenzfrequenzerzeugung breitbandige und phasenstarre Strahlung im mittleren Infrarot zu erzeugen. Letztere zeichnet sich insbesondere durch ihre außergewöhnlich niedrige Grenzwellenlänge aus. Die erreichte spektrale Ausdehnung auf 3.6 µm (auf −30 dB-Niveau) mit einer mittleren Ausgangsleistung von 7.6 mW eröffnet neue Perspektiven für die feldaufgelöste Spektroskopie von biologisch relevanten funktionellen Amidgruppen.

Um die Wellenform des nahinfraroten Lasers aktiv zu stabilisieren — unabdingbar für die Ableitung eines Frequenzkamms im XUV-Spektralbereich — wurde ein neuartiges und leistungsskalierbares Konzept entwickelt. Dieses erlaubt, die Träger-Einhüllenden-Frequenz von Kerr-Linsen-modengekoppelten Oszillatoren zu kontrollieren und zu stabilisieren. Das dabei erreichte Phasenrauschen lässt sich auf weniger als 90 mrad bei einer beispiellosen Durchschnittsleistung von 105 W beziffern. Die mögliche Kombination einer Feldverlaufstabilisierung mit den zuvor vorgestellten nichtlinearen Pulskompressionstechniken ebnet den Weg für die Entwicklung einer neuen Generation kompakter oszillatorbasierter Frequenzkämme mit hohem Photonenfluss im XUV-Spektralbereich.

Die zahlreichen in dieser Dissertation vorgestellten Entwicklungen beschränken sich nicht nur auf einen Fortschritt der jeweiligen Techniken selbst, sondern liefern auch einen wichtigen Beitrag für die zukünftige Entwicklung hochpräziser laserbasierter Spektrometer für wissenschaftliche und medizinische Anwendungen.

Abstract

The advent of precision spectroscopic techniques has brought about diverse opportunities in extending our understanding of fundamental physics and bio-medical sciences. This is especially true when harnessing radiation in the exotic extreme ultra-violet (XUV) and mid-infared (IR) regions of the electromagnetic spectrum. While the former covers a multitude of atomic and molecular electronic transitions, the latter contains fundamental vibrational and rotational modes of numerous biologically-relevant molecules.

Regardless of spectral range, many of the novel spectroscopic methodologies rely on the availability of broadband, waveform-controlled radiation with high brightness. The lack of suitable laser gain media in the aforementioned wavelength ranges means such radiation is conventionally generated by nonlinearly converting high-power, femtosecond laser pulses in the near-IR spectral range, such as those generated by thin-disk oscillators. However, those pulses generally have durations in the hundreds of femtoseconds — too long for the desired high peak-power and broad spectral coverage for effective nonlinear frequency conversion. Their electric waveform also varies randomly from pulse to pulse, hindering their applications to, among others, frequency-comb spectroscopy.

This thesis describes the experimental development of various techniques to further compress the pulse duration, and the active stabilization of the output waveform in high-power thin-disk oscillators. It is shown that dispersion-controlled Herriott-type multipass-cells constitute an efficient means to broaden the spectral bandwidth of laser pulses with, in contrast to many other techniques, practically no degradation to the spatial beam quality.

It presents the first time Herriott-cells operating in the net-negative dispersion regime have been used for spectral broadening with thin-disk oscillators. The demonstration yielded the highest broadening factor obtained from any multipass-cell broadening scheme using a single nonlinear bulk medium. Spectral broadening in the positive dispersion regime is also described. Two Herriott-cells in tandem facilitated the generation of 15.6 fs pulses with an unprecedented peak power of 463 MW — a record for a system driven directly by a laser oscillator with no amplification stages.

Further compression of this dual-stage output was achieved by introducing the distributed quasi-waveguide approach. This technique enables the independent tailoring of nonlinearity and dispersion, which is essential for pulse compression towards few-optical-cycle durations. With a pulse duration of 10.8 fs and a peak and average power of 0.64 GW and 101 W, respectively. This marks the dawn of a new class of gigawatt-scale amplifier-free thin-disk laser system.

The few-cycle laser pulses are shown to drive, via intra-pulse difference-frequency generation, the formation of broadband, waveform-stable mid-IR radiation with an exceptionally short cut-off wavelength. The achieved spectral extension down to 3.6 µm (at −30 dB

level), at an average output power of 7.6 mW, opens up new perspectives for extending field-resolved spectroscopy to the biologically important amide functional groups.

To actively stabilize the near-IR driver laser waveform — crucial for deriving from it a frequency comb in the XUV region — a novel, power-scalable concept for controlling the carrier-envelope offset (CEO) frequency of Kerr-lens mode-locked oscillators was developed. It yielded CEO-frequency-stable pulses with sub-90 mrad in-loop phase noise at an unprecedented average output power of 105 W. The envisioned combination of waveform control with the presented nonlinear pulse compression techniques will pave the way for a new generation of compact, low-noise frequency combs with high photon-flux in the XUV spectral range.

The various advancements presented in this thesis not only mark a substantial development of the respective techniques themselves, but also represent a significant contribution to the coming-of-age of high-precision laser-based spectrometers for scientific and medical applications.

Contents

List of Figures

List of Tables

List of Acronyms

AOFS	acousto-optic frequency shifter
AOM	acousto-optic modulator
APD	avalanche photodetector
AR	anti-reflective
CEO	carrier-envelope offset
CEP	carrier-envelope phase
DC	direct current
DFG	difference-frequency generation
DPD	digital phase detector
DQWG	distributed quasi-waveguide
EOS	electro-optical sampling
FOD	fourth-order dispersion
FROG	frequency-resolved optical gating
FRS	field-resolved spectroscopy
FTIR	Fourier-transform infrared
FTL	Fourier-transform limit
FWHM	full-width half-maximum
GD	group delay
GDD	group delay dispersion
GNLSE	generalized nonlinear Schrödinger equation
GVD	group velocity dispersion
HC-PCF	hollow-core photonic-crystal fiber
HHG	high-harmonic generation
IPDFG	intra-pulse difference-frequency generation
IPN	integrated phase noise
IR	infared

LGS	$LiGaS_2$
NIR	near-infrared
OPA	optical parametric amplification
OSA	optical spectrum analyzer
PID	proportional–integral–derivative
PLL	phase-locked loop
PSD	power spectral density
QED	quantum electro-dynamics
RF	radio frequency
RIN	relative intensity noise
RMS	root-mean-square
SAM	self-amplitude modulation
SFG	sum-frequency generation
SHG	second-harmonic generation
SNR	signal-to-noise ratio
SPIDER	spectral phase interferometry for direct electric field reconstruction
SPM	self-phase modulation
TFP	thin-film polarizer
THG	third-harmonic generation
Ti	Titanium
TOD	third-order dispersion
XUV	extreme ultra-violet
YAG	yttrium aluminium garnet
Yb	Ytterbium
ZnSe	zinc selenide

Introduction

Over the past two decades, remarkable progress has been made in the development of laser-based, high-precision spectroscopic techniques in virtually all ranges of the electromagnetic spectrum [1–6]. One prominent example is direct frequency comb spectroscopy in the extreme ultra-violet (XUV) range where many atoms and molecules exhibit characteristic electronic transitions [7, 8]. The plethora of applications of XUV frequency comb spectroscopy includes, for example, the development of novel nuclear clocks with unprecedented high accuracy [9, 10] or the long-awaited direct spectroscopy of the unique 1S–2S transition in singly ionized Helium [11].

The XUV-based probing of electronic transitions in atoms and molecules is complemented by spectroscopic applications towards the other end of the electromagnetic spectrum, namely in the mid-infared (IR) (2.5 to 20 µm), where many biologically relevant molecules exhibit fundamental rotational and vibrational modes [12]. Among the many fascinating possibilities created by vibrational spectroscopy is the direct analysis, in medical settings, of biological samples, such as human blood serum and plasma [13, 14]. Blood serum is known to contain a variety of proteins, carbohydrates, lipids and amino acids as well as a vast amount of metabolites [15]. Minor changes in the composition or concentration of the individual components can readily be used as early indicators in, for example, early diagnostic of illnesses [14, 16].

Nevertheless, the detection of miniscule yet representative changes in the composition of real-world biological samples via vibrational spectroscopy is technically challenging. As a result of its numerous different constituents, human blood serum exhibits a highly complex spectral response extending more or less across the entire mid-IR spectral range [17]. Furthermore, the various molecules which contribute to the spectroscopic signal are present at vastly different concentrations — often multiple orders of magnitude apart [18]. Obtaining meaningful results from the vibrational spectroscopy of blood serum and plasma thus requires utilizing state-of-the-art measurement methods such as field-resolved spectroscopy (FRS) which combines high sensitivity with high dynamic range over a broadband spectral range [6].

While direct XUV frequency comb spectroscopy and field-resolved IR spectroscopy appear, at first sight, to have little in common, both techniques rely heavily on the availability of broadband, waveform-controlled radiation of high brightness. The radiation should, furthermore, be contained in short pulses with low amplitude- and phase noise, and delivered at megahertz pulse repetition rates to boost the achievable signal-to-noise ratio (SNR)

of the targeted spectroscopic applications. As the direct generation of such radiation in the XUV and mid-IR is hindered by a lack of suitable gain media in the respective ranges, they are conventionally obtained by converting near-IR light via such nonlinear processes as intra-pulse difference-frequency generation (IPDFG) and high-harmonic generation (HHG).

A promising class of lasers for driving the required frequency conversion are high-power mode-locked femtosecond oscillators, in which the Ytterbium (Yb)-doped gain material is in a thin-disk geometry [19, 20]. With this relatively mature technology, microjoule, femtosecond pulses have already been generated at megahertz repetition rates, which translates to hundreds of watts of average power — potentially further scalable into the kilowatt range [21–23]. In particular, Kerr-lens mode-locked thin-disk oscillators based on Yb-doped yttrium aluminium garnet (YAG) as gain medium exhibit excellent noise characteristics, reaching shot-noise limited performance at a wide frequency range down to 100 kHz. Augmented with active noise suppression in the acoustic frequency range, they are ideal for applications demanding low-noise performance [24]. Unfortunately, the relatively narrow gain-bandwidth of Yb:YAG typically limits the output pulse durations to multiple hundreds of femtoseconds. As a result, extra-cavity spectral broadening and subsequent temporal compression of the emitted pulses are required to enhance the peak power to a level that is sufficient for effectively generating broadband radiation in the XUV and mid-IR spectral ranges. Moreover, for applications based on frequency combs, the electric waveform under the intensity envelope of the emitted pulse needs to be identical, or at least periodically reproducible between pulses. This is equivalent to having, in the frequency domain, a constant frequency offset for the so called CEO frequency. However, the waveform generated from a laser oscillator generally fluctuates randomly from pulse to pulse. While the process of IPDFG inherently stabilizes the CEO frequency in the nonlinear mixing process, for near-infrared (NIR)-laser driven frequency-comb applications in the XUV range, there is an indispensable need to actively stabilize the driver laser's waveform.

The goal of this thesis is to devise methods and construct experimental demonstrations for mitigating the above-mentioned shortcomings of Kerr-lens mode-locked thin-disk oscillators. By extending the parameter ranges that nonlinear pulse compression and waveform control can attain to unprecedented levels, this thesis contributes to the ongoing development of high-precision spectrometers in the XUV and mid-IR spectral ranges.

This thesis is structured in the following way: In *chapter 2*, Herriott-type multipass-cells — an efficient scheme for spectrally broadening the output of high-power thin-disk oscillators — are introduced. After a brief review of the geometrical design considerations and the fundamentals of nonlinearity and dispersion control of Herriott-cells, it presents the first demonstration of spectral broadening in a Herriott-cell operating in the net-negative dispersion regime and driven by an oscillator at around a wavelength of 1 µm. The achieved spectral broadening factors are unprecedented for an all-bulk Herriott-cell with a single nonlinear medium. However, the complicated soliton dynamics in the net-negative dispersion regime limited the compression quality and hindered the gain in peak power.

These limitations can be overcome by progressing to spectral broadening in Herriott-cells operating in the net-positive dispersion regime, which are investigated in *chapter 3*.

The cascading of two dispersion-optimized Herriott-cell stages with intermediate recompression facilitated the generation of sub-20 fs pulses with close to diffraction-limited spatial quality. Most importantly, the achievable peak power of more than 460 MW after temporal recompression is one of the highest peak powers that is currently available from an ultrafast laser system without extra-cavity amplification. It already constitutes a significant step in the development of low-noise driver lasers for the efficient frequency conversion into different ranges of the electromagnetic spectrum.

A concept for compressing the obtained pulses towards even shorter durations is introduced in *chapter 4*. The DQWG approach, where the spectral broadening occurs in multiple individual plates, enables the fine control of the nonlinearity and dispersion in each propagation segment — crucial for reaching few-cycle pulse durations. In a proof-of-concept experiment, the DQWG setup is shown to generate pulses with durations as short as 10.8 fs, corresponding to a peak power of 0.64 GW. This demonstration of gigawatt-scale peak powers from an amplifier-free system at megahertz repetition rates represent a milestone in the coming-of-age of modern thin-disk laser technology.

The few-cycle pulses are subsequently put to test in the generation of short-wavelength mid-IR radiation via IPDFG in a nonlinear crystal (*chapter 5*). The resulting mid-IR radiation features an exceptionally low cut-off wavelength of 3.6 µm (at −30 dB level) at an average output power of 7.6 mW. This extends the range of chemicals detectable by the envisioned application of FRS on human blood sera to include important compounds such as those containing amide functional groups.

Lastly, a novel, power-scalable method for stabilizing the CEO frequency of high-power Kerr-lens mode-locked thin-disk oscillators is described in *chapter 6*. The method is based on intra-cavity loss-modulation using an acousto-optic modulator (AOM), which at the same time serves as the nonlinear Kerr-medium inside the laser resonator. The CEO frequency is stabilized with a low residual in-loop phase noise < 90 mrad at a record average output power of 105 W. This paves the way for the generation of highly stable, high-photon-flux XUV frequency combs for high-precision spectroscopic applications.

These chapters are accompanied by *chapter 1*, which provides a brief introduction to the mathematical description of the underlying theory and a *concluding chapter*, which summarizes the main results and provides an outlook on the further optimization of the presented methods.

1

Fundamentals of ultrafast optics

This chapter gives a short introduction into the basic concepts of laser beam propagation and selected linear and nonlinear light-matter interactions utilized in this thesis. In the following sections, laser radiation is treated as an electro-magnetic field in a source-free dielectric medium which can, in general, be described by Maxwell's equations [25, p. 164]

$$\nabla \times \boldsymbol{\mathcal{H}} = \frac{\partial \boldsymbol{\mathcal{D}}}{\partial t} \tag{1.1}$$

$$\nabla \times \boldsymbol{\mathcal{E}} = -\frac{\partial \boldsymbol{\mathcal{B}}}{\partial t} \tag{1.2}$$

$$\nabla \cdot \boldsymbol{\mathcal{D}} = 0 \tag{1.3}$$

$$\nabla \cdot \boldsymbol{\mathcal{B}} = 0 \tag{1.4}$$

where $\boldsymbol{\mathcal{E}}(\boldsymbol{r}, t)$ and $\boldsymbol{\mathcal{H}}(\boldsymbol{r}, t)$ are vector fields representing the electric- and magnetic field and $\boldsymbol{\mathcal{D}}(\boldsymbol{r}, t)$ and $\boldsymbol{\mathcal{B}}(\boldsymbol{r}, t)$ are vector fields corresponding to the electric- and magnetic flux density as functions of the position $\boldsymbol{r}$ and time t. The contribution of the electric and magnetic properties of the medium are contained in the polarization density $\boldsymbol{\mathcal{P}}(\boldsymbol{\mathcal{E}}, \boldsymbol{r}, t)$ and the magnetization density $\boldsymbol{\mathcal{M}}(\boldsymbol{\mathcal{H}}, \boldsymbol{r}, t)$ which themselves can depend on the respective fields. These polarization- and magnetization densities link the flux densities and fields via [25, p. 164]

$$\boldsymbol{\mathcal{D}} = \epsilon_0 \boldsymbol{\mathcal{E}} + \boldsymbol{\mathcal{P}} \tag{1.5}$$

$$\boldsymbol{\mathcal{B}} = \mu_0 \boldsymbol{\mathcal{H}} + \mu_0 \boldsymbol{\mathcal{M}}\,, \tag{1.6}$$

where ϵ_0 is the free space electric permittivity and μ_0 is the free space magnetic permeability, both of which are electromagnetic constants which are related to the speed of light in vacuum c_0 by [25, p. 163]

$$c_0 = \frac{1}{\sqrt{\epsilon_0 \mu_0}}\,. \tag{1.7}$$

Applying the curl operator to equation 1.2 yields

$$\nabla \times (\nabla \times \boldsymbol{\mathcal{E}}) = -\frac{\partial}{\partial t}(\nabla \times \boldsymbol{\mathcal{B}})\,. \tag{1.8}$$

For nonmagnetic, homogeneous and isotropic media, using equations 1.1 and 1.5 as well as the vector identity $\nabla \times (\nabla \times \boldsymbol{V}) = \nabla(\nabla \cdot \boldsymbol{V}) - \nabla^2 \boldsymbol{V}$, this equation can be transformed into the wave-equation [25, p. 1019]

$$\nabla^2 \boldsymbol{\mathcal{E}} - \frac{1}{c_0^2}\frac{\partial^2 \boldsymbol{\mathcal{E}}}{\partial t^2} = \mu_0 \frac{\partial^2 \boldsymbol{\mathcal{P}}}{\partial t^2} \tag{1.9}$$

which can be used to efficiently describe the spatial and temporal evolution of laser radiation in the respective optical medium.

1.1 Linear pulse propagation

1.1.1 Gaussian beams

In the absence of higher order field contributions and dispersion, the polarization density of a nonmagnetic, homogeneous and isotropic medium can be expressed as a linear function of the electric field [25, p. 166]

$$\boldsymbol{\mathcal{P}} = \epsilon_0 \chi \boldsymbol{\mathcal{E}} \tag{1.10}$$

where $\chi = n^2 - 1$ is the electric susceptibility which is defined via the refractive index n. The refractive index can be understood as a material property which relates the speed of light c within the medium to the speed of light in vacuum via

$$n = \frac{c_0}{c} = \sqrt{\frac{\epsilon}{\epsilon_0}\frac{\mu}{\mu_0}} \tag{1.11}$$

where ϵ and μ are electric permittivity and the magnetic permeability of the medium, respectively. Substituting the linear, non-dispersive polarization density from equation 1.10, the wave equation 1.9 can be simplified to

$$\nabla^2 \boldsymbol{\mathcal{E}} - \frac{1}{c^2}\frac{\partial^2 \boldsymbol{\mathcal{E}}}{\partial t^2} = 0\,. \tag{1.12}$$

For the simplest case of a monochromatic wave

$$\boldsymbol{\mathcal{E}}(\boldsymbol{r}, t) = \mathrm{Re}\{\boldsymbol{E}(\boldsymbol{r}) \cdot e^{i\omega t}\}\,, \tag{1.13}$$

where $\boldsymbol{E}(\boldsymbol{r})$ denotes the complex-valued electric field amplitude vector and ω is the angular frequency with corresponding wavenumber $k = \omega/c$, equation 1.12 can be transformed into the Helmholtz-equation

$$\nabla^2 \boldsymbol{E}(\boldsymbol{r}) + k^2 \boldsymbol{E}(\boldsymbol{r}) = 0\,. \tag{1.14}$$

It should be noted that while the preceding transformation is generally not restricted to monochromatic waves, a similar equation can only be found for electric fields in which the spatial- and temporal dependence is separable. A more detailed analytical approach including first-order space-time couplings can for example be found in reference [26].

Laguerre-Gaussian modes

For a monochromatic wave propagating along the z direction, the position dependant electric field amplitude $\boldsymbol{E}(\boldsymbol{r})$ can be further decomposed into

$$\boldsymbol{E}(\boldsymbol{r}) = \boldsymbol{A}(\boldsymbol{r}) \cdot e^{-ikz} \tag{1.15}$$

where $\boldsymbol{A}(\boldsymbol{r})$ describes the amplitude envelope of an oscillation along the z-axis with carrier frequency k. Substituting the field amplitude $\boldsymbol{E}(\boldsymbol{r})$ in equation 1.14 then results in

$$\frac{\partial^2 \boldsymbol{A}(\boldsymbol{r})}{\partial x^2} + \frac{\partial^2 \boldsymbol{A}(\boldsymbol{r})}{\partial y^2} + \frac{\partial^2 \boldsymbol{A}(\boldsymbol{r})}{\partial z^2} - 2ik\frac{\partial \boldsymbol{A}(\boldsymbol{r})}{\partial z} = 0\,. \tag{1.16}$$

By assuming that the amplitude envelope varies slowly along the propagation direction, i.e. [25, p. 51]

$$\left|\frac{\partial^2 \boldsymbol{A}(\boldsymbol{r})}{\partial z^2}\right| \ll k \left|\frac{\partial \boldsymbol{A}(\boldsymbol{r})}{\partial z}\right| \tag{1.17}$$

the third term in equation 1.16 can be dropped yielding the so-called paraxial approximation of the Helmholtz equation [25, p. 51]

$$\frac{\partial^2 \boldsymbol{A}(\boldsymbol{r})}{\partial x^2} + \frac{\partial^2 \boldsymbol{A}(\boldsymbol{r})}{\partial y^2} - 2ik\frac{\partial \boldsymbol{A}(\boldsymbol{r})}{\partial z} = 0\,. \tag{1.18}$$

The solution space to equation 1.18 is spanned by a set of orthogonal modes $\boldsymbol{A}_{l,p}$ where the exact subset depends on the boundary conditions of the eigenvalue problem which best match the experimental geometry. It should be noted that for a set of orthogonal modes, every linear combination of $\boldsymbol{A}_{l,p}(\boldsymbol{r})$ is also a valid solution to the paraxial Helmholtz equation. Since the laser radiation described in this thesis features a cylindrical symmetry it is usually best described by the subset of Laguerre-Gaussian modes [25, p. 102]

$$\begin{aligned}\boldsymbol{A}_{l,p}(\boldsymbol{r} = (r, \phi, z)) = \boldsymbol{A}_{l,m}\frac{w_0}{w(z)}\left(\frac{r}{w(z)}\right)^l \mathbb{L}_p^l\left(\frac{2r^2}{w^2(z)}\right)\exp\left(\frac{-r^2}{w^2(z)}\right)\times \\ \exp\left[-ik\frac{r^2}{2R(z)} \mp il\phi + i\psi(z)\right]\end{aligned} \tag{1.19}$$

with the peak amplitude $\boldsymbol{A}_{l,m}$, the radial index $p \in \mathbb{N}_0$ and azimuthal index $l \in \mathbb{N}_0$ and the generalized Laguerre polynomials $\mathbb{L}_p^l$. The sign of the ambiguous phase term in the second line in equation 1.19 describes the handedness of the waveform rotation and is described in further detail in reference [25, p. 103]. Furthermore, equation 1.19 introduces the parameters which are conventionally used to describe the linear propagation of a laser beam, namely the beam width [25, p. 82]

$$w(z) = w_0\sqrt{1 + \left(\frac{z}{z_r}\right)^2}\,, \tag{1.20a}$$

the radius of the wavefront curvature

$$R(z) = z\left(1 + \left(\frac{z_r}{z}\right)^2\right), \tag{1.20b}$$

and the Gouy phase

$$\psi(z) = (|l| + 2p + 1) \cdot \arctan\left(\frac{z}{z_r}\right), \tag{1.20c}$$

as well as the beam waist

$$w_0 = \sqrt{\frac{z_r \lambda}{\pi n}} \tag{1.20d}$$

which serves as a measure for the beam size in a focal plane (i.e. a plane where $R(z) = 0$). From equations 1.20 it is obvious that the shape of the two dimensional beam profile for a monochromatic wave solely depends on the Rayleigh length

$$z_r = \frac{\pi w_0^2 n}{\lambda} \tag{1.21}$$

and the distance z to the focus as well as the order of the mode.

Ideal Gaussian beams

In this thesis, a special emphasis is placed on the zero-order Laguerre-Gaussian mode ($l = 0, p = 0$) with the electric field amplitude

$$E_{0,0}(r,z) = A_0 \frac{1}{\sqrt{\pi}} \frac{w_0}{w(z)} \exp\left(\frac{-r^2}{w^2(z)}\right) \exp\left(-i\left(kz + k\frac{r^2}{2R(z)} - \psi(z)\right)\right) \tag{1.22}$$

In equation 1.22, a linear polarization of the electric field has been assumed to facilitate the scalar treatment of the electric field in the following discussion. Since the field amplitude given in equation 1.22 is not an observable in the experiment, it is common to define the intensity [25, p. 82]

$$I(r,z) = |E_{0,0}(r,z)|^2 = I_0 \left(\frac{w_0}{w(z)}\right)^2 \exp\left(\frac{-2r^2}{w^2(z)}\right) \tag{1.23}$$

where

$$I_0 = |A_0|^2 = 2 \cdot P_{peak}/\pi w_0^2 = 2 \cdot I_{peak} \tag{1.24}$$

is the on-axis value of the peak intensity I_{peak} generated by a laser beam with peak power P_{peak} at the beam waist w_0. Equation 1.23 describes the propagation of light which is confined to a two-dimensional Gaussian intensity profile in each fixed plane z (cf. Fig. 1.1 a) and is therefore called a *Gaussian beam*.

For a Gaussian beam, the previously introduced beam width $w(z)$ defines the size of a spot where the intensity is larger than I_0/e^2. Furthermore, the Rayleigh length z_r is found to represent the axial distance to the beam waist w_0 at which the on-axis intensity has

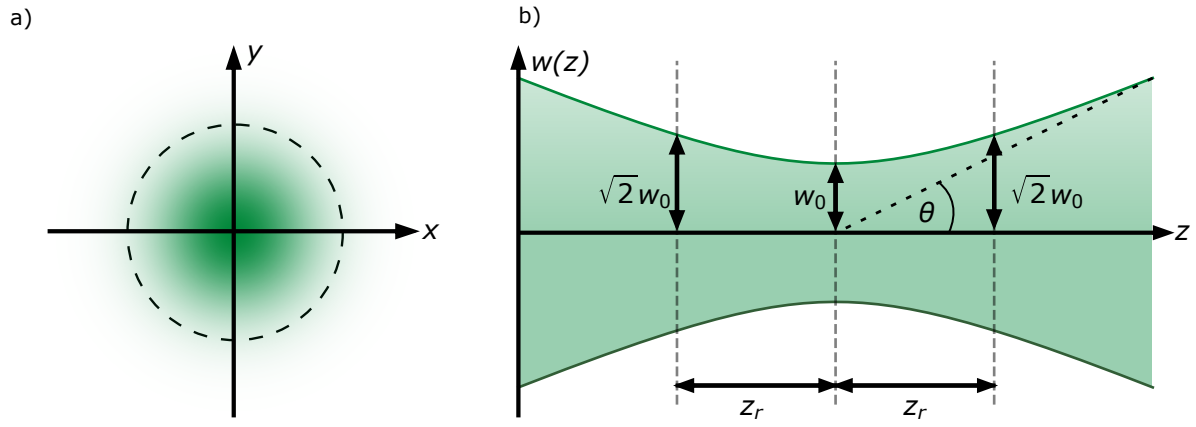

Fig. 1.1: Schematic depiction of a Gaussian beam. **a)** Two-dimensional Gaussian intensity profile $I(x, y)$ (green). The dashed black line indicates the circumference beyond which the intensity has dropped below the $1/e^2$ value (cf. equation 1.20). **b)** Exemplary evolution of the $1/e^2$ diameter of a Gaussian beam with waist size w_0, Rayleigh range z_r and divergence angle θ propagating in z-direction.

dropped by a factor of two. Since the Rayleigh length effectively determines the length over which a beam can propagate without diverging significantly it is also called the focus length. A Gaussian beam is conventionally called collimated, if its Rayleigh length is significantly longer than the intended propagation distance which is typically equivalent to having a beam that features a large waist w_0. As a consequence, the spot size of a collimated beam only changes marginally during propagation. For a propagation distance which is significantly longer than the Rayleigh length ($z \gg z_r$), the beam width increases approximately linearly with z with the slope of [25, p. 85]

$$\theta = \left(\frac{\lambda}{\pi n w_0} \right) \tag{1.25}$$

where θ denotes the divergence of the beam. An exemplary propagation of a Gaussian beam with the relevant beam parameters is schematically depicted in Fig. 1.1 b.

As a special peculiarity, Laguerre-Gaussian beams exhibit an on-axis phase shift called Gouy-phase which has been introduced in equation 1.20c and which for a Gaussian beam can be written as

$$\psi(z) = \arctan\left(\frac{z}{z_r} \right) . \tag{1.26}$$

This additional phase retardation describes a delay of the wavefronts with respect to those of an infinite plane wave. The phase shift $\psi(z)$ increases continuously while the beam passes through a beam waist and can be shown to take a value of π for a full transition from $z = -\infty$ to $z = \infty$ [25, p. 86]. An intuitive derviation of the Gouy phase-shift can

for example be found in reference [27]. The Gouy phase shift can be shown to originate from the transverse spatial confinement of a Gaussian beam. A detailed mathematical treatment of this effect is given in reference [28].

In a more geometric interpretation, the Gouy-phase shift can be considered an absolute measure of the distance between two transversal planes along the propagation direction z which is invariant under transformation of the beam caustic [29]. More specifically, consider the example where an obstacle (such as an aperture) is placed in a collimated Gaussian beam at position z_1 where the Gouy-phase has a fixed value of ψ_1. After propagation of a distance Δz, the beam profile exhibits a distinct diffraction pattern at position $z_2 = z_1 + \Delta z$, where the Gouy-phase takes a value of $\psi_2 = \psi_1 + \Delta\psi$. The beam caustic is subsequently transformed by an optical system, e.g. focused down by a lens. In the focused beam, the image plane of the obstacle and the plane in which the diffraction pattern is observable is generally no longer separated by the axial distance Δz. However, the corresponding planes have retained their relative Gouy phase difference $\Delta\psi$ since the Gouy-phase scales the propagation distance z with the transformed value of z_r. The Gouy-phase can therefore efficiently be used for distinguishing the relative position of particular transversal planes independent of whether the beam is focused or collimated. A more comprehensive description of the geometric interpretation of the Gouy-phase is given for example in reference [29].

The M^2 factor

While the description of laser beams by the zero-order Gaussian mode can help to markedly simplify the underlying calculation, in reality, most beams can only be described accurately by a linear combination of the zero- and higher-order solutions to the paraxial wave equation. However, such *mixed mode* beams are often still dominated by the Gaussian nature of the zero-order solution. It can therefore be instructive to relate the propagation parameters of a real laser beam to that of an ideal Gaussian beam to be able to approximate, for example, the evolution of the beam caustic without first performing a rigorous analysis of the underlying mode structure.

The deviation of a real laser beam from an ideal Gaussian beam can be quantified by determining its M^2 factor — which also serves as a measure for the focusability and hence the quality of the laser beam [30]. The M^2 factor is defined as the ratio of the beam parameter product $BPP = \theta(\tilde{w}_0) \cdot \tilde{w}_0$ of the measured beam to that of an ideal Gaussian beam, where $D4\sigma = 2\tilde{w}_0$ is the second-moment beam width (also termed D4σ-width) which for the x-dimension is defined as

$$D4\sigma = 4\sqrt{\frac{\int_{-\infty}^{\infty}\int_{-\infty}^{\infty} I(x,y)(x-\overline{x})^2 \,\mathrm{d}x\,\mathrm{d}y}{\int_{-\infty}^{\infty}\int_{-\infty}^{\infty} I(x,y)\,\mathrm{d}x\,\mathrm{d}y}} \tag{1.27}$$

with the centroid position of the beam profile in the x-direction

$$\overline{x} = \frac{\int_{-\infty}^{\infty}\int_{-\infty}^{\infty} I(x,y)x \,\mathrm{d}x\,\mathrm{d}y}{\int_{-\infty}^{\infty}\int_{-\infty}^{\infty} I(x,y)\,\mathrm{d}x\,\mathrm{d}y}\,. \tag{1.28}$$

Although the definition of the $D4\sigma$ beam width in equation 1.27 looks rather mathematical, it can be calculated directly by most commercial beam profilers available today.

While in principle the M^2 factor can be determined by simply measuring the $D4\sigma$ beam width in the focus and in the far field ($z \gg z_r$), a standardized measurement procedure has been defined in ISO 11146-1 (cf. reference [31]) to yield more consistent and precise results:

1. Create a focus with an adequate spot size, i.e. the $D4\sigma$ beam width should not be smaller than approximately 20 times the spatial resolution of the utilized beam profiler

2. Measure the $D4\sigma$ beam width for two orthogonal axes for at least ten different axial positions for which:

   - Five measurements should be taken at an axial position distributed around the beam waist ($z < z_r$)
   - Five measurements should be taken at an axial position corresponding to the far-field of the laser beam ($z > 2z_r$)

3. Perform a fit of the hyperbolic function [32]

$$\tilde{w}^2(z) = \tilde{w}_0^2 + \left(M^2 \frac{\lambda}{\pi n \tilde{w}_0} \right)^2 (z - z_0)^2 \,, \tag{1.29}$$

   where z_0 is the axial position of the beam waist, to the measurement of the beam caustic to determine the M^2 factor.

It should be noted that the above enumeration is a strongly condensed and simplified version of the required test procedure. A comprehensive explanation including various exceptions as well as additional information and the applicability ranges can be found in the corresponding ISO norm [31]. Comparing equations 1.20d and 1.29, the M^2 factor is found to always be one for an ideal Gaussian beam and larger than one for mixed-mode beams.

In practice, the M^2 factor relates the beam divergence to the achievable minimum waist size of the focused beam. It can therefore be understood as a measure for describing how tightly a beam that was previously collimated to a fixed size can be focused. For a mixed-mode beam, the measured waist size $\tilde{w}_{0,meas}$ is a factor $\sqrt{M^2}$ larger than that of an *embedded Gaussian beam* with the same divergence angle θ_{meas}. The caustic of the mixed mode beam can therefore typically be approximated by

$$w_{mm}(z) = \sqrt{M^2} \cdot w_{0,emb} \cdot \sqrt{1 + \left(\frac{z}{z_{r,emb}} \right)^2} \tag{1.30}$$

where w_{mm} is the spot size of the mixed-mode beam and $w_{0,emb} = \tilde{w}_{0,meas}/\sqrt{M^2}$ and $z_{r,emb}$ are the waist size and Rayleigh length of the embedded Gaussian beam, respectively. It

should be emphasized that the above definition of the M^2 factor is based on the assumption of a monochromatic beam. However, the calculation of the beam caustic using the concept of M^2 factor and embedded Gaussian beam still provides reasonable results for non-monochromatic radiation as long as the wavelength spread remains much smaller than the center wavelength (i.e. $\Delta\lambda \ll \lambda_0$).

1.1.2 Beam propagation: ABCD-Matrix formalism

In the previous section, a formalism has been introduced which enables the calculation of the beam caustic $w(z)$ along the optical axis as a function of the Rayleigh length z_r for Gaussian- and mixed-mode beams (cf. equation 1.30). Up to this point, however, only the propagation in a single, nonmagnetic, homogeneous and isotropic medium has been considered which does not provide any information on how the caustic is influenced by an optical system consisting of various optical elements such as lenses or mirrors or even much simpler things such as a change of the propagation medium. While in principle, arbitrary linear transformations to the beam caustic can be modelled by appropriately modifying the amplitude- and phase of the electric field (c.f. equation 1.22), the exact calculation quickly becomes cumbersome due to the rather high complexity.

Fortunately, for Gaussian beams, the calculation of the beam caustic throughout an optical system can be simplified significantly as long as the individual optical components can be assumed to only act on the phase of the electric field (i.e. neglecting gain and losses). For a more convenient notation, the complex beam parameter q is introduced as

$$\begin{aligned} q(z) &= z + iz_r \\ \frac{1}{q(z)} &= \frac{1}{R(z)} - i\frac{\lambda}{\pi n w^2(z)} \end{aligned} \tag{1.31}$$

which contains the full information needed to calculate the beam parameters (equations 1.20). Any optical system that can be characterized by a *transfer matrix* (also termed *ABCD-matrix*)

$$\mathbf{M} = \begin{pmatrix} A & B \\ C & D \end{pmatrix} \tag{1.32}$$

where $(A, B, C, D) \in \mathbb{R}$ will then transform the complex beam parameter according to [25, p. 97]

$$q_{out} = \frac{Aq_{in} + B}{Cq_{in} + D} \tag{1.33}$$

where q_{in} and q_{out} are the complex beam parameters of the input- and output beam, respectively. For an optical system containing N subsequent elements, the transfer matrix of the whole system $\mathbf{M}_{tot}$ can simply be determined by multiplying the transfer matrices of the individual components [25, p. 98]

$$\mathbf{M}_{tot} = \mathbf{M}_N \cdot \mathbf{M}_{N-1} \cdot ... \cdot \mathbf{M}_2 \cdot \mathbf{M}_1 \tag{1.34}$$

where $\mathbf{M}_k$ with $1 \leq k \leq N$ is the transfer matrix of the k^{th} component. A comprehensive list of ABCD-matrices for various optical elements can be found in reference [25, p. 29-30]. Importantly, the results of the beam caustic calculation using the transfer matrix method are only valid if both the input and output electric fields can be described within the paraxial approximation (cf. equation 1.17). The validity of the approximation can for example be assessed by calculating the beam paraxiality, which is described in further detail in reference [33].

Knowledge of the complex beam parameter throughout an optical system can undoubtedly be extremely valuable for estimating beam size and intensity at different axial positions z. However, the underlying calculation is restricted to electric fields for which the optical axis coincides with the propagation direction of the carrier oscillation (which has arbitrarily been chosen to be the z-direction in equation 1.15). Consequently, the positional evolution of off-axis beams needs to be described using a different approach: In linear optical systems, a light ray can be defined as a curve whose tangent is collinear with the propagation direction of the carrier oscillation [25, p. 5]. The evolution of a light ray with initial distance x_0 and angle x_0' to the center axis of an optical system is then given by [25, p. 28]

$$\begin{pmatrix} x_1 \\ x_1' \end{pmatrix} = \mathbf{M} \cdot \begin{pmatrix} x_0 \\ x_0' \end{pmatrix} = \begin{pmatrix} A & B \\ C & D \end{pmatrix} \cdot \begin{pmatrix} x_0 \\ x_0' \end{pmatrix} \tag{1.35}$$

where x_1 and x_1' are the position and angle corresponding to the output ray of the optical system, respectively. In analogy to equation 1.33, equation 1.35 is only valid in the paraxial approximation. This is equivalent to claiming

$$\sin(x') = x' \tag{1.36}$$

which is known as the *small-angle approximation*. The method for calculating the ray position and angle is termed *ray tracing* and can effectively be used to parametrize the evolution of the centroid position of a Gaussian beam in a coordinate system spanned by the optical components.

1.1.3 Laser pulses and the spectral phase

Up to this point, laser radiation has been treated as a spatially modulated monochromatic wave (cf. equation 1.22) with the electric field given by

$$\boldsymbol{\mathcal{E}}(\boldsymbol{r}, t) = \mathrm{Re}\{\boldsymbol{E}(\boldsymbol{r}, t) \cdot e^{i\omega t}\} = \mathrm{Re}\{\boldsymbol{A}(\boldsymbol{r}) \cdot e^{i(\omega t - kz)}\}\,. \tag{1.37}$$

In order to describe the temporal structure of laser radiation, it is instructive to drop the spatial terms in equation 1.37. Setting $\boldsymbol{A}(\boldsymbol{r})$ constant and assuming a linear polarization of the electric field, a monochromatic plane wave propagating in z-direction can simply be described by

$$\mathcal{E}(z, t) = \mathrm{Re}\{E(z, t) \cdot e^{i\omega t}\} = \mathrm{Re}\{e^{i(\omega t - kz)}\}\,. \tag{1.38}$$

Description of laser pulses

While the previously used monochromatic approximation has been shown to allow a simple derivation of the spatial beam properties it is not suitable for the description of laser pulses containing a multitude of different frequency components. To adequately represent such laser pulses, the electric field is — analogous to equation 1.15 — commonly separated into a slowly-varying complex envelope function $E(z,t)$ and a fast carrier oscillation with angular frequency ω_0, yielding [34, p. 27]

$$\mathcal{E}(z,t) = \mathrm{Re}\{E(z,t) \cdot e^{i\omega_0 t}\}\,. \tag{1.39}$$

The complex envelope function $E(z,t)$ can then be decomposed into [34, p. 87]

$$E(z,t) = A(z,t) \cdot e^{i\phi(z,t)} \tag{1.40}$$

where $A(z,t)$ is the real-valued amplitude envelope and $\phi(z,t)$ is the *temporal phase* of the pulse.

Since laser pulses consist of a coherent superposition of monochromatic waves with frequencies ω and with well-defined relative phase, the complex electric field amplitude $E(z,t)$ can alternatively be written as the inverse Fourier-transform of the single-sided complex frequency amplitude $E(\omega-\omega_0)$ centred around the carrier frequency ω_0 [34, p. 28], yielding

$$E(z,t) = \frac{1}{2\pi}\int_{-\infty}^{\infty} E(z,\omega-\omega_0)e^{i\omega t}\mathrm{d}\omega = \mathcal{IFT}\{E(z,\omega-\omega_0)\}\,. \tag{1.41}$$

In analogy to equation 1.23, the observable in the experiment is the temporal intensity $I(t)$ which at a fixed axial position z is given by

$$I(t) = \frac{\epsilon_0 c}{2} \cdot A^2(t) \tag{1.42}$$

where the amplitude envelope $A(t)$ has been assumed to vary much slower than the electric field. This allows the time domain electric field to be expressed as a simple function of the intensity and temporal phase

$$E(t) \propto \sqrt{I(t)} \cdot e^{i(\omega_0 t+\phi(t))}\,. \tag{1.43}$$

In analogy to equation 1.40, the complex frequency amplitude $E(z,\omega)$ — which is the Fourier-transform of the time-domain field envelope $E(z,t)$ — can be written as [34, pp. 27, 87]

$$E(z,\omega) = \mathcal{FT}\{E(z,t)\} = A(z,\omega) \cdot e^{i\varphi(z,\omega)}\,, \tag{1.44}$$

where $A(z,\omega)$ is the real-valued frequency amplitude envelope and $\varphi(z,\omega) = k \cdot z$ is the *spectral phase* of the pulse. It is easily seen that equation 1.41 can describe a laser pulse with a temporal pulse shape that for each axial position z is dictated by the spectral amplitude envelope $A(\omega)$ and spectral phase $\varphi(\omega)$. For a given spectral amplitude envelope, the shortest pulse duration is always achieved for a constant spectral phase across all

frequencies ω. Laser pulses with $\varphi(\omega) = \text{const.}$ are therefore also termed *Fourier-limited* or *bandwidth-limited*. Generally, $S(\omega)$ can be defined as the *spectrum* of the pulse via

$$S(\omega) = \frac{\epsilon_0 c}{4\pi} \cdot A^2(\omega) \tag{1.45}$$

which yields the simplified expression for the frequency domain electric field

$$E(\omega) \propto \sqrt{S(\omega)} \cdot e^{i\varphi(\omega)} \,. \tag{1.46}$$

Pulses generated by a Kerr-lens mode-locked laser can typically be described by an amplitude envelope [34, p. 64 ff., 35, p. 72]

$$A(t) = \text{sech}\left([2 \cdot \ln(1+\sqrt{2})] \cdot \frac{t}{\tau_{FWHM}} \right) \tag{1.47}$$

where τ_{FWHM} denotes the full-width half-maximum (FWHM) pulse duration of the temporal intensity profile. According to the shape of their intensity profile, such pulses are therefore often termed *sech²-pulses*. For a Fourier-transform limited pulse with constant temporal phase $\phi(t)$, the corresponding spectral amplitude envelope can be obtained from the Fourier-transform of $A(t)$ yielding

$$A(\omega) = \mathcal{FT}\{A(t)\} = \frac{\pi \tau_{FWHM}}{2 \cdot \ln(1+\sqrt{2})} \cdot \text{sech}\left([2 \cdot \ln(1+\sqrt{2})] \cdot \frac{\omega}{\omega_{FWHM}} \right) . \tag{1.48}$$

By comparing coefficients, the FWHM spectral bandwidth is then found to be

$$\nu_{FWHM} = \frac{\omega_{FWHM}}{2\pi} = \frac{4 \cdot [\ln(1+\sqrt{2})]^2}{\pi^2 \tau_{FWHM}} \approx \frac{0.315}{\tau_{FWHM}} \,. \tag{1.49}$$

From equation 1.49 it is immediately evident that the pulse duration and spectral bandwidth of a laser pulse are linked by a numerical factor (0.315 for a sech² pulse) which depends on the spectral shape of the pulse and which is named the *time-bandwidth product*. It should be noted that the time-bandwidth product is defined using a Fourier-limited pulse and therefore only gives an estimate of the shortest possible pulse duration that is achievable for a given bandwidth. In practice, pulse compression towards the bandwidth-limit can be achieved by meticulously controlling the spectral phase.

Propagation of pulses in a dispersive medium

To gain deeper insights into how a laser pulse can be compressed close to its bandwidth-limit, it is instructive to take a closer look at how the spectral phase and temporal pulse shape evolve during the linear propagation in a nonmagnetic, homogeneous and isotropic medium. In equation 1.10, the polarization density $\boldsymbol{\mathcal{P}}$ of a medium has been defined as a function of its electric susceptibility χ, which can be interpreted as a proportionality factor describing how the polarization of a material changes with the applied electric field.

For the preceding derivations, χ has been assumed to be a constant, i.e. time-independent — which is known as the non-dispersive approximation. However, in a real material, the polarization response is never instantaneous. As a consequence, the time-dependent polarization density can be introduced as [p.171][25]

$$\boldsymbol{\mathcal{P}}(t) = \epsilon_0 \cdot \int_{-\infty}^{\infty} \chi(t - t')\boldsymbol{\mathcal{E}}(t')\mathrm{d}t' \,. \tag{1.50}$$

where the condition $\chi(t < t') = 0$ has to hold in order to maintain causality. Since equation 1.50 represents a convolution of the electric field with the susceptibility function, it can be expressed more elegantly in the frequency domain as [25, p. 174]

$$\boldsymbol{P}(\omega) = \epsilon_0 \chi(\omega)\boldsymbol{E}(\omega) \tag{1.51}$$

where $\chi(\omega)$ is the the Fourier-transform of $\chi(t)$. In analogy to the method presented in section 1.1.1, the complex frequency dependent refractive index can be defined as

$$\overline{n}(\omega) = n(\omega) + i\kappa(\omega) = \sqrt{\chi(\omega) + 1} \tag{1.52}$$

where κ is the loss coefficient which is related to the real part of the refractive index $n(\omega)$ by the Kramers-Kronig relations as a result of the previously stated causality condition. Using the frequency dependant refractive index $n(\omega)$ for describing the propagation in a dispersive medium, the spectral phase evolution $\varphi(z, \omega)$ can be expressed by the dispersion relation

$$\varphi(z, \omega) = k(\omega) \cdot z = \frac{\omega}{c_0} \cdot n(\omega) \cdot z \,. \tag{1.53}$$

For narrowband pulses where the spectrum is centred around the carrier frequency ω_0, the spectral phase evolution can be expanded in a Taylor-series around ω_0 [34, p. 147 f.]

$$\varphi(z, \omega) = \sum_{m=0}^{\infty} \frac{(\omega - \omega_0)^m}{m!} \cdot \left(\frac{\partial^m}{\partial \omega^m} \varphi(z, \omega) \right)_{\omega=\omega_0} = \sum_{m=0}^{\infty} \frac{(\omega - \omega_0)^m}{m!} \cdot D_m(z) \tag{1.54}$$

where $m \in \mathbb{N}_0$ denotes the order of the expansion. The coefficients D_m in equation 1.54 are called the characteristic *dispersion coefficients* which are found by evaluating the m^{th} derivative of k with respect to ω at ω_0:

$$D_m(z) = \sum_{m=0}^{\infty} \left(\frac{\partial^m}{\partial \omega^m} \varphi(\omega) \right)_{\omega=\omega_0} = \frac{z}{c_0} \cdot \left(\frac{\partial^m (\omega \cdot n(\omega))}{\partial \omega^m} \right)_{\omega=\omega_0} . \tag{1.55}$$

The effect of the different expansion orders of the material dispersion on a short pulse can be assessed easily by comparing its time-domain electric field before and after propagation: Keeping only the zero order terms of the expansion in equation 1.54 yields a frequency independent spectral phase

$$\varphi(z, \omega) = \frac{(\omega - \omega_0)^o}{0!} \cdot D_0(z) = \varphi(z, \omega_0) \,. \tag{1.56}$$

An initially bandwidth-limited pulse with $\varphi(z=0,t)=0$, after the propagation through a dispersive medium of length L, can then be described by

$$\begin{aligned} E(L,t) &= \frac{1}{2\pi}\int_{-\infty}^{\infty} A(0,\omega-\omega_0)\cdot e^{i\omega t}e^{\varphi(L,\omega)}\mathrm{d}\omega \\ &= \frac{1}{2\pi}\int_{-\infty}^{\infty} A(0,\omega-\omega_0)\cdot e^{i(\omega t+\varphi(L,\omega_0))}\mathrm{d}\omega \\ &= A(0,t)\cdot e^{i\omega_0\left(t+\frac{L}{v_p}\right)} \end{aligned} \tag{1.57}$$

where $v_p=\omega_0/k(\omega_0)$ describes the propagation velocity of the wavefronts of the carrier oscillation which is called the *phase velocity* of the pulse. The corresponding phase term $\phi_0=\omega_0\cdot z/v_p$ describes the relative phase of the carrier oscillation with respect to the envelope function and is thus named *carrier-envelope phase (CEP)*. While the CEP is often omitted in description of light-matter interaction it can be a critical parameter for the description of laser pulses containing only few cycles of the carrier oscillation. A more detailed description on the implications of a non-zero CEP is given in chapter 5.

When the expansion in equation 1.54 is extended to the first order, the frequency dependent spectral phase is given by

$$\varphi(z,\omega)=\sum_{m=0}^{1}\frac{(\omega-\omega_0)^m}{m!}\cdot D_m(z)=\varphi(\omega_0)\ +(\omega-\omega_0)\cdot D_1(z) \tag{1.58}$$

where the first-order dispersion coefficient is given by

$$D_1(z)=\frac{z}{c_0}\left(\frac{\partial(\omega\cdot n(\omega))}{\partial\omega}\right)_{\omega=\omega_0}. \tag{1.59}$$

An initially Fourier-transform limited pulse will, after the propagation through a dispersive medium, be transformed into

$$\begin{aligned} E(L,t) &= \frac{1}{2\pi}\int_{-\infty}^{\infty} A(0,\omega-\omega_0)\cdot e^{i\omega t}e^{(\varphi(\omega_0)+(\omega-\omega_0)\cdot D_1(L))}\mathrm{d}\omega \\ &= A\left(0,t-\frac{L}{v_g}\right)\cdot e^{i\omega_0\left(t+\frac{L}{v_p}\right)} \end{aligned} \tag{1.60}$$

where $v_g=z/D_1$ describes the propagation velocity of the pulse envelope and is named the *group velocity* of the pulse. The first-order expansion coefficient D_1 is correspondingly termed the *group delay (GD)* since it describes a temporal delay of the pulse envelope with respect to the carrier oscillation. Importantly, the group delay thus introduces a material-specific frequency dependence to the laser pulse's CEP.

Since the group delay itself does not affect the shape of the pulse, the result of equation 1.60 can be re-written as

$$E(L,t')=A(0,t')\cdot e^{i\omega_0\left(t'+L\left(\frac{1}{v_g}+\frac{1}{v_p}\right)\right)} \tag{1.61}$$

where $t' = t - L/v_g$ is the local time of the pulse which describes the pulse in a timeframe that co-propagates with its amplitude envelope. The description of laser pulses using their local time can be of special importance when solving the pulse propagation equations numerically, as presented in section 2.3.2. In such cases, the local time can be used to ensure that the pulse envelope does not shift excessively with respect to a pre-defined temporal grid.

To enhance the readability of the equations, the first order dispersion coefficient is omitted in the following description of the higher order dispersion contributions (i.e. t corresponds to the local time of the pulse). The continuation of the spectral phase expansion to the second order then yields

$$\varphi(z,\omega) = \varphi(\omega_0) \; + \frac{(\omega-\omega_0)^2}{2} \cdot D_2(z) \tag{1.62}$$

where the second order expansion coefficient D_2 can be calculated from equation 1.55 analogous to the previous examples. Since D_2 alternatively can be expressed as the derivative of D_1 with respect to the angular frequency, it is named *group delay dispersion (GDD)*. For a bandwidth-limited pulse with arbitrary shape, the electric field after propagation can only be given in integral form

$$E(L,t) = \frac{1}{2\pi}\int_{-\infty}^{\infty} A(0,\omega-\omega_0)\cdot e^{\left(i(\omega t+\varphi(\omega_0)+\frac{(\omega-\omega_0)^2}{2}\cdot D_2(L)\right)}\mathrm{d}\omega\,. \tag{1.63}$$

A more instructive understanding of the second order dispersion coefficient can be obtained by evaluating its impact on an initially bandwidth-limited Gaussian pulse which can be described by the electric field

$$E(0,t) = E_0 \cdot e^{-\left(\frac{t}{\xi_I\sqrt{2}}\right)^2} \cdot e^{i\omega_0 t} \tag{1.64}$$

where ξ_I denotes the $1/e^2$ width of the intensity profile ($\tau_{FWHM} = \xi_I \cdot 2\sqrt{\ln(2)}$). The electric field after propagation can then be written as

$$E(L,t) = A(L,t)\cdot e^{i(\omega_0 t+\phi(L,t))} \tag{1.65}$$

where the amplitude envelope is given by

$$A(L,t) = \frac{E_0\xi_I}{\sqrt[4]{\xi_I^4+D_2^2}} \cdot e^{-\left(\frac{t\cdot\xi_I}{\sqrt{2\cdot(\xi_I^4+D_2^2)}}\right)^2} \tag{1.66}$$

and the temporal phase is given by

$$\phi(L,t) = \frac{D_2(L)}{2(\xi_I^4+D_2^2(L))}\cdot t^2 + \frac{1}{2}\cdot\arctan\left(\frac{D_2(L)}{\xi_I^2}\right)\,. \tag{1.67}$$

From equation 1.66 it is apparent that in contrast to the previously discussed dispersion terms, the second order dispersion also affects the amplitude envelope of the pulse. More specifically, the pulse duration of an initially transform-limited Gaussian pulse is increased to

$$\xi_I(L) = \xi_I(0) \cdot \sqrt{1 + \left(\frac{D_2(L)}{\xi_I^2}\right)^2} \,. \tag{1.68}$$

upon propagation through a dispersive medium of length L. It is important to note that for an initially Fourier-transform-limited pulse, the temporal broadening does not depend on the sign of D_2. Consequently, pulse compression towards the bandwidth-limit requires the absolute value of the GDD to be as low as possible. Taking a closer look at the last term in equation 1.68 further shows that the extent of temporal broadening depends strongly on the incident pulse duration for a given GDD value. While for $D_2 < \xi_I^2$ the pulse duration is only weakly affected, it increases almost quadratically with decreasing input pulse duration for $D_2 \gg \xi_I^2$. As a consequence, the generation and propagation of ultrashort pulses typically relies on an exceptionally high accuracy of dispersion control, as discussed in chapters 2 and 3.

The effect of GDD on the temporal phase of the pulse can best be analysed by introducing the *instantaneous angular frequency* $\omega_i(t)$ of the pulse, which describes how the polychromatic oscillation frequency of the carrier wave evolves with respect to the local time of the pulse. The instantaneous angular frequency is thus equivalent to the time derivative of the argument of the time dependent electric field [25, p. 1081]

$$\omega_i(z,t) = \frac{\partial(\arg(E(z,t)))}{\partial t} = \frac{\partial(\omega_0 t + \phi(z,t))}{\partial t} \,. \tag{1.69}$$

For the Gaussian pulse described above, the instantaneous angular frequency after propagation is given by

$$\omega_i(z,t) = \omega_0 + \frac{D_2}{(\xi_I^4 + D_2^2)} \cdot t \tag{1.70}$$

which corresponds to a linear increase of the carrier frequency with time. The corresponding pulses are referred to as exhibiting a positive *linear chirp*. Comparing equations 1.70 and 1.61 it can further be seen that bandwidth-limited pulse can always be described by having a constant instantaneous angular frequency. Since the cascaded propagation through different dispersive materials corresponds to a simple addition of the induced instantaneous angular frequencies, the effect of GDD in one medium can be nullified by applying the same amount of GDD but with opposite sign. The concept of chirped pulses will be further exploited in the subsequent section on nonlinear light-matter interactions.

It should be noted that while the above derivation was given for a Gaussian pulse, temporal broadening can analogously be observed for arbitrary pulse shapes. However, in contrast to Gaussian pulses, the shape of the intensity profile will generally not remain invariant under the influence of GDD. Furthermore, the transformation from the frequency into the time domain (cf. equation 1.63) can in most cases only be performed numerically.

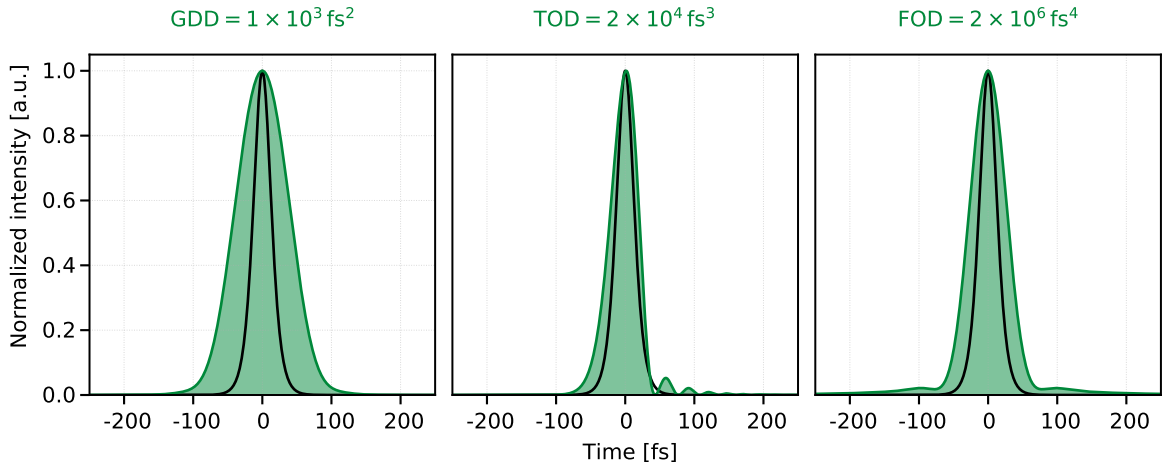

Fig. 1.2: Numerically calculated pulse shapes of a sech^2 pulse after numerically adding purely second-, third- or fourth order dispersion (green shaded curves). The initial pulse (black lines) has a full-width half-maximum duration of 30 fs. **a)** The resulting pulse shape after numerically adding a GDD of 1000 fs^2 shows a symmetrical temporal broadening. **b)** After numerically adding a third-order dispersion (TOD) of 2×10^4 fs^3, the main pulse is broadened asymmetrically and exhibits pronounced satellite features. **c)** By numerically adding a fourth-order dispersion (FOD) of 2×10^6 fs^4 the symmetrical pulse shape is maintained. The pulse is again broadened temporally but shows a weak, symmetric pedestal.

A numerically calculated example of how a sech^2-shaped pulse is transformed under the influence of differing GDD values is given in Fig. 1.2 a.

Due to their complex effect on the pulse shape, higher-order dispersion terms are conventionally named simply after their expansion order ($D_3 =$ TOD, $D_4 =$ FOD etc.). In analogy to the GDD, their impact on the pulse shape grows with decreasing pulse duration. For the generation of ultrashort pulses it is therefore common practice to at least take the effects of TOD into consideration. Examples of the influence of TOD and FOD on a sech^2 pulse are shown in Fig. 1.2 b and c, respectively. It is easily seen that the temporal broadening attributed to TOD and FOD is considerably less significant compared to the effect of GDD. However, both higher order dispersion terms evoke the appearance of satellite pulses — strongly asymmetrically in the TOD case — which reduces the peak intensity of the pulse.

In practice, the different expansion orders of the spectral phase usually do not occur in isolation. Quite the contrary, the spectral phase is most commonly shaped by propagation through various dispersive materials, where the expansion orders are interconnected by the frequency dependent refractive index. The refractive index curves of individual materials can be approximated well by the Sellmeier equation which states that

$$n(\lambda_0) = 1 + \sum_{i=1}^{M} \frac{B_i \lambda_0^2}{\lambda_0^2 - C_i} \tag{1.71}$$

where $\lambda_0 = 2\pi c/\omega_0$ is the center wavelength of the pulse and B_i and C_i are called the Sellmeier coefficients. For the values of B_i and C_i which can be found in the literature, λ_0 typically has to be given in the unit of micrometers. A comprehensive list of the Sellmeier coefficients for a wide variety of optica materials can be found in [36]. In the frame of this thesis, the spectrum of the generated laser pulses is centred at a frequency of approximately $\omega_0 = 1.9 \times 10^3$ THz (1 µm). At this wavelength, virtually all optically important materials exhibit a positive GDD, which causes the pulse to accumulate a positive chirp during propagation. Temporal compression close to the bandwidth limit is therefore conventionally achieved by introducing negative GDD, mostly by using dispersive mirrors [37].

1.2 Nonlinear light-matter interaction

1.2.1 Perturbative nonlinear optics

In the previous section, the key concepts of linear pulse propagation in both the spatial and temporal domain have been introduced. The derivation of the descriptive model has therein been based on a polarization density which linearly depends on the electric field (cf. equation 1.10). However, this assumption only remains valid for weak fields. The energy for laser pulses can be confined to extremely short durations (down to a few femtoseconds) while simultaneously being focused to very small spot sizes of only a few micrometers. For laser pulses with a radial Gaussian distribution, the highest occurring field strength in

vacuum $|E_{0,0}|_{peak}$ can be estimated by

$$|E_{0,0}|_{peak} = \sqrt{\frac{2}{\epsilon_0 c_0} \cdot 2I_{peak}} = \sqrt{\frac{2}{\epsilon_0 c_0} \cdot \frac{2P_{peak}}{\pi w_0^2}} \tag{1.72}$$

where P_{peak} is the peak power of the pulse which for a sech^2-pulse is given by

$$P_{peak} \approx \frac{0.88 \cdot E_p}{\tau_{FWHM}} \tag{1.73}$$

where E_p is named the *pulse energy*. For a regular pulse train, the pulse energy can be calculated by dividing the average power P_{avg} by the pulse repetition frequency f_{rep}. For the laser pulses in this thesis, typical peak intensities of a focused laser beam are in the range of $1\,\mathrm{TW\,cm^{-2}}$. For the corresponding field strengths on the order of $5\,\mathrm{GV\,m^{-1}}$, the linear approximation is not well suited anymore since most dielectric materials already exhibit a noticeable nonlinear response.

Assuming that the linear effects still dominate the propagation characteristics, the nonlinear polarization density can be understood as a perturbation of the linear response and can thus be expressed by a series expansion [38, p. 2]

$$\boldsymbol{\mathcal{P}} = \boldsymbol{\mathcal{P}}^{(L)} + \boldsymbol{\mathcal{P}}^{(NL)} = \epsilon_0 \chi^{(1)} \boldsymbol{\mathcal{E}} + \sum_{m=2} \epsilon_0 \chi^{(m)} \boldsymbol{\mathcal{E}}^m \,, \tag{1.74}$$

where $\chi^{(1)}$ is called the linear susceptibility and the $\chi^{(m)}$ are the m^{th} order optical susceptibility tensors of the material, respectively. Using the nonlinear expansion of the polarization density, the wave equation 1.9 for a non-dispersive, non-magnetic, homogeneous and isotropic material can be written as [25, p. 1020]

$$\nabla^2 \boldsymbol{\mathcal{E}} - \frac{1}{c^2} \frac{\partial^2 \boldsymbol{\mathcal{E}}}{\partial t^2} = \mu_0 \frac{\partial^2 \boldsymbol{\mathcal{P}}^{(NL)}}{\partial t^2} \tag{1.75}$$

where the linear term of the polarization density expansion has been absorbed in the second term on the left hand side of the equation. In analogy to the methodology in section 1.1.1, equation 1.75 can be expressed in the frequency domain by means of Fourier-transformation, yielding

$$\nabla^2 \boldsymbol{E} + k^2 \boldsymbol{E} = -\mu_0 \omega^2 \boldsymbol{P}^{(NL)} \tag{1.76}$$

which represents an inhomogeneous Helmholtz equation where $\omega^2 \boldsymbol{P}^{(NL)}$ acts as a source term for the generation of new frequency components. It is this source term which describes the origin of a variety of nonlinear effects and thus forms the basis for the field of nonlinear optics [25, p. 1020]. In equation 1.76, $\boldsymbol{P}$ has been introduced to represent the complex slowly-varying envelope function of the polarization density. Since equation 1.76 is the inhomogeneous form of the Helmholtz equation presented in section 1.1.1, its solution can be expressed as

$$\boldsymbol{E} = \boldsymbol{E}^{(L)} + \boldsymbol{E}^{(NL)} \tag{1.77}$$

where $\boldsymbol{E}^{(L)}$ is the linear component of the electric field — i.e. the solution to the homogeneous equation 1.14 — and $\boldsymbol{E}^{(NL)}$ describes the nonlinearly generated electric field which is the particular solution that depends on the form of $\boldsymbol{P}^{(NL)}$.

Taking a closer look at equation 1.74, it can be seen that the nonlinear polarization density is itself a function of the electric field. At the same time, however, the evolution of the electric field upon propagation through a nonlinear medium depends on the exact form of $\boldsymbol{P}^{(NL)}$. Since this inter-dependence of nonlinear polarization density and electric field severely complicates the analytical evaluation of the nonlinear material response, the description is conventionally based on the first-order Born approximation. In this approximation, the total driving field of the nonlinear process is replaced by an incident field $\boldsymbol{E}_0$ such that the nonlinear polarization density can be written as [25, p. 1020]

$$\boldsymbol{P}^{(NL)}(\boldsymbol{E}) = \boldsymbol{P}^{(NL)}(\boldsymbol{E}_0)\,. \tag{1.78}$$

Consequently, the effect of the newly generated frequency components on the shape of the nonlinear polarization density is assumed to be negligible.

As introduced in the previous paragraphs, the source term on the right hand side of equation 1.76 gives rise to a multitude of nonlinear effects which are often associated with the generation of new frequency components. However, a comprehensive description of all known nonlinear effects is by far beyond the scope of this thesis. This section therefore aims to give an introduction to the relevant effects that where observed and exploited in the experiments described in the upcoming chapters.

1.2.2 Second-order nonlinear effects

In analogy to the description of the dispersive effects in section 1.1.3 it is instructive to analyse the influence of the different expansion orders of the nonlinear polarization density in an isolated manner. Second order nonlinear effects are induced by a time-domain nonlinear polarization density described by [38, p. 6]

$$\boldsymbol{\mathcal{P}}^{(2)} = \epsilon_0 \chi^{(2)} \boldsymbol{\mathcal{E}}^2\,, \tag{1.79}$$

where $\chi^{(2)}$ is the second order optical susceptibility. It should be emphasized that $\chi^{(2)}$ vanishes for all centrosymmetric optical materials such as most gases, liquids and glasses and is only non-zero for crystals that do not exhibit inversion symmetry [38, p. 2]. Furthermore, the magnitude of the nonlinear optical susceptibility is extremely low for most crystals [39]. Consequently, high field strength such as those in ultrashort laser pulses are typically required to facilitate the observation of second order nonlinear effects. To simplify the calculations, an input electric field consisting of only two monochromatic plane waves that are linearly polarized along a common axis and with distinct frequencies ω_1 and ω_2 instead of a continuous spectral distribution is considered. Such an electric field can be written as

$$\mathcal{E}(t) = \mathcal{E}_1(t) + \mathcal{E}_2(t) = \mathrm{Re}(E_1 \cdot e^{i\omega_1 t} + E_2 \cdot e^{i\omega_2 t}) \tag{1.80}$$

where E_1 and E_2 are the amplitudes of the first- and second monochromatic wave, respectively. Plugging equation 1.80 into equation 1.79, the nonlinear polarization density can be expressed as

$$\begin{aligned}\mathcal{P}^{(2)}(t) =& \frac{1}{2}\epsilon_0\chi^{(2)} \cdot \mathrm{Re}\{E_1^2 \cdot e^{-2i\omega_1 t} + E_2^2 \cdot e^{-2i\omega_2 t} \\ &+ 2E_1E_2e^{i(\omega_1+\omega_2)t)} + 2E_1E_2^*e^{(i(\omega_1-\omega_2)t)}\} \\ &+ \epsilon_0\chi^{(2)}\left(E_1E_1^* + E_2E_2^*\right)\end{aligned} \tag{1.81}$$

where the asterisk denotes the complex conjugate. Close analysis of equation 1.81 reveals that for a bi-chromatic input field, the second order nonlinear polarization evokes the generation of five new frequency components. To enhance the readability, it is convenient to rewrite equation 1.81 as

$$\mathcal{P}^{(2)}(t) = \sum_n P(\omega_n) \cdot e^{i\omega_n t} \tag{1.82}$$

with the summation extending over both positive and negative frequencies ω_n [38, p. 6]. The individual complex amplitudes of the nonlinear polarization density are then given by

$$P(2\omega_1) = \frac{1}{2}\epsilon_0\chi^{(2)}E_1^2 \tag{1.83}$$

$$P(2\omega_2) = \frac{1}{2}\epsilon_0\chi^{(2)}E_2^2 \tag{1.84}$$

$$P(\omega_1+\omega_2) = \epsilon_0\chi^{(2)}E_1 \cdot E_2 \tag{1.85}$$

$$P(\omega_1-\omega_2) = \epsilon_0\chi^{(2)}E_1 \cdot E_2^* \tag{1.86}$$

$$P(0) = \epsilon_0\chi^{(2)}\left(E_1E_1^* + E_2E_2^*\right) . \tag{1.87}$$

Since in all terms a third wave is generated from the incident two waves, the underlying process is also referred to as *three-wave mixing*. The two terms $P(2\omega_1)$ and $P(2\omega_2)$ correspond to the generation of radiation with twice the angular frequency of the input wave. The underlying nonlinear process is therefore called *second-harmonic generation (SHG)*. The terms $P(\omega_1+\omega_2)$ and $P(\omega_1-\omega_2)$ are named *sum-frequency generation (SFG)* and *difference-frequency generation (DFG)*. The last term $P(0)$ is termed *optical rectification* since it describes the emergence of a quasi-direct current (DC) potential difference across the dielectric medium [38, p. 6].

Theoretically, all five presented nonlinear effects can be observable at the same time. However, in reality, the amplitudes of the newly generated frequencies will be extremely low for all but one or two of the frequency components. The main reason for this is that the different frequency conversion processes need to fulfil extra *phase matching* conditions to be efficient, which usually can only be satisfied for one of the generated frequencies at a time [38, p. 7]. In the frame of this thesis, second order nonlinear effects were mainly exploited for the frequency conversion experiments which are described in chapter 4.1. More specifically, the concept of intra-pulse difference-frequency generation (IPDFG) was used for converting broadband NIR-radiation into the mid-IR spectral range. IPDFG represents a special form of the classical DFG process described above, where both driving

frequencies are contained within the same laser pulse. This helps in reducing the complexity of the setup significantly, since the two input field inherently propagate collinearly. In the following equations, ω_{IPDFG} represents the angular frequency of the nonlinear electric field component which is generated in the IPDFG process. For a collinear propagation direction of the incident fields (e.g. both input fields propagate in z-direction), the phase matching condition can be obtained in scalar form from the requirement for energy and momentum conversation which, in the photon picture of light, states that [25, p. 1028]

$$\hbar\omega_1 - \hbar\omega_2 = \hbar\omega_{IPDFG} \tag{1.88}$$

and

$$\omega_1 \cdot n(\omega_1) - \omega_2 \cdot n(\omega_2) = \omega_{IPDFG} \cdot n(\omega_{IPDFG}) \tag{1.89}$$

must both be satisfied simultaneously. This can for example be achieved by utilizing birefringent (anisotropic) materials for the frequency conversion. In such materials, the refractive index of the individual frequencies further depends on the polarization of the carrier oscillation with respect to the principal axis of the crystal. Phase matching for a specific set of frequencies can thus be achieved by adjusting the input polarizations or the crystal orientation.

By taking a closer look at equation 1.88 it can be seen that the maximum frequency of the generated mid-IR radiation is directly proportional to the bandwidth of the driving laser pulse. Additionally, even if both driving frequencies are contained within the same pulse, the temporal overlap of both frequency components must be ensured. Consequently, the instantaneous angular frequency of the pulse should be constant across the pulse for efficient conversion. In other words, the incident pulse needs to be compressed close to its Fourier-transform limit. Furthermore it can be shown that the intensity of the generated wave I_{IPDFG} increases linearly with the squared integral of the driving field amplitudes $A(\boldsymbol{r}, \omega_i)$ over the total volume V of the nonlinear interaction [25, p. 1032]

$$I_{IPDFG} = \left| \int_V \epsilon_0 \chi^{(2)} A(\boldsymbol{r}, \omega_1) \cdot A(\boldsymbol{r}, \omega_2) e^{i\Delta k \cdot z} \mathrm{d}\boldsymbol{r} \right|^2 \tag{1.90}$$

where $\Delta k = (\omega_1 \cdot n(\omega_1) - \omega_2 \cdot n(\omega_2) - \omega_{IPDFG} \cdot n(\omega_{IPDFG}))/c_0$ takes into account the phase matching of the propagating beams in the nonlinear material. As a result, the efficient generation of broadband, intense mid-IR radiation via IPDFG is best achieved using ultrashort, high-power driving pulses with high spatial beam quality which motivates the experiments on nonlinear pulse compression presented in chapter 2 and 3.

1.2.3 The optical Kerr-effect

Since centrosymmetric materials do not exhibit second-order nonlinear effects, their nonlinear polarization response is dominated by the third order dependence on the electric field which can be formally expressed as [38, p. 10]

$$\boldsymbol{\mathcal{P}}^{(3)} = \epsilon_0 \chi^{(3)} \boldsymbol{\mathcal{E}}^3 \,, \tag{1.91}$$

where $\chi^{(3)}$ is the third order optical susceptibility. In analogy to the previous section, third-order nonlinear effects can be efficiently described in the frame of *four-wave mixing* where an incident electric field consisting of three monochromatic waves leads to the generation of a fourth wave with new angular frequency. However, taking into account the cubed form of the electric field, already for the third order this leads to generation of 22 new frequency components [38, p. 12] — most of which play no important role in the experiments conducted in this thesis.

Fortunately, the decisive characteristics of the third order nonlinear polarization response can also be obtained from a different, much simpler approach. Assuming a single monochromatic wave

$$\boldsymbol{\mathcal{E}}(t) = \mathrm{Re}\{\boldsymbol{E}(\boldsymbol{r},t)\cdot e^{i\omega t}\} \tag{1.92}$$

with angular frequency ω and amplitude $\boldsymbol{E}(\boldsymbol{r},t)$ as input electric field, the third order nonlinear polarization response can be rewritten as [38, p. 10]

$$\mathcal{P}^{(3)}(t) = \mathrm{Re}\left\{\frac{1}{4}\epsilon_0\chi^{(3)}\cdot\boldsymbol{E}(\boldsymbol{r},t)^3 e^{i3\omega t} + \frac{3}{4}\epsilon_0\chi^{(3)}\boldsymbol{E}(\boldsymbol{r},t)^3\cdot e^{i\omega t}\right\}. \tag{1.93}$$

The first term on the right hand side of equation 1.93 corresponds to the generation of a new frequency component with angular frequency 3ω and is hence called *third-harmonic generation (THG)*. The second term on the right hand side, however, describes a modification of the input field since it radiates at an identical frequency ω. By considering only this second term, the polarization density from equation 1.74 can be expressed as

$$\boldsymbol{\mathcal{P}} = \boldsymbol{\mathcal{P}}^{(L)} + \boldsymbol{\mathcal{P}}^{(NL)} = \epsilon_0\chi^{(1)}\boldsymbol{\mathcal{E}} + \frac{3}{4}\epsilon_0\chi^{(3)}|\boldsymbol{\mathcal{E}}|^2\boldsymbol{\mathcal{E}} = \left(\epsilon_0\left(\chi^{(1)} + \frac{3}{4}\chi^{(3)}|\boldsymbol{\mathcal{E}}|^2\right)\right)\boldsymbol{\mathcal{E}}. \tag{1.94}$$

The polarization response of the material is therefore found to be linear with respect to the electric field, but characterized in having a modified, time and position dependent change of the electric susceptibility $\chi(t)$ which is given by

$$\chi(\boldsymbol{r},t) = \chi^{(1)} + \Delta\chi = \chi^{(1)} + \frac{3}{2\epsilon_0 c}\chi^{(3)}\cdot\boldsymbol{I}(\boldsymbol{r},t) \tag{1.95}$$

where the intensity $\boldsymbol{I}(\boldsymbol{r},t)$ is defined analogous to equation 1.42. By using the relation $n^2 = 1+\chi$ (cf. equation 1.52), the modified electric susceptibility is found to induce an intensity dependent modification of the refractive index [38, p. 11]

$$n(\boldsymbol{I}) = n_0 + n_2\cdot\boldsymbol{I}(\boldsymbol{r},t) \tag{1.96}$$

where n_0 denotes the linear refractive index of the material and the *nonlinear refractive index* n_2 is given by [38, p. 11]

$$n_2 = \frac{3}{4\epsilon_0 n_0^2 c_0}\chi^{(3)}. \tag{1.97}$$

Due to its similarity to the electro-optic Kerr-effect (cf. [25, chap. 21]), the self-induced intensity dependence of the refractive index is also named the *optical Kerr-effect*. This effect causes a variety of nonlinear phenomena, some of which are presented in the following sections.

Self-phase modulation

In analogy to the description of the dispersion effects in section 1.1.3, it is instructive to evaluate how the optical Kerr-effect affects the amplitude and phase of a laser pulse that propagates through a nonlinear medium — which for now is assumed to be homogeneous, isotropic and non-dispersive. By neglecting spatio-temporal coupling effects, the description can be further separated into spectro-temporal and spatial effects. The spectro-temporal contributions of the optical Kerr-effect can be well described by neglecting the spatial dependence of the electric field. When using a linearly polarized plane wave with carrier frequency ω_0 that propagates in z direction as input, the complex field amplitude at position $z = 0$ can be written as (cf. equation 1.41)

$$E(z = 0, t) = A(0, t) \cdot e^{i\omega_0 t} \tag{1.98}$$

The incident pulse described by the complex field amplitude in equation 1.98 is assumed to be Fourier-transform limited which is why the temporal phase of the electric field vanishes. After the propagation through a nonlinear medium of length L, the complex field amplitude will be transformed into

$$E(z, t) = A(0, t) \cdot e^{i\omega_0 t} e^{i\phi(z,t)} = A(0, t) \cdot e^{i(\omega_0 t - k(I)L)} \tag{1.99}$$

where $k(I)$ describes the intensity dependent wave vector which, using equation 1.96, can be expressed as

$$k(I) = \frac{\omega_0 n(I)}{c_0} = \frac{\omega_0 n_0}{c_0} + \frac{\omega_0 n_2}{c_0} \cdot I(t) \ = k_0 + k_{NL}\,. \tag{1.100}$$

Taking a closer look at equation 1.99 it can be seen that the output pulse after propagation has accumulated a total temporal phase

$$\phi(z, t) = \phi_0 + \phi_{NL}(z, t) \tag{1.101}$$

consisting of a linear phase term $\phi_0 = k_0 z$ and an additional *nonlinear phase* $\phi_{NL}(z, I)$ which is given by

$$\phi_{NL}(z, t) = \frac{n_2 \omega_0}{c_0} I(t) z\,. \tag{1.102}$$

Since the variation of the temporal phase is induced by the driving field itself, this process is named *self-phase modulation (SPM)*.

It should be emphasized that in a non-dispersive medium, the amplitude envelope $A(t)$ remains invariant under the influence of SPM since the optical Kerr-effect only acts on the temporal phase of the pulse. However, the variation of the temporal phase results in a change of the spectral amplitude $A(\omega)$. In the frequency domain, SPM therefore induces the generation of new frequency components due to the additional time dependent phase. The effect of SPM can hence be used to achieve a *spectral broadening* of the input pulse. It is important to note that the preceding description is based on an bandwidth-limited

incident laser pulse. If the SPM process is driven by a positively chirped incident pulse, spectral broadening is commonly still observed. However, the spectral shape observed after the nonlinear interaction can differ significantly for pre-chirped and bandwidth-limited incident pulses [40]. In contrast, the presence of a negative chirp on the incident pulse often results in *spectral narrowing* [35, p. 106]. For an arbitrarily shaped incident pulse with field amplitude $E(z,t)$, the spectral shape $S(\omega)$ after the nonlinear interaction can generally be determined by calculating the Fourier-transform [35, p. 101]

$$S(\omega) \propto A^2(z,\omega) = \left| \mathcal{FT}\{E(z,t) \cdot e^{i\phi_{NL}(z,t)}\} \right|^2 . \tag{1.103}$$

In many cases, the broadened spectrum exhibits strong amplitude oscillations. An exemplary output spectrum for the case of SPM driven by a sech^2-shaped incident pulse is depicted in Fig. 1.3 a. As a consequence of the oscillatory structure of the spectrum, the complexity of the Fourier-transform limited pulse shape is likewise increased. In many cases, the main pulse is accompanied by symmetrically distributed satellite pulses which contain a small fraction of the pulse energy.

To determine the temporal distribution of the newly generated frequency components around the carrier frequency ω_0, the instantaneous angular frequency defined in equation 1.69 can be used

$$\omega_{i,SPM}(t) = \frac{\partial \left(\omega_0 t - k(I)z\right)}{\partial t} = \omega_0 + \frac{n_2\omega_0}{c_0} z \cdot \frac{\partial I(t)}{\partial t} . \tag{1.104}$$

From equation 1.104 it is easily seen that the instantaneous angular frequency is shifted to lower frequencies in the rising edge of the pulse ($t < 0$) and shifted to higher frequencies for the trailing edge of the pulse ($t > 0$), thus, yielding a positively chirped pulse.

For a sech^2-shaped pulse with a pulse duration of τ_{FWHM}, the intensity profile of the pulse can be written as

$$I(t) = I_{peak} \cdot \operatorname{sech}^2\left(\frac{\alpha \cdot t}{\tau_{FWHM}}\right) \tag{1.105}$$

where I_{peak} is the spatially averaged peak intensity of the laser pulse as given in equation 1.72, and

$$\alpha = 2 \cdot \operatorname{arcsech}\left(\frac{1}{\sqrt{2}}\right) \tag{1.106}$$

is a numerical constant. The intensity profile of an exemplary sech^2 pulse is shown in Fig. 1.3 b. The instantaneous angular frequency after propagation through a non-dispersive material exhibiting a third-order nonlinearity can be calculated by inserting equation 1.105 into equation 1.104. The result is

$$\omega_{i,SPM}(t) = \omega_0 + \frac{n_2\omega_0}{c_0} z \cdot \frac{2\alpha}{\tau_{FWHM}} \cdot I(t) \cdot \tanh\left(\frac{\alpha \cdot t}{\tau_{FWHM}}\right) . \tag{1.107}$$

which is exemplary depicted in Fig. 1.3 c). In the case of a sech^2-shaped incident pulse, the effect of SPM results in a chirp that is almost linear over the central part of the pulse

where most of the pulse energy is contained. The spectrally broadened pulse can hence be efficiently compressed to a shorter pulse duration by removing the linear part of the chirp, which is equivalent to adding a negative GDD to the pulse. Unfortunately, the addition of negative GDD leaves the temporal wings of the pulse uncompressed. This typically results in the appearance of weak satellite pulses which accompany the compressed main pulse. It should be noted that the satellite pulses which occur due to imperfect chirp compensation differ from the previously mentioned satellite pulses observed for bandwidth-limited pulses with oscillatory structure in their spectrum. In the frame of this thesis, the combination of spectral broadening and subsequent temporal compression by chirp removal is exploited in the nonlinear pulse compression experiments presented in chapters 2 and 3.

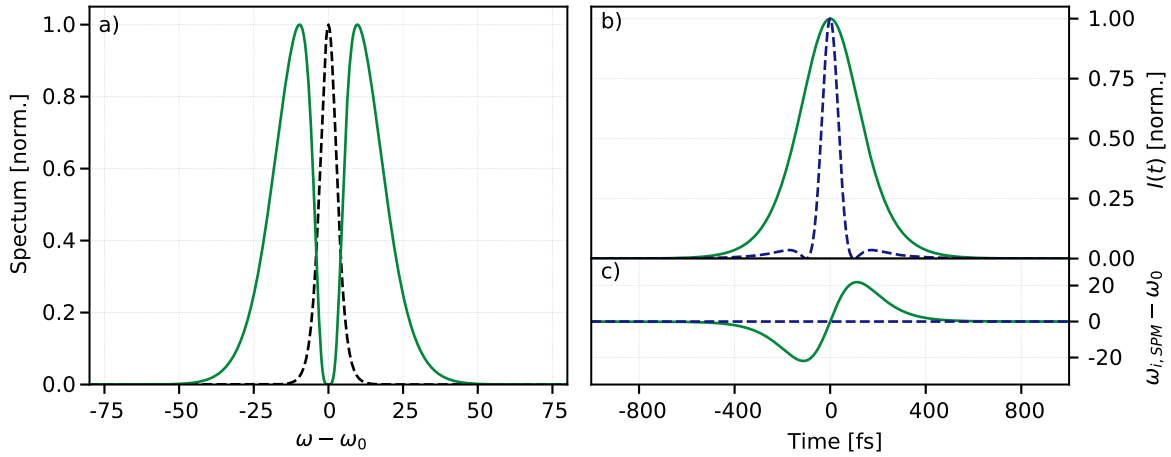

Fig. 1.3: Numerically calculated spectrum, pulse shape and instantaneous angular frequency of a sech^2 pulse after spectral broadening. **a)** Exemplary output spectrum with pronounced oscillations (green curve) for the case of SPM driven by a sech^2 incident pulse (dashed black line). **b)** sech^2 intensity profile of the spectrally broadened pulse (green) and corresponding Fourier-transform limited pulse shape (dashed blue curve) exhibiting satellite pulses. **c)** Instantaneous angular frequency $\omega_{i,SPM}$ (green curve) of the spectrally broadened pulse. The dashed blue line depicts the instantaneous frequency of the Fourier-transform limited pulse in b). For both curves, the carrier frequency ω_0 has been subtracted.

The magnitude of the spectral broadening can generally be estimated by the maximum deviation of the instantaneous frequency $\Delta\omega_{max}$ from its mean value ω_0 [35, p. 100]. For an incident pulse of the form given in equation 1.105, $\Delta\omega_{max}$ can be expressed by [29]

$$\Delta\omega_{max} = \frac{n_2\omega_0 z}{c_0}\frac{I_{peak}}{\tau_{FWHM}} \cdot \frac{4\alpha}{3\sqrt{3}} = \frac{4\alpha}{3\sqrt{3}\tau_{FWHM}} \cdot \phi_{NL}^{peak} \tag{1.108}$$

using the peak nonlinear phase shift

$$\phi_{NL}^{peak} = \frac{n_2\omega_0}{c_0} I_{peak} \cdot z \tag{1.109}$$

as a measure for the maximum nonlinear phase shift at the center of the pulse. Under the assumption that the spectrally broadened pulses exhibit the same time-bandwidth product TBP as the input pulses, a spectral broadening factor F_ω can be defined as [29]

$$F_\omega = \frac{2\Delta\omega_{max}}{\omega_{FWHM}} = \frac{8}{3\sqrt{3}}\frac{\alpha}{TBP}\cdot\phi_{NL}^{peak} \tag{1.110}$$

where ω_{FWHM} is the FWHM bandwidth of the incident pulse and

$$TBP = \omega_{FWHM}\cdot\tau_{FWHM} = \frac{8(\ln(1+\sqrt{2}))^2}{\pi} \tag{1.111}$$

is the time-bandwidth product of a sech^2-shaped pulse (cf. equation 1.49). From equation 1.110 it is apparent that the amount of spectral broadening scales linearly with the peak nonlinear phase shift of the pulse. In the context of nonlinear pulse compression, large broadening factors are typically desired. Since the the second-order nonlinear refractive index n_2 is small for most materials (typical values are $n_2 \approx 1\times10^{-20}\,\mathrm{m^2/W}$ for glasses and $n_2 \approx 1\times10^{-22}\,\mathrm{m^2/W}$ for gases), high intensities of the driver laser are commonly required for obtaining a significant amount of spectral broadening.

It should be noted that the above description of the SPM is based on a variety of assumptions which overly simplify the experimental conditions. The preceding paragraphs can therefore only provide a phenomenological explanation of the spectral broadening observed in the experiments. To avoid the occurence of spatio-temporal couplings, the nonlinear phase as defined in equation 1.102 has been assumed to be independent of the spatial coordinate r. However, in a real laser beam the intensity generally varies over the beam profile. For a Gaussian beam, the intensity is highest in the beam center and radially decreases towards the edge of the beam. Since the amount of spectral broadening is directly linked to the incident intensity, a Gaussian beam will, after spectral broadening, exhibit a radially varying output spectrum. This is referred to as *spectral inhomogeneity* of the laser beam. The implications of a spectrally inhomogeneous laser beam and methods which facilitate a homogenization of the spectral broadening are discussed in section 2.2.2.

Furthermore, it has so far been assumed that the nonlinear material is free of dispersion and absorption and features an instantaneous response. As a result, the intensity profile of the pulse remained invariant under the nonlinear interaction, which justifies the application of the first order Born approximation. In reality, all materials exhibit a non-negligible dispersion and absorption. The resulting change of the pulse shape during propagation feeds back on the value of the intensity dependent nonlinear phase. As a consequence, the spectral broadening in a dispersive and absorbing medium will evolve differently than in the non-dispersive approximation. Since a non-negligible absorption only affects the magnitude of the electric field, it can typically be associated with a reduction of the spectral broadening factor which does not significantly affect the spectral or temporal shape of the pulse. A non-negligible dispersion, on the contrary, induces a temporal narrowing or broadening of the temporal pulse shape during propagation, which can result in a significant modification of the generated spectrum.

For the case of a negative dispersion environment (i.e. a net-negative GDD inside the effective nonlinear medium), the linear part of the positive chirp generated by SPM will partially be removed already during the propagation in the nonlinear medium. As a result the pulse experiences temporal narrowing, which is also known as *self-compression*. With decreasing pulse duration, the steepness of the pulse slope ($\partial I(t)/\partial t$) increases, which according to equation 1.107, likewise enhances the total amount of spectral broadening with increasing propagation distance. However, the pulse shape is typically affected negatively due to the continuous imperfect subtraction of the non-linear chirp components. In many cases, the appearance of satellite pulses containing a large fraction of the pulse energy can be observed [40]. In the frame of this thesis, spectral broadening in the net-negative dispersion regime was investigated in the self-compression experiments presented in section 2.2.

If the SPM takes place in a net positive dispersion environment, the pulse duration increases during the nonlinear interaction causing a reduction of the total magnitude of the spectral broadening. However, the combined effect of SPM and GDD induce a linearization of the positive chirp which allows for a more efficient compression after the propagation [40]. After extensive propagation through a positively dispersive, nonlinear medium, the pulse typically develops an almost rectangular shape with steep leading and trailing edges [41]. Due to the extremely steep intensity slopes, the instantaneous frequency can then reach very high values which ultimately can lead to *optical wave-breaking* [42, 43].

A more general mathematical description of SPM that is applicable to the case of dispersive, nonlinear and absorbing media, and which also covers the contribution of time-delayed material responses, is briefly introduced in section 1.2.3.

Self-focusing

Analogous to the spectro-temporal effect of self-phase modulation described previously, the optical Kerr-effect, causes a modification of the spatial profile of the propagating laser beam. In this section, the influence of the optical Kerr-effect on the spatial distribution of a monochromatic Gaussian beam with the field amplitude given by equation 1.22 and the intensity profile given by equation 1.23 is discussed. Due to the Gaussian shape of the intensity profile, the propagating beam accumulates a radially varying nonlinear phase which is highest in the beam center and decreases in radial direction. Assuming that the third-order nonlinear interaction starts in the focal plane corresponding to $z = 0$, the additional nonlinear phase φ_{sf} which is accumulated during the propagation of the beam over a small distance Δz can be written as [44, p. 206]

$$\varphi_{sf}(r, \Delta z) = -\frac{n_2 \omega_0}{c_0} \Delta z \cdot I_0 \cdot e^{\left(\frac{-2r^2}{w_0^2}\right)} \tag{1.112}$$

where ω_0 is the carrier frequency of the monochromatic wave. Near the beam center, equation 1.112 can be approximated by

$$\varphi_{sf}(r, \Delta z) = -\frac{n_2 \omega_0}{c_0} \Delta z \cdot I_0 \left(1 - \frac{2r^2}{w_0^2}\right) . \tag{1.113}$$

Taking a closer look at equations 1.113 and 1.22 it can be seen that the additional nonlinear phase term causes a concave curvature of the wavefront, which results in a *self-focusing* of the beam upon propagation through a nonlinear medium. Since the focusing effect is caused by the optical Kerr-effect, the lens-like structure is also named *Kerr-lens*. It should be noted that equation 1.113 is only a valid approximation in the central part of the beam. Towards the edge of the beam, the Kerr-lens cannot be described by a radial quadratic dependence of the refractive index anymore. Consequently, Kerr-lensing causes an aberration of the incident beam profile — resulting in a reduction of the peak intensity of the beam — as described using the coupled-mode theory [45]. Comparing the phase term corresponding to the propagation through a thin lens to the approximated nonlinear phase in the beam center, the effective focal length f_{Kerr} of the Kerr-lens corresponding to the propagation through a thin nonlinear material of length d can be defined as [44, p. 321]

$$f_{Kerr} = \frac{w_0^2}{4n_2 d I_0} \,. \tag{1.114}$$

In general, the self-focusing of the laser beam is counteracted by its natural diffraction. In the vicinity of the beam waist, this can be described by the approximated phase term [44, p. 205]

$$\varphi_{diff}(\Delta z) = -\frac{K\Delta z}{2z_r} r^2 \,. \tag{1.115}$$

The critical power of a laser beam with a carrier wavelength $\lambda_0 = 2\pi c_0/\omega_0$ is defined by [44, p.206]

$$P_{cr} = \frac{\lambda_0^2}{8\pi n_0 n_2} \,. \tag{1.116}$$

At this power, the effect of self-focussing exactly counteracts the inherent diffraction of the beam, i.e. $\varphi_{sf} = -\varphi_{diff}$. Such types of beams are also referred to as *self-trapped* since their beam radius appears to be invariant under further propagation within the nonlinear medium [46]. If the peak power of the incident beam is lower than P_{cr}, the natural diffraction of laser beam governs the evolution of the beam caustic. In contrast, if the peak power of the beam exceeds the critical power defined in equation 1.116, the beam will be focused continuously. For a sufficiently long nonlinear medium, this will ultimately lead to a collapse of the beam and, in practice, the damaging of the nonlinear medium. It should be emphasized that the appearance of critical self-focusing only depends on the power and not on the intensity of the beam.

Unlike in the SPM case, the intensity profile of a Gaussian beam is directly affect by the effect of self-focusing. As a result, the first Born-approximation is only valid as long as the calculation is performed for sufficiently small propagation distances Δz — which is equivalent to requiring the beam caustic to only change weakly during propagation. For strong self-focusing effects, the evolution of the beam can only be calculated numerically since the intensity does not retain its Gaussian profile during extended propagation in the nonlinear material [47].

1.2.4 Generalized nonlinear Schrödinger equation

In the preceding section, the effect of SPM has been introduced as a method for spectrally broadening laser pulses which, in combination with subsequent chirp removal, provides an efficient means for nonlinear pulse compression. For clearer insights, the description has so far been restricted to non-dispersive, non-absorbing materials featuring an instantaneous response. Furthermore, the incident pulses have implicitly been assumed to exhibit a smooth intensity profile which can for example be described by a simple sech^2-function. For a more general description of pulse propagation in nonlinear dispersive media, a generalized scalar propagation equation that takes the form of a generalized nonlinear Schrödinger equation (GNLSE) can be used. The detailed derivation of the GNLSE is beyond the scope of this thesis, but can be found in, for example, reference [35, chap. 2].

The GNLSE used in this thesis to simulate the nonlinear pulse propagation can be written as [48]

$$\begin{aligned}\frac{\partial A}{\partial z} =& -\frac{\alpha}{2}A - \left(\sum_{m\geq 2}\beta_m \frac{i^{m-1}}{m!}\frac{\partial^m}{\partial T^m}\right) + i\gamma\left(1+\frac{1}{\omega_0}\frac{\partial}{\partial T}\right) \\ &\times\left((1-f_R)A|A|^2 + f_R A\int_0^\infty h_R(\tau)|A(z,T-\tau)|^2\mathrm{d}\tau\right).\end{aligned} \tag{1.117}$$

Equation 1.117 describes the evolution of the slowly varying (cf. equation 1.17) time domain field amplitude $A(z,T)$ with a carrier wave oscillation frequency ω_0 . In the above description, T corresponds to the local time of the pulse (cf. section 1.1.3). Furthermore, spatio-temporal couplings are neglected, meaning that the spatial amplitude of the field is assumed to be separable from the temporal amplitude. The parameter α denotes the absorption coefficient while the $\beta_m = D_m/z$ represent the dispersion coefficients which can be obtained from the Taylor-expansion given in equation 1.55. The third term on the right hand side of equation 1.117 describes the nonlinear effects where [35, p. 44]

$$\gamma = \frac{n_2\omega_0}{c_0 A_{eff}} \tag{1.118}$$

is termed the effective nonlinear coefficient and sufficiently describes the influence of SPM on the pulse. In equation 1.118, A_{eff} denotes the effective area of the intensity profile during the nonlinear interaction which, for a Gaussian beam, is simply given by

$$A_{eff} = \pi w(z)^2 \tag{1.119}$$

where $w(z)$ is the spot size of the Gaussian beam at the axial position of the nonlinear interaction z. The temporal derivative $\partial/\partial T$ in the third term on the right hand side of equation 1.117 takes into consideration the higher order nonlinear effects of *self-steepening* and *optical shock formation* which are described in further detail in references [35, p. 123] and [35, p. 126]. Finally, the first term in the second line of equation 1.117 takes into account the nearly instantaneous electronic contribution of the Raman response while

the convolution integral describes the delayed Raman response and Raman gain of the material [35, p. 46 ff, 49].

Since no analytical solutions to equation 1.117 are known, the GNLSE was solved numerically using the open-source python module *pyNLO* [50], which is based on a fourth-order Runge-Kutta solver in the interaction picture described in further detail in reference [48]. Further information on the *pyNLO*-module and the modifications implemented in the frame of this thesis are given in section 2.2.2.

2

Dispersion controlled all-bulk multipass spectral broadening

2.1 Thin-disk oscillator driven pulse compression

For several decades, high-power few-cycle laser pulses have most commonly been generated by Titanium (Ti):sapphire laser systems, often referred to as the "workhorse of ultrafast technology". Its reputation in the ultrafast scientific community is easily understood considering that, especially when based on Kerr-lens mode-locking, it allows the generation of pulses down to only few optical cycles at watt-level average powers and megahertz repetition rates directly from a laser oscillator [51, 52]. When combined with amplification stages and operated at reduced pulse repetition rates, such Ti:sapphire based laser systems allow the generation of joule-level pulse energies with pulse durations of only a few tens of femtoseconds reaching peak powers on the petawatt scale [53]. However, ultrafast Ti:sapphire based laser systems are generally difficult to scale in average power mainly due to the large quantum defect and the associated heat generation. Even in the best case, only few tens of watts can be achieved when utilizing cryogenic cooling [54]. As a result, the generation of high-energy laser pulses has so far only been realized at kilohertz repetition rates which induces long acquisiton times and low signal-to-noise ratio in subsequent experiments.

This limitation can be avoided by progressing to laser systems based on Yb:doped gain materials which possess better thermal properties.. Moreover, these can be manufactured in a variety of different geometries that improve heat dissipation including for example innoslab, fiber or thin-disk, all of which have been demonstrated capable of handling significantly higher average powers up to the kilowatt scale [55–57]. Thin-disk technology in particular, with its almost one-dimensional heat flow that reduces thermal lensing and short interaction length that diminishes parasitic nonlinear effects has become a powerful

tool for modern ultrafast systems [58]. The combination of diode-pumped Yb:YAG thin-disk gain media and soliton mode-locking techniques nowadays facilitates laser oscillators emitting femtosecond pulses at 100 W-level average powers and megahertz repetition rates without requiring external amplification [21, 23, 59–63]. Unfortunately, the narrow emission bandwidth — approximately 9 nm centered at 1030 nm — typically limits the pulse durations from Yb:YAG thin-disk lasers to few hundreds of femtoseconds. Shorter pulses have been generated by exploiting additional intra-cavity self-phase modulation or by utilizing alternative gain materials such as Yb:CALGO or Yb:KGW, which feature broader emission spectra [64–67]. However, these approaches resulted in a significant reduction of both average- and peak power. Therefore, the generation of high-energy ultra-short pulses down to the few-cycle regime is conventionally achieved by extra-cavity nonlinear pulse compression instead.

Until recently, spectral broadening and pulse compression of ultrashort pulses from high-peak-power lasers (10 MW – GW) was typically performed in gas-filled capillaries, photonic bandgap or Kagomé-type hollow-core photonic-crystal fibers (HC-PCFs) [68]. In particular, spectral broadening in gas-filled hollow-core fibers has been proven a powerful tool for the temporal compression of high average- and peak-power lasers. It yielded for example a 16-fold compression to 88 fs at >100 W of average power by spectral broadening in a single argon-filled Kagomé HC-PCF in the normal dispersion regime in combination with a chirped-mirror compressor [69]. By choosing an appropriate combination of gas and pressure, HC-PCFs can furthermore be operated in the anomalous dispersion regime, where the generation of <10 fs pulses has been demonstrated in a two-stage Kagomé-fiber system seeded by a Kerr-lens mode-locked thin-disk oscillator [70, 71]. Only recently, this powerful technique has further been shown to facilitate the efficient generation of single-cycle laser pulses at 100 W-level average power and gigawatt-scale peak power from an all-fiber laser system at megahertz repetition rate [72].

Despite providing an efficient measure for temporal pulse compression with excellent beam quality, fiber-based spectral broadening is alignment sensitive and couples pointing-drifts to laser power fluctuations which in turn affects the power-dependent nonlinear pulse compression process. Additionally, with their delicate microstructure, fibers show increased susceptibility to damage at high average- and peak powers. Moreover, photoionization in gas-filled HC-PCFs might limit their use in high average power systems at high repetition rates [73, 74]. Such detrimental effects can mostly be alleviated by employing pulse compression schemes in which the nonlinear spectral broadening is realized in bulk materials. Due to the large and homogeneous optical apertures of bulk broadening media, this approach can allow an efficient decoupling of the spatial beam stability and the broadening efficiency. Despite facilitating significant amounts of spectral broadening even in single-pass geometries, the lack of spatio-temporal homogenization in all-bulk spectral broadening approaches typically causes a significant degradation in spatial beam quality [75, 76].

Lately, a new spectral broadening method relying on a waveguide-like periodic assembly consisting of focusing elements (concave dispersive mirrors) and nonlinear media was suggested and demonstrated [77–79]. It combines the advantages of using bulk nonlinear media with the benefits of the long interaction length of waveguides without sacrificing the

spatial beam quality. Especially when realized in the form of a Herriott-type multipass-cell, such quasi-waveguides can provide a highly robust, compact and simple means of spectral broadening [80]. Both all-bulk and gas-filled multipass-cell geometries were successfully realized in high average and peak power regimes, pushing the broadened spectrum to sub-10 fs Fourier limit and pulse durations to sub-20 fs [81–83]. Recently, a first demonstration of pulse compression into the few-cycle regime ($\tau_{FWHM} = 6.9$ fs at 1030 nm wavelength) using a gas-filled multipass geometry seeded by a fiber amplifier system with several 100 µJ pulse energy was demonstrated experimentally [84]. In the frame of this thesis it was investigated, whether an extension of the nonlinear pulse compression towards the few-cycle regime is likewise feasible using all-bulk multipass-cells directly driven by a thin-disk laser oscillator with a pulse energy of only few microjoules.

2.2 Multipass-cell spectral broadening fundamentals

2.2.1 Geometric design considerations

In the preceding section, the advantages of waveguide-like periodic assemblies for spectral broadening applications have briefly been introduced. Such quasi-waveguides often represent a form of optical resonators and can be well described by the linear beam propagation methods described in section 1.1. Herriott-type multipass cells are a specific variant of stable resonators which consist of two concave mirrors facing each other on a common optical axis (cf. Fig. 2.1) and a method of injecting and extracting a laser beam [80]. For some combinations of mirror curvatures and distance, an incident laser beam with a specific q-parameter (see section 1.1.2) injected under just the correct angle will be reflected multiple times between the mirror surfaces, forming a characteristic elliptic or circular pattern upon them, before being extracted again with the incident q-parameter being preserved. To behave in such a way, both the Herriott-cell and the injected beam need to fulfil certain conditions.

Resonator stability and eigenmode

As mentioned above, the propagation of a beam inside a Herriott-cell can be described by the same formalism as used for stable two-mirror resonators. Stable resonators are generally defined by having an eigen-q-parameter q_E which is reproduced after one cycle through the resonator characterized by its roundtrip transfer matrix $\mathbf{M}$. In a more geometric interpretation, q_E thus describes a beam which is transversely limited and will stay confined to the resonator independent of the number of propagated roundtrips. Using the ABCD-matrix formalism introduced in section 1.1.2, this condition can be formally expressed by

$$q_E = \frac{Aq_E + B}{Cq_E + D} \tag{2.1}$$

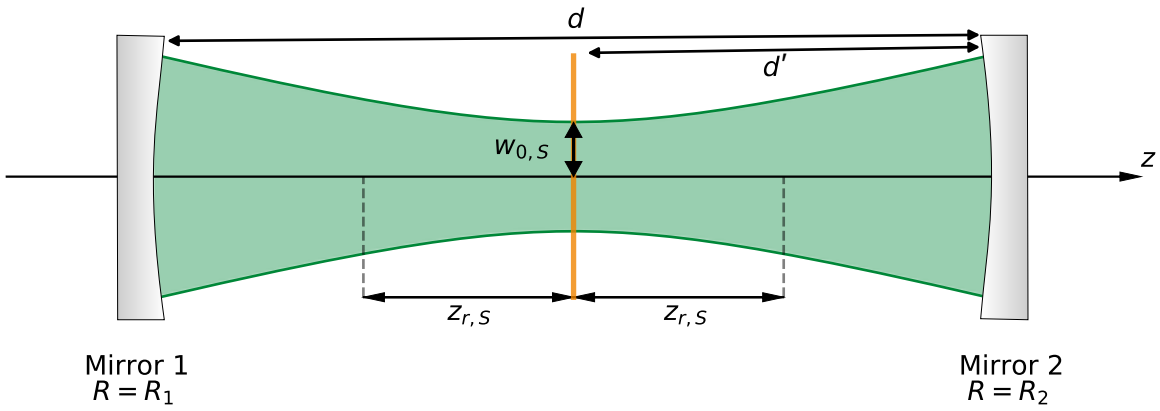

Fig. 2.1: Schematic of a Herriott-type multipass cell consisting of two mirrors with radius of curvatures R_1 and R_2 facing each other on a common optical axis (z) at a distance $d = 2 \cdot d'$. The green shaded area depicts the eigenmode of the two-mirror resonator characterized by the waist size $w_{0,S}$ and the Rayleigh range $z_{r,S}$ given in equation 2.9. The yellow line indicates the position of the reference plane for the single-pass transfer matrix given in equation 2.7.

which can be solved for q_E yielding

$$q_{E_{1,2}} = \frac{A - D \pm \sqrt{(D-A)^2 + 4BC}}{2C}. \tag{2.2}$$

where the eigen-q-parameters $q_{E_{1,2}}$ are given by the positive and negative solution of the quadratic equation 2.1, respectively. Knowing that the determinant $\det(\mathbf{M})$ of a roundtrip ray transfer matrix fulfills [25, p. 34]

$$\det(\mathbf{M}) = AD - BC = 1\ , \tag{2.3}$$

equation 2.2 can be transformed into

$$q_E = \underbrace{\frac{A-D}{2C}}_{z_{0,E}} + i \underbrace{\frac{\sqrt{-(A+D)^2+4}}{2|C|}}_{z_{r,E}}. \tag{2.4}$$

Since the Rayleigh length $z_{r,E}$ of the eigen-q-parameter has to be real and positive, the negative imaginary solution on the right hand side of equation 2.4 has been dropped. Furthermore, the radicand in eqation 2.4 has to be positive which leads to the resonator stability condition

$$-1 < \frac{A+D}{2} < 1. \tag{2.5}$$

Only if this condition is met, the optical system described by the transfer matrix $\mathbf{M}$ represents a stable resonator that features an eigenmode which is described by the complex beam parameter q_E. Analogous to a beam propagating in free-space, the Gouy-phase shift $\Delta\psi$ accumulated over one resonator roundtrip by a beam with the eigen-q-parameter can be calculated yielding [29]

$$\psi_E = \Delta\psi_{Gouy} = \text{signum}(B) \cdot \arccos\left(\frac{A+D}{2}\right) \tag{2.6}$$

Here, the Gouy-parameter ψ_E has been introduced as an alternative way of describing the propagation of a beam inside the resonator which will be used later on to characterize various important resonator properties.

While the formalism introduced above can in principle be applied to arbitrary geometries, the Herriott-cells used in this thesis are the simplest case of an optical resonator which consists of only two concave mirrors with equal radius of curvature $R = R_1 = R_2$ facing each other on a common optical axis at a distance d (cf. Fig 2.1). Since the resonator is symmetric, it is sufficient to evaluate the transfer matrix for a single pass through the optical system [85]. Starting the propagation at the reference plane marked in yellow in Fig. 2.1, the single pass transfer matrix $\mathbf{M_S}$ of the corresponding optical system can be written as

$$\mathbf{M_S} = \mathbf{M_{d'}} \cdot \mathbf{M_R} \cdot \mathbf{M_{d'}} = \begin{pmatrix} 1 & d' \\ 0 & 1 \end{pmatrix} \cdot \begin{pmatrix} 1 & 0 \\ -\frac{2}{R} & 1 \end{pmatrix} \cdot \begin{pmatrix} 1 & d' \\ 0 & 1 \end{pmatrix} = \begin{pmatrix} 1-\frac{d}{R} & d-\frac{d^2}{2R} \\ -\frac{2}{R} & 1-\frac{d}{R} \end{pmatrix}. \tag{2.7}$$

where $d' = d/2$ is half the mirror separation distance With this result, equation 2.5 can be rewritten as

$$0 < d < 2R \tag{2.8}$$

which is the stability condition for a symmetric Herriott-cell. The eigenmode can be interpreted as a Gaussian beam where the eigen-parameters are functions of the mirror separation and curvature and can be derived by substituting 2.7 into equations 2.4 and 2.6 yielding

$$z_{0,S} = 0, \qquad z_{r,S} = \frac{d}{2}\sqrt{\frac{2R}{d}-1} \quad \text{and} \quad \psi_S = \frac{\psi_E}{2} = \arccos\left(1-\frac{d}{R}\right). \tag{2.9}$$

From equation 2.9 it can further be seen, that for a symmetric Herriott-cell the waist $w_{0,S}$ of a Gaussian beam which corresponds to the eigenmode is centered between the two mirrors and can be described by [85]

$$w_{0,S} = \sqrt{\frac{\lambda}{\pi n} \cdot \frac{d}{2}\sqrt{\frac{2R}{d}-1}} \tag{2.10}$$

where λ is the laser wavelength and n is the refractive index of the ambient medium (typically $n \approx 1$ for a Herriott-cell in air). This notation furthermore allows the simple calculation of the mode size at an arbitrary axial distance z to the focus as described in section 1.1 which can later on be useful for estimating beam intensities in e.g. a nonlinear medium placed off-centered in the Herriott-cell.

Ray propagation formalism

It should be noted that for all mirror separation distances smaller than twice the radius of curvature (c.f. equation 2.8) an eigenmode for a symmetric Herriott-cell can be found. However, the transfer matrix $\mathbf{M}$ clearly generally does not take the form of an identity matrix $\mathbf{I}$. As a result, a ray of light injected into the Herriott-cell at an arbitrary position x_0 and under an angle x_0' will, after a number of N roundtrips, have shifted to a new position x_N and inclination x_N', which in vectorial form can be written as

$$\begin{pmatrix} x_N \\ x_N' \end{pmatrix} = \underbrace{\mathbf{M} \cdot \mathbf{M} \cdot \ldots \cdot \mathbf{M}}_{N-times} \cdot \begin{pmatrix} x_0 \\ x_0' \end{pmatrix} = \mathbf{M}^N \cdot \begin{pmatrix} x_0 \\ x_0' \end{pmatrix}. \tag{2.11}$$

Calculation of $\mathbf{M}^N$ can be accomplished easily by making use of Sylvester's formula which allows expressing an analytic function $f(\mathbf{M})$ of a matrix $\mathbf{M}$ in terms of its eigenvalues and eigenvectors [86]. If $\mathbf{M}$ is diagonalizable, Sylvester's formula states that

$$f(\mathbf{M}) = \sum_{i=1}^{k} f(\lambda_i)\mathbf{M}_i \tag{2.12}$$

where λ_i are the eigenvalues of $\mathbf{M}$ and the matrices

$$\mathbf{M}_i \equiv \prod_{\substack{j=1 \\ j\neq i}}^{k} \frac{1}{\lambda_i - \lambda_j}(\mathbf{M} - \lambda_j \mathbf{I}) \tag{2.13}$$

are the Frobenius covariants of $\mathbf{M}$. The corresponding eigenvalues of $\mathbf{M}$ are determined by the characteristic equation

$$\det(\mathbf{M} - \lambda_{1,2}\mathbf{I}) = 0. \tag{2.14}$$

Using the results from 2.3 and 2.6 the eigenvalues found by solving equation 2.14 can be expressed as

$$\lambda_1 = e^{i\psi_E}, \qquad \lambda_2 = e^{-\mathrm{i}\psi_E}. \tag{2.15}$$

The N-th power of $\mathbf{M}$ can now be calculated by substituting 2.13 and 2.15 into equation 2.12 yielding

$$\mathbf{M}^N = \frac{e^{iN\psi_E}}{e^{i\psi_E} - e^{-i\psi_E}} \begin{pmatrix} A - e^{-i\psi_E} & B \\ C & D - e^{-i\psi_E} \end{pmatrix} + \frac{e^{-iN\psi_E}}{e^{-i\psi_E} - e^{i\psi_E}} \begin{pmatrix} A - e^{i\psi_E} & B \\ C & D - e^{i\psi_E} \end{pmatrix}. \tag{2.16}$$

Using simple calculus of trigonometric functions as well as 2.3 and 2.6 again, equation 2.16 can be cast into the form [87]

$$\mathbf{M}^N = \begin{pmatrix} \frac{A-D}{2}\frac{\sin N\psi_E}{\sin \psi_E} + \cos N\psi_E & B\ \frac{\sin N\psi_E}{\sin \psi_E} \\ C\ \frac{\sin N\psi_E}{\sin \psi_E} & \frac{D-A}{2}\frac{\sin N\psi_E}{\sin \psi_E} + \cos N\psi_E \end{pmatrix} \tag{2.17}$$

which now allows the derivation of some interesting properties of Herriott-type multipass cells.

Substituting 2.17 into equation 2.11 we find that an incident ray with an arbitrary position x_0, y_0 and angle and x_0', y_0' along the x- and y-direction, correspondingly, will, after N-roundtrips, be displaced transversely. The new coordinates x_N and y_N are then given by [87]

$$x_N = x_0 \cos N\psi_E + \left(\frac{x_0(A-D) + 2Bx_0'}{2\sin\psi_E} \right) \sin N\psi_E \tag{2.18}$$

and

$$y_N = y_0 \cos N\psi_E + \left(\frac{y_0(A-D) + 2By_0'}{2\sin\psi_E} \right) \sin N\psi_E. \tag{2.19}$$

If the incident ray is aligned specifically such that it can be described by

$$x_0 = r, \quad x_0' = \frac{x_0}{2B}(D-A) \tag{2.20}$$

and

$$y_0 = 0, \quad y_0' = \frac{x_0 \sin\psi_E}{B}, \tag{2.21}$$

the ray of light propagating through the Herriott-cell will trace a circular spot pattern with radius r on the multipass-cell mirror surfaces which is schematically depicted in Fig. 2.2 a.

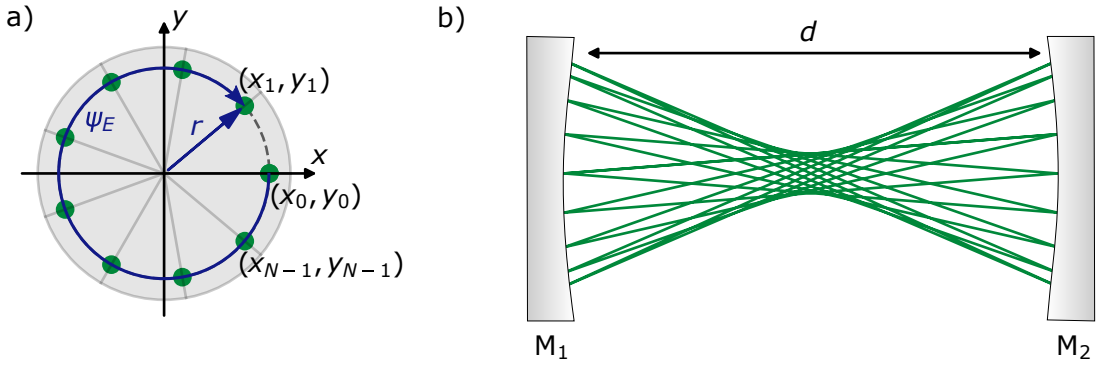

Fig. 2.2: **a)** Schematic depiction of the circular spot pattern with radius r formed on the multipass-cell mirror M_1 for a Herriott-cell with $\psi_E = 2\pi \cdot (8/9)$. The x and y positions are given by equations 2.18 and 2.19, respectively. **b)** Schematic depiction of the closed beam-path in between the two multipass-cell mirrors.

The individual spots around the circle are successively separated by an angular advance corresponding exactly to the Gouy-parameter ψ_E (c.f. Fig. 2.2 a) which was introduced in

equation 2.6 for purely analytic reasons. A similar pattern as shown for the first mirror in Fig. 2.2 a can be observed on the second mirror where the pattern is rotationally offset by an angle corresponding to $\psi_E/2$. The beam path between two subsequent reflections of the multipass-cell mirrors for a given Gouy-parameter can be calculated using linear ABCD-matrix propagation and is schematically depicted in Fig. 2.2 b. It should be noted that the transversal position after N-roundtrips in the x- and y-direction are mutually independant (equations 2.18 and 2.19) but both depend only on the value of the Gouy-parameter. As a result, the pattern traced by a light ray propagating through the Herriott-cell will generally take the form of an ellipse for initial ray parameters differing from those specified above. For the geometrical description of Herriott-cells, it is customary to choose the reference plane to coincide with one of the mirror surfaces, where the size and shape of the elliptic spot patterns need to be accurately matched to the utilized mirror geometry.

The re-entrant condition and pattern formation

In the preceding geometric treatment it has been demonstrated that the Gouy-parameter ψ_E plays an important role in describing the evolution of a ray of light propagating through a Herriott-cell. A special case is found when ψ_E is of the form

$$\psi_E = 2\pi\frac{K}{N} \tag{2.22}$$

where K and N are arbitrary positive integer numbers. When equation 2.22 holds, $\mathbf{M}^N$ reduces to the identity matrix $\mathbf{I}$ and the position and angle of any ray of light injected into the Herriott-cell are reproduced after N roundtrips at the latest. Since the propagation follows a closed path, the light ray continuously retraces the same elliptic spot pattern. Consequently, equation 2.22 is also termed the *re-entrant condition* [80].

This re-entrant condition plays an important role in the experimental realization of Herriott-cells. Here, the infinite propagation along a closed path is not possible since a mechanism for injecting and extracting the laser beam into and from the Herriott-cell assembly is physically required. This is most commonly achieved by placing a small coupling mirror (*scraper mirror*) right in front of one of the multipass-cell mirrors (see Fig. 2.3) or by drilling a small hole into one of the multipass-cell mirrors through which the beam can be injected.

By adjusting the position and angle of the incident beam, the required corresponding ray parameters for the formation of a circular spot pattern on the multipass-cell mirrors (c.f. equations 2.20 and 2.21) can then realized with either method. If the re-entrant condition is fulfilled, the scraper mirror or hole in the multipass-cell mirror can be used for both beam injection and extraction which is often preferable since it reduces system and manufacturing complexity and cost. However, the laser beam is then extracted before the closed path propagation has come full circle. This difference between the input and output beams can be expressed by a modified roundtrip ray transfer matrix which takes into account the missing final reflection from the multipass-cell mirror. If equation 2.22 holds and the reference plane is chosen such that it coincides with one of the multipass-cell

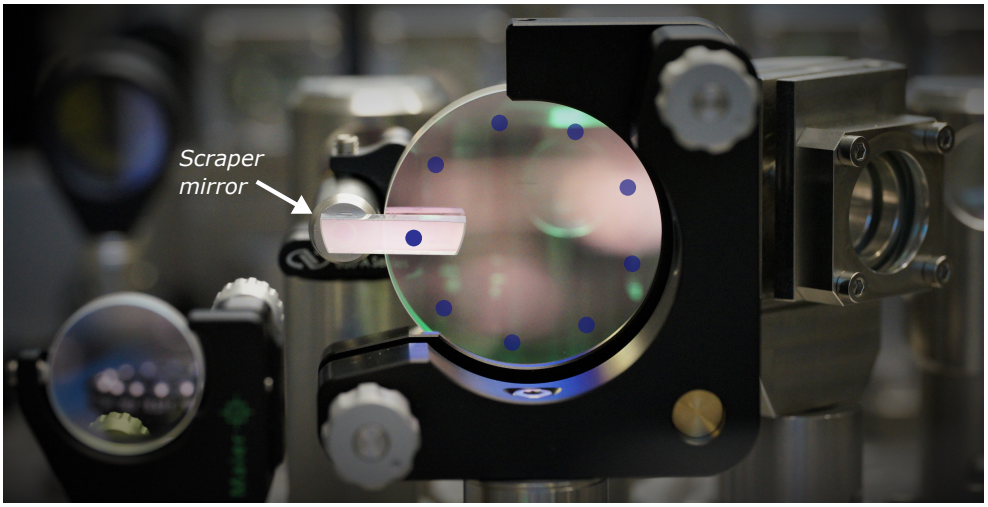

Fig. 2.3: Picture of a scraper mirror (in front of one of the multipass-cell mirrors) used to inject and extract the beam into the multipass-cell. The scraper mirror is cut from a circular mirror using a rotary diamond blade.

mirrors, the modified transfer matrix $\mathbf{M}_{out}$ of a symmetric Herriott-cell reads

$$\mathbf{M}_{out} = \mathbf{M}_R^{-1} \cdot \mathbf{M}^N = \mathbf{M}_R^{-1} \cdot \mathbf{I} = \begin{pmatrix} 1 & 0 \\ -\frac{2}{R} & 1 \end{pmatrix}^{-1} = \begin{pmatrix} 1 & 0 \\ \frac{2}{R} & 1 \end{pmatrix} \tag{2.23}$$

where R is the corresponding radius of curvature of the Herriott-cell mirror. It is easily seen that $\mathbf{M}_{out}$ is of lower unitriangular form and hence leaves the transversal position of the output beam on the multipass-cell mirror unaltered. However, the beam will exit the Herriott-cell under a well-defined, non-zero angle with respect to the input beam which subsequently allows the spatial separation of the two beams after some additional propagation distance.

The number of roundtrips which the beam has propagated in the Herriott-cell before being coupled out is found to be solely dependant on the relation between K and N. If K and N are coprime integers, the circular pattern formed in the input reference plane consists of exactly N spots. If K and N share one or more common divisors, the circular pattern will consist of $N/\mathbf{gcd}(K, N)$ spots where $\mathbf{gcd}(K, N)$ denotes the greatest common divisor of K and N. For a symmetric Herriott-cell with a given number of roundtrips N, each value of $K \leq N$ defines a mirror separation distance d according to

$$d = \left(1 - \cos\left(\pi \frac{K}{N}\right)\right) R \tag{2.24}$$

for which the beam becomes re-entrant after no later than N roundtrips.

Mode-matching

In the previous paragraphs, the ray transfer matrix of a Herriott-cell fulfilling the re-entrant condition has been shown to take the form of an identity matrix for a fixed number of roundtrips N. This implies that not only the incident beam position and angle, but also its complex beam parameter q_{in} is reproduced after the beam has propagated through the Herriott-cell N-times, where

$$q_{out} = \mathbf{M}^N \cdot q_{in} \overset{\text{re-entrant}}{=} \mathbf{I} \cdot q_{in} = q_{in}. \tag{2.25}$$

Since equation 2.25 holds for any q_{in}, the corresponding Herriott-cell configurations are termed *q-preserving*. However, it should be noted that q-preserving configurations do not impose additional restrictions on the q-parameter for the propagation of individual roundtrips. Consequently, if a beam with an arbitrary q-parameter is injected into the Herriott-cell, the beam size evaluated in a fixed reference plane can vary significantly for consecutive roundtrips.

When employing Herriott-type multipass cells for spectral broadening, which is based on exploiting the SPM occuring in a bulk medium placed inside the multipass-cell, it is therefore often desirable to have a beam caustic which is identical in each pass in the Herriott-cell. Only in this case the per-pass nonlinear phase shift is the same for each transition of the beam through the nonlinear material which ensures that the beam can experience a good homogenization during the extended propagation (cf. section 2.2.2). The desired behaviour is found for Gaussian input beams that are represented by a q-parameter that matches the eigen-q-parameter q_E of the Herriott-cell, which was introduced in the derivation of the stability condition in equation 2.4. Since the q-parameter of the incident beam thus needs to be matched to the eigenmode of the Heriott-cell, this process is also termed *mode-matching*. For the experimental realization of a symmetric Herriott-cell, the input beam should therefore preferably have a waist which lies in the center between the multipass-cell mirrors and has a waist size that is described by equation 2.10. In the frame of this thesis, mode-matching is typically achieved by using a plano-concave mirror to create a focus in the center plane of the Herriott-cell. The correct focus size is achieved by either varying the size of the collimated beam incident on the focusing mirror by means of a variable zoom beam expander or, if possible, by appropriately matching the radius of curvature of the focusing mirror to the incident beam size.

Misalignment

As discussed above, the closed path circular shape of the pattern traced by a ray injected into the Herriott-cell depends critically on the precise alignment of the optical components forming the multipass-cell and the angle and position of the input beam. For a more detailed understanding, it is instructive to evaluate how the created pattern changes for different types of misalignment. For the multipass-cell mirrors, longitudinal or transversal displacements as well as angular tilt with respect to the common optical axis constitute the most basic forms of misalignment.

From equations 2.18, 2.19, and 2.9 it can be seen that the resonator length d can be used to parametrize the angular advance ψ_E of the successive spots in the circular pattern. A longitudinal displacement δ of one of the multipass-cell mirrors will therefore result in a modified angular advance between successive roundtrips. An example of the transformed spot pattern of a previously re-entrant Herriott-cell with $\psi_E = 2\pi\cdot(8/9)$ (Fig. 2.4 a) where a longitudinal displacement of $\delta = 0.001 \cdot d$ has been added to the mirror separation distance is shown in Fig. 2.4. Closer analysis reveals that the introduced longitudinal displacement is translated into a transversal separation of the zero$^{\text{th}}$ and N^{th} spot in the reference plane coinciding with one of the mirror surfaces, where the separation angle $\Delta\varphi_L$ for a fixed δ is found to depend on the value of the Gouy-parameter ψ_E. Such spatial separation of the two relevant spots can severely complicate both beam injection and extraction, since the size of the utilized scraper mirror or coupling hole is typically minimized to close to the beam size in order to maximize the usable surface of the cell mirror and thus the achievable number of roundtrips in the multipass-cell. In the experiment, one of the cell mirrors is therefore conventionally placed on a linear translation stage to allow a precise fine-adjustment of the resonator length.

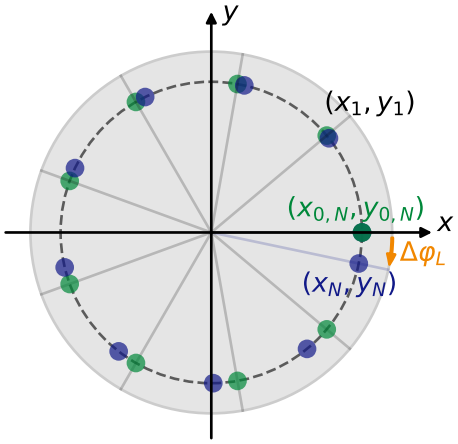

Fig. 2.4: Schematic depiction of the modified circular spot pattern for a Herriott-cell with longitudinal displacement $\delta = 0.001 \cdot d$ of one of the multipass-cell mirrors (blue circles) with respect to the original pattern (green circles). The longitudinal displacement results in a transversal angular displacement of the individual spots that increases with the number of passes, resulting in an separation angle of $\Delta\varphi_L$ between the 0^{th} and N^{th} spot.

The situation becomes somewhat more complex for transversal displacements and angular tilt of the multipass-cell mirrors which cannot be calculated trivially using the formalism introduced in section 1.1.2. Precise calculation of the spot positions in closed form for Herriott-cells including decentered or tilted optical components could be obtained by employing generalized beam matrices, e.g. using the 3×3 transfer-matrix method introduced by A. Tovar and and L. Casperson in 1995 [88]. However, the detailed mathematical treat-

ment using the 3×3 transfer-matrix method is beyond the scope of this thesis. For small transversal misalignments, however, the induced variation of the multipass-cell length can be neglected and the transversal displacement and angular tilt of a multipass-cell mirror can be approximated by a transformation of the optical axis of the corresponding optical element, instead. As a consequence, the spot patterns on the mirrors can be calculated numerically by stepwise propagation of the input ray using ABCD-matrices, where the local orientation of the optical axis is taken into account by a suitable coordinate transformation of the incident beam into the coordinate system spanned by the new optical axis.

Phenomenologically, both transversal displacement and angular tilt of the multipass-cell mirrors are found to affect the orientation of the principal axes as well as the extent and eccentricity of the elliptic spot pattern. As expected, a similar behaviour of the spot pattern is observed under misalignment of the the angle and position of the incident beam. However, in case of a misaligned input beam, the position of the spots can be obtained simply by solving equations 2.18 and 2.19 for the new set of input parameters x_0, x_0', y_0 and y_0'. It should be noted that the relative amount of change in beam position and angle varies for Herriott-cells described by different Gouy-parameters. For the sake of brevity, a more thorough investigation quantifying the alignment sensitivity of Herriott-cells to different types of misalignment is omitted here. Further details on the alignment sensitivity for stable resonators in general can be found for example in reference [29].

2.2.2 All-bulk spectral broadening in Herriott-cells

The spectral broadening of laser pulses is conventionally realized by exploiting the optical Kerr-effect in nonlinear media. This effect facilitates the generation of new optical frequencies via SPM for initially up-chirped or un-chirped pulses (cf. section 1.2.3). When combined with subsequent chirp removal, spectral broadening constitutes an efficient method for nonlinear pulse compression. When assuming a constant time-bandwidth product, the achievable temporal compression factor scales linearly with the amount of spectral broadening. The magnitude of the spectral broadening can itself be quantified by the spatially averaged peak nonlinear phase shift ϕ_{NL} which is here given in the integral form (cf. equation 1.109)

$$\phi_{NL} = \frac{2\pi}{\lambda_0} \int_0^d n_2 I_{peak}(z) \mathrm{d}z \tag{2.26}$$

where λ_0 and I_{peak} are the center wavelength and the spatially averaged peak intensity of the input pulse and n_2 and d are the the nonlinear refractive index (cf. section 1.2.3) and the length of the nonlinear material, respectively.

While the accumulated nonlinear phase provides a good measure for the broadening factor it does not contain any information about the compressibility of the spectrally broadened pulses. In the frame of this thesis, a high compression quality will be understood to correspond to a temporal pulse shape where the fractional amount of energy within any satellite pulses is as low as possible. In most cases, this means that the spectral phase of the pulse should be free of quadratic and higher order contributions and the instantaneous frequency should be as constant as possible, i.e. the pulse should be close to the transform

limit. Since the transform-limited pulse shape can also contain satellite structures due to oscillations in spectrum generated throughout the broadening process (cf. section 1.2.3), the compression quality is further quantified by the ratio

$$\eta_{comp} = \frac{P_{peak}^{comp}}{P_{peak}^{FTL}} \tag{2.27}$$

which relates the peak power of the spectrally broadened pulse after compression P_{peak}^{comp} to that of a bandwidth limited pulse with the same spectrum and output power.

For spectral broadening in the zero- and normal-dispersion regimes, the SPM-induced up-chirp is mostly linear over the central part of the spectrum as long as the temporal shape of the input pulse is reasonably smooth [40]. Consequently, a high quality temporal compression can often be achieved simply by introducing negative GDD to the pulse (cf. section 1.1.3) which can efficiently be realized for example by using chirped mirrors. On the downside, however, the spatial variation of the local intensity in a laser beam (which is typically approximated with a Gaussian intensity distribution) causes the pulses to accumulate a radially varying nonlinear phase which drops off from the center towards the wings of the beam. As a result, the spectrum is no longer broadened homogeneously over the beam profile and the temporal compression quality will depend on the spatial position in the beam.

Until recently, this difficulty has conventionally been evaded by utilizing fibers or gas filled capillaries for spectral broadening. In the underlying waveguide geometry, the beam evolution is governed by an interplay of diffraction and constant re-focussing due to the boundary conditions of the guided propagation. This gives rise to a continuous redistribution of the newly generated spectral components across the beam profile [45]. Furthermore, the field is confined to a small area for a long propagation distance which facilitates the accumulation of large nonlinear phase shifts ϕ_{NL}, since high intensities can be maintained for extended propagation lengths (compare equation. 2.26). The long propagation distances, however, typically limit the usable input peak power to values much lower than the critical power for self-focusing P_{cr} (cf. secion 1.2.3), since the excessive refractive power of the generated Kerr-lens (cf. section 1.2.3) can otherwise lead to catastrophic self-focusing inside the waveguide.

Multipass-cell based spectral broadening

In a theoretical investigation on pulse compression based on the coupled-mode theory, N. Milosevic and co-authors have suggested that large spatially uniform phase shifts can alternatively be achieved, if the accumulation of the nonlinear phase shift is distributed over a sufficiently large number of passes through a nonlinear medium with intermediate re-focusing of the beam [45]. However, their approach for homogeneous spectral broadening was only applicable when self-focusing effects are weak, i.e. the peak power of the incident laser pulse is significantly below the critical power for self-focusing. More specifically, the maximum nonlinear phase shift accumulated per pass through the nonlinear medium was required to remain on the order of unity [45]. It has since been demonstrated experimentally

by J. Schulte et al. in 2006 that an efficient homogenization can also be achieved in spectral broadening schemes employing waveguide-like periodic assemblies — such as the Herriott-type multipass-cell, which has been briefly introduced in the previous section — even for pulse energies significantly higher than P_{cr} [77].

When inserting a suitable nonlinear medium into such a Herriott-cell, the circulating pulse accumulates a nonlinear phase shift ϕ_{NL} in each pass through the nonlinear medium. The amount of the per-pass accumulated nonlinear phase can simply be adjusted by varying the position (peak intensity), material (nonlinear refractive index) and thickness of the nonlinear medium. If dispersive effects are negligible, the per-pass nonlinear phase shift is the same for each consecutive pass through the nonlinear medium as long as the input beam is *mode-matched* to the Herriott-cell (see following paragraph for further details). The total nonlinear phase $\Sigma\phi_{NL}$ which is accumulated within the Herriott-cell is then simply given by

$$\Sigma\phi_{NL} = N \cdot \phi_{NL}^{(i)} \tag{2.28}$$

where N is the number of passes and $\phi_{NL}^{(i)}$ is the nonlinear phase shift in the first pass though the nonlinear medium. The amount of spectral broadening can then be estimated e.g. by using equation 1.110.

It should be noted that the spatio-temporal homogenization only works efficiently if the value of the per-pass nonlinear phase is chosen low enough to avoid significant self-focusing and beam aberrations due to the non-spherical shape of the Kerr-lens [45, 77]. In earlier work by K. Fritsch et al., numerical simulations have indicated that for bulk spectral broadening in a multipass-cell operated in the normal dispersion regime, a nonlinear phase-shift of 0.3 rad ($\approx \pi/10$) per pass through the broadening medium represents the upper limit for which a clean output beam can be obtained [81]. Exceeding the aforementioned per-pass phase shift can result in a decreased beam homogeneity which often causes a deterioration of the spatial beam quality, typically manifesting itself in additional conical emission causing the formation of a characteristic ring pattern around the main beam and reducing its focusability [76]. An empirical evaluation of the validity of the above stated maximum value of the per-pass nonlinear phase shift for Herriott-cells which are operated in the net-positive dispersion regime is provided in section 3.1.2.

Material dispersion

As briefly discussed in section 1.2.3, the optical Kerr-effect which is commonly exploited for spectral broadening via SPM generally does not depend on the inversion symmetry of the utilized nonlinear material. As a result, a vast variety of different nonlinear materials ranging from gases to solids can be used for multipass-cell based spectral broadening. In this thesis, the description is restricted to bulk materials as nonlinear media since the peak power of the utilized driver laser is too low to generate a significant nonlinear response in most gases.

For the experiments described in this and the following chapter, fused silica (fused quartz) was chosen as a nonlinear material according to its beneficial optical properties:

Due to its wide band gap of 9 eV, fused silica exhibits a low linear and multiple-photon absorption for NIR radiation at around 1 µm wavelength (photon energy $E_{\hbar\nu} \approx 1.2\,\mathrm{eV}$). Combined with its low thermal expansion coefficient, this makes the material suitable for being used in high average-power laser applications. Furthermore, opposed to many crystalline wide-band gap materials such as crystal quartz or sapphire (Al_2O_3), it is isotropic and therefore free of birefringence, allowing for a uniform spectral broadening independent of the polarization of the incident beam. As an additional advantage, it is widely commercially available in a variety of different geometries and lengths and can be readily coated with high-quality anti-reflective (AR) coatings to enhance the transmission by reducing reflection losses.

As introduced in section 1.1.3, all dielectric materials exhibit a second- and higher-order dispersion which can cause a modification of the pulse shape during SPM-based spectral broadening. For arbitrary propagation distances, the material dispersion can be conveniently expressed by introducing the *group velocity dispersion (GVD)* which is the GDD of the material (cf. section 1.1.3) per unit-length. For fused silica, the GVD is positive and takes a value of $\approx 18.97\,\mathrm{fs}^2/\mathrm{mm}$, specified at the center wavelength of 1030 nm of the utilized driver laser. Since the TOD of fused silica is likewise positive, an asymmetrical temporal broadening of laser pulses propagating through fused silica nonlinear media can be observed (compare Fig. 1.2). The increase of the pulse duration associated with temporal broadening causes a reduction of the peak intensity of the pulses which feeds back and reduces the magnitude of the nonlinear phase shift ϕ_{NL} (cf. equation 2.26) and thus, the amount of spectral broadening. Furthermore, the asymmetry of the temporal pulse shape is imprinted onto the broadened spectrum and spectral phase by the effect of SPM. The temporal compression of the spectrally broadened laser pulses can therefore be significantly more complicated, since the pulse cannot be compressed by simply introducing a specific amount of negative GDD but the higher-order contributions of the spectral phase need to be removed as well.

As a consequence, for the design of a nonlinear pulse compression scheme it is often beneficial to target a propagation regime in which the spectral broadening is only weakly influenced by dispersive effects. Herein, a distinction should be made between the material dispersion for one pass through the nonlinear medium and the net-dispersion regime of the Herriott-cell. The latter consists of multiple transitions of a laser pulse through the nonlinear medium — each of which is followed by a reflection from a concave focusing mirror, the coating of which can also add dispersion.

In the single-pass case, the total magnitude of spectral broadening can be considered small due to the previously stated requirement of the per-pass nonlinear phase shift to be $<0.3\,\mathrm{rad}$ in order to facilitate a homogeneous spectral broadening and avoid strong self-focusing effects. As a result, the amount of temporal broadening in this case mainly depends on the GDD of the nonlinear medium. In practice, dispersive effects within one pass through the nonlinear medium can often be neglected as long as the length of the medium d can be described by

$$d \ll \frac{\tau_{FWHM}^2}{GVD} \tag{2.29}$$

where τ_{FWHM} is the pulse duration of the incident pulse. The approximation in equation 2.29 is based on the increasing effect of GDD on the temporal broadening with decreasing input pulse duration τ_{FWHM} which has previously been derived for a Gaussian temporal profile in equation 1.68.

Mirror dispersion

It is important to note that the realization of high spectral broadening factors requires the accumulated nonlinear phase shift to be large as well (compare equation. 1.110). In multipass-cell based spectral broadening schemes, this can be achieved by propagating the pulse many times through the nonlinear medium. However, the pulse will as a result not only be temporally broadened once, but in each successive pass through the nonlinear medium. Consequently, a siginificant reduction of the peak intensity can typically be observed after only a few passes as a result of the accumulated dispersive effects — even if the nonlinear medium is only a few millimeters thin. The reshaping of the temporal pulse shape can efficiently be counteracted by utilizing dispersive mirrors with opposing sign to the material GDD for the refocusing of the beam between each pass through the nonlinear medium. Not only that, the temporal evolution of the pulse propagating through the Herriott-cell can be precisely engineered by varying the dispersion profiles of the utilized multipass-cell mirrors. Depending on the GDD value of the dispersive mirror, the propagation can roughly be divided into three different dispersion environments.

In the *zero-dispersion environment*, the focusing mirrors are equipped with a dispersive coating which closely compensates the second- (and higher) order dispersion induced by the utilized broadening medium. If the nonlinear contribution per pass is weak, this allows the pulse to maintain its initial pulse shape and peak intensity throughout the propagation while continuously acquiring a fixed per-pass nonlinear phase. In the zero-dispersion environment, the propagation of a pulse is typically well described by the framework presented in section 1.2.3. However, in real world applications it is often difficult to exactly compensate the GDD of the nonlinear material due to manufacturing tolerances of the dispersive mirror coating. As a result, the pulse propagation in real-world multipass-cells typically takes place in either a *net-negative* or *net-positive* dispersion environment.

In the net-negative dispersion environment, the dispersive coating of the multipass-cell mirror over-compensates the positive chirp which is added to the pulse during each pass through the nonlinear medium as a result of dispersion and SPM. The continuous propagation of a pulse through a Herriott-cell in the net-negative dispersion environment can therefore cause self-compression of the incident pulse. A more detailed investigation of self-compression in Herriott-type multipass-cells including experimental results and further discussion of the underlying beam evolution is presented in section 2.3.

In contrast, if the GDD of the multipass-cell mirror only partially compensates the positive material dispersion, the propagation effectively takes place in a net-positive dispersion environment. As a result, the peak intensity of a pulse will gradually decrease during propagation due to temporal broadening, which inhibits further spectral broadening. As mentioned in the beginning of this section, the spectral broadening in a net-positive disper-

sion environment can however be beneficial for the temporal compression quality since it evokes a linearisation of the accumulated up-chirp [40]. The results on spectral broadening using Herriott-cells in the positive dispersion regime which were obtained in the frame of this thesis are presented in chapter 3.

Numerical modeling

To gain a better understanding of the pulse evolution in a Herriott-type multipass-cell under the influence of nonlinearity and dispersion, the process can be modelled numerically by solving the GNLSE described in section 1.2.4. As further introduced in section 1.2.4, the utilized solver is based on the open source python module *pyNLO* which uses an adaptive step-size implementation of the fourth-order Runge-Kutta in the interaction picture [48, 50]. However, this version of *pyNLO* is mostly focused on the simulation of pulse propagation in optical fibers. Therefore, to facilitate the efficient simulation of pulse propagation in multipass-based quasi-waveguide assemblies, several modifications to the main simulation code were made.

To accurately represent the discrete nature of the Herriott-cell in the simulations, the code was re-written to simulate each pass in the Herriott-cell independently. The simulation of a Herriott-cell with N passes through the nonlinear medium and corresponding dispersive mirror reflection therefore corresponds to N simulations which are automatically performed consecutively, with the input pulse of each simulation being identical to the output pulse of the previous simulation. Each of the simulations can be further subdivided into two parts: the propagation in the nonlinear medium which is simulated by solving the GNLSE in equation 1.117 and the reflection from the multipass-cell mirror which corresponds to a simple manipulation of the pulse spectrum and spectral phase. It should be noted that in the above approximation, the nonlinearity of the ambient medium (typically air) which fills the space between the bulk nonlinear medium and the multipass-cell mirrors was considered to be negligible, i.e. that the nonlinear phase contribution from the ambient medium is significantly smaller than that of the bulk nonlinear medium ($\phi_{NL}^{Air} \ll \phi_{NL}^{Bulk}$).

For the propagation part, the nonlinear coefficient γ (cf. equation 1.118) of the medium is calculated using a frequency independent nonlinear refractive index n_2 of the bulk nonlinear medium, which is a good approximation for most wide band gap materials at around a wavelength of 1030 nm [89, 90]. In contrast to fibers, the pulse energy in free-space propagation is not confined to a fixed beam size over the entire propagation distance owing to the natural diffraction of a real laser beam. Therefore, a position dependent nonlinear coefficient $\gamma(z)$ is introduced as a function of the axial position in the nonlinear medium which, using equation 1.118, can be written as

$$\gamma(z) = \frac{n_2 \omega_0}{c_0} \cdot \frac{1}{\pi \left(w_E(z)\right)^2} \tag{2.30}$$

where $w_E(z), z \in [-d/2, d/2]$ is the caustic of the eigenmode of a Herriott cell of length d which can be calculated using equations 1.20 and 2.10. The nonlinearity can then be

accurately modelled by updating the γ-parameter according to equation 2.30 for each step in the simulation.

For the simulations of the Herriott-cells in this thesis, a spatially Gaussian input beam which is perfectly matched to the eigenmode of the Herriott-cell is assumed. Furthermore, since for the Herriott-cells described in this thesis the length of the nonlinear medium l_{mat} is much shorter than the Rayleigh length of the eigenmode z_E, a position independent nonlinear coefficient can be introduced according to equation 1.118 where the effective area A_{eff} is calculated according to equation 1.119 using an effective beam radius w_{eff} given by

$$w_{eff} = \frac{w_E(z_m) + w_E(z_m + l_{mat})}{2} \tag{2.31}$$

where $w(z_m)$ is the spot size of the eigenmode at the incident plane of a nonlinear medium of length l_{mat} which is positioned at an axial distance z_m to the focal plane of the Herriott-cell. The above approximation can help to significantly speed up the simulations since the nonlinear coefficient doesn't need to be updated for each simulation step. The influence of higher order nonlinear effects such as self-steepening as well as the instantaneous and delayed Raman-reponse of the material were adopted from the original *pyNLO* code without further modifications.

To appropriately consider the effects of second- and higher order dispersion on the pulse evolution inside the nonlinear medium, the wavelength dependant refractive index of the nonlinear medium is modelled using a Sellmeier equation of the form given in equation 1.71. The individual dispersion coefficients β_m (cf. equation 1.117) are then determined by spline interpolation of the refractive index curve. Finally, the dispersion of the multipass-cell mirror is taken into account after each propagation through the nonlinear medium by directly applying the measured GDD curve of the corresponding multipass-cell mirror to the spectral phase of the pulse. As an alternative, it is also possible to approximate the mirror dispersion curve by providing the corresponding GDD, TOD and FOD values of the dispersive coating. It should be noted that in the simulations performed in this thesis, the dispersion of the ambient medium was typically neglected due to its weak impact on the pulse evolution. However, in cases where the dispersion of the ambient medium can not be omitted, it should be feasible to model its influence e.g. by appropriately modifying the dispersion curves of the multipass-cell mirrors.

In this thesis, numerical simulations were used to model the evolution of spectrum and pulse shape for the multipass-cell spectral broadening experiments in the negative dispersion regime which are described in further detail in section 2.3.2 as well as to optimize the dispersion parameters of Herriott-cells for efficient spectral broadening in a positive dispersion environment which is described in section 3.1 It should be emphasized that the modifications to the *pyNLO*-module were developed in close collaboration with K. Fritsch. Further informations on the simulation code as well as extensive benchmarking results can be found in reference [91].

2.3 Negative dispersion: Self-compression in all-bulk multipass geometry

2.3.1 Experimental realization and compression results

Up until today, all-bulk multipass spectral broadening has predominantly been investigated in the net-zero- or normal dispersion regime. However, multipass-cell based spectral broadening can become increasingly interesting when high peak power levels are combined with operation in the anomalous dispersion regime where self-compression, Raman soliton self-frequency shifting, supercontinuum generation and other highly nonlinear effects are expected to come into play [92]. Self-compression and supercontinuum generation can potentially be exploited for significantly extending the spectral broadening factors of single-stage multipass-cell assemblies resulting in a significant reduction of complexity in existing multipass-cell-based spectral broadening setups. On the other hand, Raman soliton self-frequency shifting can be used to generate a power-tunable, asymmetric red-shift of the spectrum as it has previously demonstrated in optical fibers, albeit, at nanojoule pulse energies [93].

In 2018, G. Jargot et al. demonstrated, for the first time, that self-compression can occur in all-bulk Herriott-type multipass cells operated in the anomalous dispersion regime. In their experiment, the output of a fiber amplifier seeded optical-parametric chirped-pulse amplification system delivering 63 fs pulses with 19 µJ pulse energy at 125 kHz pulse repetition rate was self-compressed down to 22 fs with a transmission of 73 %. The utilized multipass-cell was tuned to operate in the net-negative dispersion regime by using a 2 mm-thick fused silica plate as a nonlinear medium, which exhibits a slightly negative GVD of $-28\,\mathrm{fs}^2$ at the operation wavelength of 1550 nm [94].

Unfortunately, the absence of suitable materials with negative GVD does not permit a similar approach at 1 µm wavelength where high power Yb-based lasers are readily available. However, the negative dispersion can alternatively be provided by an anomalously dispersive mirror coating that slightly overcompensates the normal material dispersion of the broadening substrate. The experimental results obtained for self-compression in an all-bulk multi-pass geometry driven directly by a powerful thin-disk oscillator at around 1 µm are presented and discussed in the following section.

The driving laser

For the self-compression experiments, a high power Kerr-lens mode-locked thin-disk oscillator based on Yb:YAG as gain medium was used as a driving laser [23]. The state-of-the-art thin-disk oscillator was developed in-house by M. Poetzlberger (see reference [95]) and is based on an imaging concept termed active multipass cell. The resulting increase in roundtrip gain facilitates operation with a significantly increased output coupling ratio,and thus high peak output power, when compared to more conventional oscillator designs [96]. At the time of the experiment, the oscillator could reproducibly emit an average output

power of 149 W in a continuous mode-locked pulse train with 10.6 MHz pulse repetition frequency. A pulse duration of approximately 300 fs was measured using a home-built dispersion-free SHG-FROG device (the pulse duration measurements were performed by bachelor student Benedikt Schneider), corresponding to a peak power of 41 MW.

The transverse profile of the emitted laser beam features a Gaussian shape surrounded by a faint circular pattern (Fig. 2.5). This likely originates from a combination of diffraction at the hard aperture inside the laser cavity and accumulated aberrations imprinted on the beam during the multiple imaged transmissions through the thin-disk gain medium. For the spectral broadening experiments, the oscillator output was cleaned up spatially by placing a water-cooled copper aperture with a diameter of 3.4 mm in the collimated beam, blocking the diffraction ring. The transmitted central section contained 92 % of the total power.

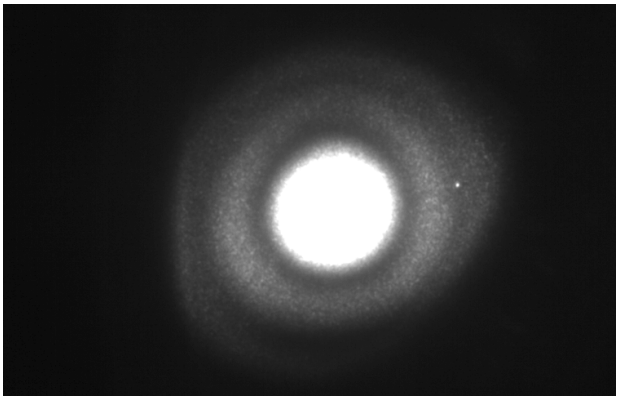

Fig. 2.5: Picture of the emitted far field beam profile at the oscillator output. The central part of the beam is surrounded by a faint, undesired, circular pattern. To enhance the visibility of the diffraction rings, the picture was taken by photographing the response of a highly saturated detector card placed in the collimated beam using a CCD camera.

In addition, the output polarization of the oscillator was linearized using an AR-coated thin-film polarizer (TFP), yielding a remaining average power of 136 W. Inserting a half-wave retarder plate followed by a second TFP into the beam path enables the stepless adjustment of the power level used in the experiment. At maximum power, pulses with 12.8 µJ pulse energy and 38 MW peak power are launched into the subsequent multipass-cell arrangement.

Multipass-cell configuration and alignment

The multipass cell which was used for investigating the nonlinear effects in the anomalous dispersion regime comprises two plano-concave multipass-cell mirrors having an outer diameter of 50 mm and a radius of curvature of 300 mm. A plane-parallel fused silica window was placed between them as a nonlinear medium. The mirrors are aligned such that the concave surfaces face each other on a common optical axis. Furthermore, one of the mirrors

is mounted on a linear translation stage which allows fine tuning of the resonator length (cf. Fig. 2.6).

The Herriott-cell is configured to become re-entrant after 23 roundtrips with $\psi_E = 2\pi \cdot (17/23)$ corresponding to a mirror separation distance of $d \approx 532\,\mathrm{mm}$. Consequently, a total number of 46 passes through the 6.35 mm-thick fused silica plate is achieved. To avoid excessive power loss from surface reflections, the nonlinear medium furthermore features an AR coating on both surfaces increasing the single pass transmission within the Herriott-cell to $T_S > 99.7\,\%$. By placing the fused silica window off-centered with a distance of approximately 180 mm to one of the Herriott-cell mirrors, the nonlinear phase shift accumulated in the first pass through the nonlinear medium is adjusted to a low value of approximately 0.2 rad.

Beam injection and extraction into and from the Herriott-cell are realized by placing a small, plane scraper mirror close to the front of one of the multipass-cell mirrors (cf. Fig. 2.3). This scraper mirror is aligned such that the propagating beam forms a circular spot pattern on the multipass-cell mirrors. To avoid variation of the per-pass nonlinear phase shift due to changes of the beam size in the nonlinear medium over consecutive passes, the size of the beam exiting the oscillator needs to be adjusted to match the eigenmode of the Herriott-cell. For this, a commercially available zoom-beam expander is used in conjunction with a concave focusing mirror with a radius of curvature of 900 mm placed at a distance of approximately 450 mm to the center plane of the Herriott-cell. The quality of the mode-matching is assessed by positioning a ground glass diffuser closely behind one of the cell mirrors. Due to the non-vanishing transmission T_M of the multipass-cell mirror coating (typically $T_M < 0.05\,\%$ for a high-quality coating), a small fraction of the beam power leaks through the cell mirrors. Consequently, a copy of the spot pattern that is visible on the Herriott-cell mirror appears on the ground glass screen where it can be monitored using a commercial silicon-based CCD camera. The mode-matching is then optimized experimentally by adjusting the size and divergence of the incident beam by varying the zoom beam expander settings until all the spots in the pattern appear to be identical in size (see Fig. 2.7).

The divergent beam, which leaves the Herriott-cell under a slight vertical angle with respect to the input beam, is collimated using a plano-concave mirror with a radius of curvature of 1000 mm placed at a distance of 500 mm to the center plane of the Herriott-cell. For diagnostics, an AR-coated fused silica wedge can be inserted in the collimated beam to extract a small fraction of the full power beam while the transmitted power is dumped on a thermal power sensor.

Mirror dispersion

For self-compression to occur during spectral broadening in the quasi-waveguide structure, the Herriott-cell has to be operated in the net-negative dispersion regime. To reach this regime, the cell mirrors feature a dispersive coating with a group delay dispersion of $-150\,\mathrm{fs}^2$ at 1030 nm, slightly overcompensating the second order dispersion of the fused silica window which is approximately $120\,\mathrm{fs}^2$ at this wavelength. The combination of the

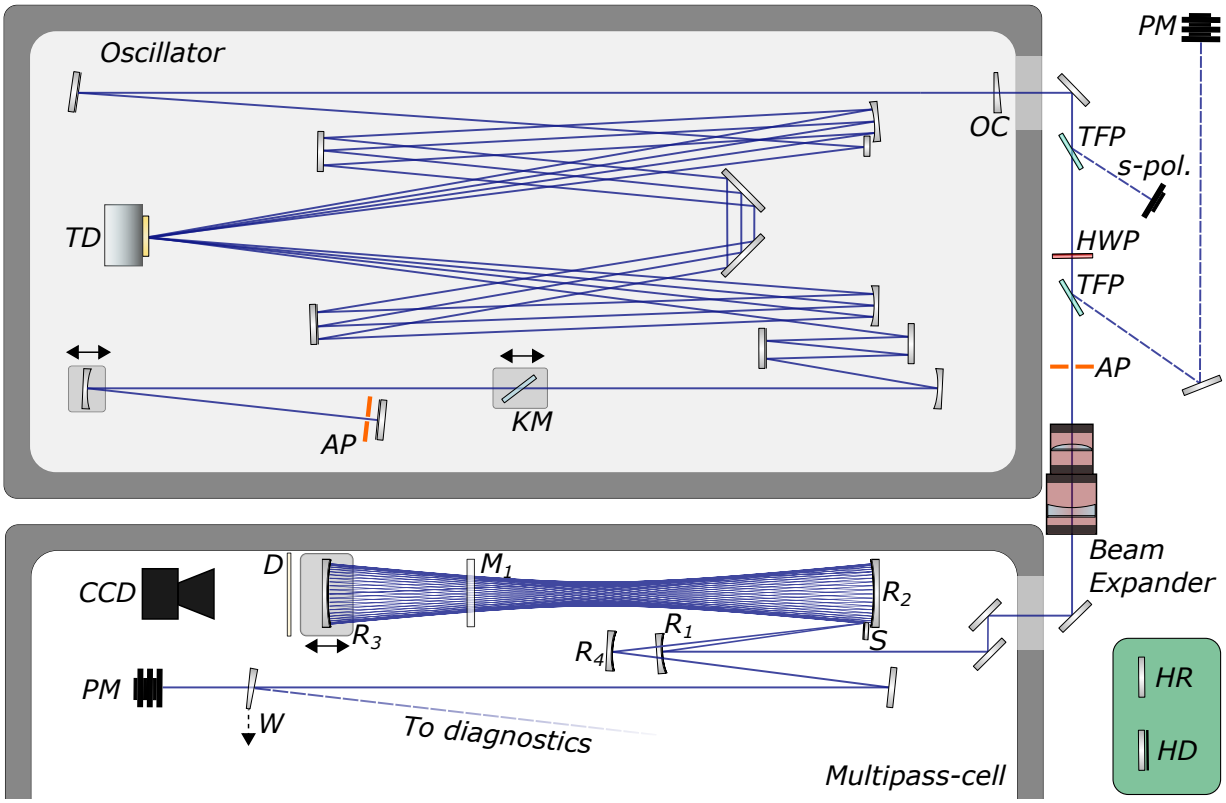

Fig. 2.6: Schematic of the self-compression setup. The hard-aperture Kerr-lens mode-locked Yb:YAG oscillator contains the thin-disk module *(TD)*, output coupler *(OC)*, a copper aperture *(AP)* and the Kerr-medium *(KM)* as well as several highly reflective *(HR)* mirrors for beam folding and imaging and highly dispersive *(HD)* mirrors to facilitate soliton mode-locking. The Kerr-medium as well as one of the curved oscillator mirrors are mounted on a translation stage to facilitate optimization of the oscillator performance. The oscillator is followed by a setup for polarization and mode-cleaning and a subsequent multipass-cell described in the text. The abbreviations are: *TFP*, thin-film polarizer; *HWP*, half-wave plate; *PM*, power meter; R_1, focusing mirror with a radius of curvature of 900 mm; *S*, scraper mirror; R_2, R_3, multipass-cell mirrors with outer diameter of 50 mm and a radius of curvature of 300 mm; M_1, 6.35 mm-thick fused silica plate; *D*, ground-glass diffuser screen; R_4, collimating mirror with a radius of curvature of 1000 mm; *W*, removeable broadband AR-coated fused-silica wedge.

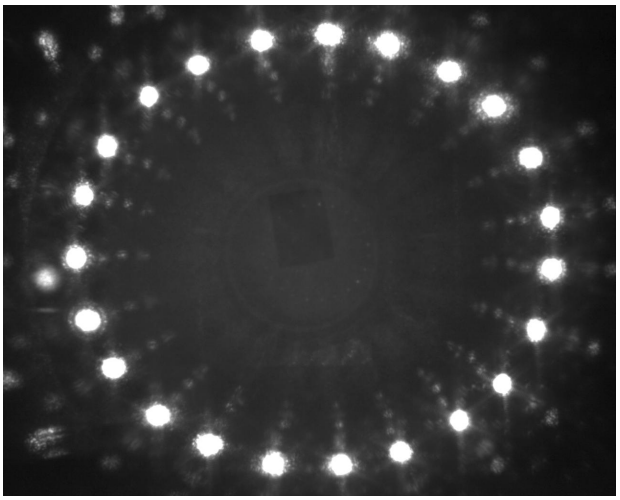

Fig. 2.7: Spot pattern on the ground-glass diffuser screen, recorded using a commercial silicon-based CCD camera. Decent quality of the mode-matching is indicated by the approximately identical size of the individual spots.

required broadband reflection bandwidth paired with the specific dispersion curve necessitated the mirror coating to be realized in the form of a complementary dispersive pair, where the GDD oscillations of two mirrors are offset against each other such that the overall oscillation amplitude is strongly reduced [37]. However, even when employing such a complementary design, the GDD curve of the mirrors shows significant residual oscillations in the wavelength range from 890 nm to 1070 nm (see Fig. 2.8).

The effect of these oscillations on the spectral phase of the pulse during propagation in the quasi-waveguide was assessed in simulations and is discussed in further detail in section 2.3.2. It should be noted that the measurement range for the long wavelength response of the coating was limited by the responsivity of the available silicon-based photodetector. However, by design, the mirrors are specified for a usable wavelength range spanning from 750 nm to 1350 nm which is broadband enough to cover pulses with a Fourier-transform limited pulse duration down to sub-10 fs. Thus, it can be ensured that the spectral broadening which is seen in the experiment is not inhibited by the mirror bandwidth.

Spectral broadening results

Sending an average power of 136 W into the multipass-cell, an output power of 119 W was measured on the thermal power sensor corresponding to a total optical efficiency of $\eta_{total} = 88\,\%$. The output spectrum was recorded using an optical spectrum analyzer (OSA) and is shown in Fig. 2.9 a). The spectral shape exhibits strong oscillations which is characteristic for SPM-based spectral broadening far from the strongly net-positive dispersion regime [35, p. 101 f.]. The measured spectral bandwidth extends from approximately 935 nm to 1085 nm at −30 dB level and supports a Fourier-transform limited pulse dura-

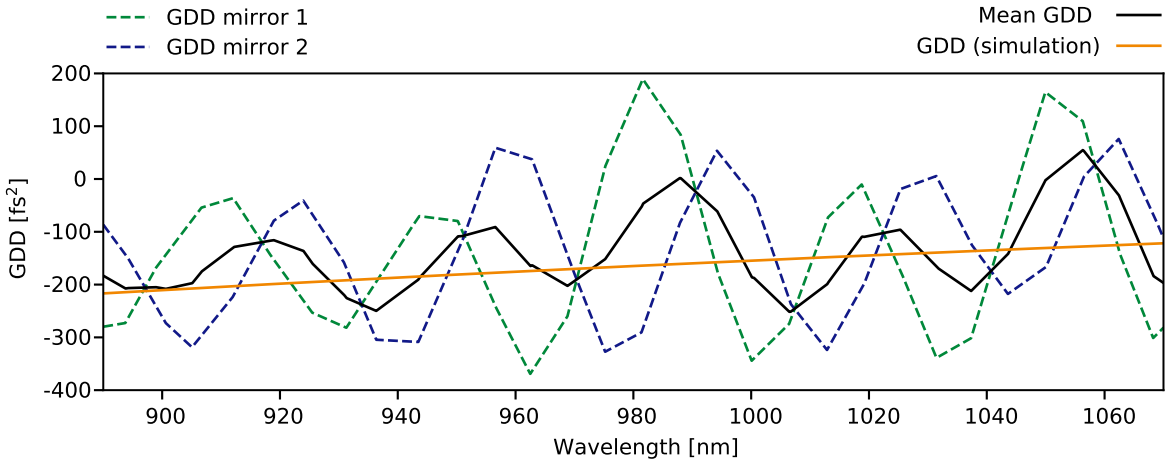

Fig. 2.8: Group delay dispersion (GDD) measurements of the utilized multipass cell mirrors. The measurements were performed on a reference pair of flat 1-inch mirrors. The dashed green and blue lines display the GDD of the two individual sample mirrors. The solid black line displays the arithmetic mean GDD of the two measured complementary curves with a resulting GDD of $-150\,\mathrm{fs}^2$ at 1030 nm wavelength. The yellow line shows the GDD curve for which best agreement between simulation and experiment was found.

tion of 28 fs (see Fig. 2.9 b)). The temporal shape of the output pulses was characterized in further detail using a SHG-FROG. The measured trace was reconstructed by the retrieval algorithm (Fig. 2.9 c and d) with a residual error < 0.0074 on a 512×512 grid. Furthermore, the retrieved fundamental spectrum reproduces well the one measured by the OSA is reproduced well, indicating a high quality of the retrieval (cf. Fig. 2.9 a). The output pulses are found to be self-compressed to a FWHM-pulse duration of 31 fs, corresponding to a temporal compression factor of just below ten. Importantly, these pulse durations can be achieved directly from the multipass-cell and without the use of additional dispersive optics.

Although the FWHM-pulse duration is close to the calculated Fourier-transform limit of the spectrum, it is easily seen in Fig. 2.9 that the short pulse is accompanied by a wide temporal pedestal. By comparing the area under the main peak (evaluated between the adjacent local minima) to the total area under the curve, the main pulse feature was found to carry about 42 % of the total pulse energy. The resulting output peak power of 140 MW is only slightly more than a factor of three higher than the peak power of the driving oscillator. The corresponding poor compression efficiency of the self-compressed pulses of only 47 % (c.f. equation 2.27) can be attributed to a pronounced kink in the spectral phase at the central wavelength of 1030 nm. The origin and implications of this characteristically shaped spectral phase will be discussed in further detail in the following sections.

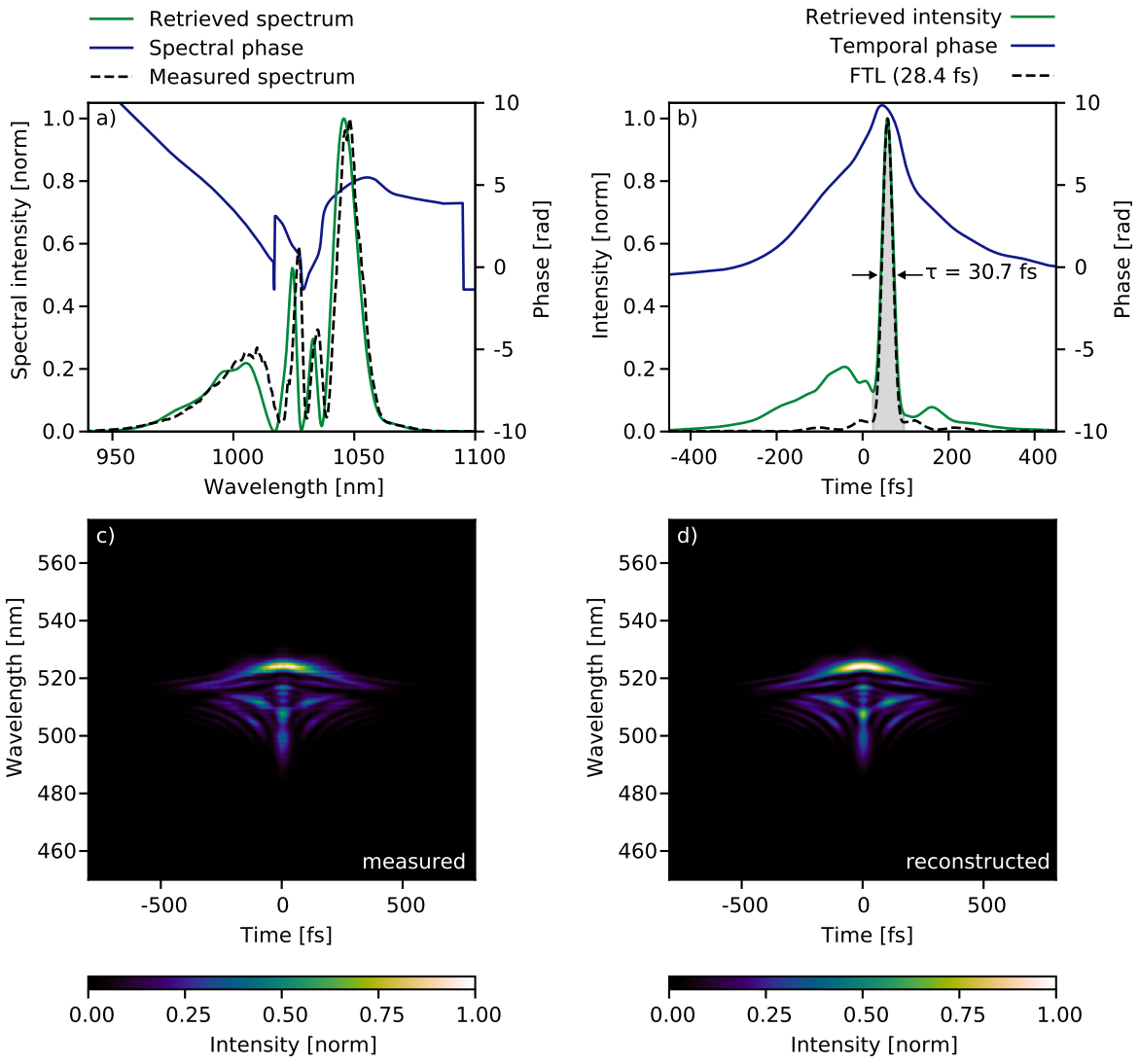

Fig. 2.9: Temporal characterization of the self-compressed multipass-cell output at 119 W output power. **a)** Spectral phase and intensity, compared to reference measurement with an OSA. **b)** temporal phase and intensity compared with the Fourier-transform limit (FTL) of the spectrum. The area under the main peak is shaded in light grey. **c)** measured SHG-FROG trace, and **d)** reconstructed FROG trace with < 0.0074 error on a 512×512 grid. For the temporal characterization measurement a small fraction of the full power beam was extracted using a broadband AR-coated wedge.

2.3.2 Pulse shaping mechanism - theory and simulation

Until today, the effects of soliton self-compression have predominantly been studied in optical fibers. The quasi-waveguide structure of Herriott-cells can be used to emulate many characteristics of the fiber geometry such as a fixed beam-diameter throughout the spectral broadening process or the spatio-temporal homogenization effects resulting from the constant refocusing in a waveguide. However, in the case of multipass-cell based self-compression as it is realized in this thesis, the negative dispersion is not distributed uniformly over the entire propagation distance in the nonlinear medium. Instead, it is provided in discrete steps corresponding to the reflections from the multipass-cell mirrors while the spectral broadening takes place inside the nonlinear medium in between in which the dispersion in positive. It is therefore instructive to first take a closer look at the modified propagation dynamics in the presented all-bulk case.

Soliton order - an inital assessment

Analogous to optical fibers, the propagation dynamics of a short pulse inside a multipass-cell can be characterized by a unitless number $\mathcal{N}$ which is termed soliton order [94]. Self-compression can be observed in the net-negative dispersion regime for soliton orders

$$\mathcal{N} = \sqrt{\frac{L_d}{L_{SPM}}} > 1 \tag{2.32}$$

where L_d is the dispersion length and L_{SPM} is the characteristic length for self-phase modulation [35, p. 64]. Neglecting higher-order dispersion terms, the dispersion length of a fiber is given by

$$L_d = \left| \frac{T_0^2}{\beta_2} \right| \tag{2.33}$$

where T_0 is the FWHM input pulse duration and β_2 is the total GVD of the fiber. To account for the discrete nature of the mirror dispersion in multipass-cell based all-bulk spectral broadening, one can define an effective GVD coefficient β_2^{eff} as

$$\beta_2^{eff} = \beta_2^{mat} + \frac{\overline{GDD_M}}{l_{mat}} \tag{2.34}$$

where β_2^{mat} is the GVD of the nonlinear material, $\overline{GDD_M}$ is the arithmetic mean of the group delay dispersion value of the multipass-cell mirrors evaluated at the center wavelength and l_{mat} is the thickness of the nonlinear medium. Here it is assumed that the contribution from air in the space between the mirrors and the nonlinear medium is negligible. It should be noted that the above approximation is only valid for small differences between the GDD curves of the two utilized multipass cell mirrors and if both of the addends in equation 2.34 are indivudally significantly smaller than T_0^2. Only then can it be ensured that a dispersion induced change of the propagating pulse shape is distributed

over many roundtrips through the multipass-cell. The influence of SPM on the propagating pulse can be described by the characteristic length

$$L_{SPM} = \mathrm{c}\frac{A_{eff}}{w_0 n_2 P_{peak}} \tag{2.35}$$

where c is the speed of light, A_{eff} is the effective beam area, w_0 is the optical angular frequency, n_2 is the nonlinear refractive index of the bulk medium and P_{peak} is the peak power of the input pulse.

For the Herriott-cell presented in section 2.3.1 the nonlinear material is fused silica with $l_{mat} = 6.35\,\mathrm{mm}$ and $\beta_2^{mat} = 18.97\,\mathrm{fs}^2/\mathrm{mm}$. The arithmetic mean of the group delay dispersion of the complementary dispersive mirror pair is $\overline{GDD_M} = -150\,\mathrm{fs}^2$, yielding an effective group velocity dispersion coefficient $\beta_2^{eff} = -4.65\,\mathrm{fs}^2/\mathrm{mm}$. The pulse duration from the oscillator is $T_0 = 300\,\mathrm{fs}$. Therefore, the dispersion length calculated according to equation 2.33 takes a value of $L_d = 19.35\,\mathrm{m}$.

To determine the characteristic length for self-phase modulation, the effective beam radius needs to be determined from equation 2.31 using $w(z)$ as the radius of a Gaussian beam corresponding to the eigenmode of the multipass-cell and $z_m = 86\,\mathrm{mm}$ as the distance of the nonlinear medium to the center plane of the multipass-cell yielding $w_{eff} = 242\,\mu\mathrm{m}$. Using $A_{eff} = \pi w_{eff}^2$ and the nonlinear refractive index of fused silica $n_2 = 2.46 \times 10^{-20}\,\mathrm{m}^2/\mathrm{W}$ at a central wavelength of 1030 nm (from reference [97]) and an incident peak power of $P_{peak} = 38\,\mathrm{MW}$, the resulting characteristic length for SPM is $L_{SPM} = 32.90 \times 10^{-3}\,\mathrm{m}$.

It is easily seen that for the experimental parameters described above, the characteristic length for self-phase modulation is significantly shorter than the dispersion length. Consequently, the evolution of a pulse injected into the multipass-cell is dominated by SPM-induced spectral broadening within the first few roundtrips. However, in the later part of the propagation through the multipass-cell, the influence of the net-negative GVD grows and leads to a temporal compression of the pulse due to chirp removal. Substituting the values of L_D and L_{SPM} into equation 2.32 we find that for the experimental parameters given above, the soliton order is $\mathcal{N} = 28.41$. Therefore, self-compression can be identified as the prevalent effect for the observed pulse shorting in the multipass-cell. In fibers, the achievable compression ratio and the corresponding optimal compression distance have been shown to scale linearly with $\mathcal{N}$ and $1/\mathcal{N}$, respectively [98]. The high compression ratio of almost a factor of ten together with the observed re-distribution of the energy content into both a short peak and a significant residual pedestal is in good qualitative agreement with the large soliton order $\mathcal{N} >> 1$.

1D-simulation parameters

While knowledge of the soliton order and the relevant characteristic lengths can provide a first idea of the propagation dynamics in multipass-cells operated in the anomalous dispersion regime, the above treatment is based on several simplifications. Specifically, it does not take into account higher-order dispersion terms which are commonly understood to be responsible for the energy transfer into satellite pulses, ultimately causing a fragmentation

of the main pulse structure [35, p. 120 ff.]. In addition, nonlinear effects other than SPM (such as self-steepening or the instantaneous and delayed Raman-response) can play a significant role in the propagation of femtosecond pulses but are not considered which further reduces the accuracy of the preceding evaluation.

As a consequence, for obtaining a more detailed and accurate understanding of the temporal pulse evolution in the quasi-waveguide, its propagation was simulated using the methods described in section 2.2.2. The simulations were run with 2^{14} points on a one-dimensional grid spanning 16 ps in time resulting in a frequency resolution of 0.062 THz. The Herriott-cell is represented by 46 consecutive passes, each of which is modelled by numerically propagating the pulse through a 6.35 mm long block of fused silica material and subsequently applying the averaged dispersion curve of the respective multipass-cell mirror pair (yellow curve in Fig. 2.8). By doing so, the discrete nature of the quasi-waveguide is explicitly being accounted for. Furthermore, the simulation thus closely matches the experimental conditions, where the nonlinear interaction takes place in a net-positive dispersion environment.

For the simulations, a sech^2 temporal input pulse shape with a FWHM pulse duration of 300 fs at a central wavelength of 1030 nm is used in accordance with the measured output of the driver oscillator. The input pulse energy is fixed to 12.8 µJ. The nonlinear interaction inside the fused silica window is modelled using the values for n_2 and A_{eff} as given in the previous section. To adequately represent higher-order contributions, the dispersion profile inside the nonlinear material is based on the wavelength dependant refractive index of fused silica which is calculated using the Sellmeier equation with the coefficients given in reference [99]. Furthermore,the effects of self-steepening and the time-delayed Raman-response are included according to reference [92] with the Raman coefficient set to $f_R = 0.18$.

For a qualitative assessment of the pulse evolution inside the multipass-cell, the exact, complementary nature of the mirror coating design was first neglected in the simulations. Instead, a simplified model was chosen in which both mirrors exhibit the same, smoothed dispersion profile corresponding to the yellow curve in Fig. 2.8. This approach allows a clear separation of the influence of the anomalous dispersion environment from additional dispersive effects caused by the oscillatory behaviour of the measured dispersion profile, which will be discussed in a later paragraph. The values for the dispersion parameters for which the best agreement between simulation and experiment was found had to be determined experimentally using a dispersion parameter sweep due to a residual uncertainty in the dispersion measurement of the utilized mirrors. Further detail on the dispersion measurement of the multipass-cell mirrors can be found in the subsequent subsection. The properties of the dispersive cell mirror coating were approximated with a GDD of $-140\,\text{fs}^2$ and a third-order dispersion of $-800\,\text{fs}^3$ at 1030 nm wavelength.

Using the above parameters, the measured temporal and spectral shapes are reproduced well by the simulation (Fig 2.10 a and b). The obtained pulse duration and bandwidth are in good agreement with the experimental results. However, the power loss into the pedestal is slightly overestimated by the simulation which is likely a result of residual higher-order dispersion terms which are not considered appropriately by the approximated dispersion

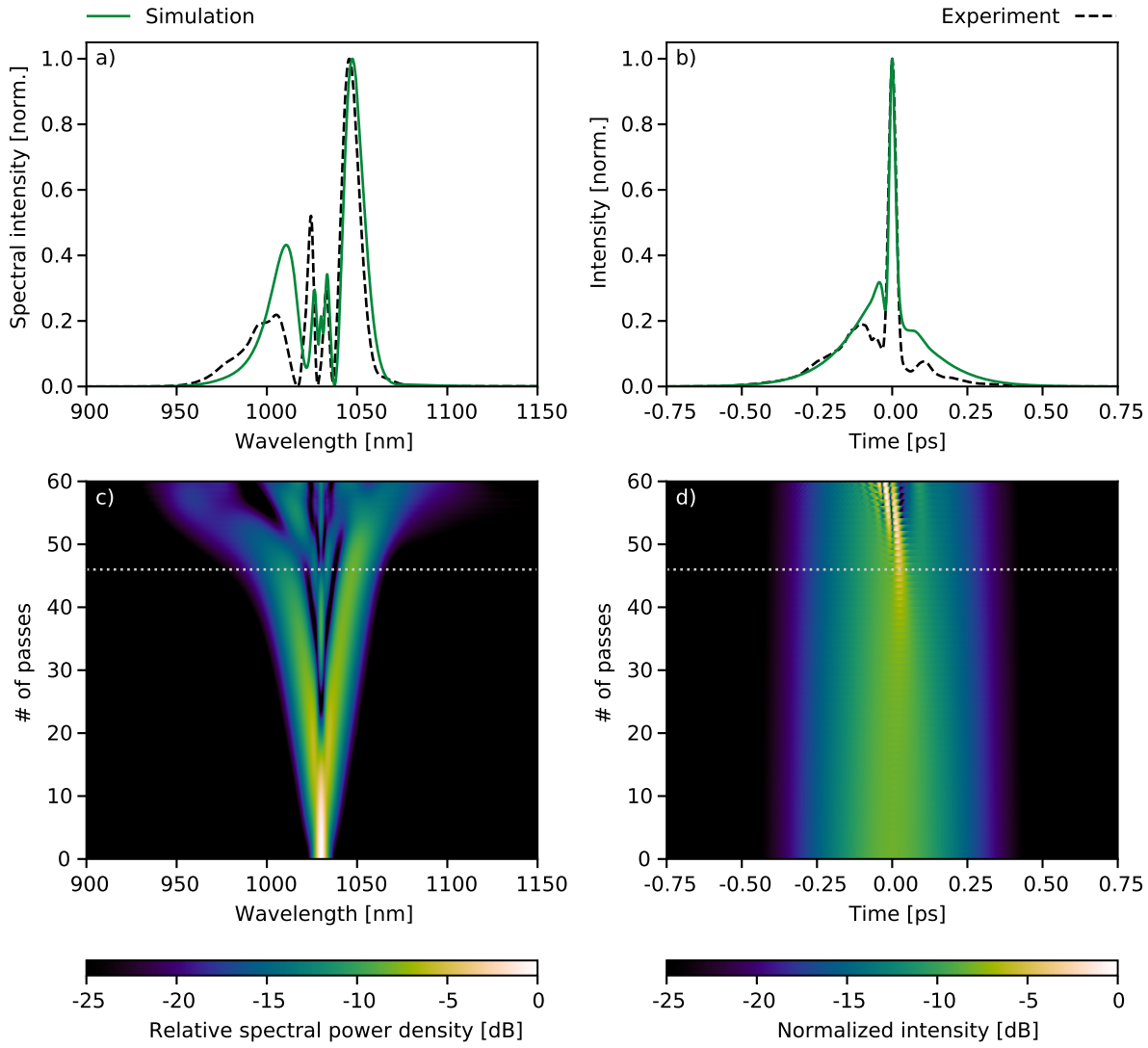

Fig. 2.10: Simulation of the self-compression inside the multipass-cell using an adaptive step-size implementation of the fourth-order Runge-Kutta method in the interaction picture to solve the nonlinear Schrödinger equation (see section 2.2.2 for details). **a)** Spectrum and **b)** time domain representation of the multipass-cell output when operated at 136 W input average power. **c)** Spectrum and **d)** time domain evolution vs. number of passes through the fused silica medium inside the multipass-cell. The dotted white line indicates the number of passes used in this experiment.

curve utilized in the simulations. The spectral and temporal evolution of the pulse in the multipass-cell against the number of propagated passes are shown in Fig 2.10 c and d, respectively. As predicted by the results of the previous section, the propagation dynamics of a pulse inside the multipass-cell can be divided into multiple segments where different characteristic behaviours can be observed.

Analysis of the temporal and spectral evolution

Fig. 2.11 shows the simulated spectral and temporal pulse shapes (green lines) together with the respective spectral phase and bandwidth-limited pulse duration (dashed lines) at the input (a), after 20 passes (b), after 38 passes (c), at the output corresponding to 46 passes (d) and after a hypothetical propagation of 52 passes (e) and 54 passes (f) through the multipass-cell. Furthermore, the temporal compression that can be achieved by only compensating the residual GDD is shown in blue for propagation of 20, 38 and 46 passes.

At the input (Fig. 2.11 a), the pulse is approximated with a bandwidth-limited sech^2 temporal shape with 300 fs pulse duration corresponding to an equally shaped spectrum owing to the characteristics of the underlying Fourier-transformation. This approximation is in good agreement with the measured temporal and spectral profile of the pulses at the output of the soliton mode-locked Yb:YAG thin-disk oscillator.

After 20 passes (Fig. 2.11 b), the spectrum has been broadened visibly and the FTL has reduced by more than a factor of three while the pulse duration has only decreased by approximately 10 % . It is up to this point that the nonlinear effects inside the multipass-cell dominate over the dispersive effects, giving rise to significant spectral broadening but leaving the pulse shape mostly unaltered. This is further supported by the spectral phase which is characterized by a quadratic contribution that corresponds to a linear up-chirp which is typical for SPM-induced spectral broadening (cf. section 1.1.3). The accumulated third order dispersion from the multipass-cell mirrors becomes already visible at this point, causing an asymmetry of the accumulated spectral phase and associated spectral broadening. A small phase kink at around a wavelength of 1030 nm is further already visible after 20 passes. While the pulse can still be compressed close to the FTL, this small kink in the spectral phase causes the formation of a pedestal in the time domain that starts lowering the achievable peak power.

For propagation beyond 20 passes, the influence of the anomalous mirror dispersion on the pulse shape significantly gains in relevance. After 38 passes (Fig. 2.11 c) the bandwidth of the spectrum is further increased while the pulse shape is now likewise affected visibly. Specifically, both the FTL of the spectrum and the pulse duration are reduced by a factor of two when compared to the result after 20 passes, indicating that nonlinear and dispersive effects now contribute equally to the propagation dynamics. The phase kink at 1030 nm is clearly more distinct, giving a first hint of the formation of a short pulse feature that separates from the main pulse structure in the time domain. Nonetheless, the compressibility still remains on a high level albeit at the expense of even more power being transferred into the pedestal.

When propagating the pulse even further, the continuing reduction in pulse duration

causes an acceleration of the spectral broadening. After 46 passes, the simulated duration of the short pulse feature reaches 10 % of the input pulse duration and matches the calculated FTL of the spectrum (Fig. 2.11 d). Owing to the imperfect removal of the nonlinear phase by the multipass-cell mirrors, an additional, much sharper phase kink is superimposed on the spectral phase at around 1030 nm. The generation of this second kink can be related to the difference in slope steepness of the short pulse feature compared to the underlying long pedestal [35, p. 104 f.]. It is noteworthy, that while the pulse duration is already self-compressed to the FTL, the energy content in the short pulse structure can still be optimized slightly by reducing the residual GDD.

Due to the geometry of the scraper mirror and the outer diameter of the multipass-cell mirrors, the achievable number of passes is limited to 46 in the self-compression experiment. However, the simulation can allow a first prediction of the pulse shape for multipass-cells in which more passes can be realized. The spectrum and temporal shape of a pulse that has a propagated 52 passes through a multipass-cell is shown in (Fig. 2.11 e). When compared to the results after 46 passes, it is evident that the spectrum continues to broaden rapidly especially towards the shorter wavelengths. This asymmetry of the spectral broadening is likely caused by an interplay between third-order dispersion and the increasing influence of self-steepening that modifies the steepness of the rising slope of the pulse. The duration of the short pulse feature stays close to the FTL of the spectrum. However, while the pedestal is certainly still very noticeable, it appears to contain slightly less energy than after 46 passes. Furthermore, the beginning fragmentation of the pulse structure can be observed which manifests itself in the appearance of a short satellite pulse. If the pulse is propagated even further, it ultimately splits up into multiple features which is depicted exemplary for 54 passes in 2.11 e).

The analysis of the spectral and temporal evolution given above shows that for the large soliton order $\mathcal{N} > 25$, precise tuning of the nonlinear interaction length represented by the number of passes through the nonlinear medium is required. If the interaction length is chosen too short, the propagation dynamics are dominated by SPM and the achievable bandwidth is comparable to operation in the net-positive dispersion regime, albeit, with a reduction of the achievable compression quality. For the Herriott-cell parameters given in section 2.3.1, the optimal propagation distance for self-compression which corresponds to the shortest possible duration of a single pulse feature is reached after 52 passes. Excessive propagation through the broadening medium ultimately results in a fragmentation of the main pulse structure into multiple pulses which renders the pulse unusable for most applications. In the experimental realization, the number of passes was geometrically limited to 46. Consequently, the self-compression was not exploited fully, leaving room for further optimization. This could be achieved by fine-tuning either the multipass-cell geometry to allow the realization of a larger amount of passes or by adjusting the dispersion or nonlinearity inside the Herriott-cell e.g. by varying the mirror coating or plate thickness such that the optimal propagation distance for self-compression is sufficiently reduced.

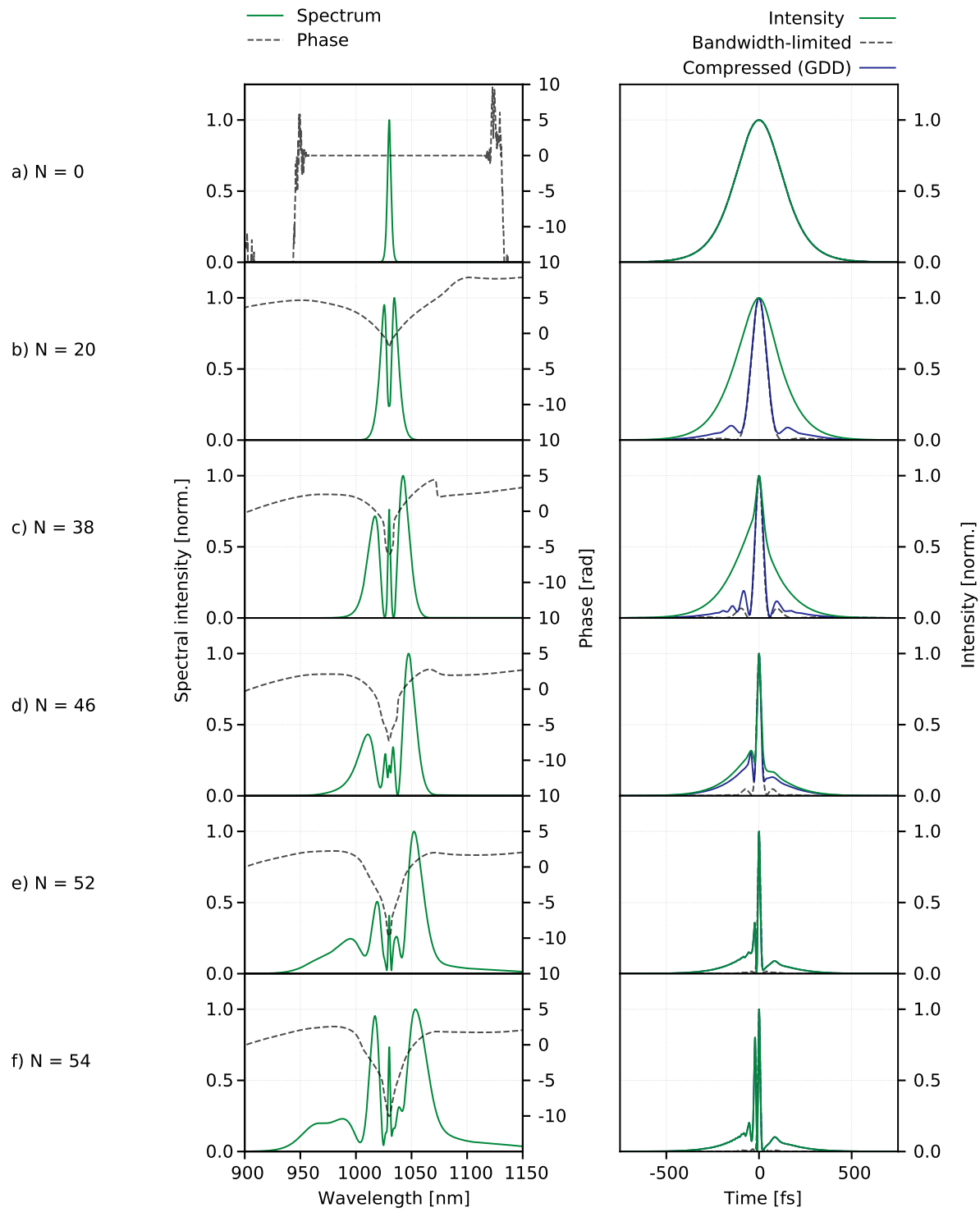

Fig. 2.11: Simulation of the spectral (left panel) and temporal (right panel) evolution inside the multipass-cell. **a)** Transform limited sech^2 pulse with 300 fs pulse duration which was used as input pulse. The calculated spectrum and pulse shape is shown after **b)** 20 passes, **c)** 38 passes, **d)** 46 passes, **e)** 52 passes, and **f)** 54 passes through the nonlinear medium. For subfigures b) – d), the best temporal compression that can be achieved by only compensating the residual GDD is shown in blue in the right panel.

Influence of residual dispersion ripple

Although the above simulations reproduce the experimentally observed pulse evolution inside the multipass-cell well, they are still based on the simplification of a smoothed dispersion profile being identical for both of the dispersive mirrors (yellow curve in Fig. 2.8). To evaluate the influence of the complementary oscillations in the dispersion profile of the individual mirrors, the simulation from the previous section is repeated with the exact same parameters. However, this time, the reflection from the first multipass-cell mirror is assigned the green dispersion curve while the second mirror reflection is assigned the blue dispersion curve shown in Fig. 2.8, respectively. It should be noted that the measured dispersion profiles in Fig. 2.8 were taken of flat reference substrates from the same coating runs in which the actual multipass-cell mirrors were fabricated.

While the self-compression effect observed in the experiment can be qualitatively reproduced numerically when applying the measured dispersion profiles of the multipass-cell mirrors, the quality of the simulation is reduced significantly (c.f. blue lines in Fig. 2.12). This behaviour indicates, that the dispersion profile of the multipass-cell mirror samples which were used in the experiment does not exactly follow the curves of the reference mirrors measurement. It should be noted that it can be commonly observed that individual mirrors from the same coating run can be shifted in wavelength with respect to each other depending on their substrate thickness, radius of curvature and even position in the coating chamber.

The reduced agreement between the experiment and the simulation can be somewhat alleviated by numerically shifting the GDD profile of the first mirror (green curve in Fig. 2.8) towards shorter wavelengths and the GDD profile of the second mirror (blue curve in Fig. 2.8) towards longer wavelengths by 2 nm each, which causes a slight alteration to the arithmetic mean GDD. This approach provides an improved agreement between simulation and experiment and seems especially well suited for a more accurate reproduction of the shorter wavelengths of the output spectrum (Fig. 2.12). The numerical shifting of the dispersions curves by ± 2 nm, which is required for obtaining an improved qualitative agreement of simulation and experiment, is likely justified by the intrinsic sample variation of different substrates from the same coating run.

While the simulations appear to react very sensitively to the average GDD- and TOD-values, the residual oscillations around the mean value of the dispersion curves of the individual mirrors do not significantly impair the quality of the simulation. A potential explanation for this behaviour is the small value of the accumulated phase between the passes of the two different complementary dispersive mirrors in the presented multipass-cell approach.

Since for multipass-cell based self-compression even small shifts of the individual dispersion profiles appears to significantly affect the arithmetic mean GDD and thus the output pulse shape, it would be highly desirable to directly measure the exact dispersion profile of the utilized mirror pair to further improve the quality of the simulation. Unfortunately, such measurements can currently not be performed in-house since the utilized measurement device does not permit direct testing of the multipass-cell mirrors due to their radius

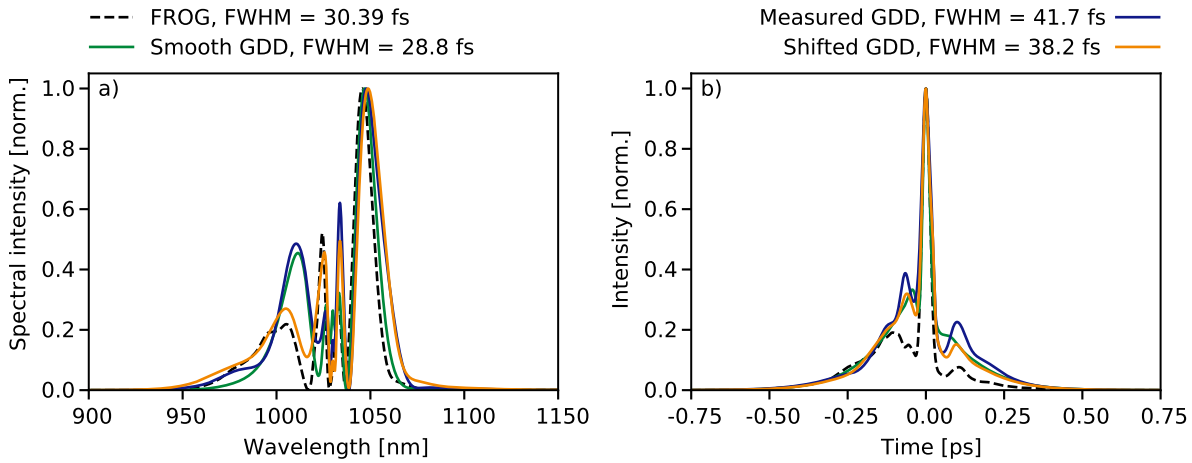

Fig. 2.12: Simulation results for the flattened vs. real GDD curve of the utilized multipass-cell mirror. **a)** Spectrum and **b)** time domain representation of the multipass-cell output when operated at 136 W input average power. For the simulation result displayed in yellow, the GDD profile of the first mirror (green curve in Fig. 2.8) was numerically shifted towards shorter wavelengths and the GDD profile of the second mirror (blue curve in Fig. 2.8) was numerically shifted towards longer wavelengths by 2 nm, respectively.

of curvature and substrate diameter. Consequently, it is highly recommended to evaluate the accuracy of the available dispersion curves for each individual multipass-cell mirror in benchmark simulations and experiments.

2.3.3 Evaluation of practical usability for applications

In addition to the temporal compression factor and achievable pulse quality, several other characterizing laser parameters exist which can play an important role in deciding whether a pulse compression scheme is suitable for being used in a specific experiment. For the purpose of using the output pulses for nonlinear frequency conversion and, ultimately, for time domain spectroscopy applications, the spatial beam quality of the output beam as well as the overall stability of the laser system are of particular interest.

Spatial beam quality

In most nonlinear frequency conversion schemes, the incident NIR laser beam is focused down tightly to increase the peak intensity of the driving laser pulse in order to enhance the conversion efficiencies. As a consequence, a high beam quality can often benefit the efficiency of the conversion process. For broadband intra-pulse frequency conversion it is furthermore important, that all frequency components of the NIR laser beam can be focused down to the same spatial position, resulting in high requirements on the spectral

homogeneity of the driver laser.

As mentioned in section 2.2.2, when employing fiber based spectral broadening in the generation of the desired, short input pulses, the mode-cleaning mechanism of the waveguide naturally yields both a high spatial quality and homogeneity of the output beam. While the quasi-waveguide structure of multipass-cell spectral broadening arrangements can be used to emulate the continuous refocusing inside a fiber, the effectiveness of the resulting homogenization has been found to critically depend on the nonlinear phase shift per pass through the nonlinear medium. Consequently, it is instructive to first take a closer look at the maximum per-pass nonlinear phase shifts occurring during multipass-cell based spectral broadening in different dispersion regimes.

When a multipass-cell is operated in the net-positive dispersion regime, the injected pulse is subject to linear losses and temporal broadening due to accumulated second-order dispersion. Both of these effects evoke a steady decrease of the pulse peak power during propagation. As a result, the maximum per-pass nonlinear phase shift is determined by the nonlinear phase shift in the first pass through the broadening medium which can easily be adjusted below the critical value of $\pi/10$ by modifying suitable input parameters or the geometrical configuration of the multipass-cell. An exemplary evolution of the per-pass nonlinear phase for a multipass-cell operated in the zero- ($\beta_2^{eff} \approx 0\,\mathrm{fs}^2/\mathrm{mm}$) and in the slightly net-positive regime ($\beta_2^{eff} = 5\,\mathrm{fs}^2/\mathrm{mm}$) is given in Fig. 2.13.

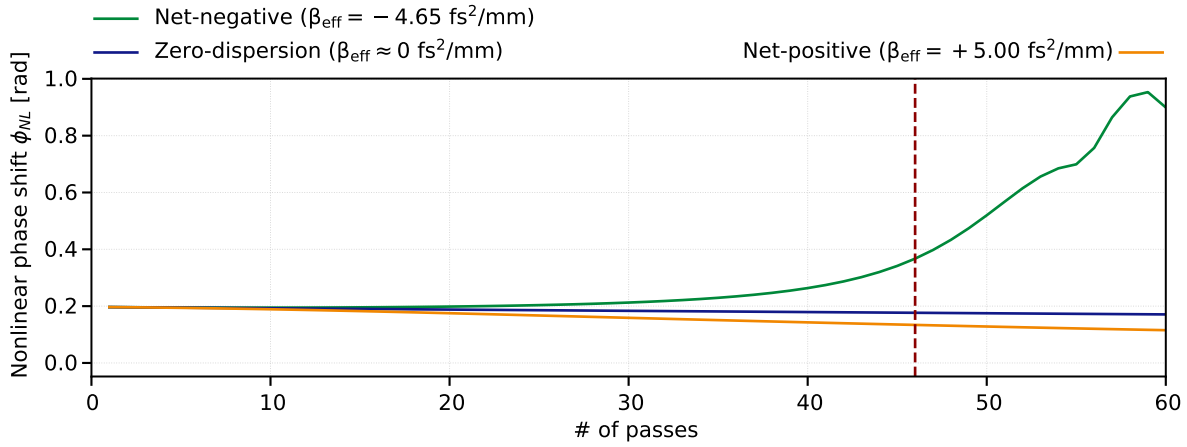

Fig. 2.13: Simulated per-pass nonlinear phase shift vs. the number of passes the pulse has propagated through the multipass-cell. The different values of the effective GVD were realized, in the simulation, by varying the arithmetic mean GDD of the multipass-cell mirrors (cf. equation 2.34) while leaving all other parameters of the simulation unaltered. The dashed red line marks the number of passes used in the self-compression experiment.

The situation is quite different when the multipass-cell is operated in the net-negative dispersion regime. As it has been shown in the previous section, the pulse duration decreases continuously during the propagation through the multipass-cell in the negative

dispersion regime. As a result per-pass nonlinear phase shift steadily grows, with the growth rate being determined by the interplay between pulse shortening and the increasing amount of energy transferred from the main pulse into the pedestal (Fig 2.13). In the net-negative dispersion experiment, adjusting the nonlinear phase shift in the first pass through the nonlinear medium to a value of 0.2 rad results in a clean Gaussian profile after propagation through the multipass-cell. No significant differences of the beam profile quality are observed between operation at low- and high power levels (5 W and 119 W, respectively, Fig. 2.14 a and b). When focused down, the Gaussian shape of the beam is maintained with no ring structure appearing (Fig. 2.14 c).

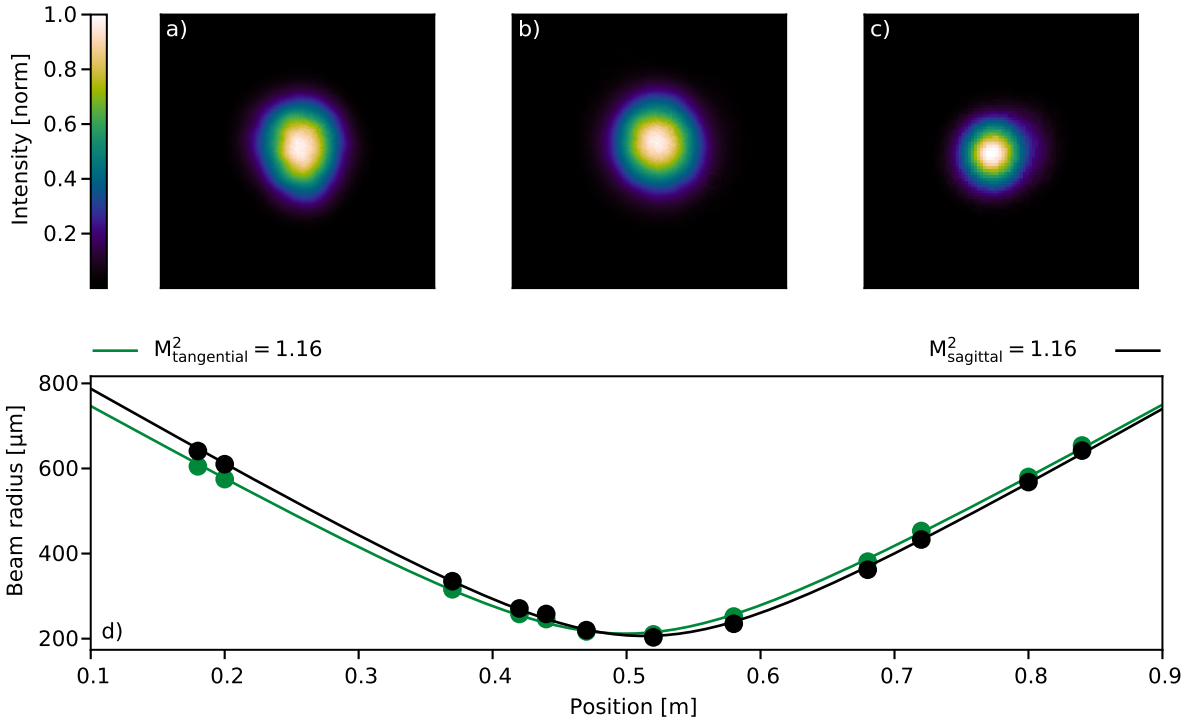

Fig. 2.14: Beam quality measurement of the multipass-cell output operated in the self-compression regime (using Cinogy CinCam CMOS-1203 beam profiler beam profiler). Beam profile of collimated beam at **a)** 5 W average output power and **b)** 119 W average output power. **c)** Beam profile of a focus created by lens with $f = 200$ mm focal length at full power. The $1/e^2$ beam diameter in the focus is 150 µm. **d)** M^2-measurement according to ISO norm [31].

Fig. 2.13 shows, that within the accuracy of the simulation, only the last 4 passes exhibit a per-pass nonlinear phase shift exceeding 0.3 rad, where a maximum per-pass phase shift of 0.37 rad is reached in the final pass through the fused silica medium. Since the major proportion of the accumulated nonlinear phase is homogeneously distributed over many passes, the slightly increased phase shift within the last few passes through the nonlinear medium appears to be insufficient to cause significant nonlinear spatio-temporal

coupling. This conclusion is further supported by measurements of the M^2 parameter, where a low homogeneity of the output beam coincides with a varying q-parameter across the spectrum leading to an overall reduction of the beam quality and increase of the M^2 parameter [100]. The measured M^2 factor is 1.16 in both the sagittal and tangential plane (Fig. 2.14 d) confirming the high spatial quality of the self-compressed multipass-cell output. The minor increase compared to the M^2 factor of the Yb:YAG driver oscillator ($M^2 = 1.08$) furthermore indicates a very reasonable homogeneity of the output beam.

Output stability

In addition to the high spatial beam quality, a good stability of the laser output is required in many use cases. Especially for medical spectroscopic applications, the stable long-term operation of the driver laser is of key relevance to enable the measurement of many samples with virtually identical laser parameters. To characterize the performance of the developed laser source presented here, the long-term average power stability and beam pointing fluctuations were measured over the duration of one hour. While fluctuations of the average power directly affect the intensity noise and should therefore be minimized for a low laser induced variance of the measurement results, beam pointing fluctuations can additionally be coupled to intensity fluctuations by optical elements with small apertures in the laser system and can therefore significantly contribute to the total laser system noise.

The long-term average power stability of the setup was measured using a thermal power sensor with a resolution of 1 Hz (Fig. 2.15). The resulting normalized root-mean-square (RMS) deviation of 0.2 % at a mean optical power of 119 W is similar to the average power stability of the driving oscillator.

To evaluate the influence of the long additional beam path inside the multipass-cell (≈ 24.5 m) on the laser beam pointing stability, the positional- and angular beam stability were measured using a CCD-camera in the collimated beam and in the focal plane of a lens with 200 mm focal length, respectively (Fig. 2.15). The resulting RMS value of the angular beam stability is below 6 µrad over one hour, which is on the same level as typically found in driver lasers (RMS < 5 µrad) and compares well to commercial laser systems [101]. Both the power- and beam pointing stability measurements were taken with the multipass-cell housing covered by a plexiglass lid to avoid excessive air turbulence, and after the setup had been allowed to thermalize for approximately 30 minutes.

The excellent preservation of the pointing stability found in the self-compression experiment can be explained by the imaging characteristics of re-entrant Herriott-cells. As explained in more detail in section 2.1, a laser beam injected into a re-entrant Herriott-cell will revert to exactly the same position on the scraper mirror after the propagation of a predetermined number of passes. The deterioration of angular and positional stability as compared to the input beam therefore depends mostly on the fluctuation of the multipass-cell length, which causes a deviation from the re-entrant condition. On the other hand, fluctuations of the multipass-cell mirror alignment are effectively filtered out. As a result, Herriott-type multipass-cell compression schemes commonly provide a good conservation of the beam pointing stability as long as the mirror separation distance is firmly fixed.

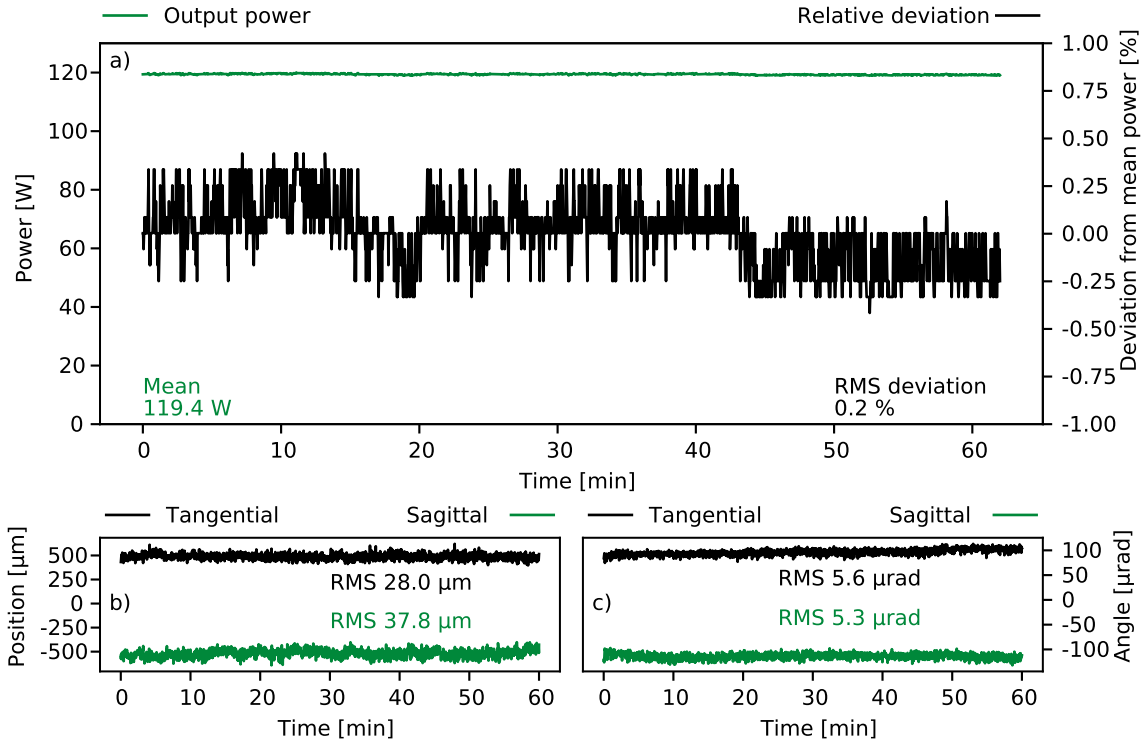

Fig. 2.15: Output stability of the multipass-cell output operated in the self-compression regime. **a)** Absolute and relative average-power stability measured over one hour with 1 Hz sampling frequency. **b)** Positional and **c)** angular beam stability over one hour measured using Cinogy CinCam CMOS-1203 beam profiler. The angular beam stability was measured in the focal plane of a $f = 200\,\mathrm{mm}$ lens. All measurements were taken after a thermalization period of approximately 30 minutes.

2.4 Chapter summary

In summary, the practical usability of an all-bulk multipass-cell spectral broadening scheme operated in the net-negative dispersion regime will likely depend on the targeted application. In the presented Herriott-cell self-compression experiment, an output peak power of 140 MW at 31 fs pulse duration could be achieved with over 42 % of the pulse energy in the main peak and a corresponding compression quality of 47 %. To the author's knowledge, the temporal compression by almost a factor of ten is unprecedented for a single-stage all-bulk pulse compression scheme using a single broadening medium. The corresponding increase in spectral bandwidth can provide a tremendous advantage for purely spectrally resolved applications such as wideband absorption spectroscopy in the NIR or, after suitable spectral filtering, as a tunable narrowband pump or seed in optical parametric amplifications. Furthermore, both the spatial beam quality and the output stability after spectral broadening are found to be on a very high level that should satisfy most experimental requirements. The high-overall throughput exceeding 85 %, together with the presented possibilities for dispersion tuning further facilitates the investigation of different nonlinear effects such as Raman soliton self-frequency shifting and supercontinuum generation.

Unfortunately, the usability of the output pulses is somewhat restricted by the suboptimal compression quality. This is especially true for the target application of intra-pulse difference frequency generation where high peak powers are required to achieve a substantial conversion efficiency. Due to the relatively small amount of energy contained in the main pulse, the peak power in the self-compression experiment is only increased by a factor of about three. This is in stark contrast to multipass-cell spectral broadening schemes operated in the positive dispersion regime, where the achievable peak power ideally scales almost linearly with the temporal compression factor. While the compression quality could potentially be improved by progressing to a lower soliton order, this would inevitably cause a significant reduction of the amount of spectral broadening — giving away the key advantage of the self-compression approach. Even higher temporal compression factors for reaching the few-cycle regime in a single broadening stage are further inhibited by the expected spatio-temporal coupling caused by excessive per-pass nonlinear phase shifts in the latter half of the propagation. Since a clean pulse compression in combination with a high compression factor appears to be unattainable from a single-stage self-compression scheme, a different ansatz was followed to obtain the desired high peak-powers for the frequency conversion experiments. The results of the self-compression experiment presented in this chapter were published in a peer-reviewed journal article [102].

3

Enhancing the peak power: The positive dispersion regime

3.1 Optimization of dispersion and nonlinearity

Since its initial demonstration by J. Schulte et al. in 2016 [77], nonlinear pulse compression using Herriott-type multipass-cells driven by Yb:based lasers has quickly been adapted by the ultrafast laser community. When tuned to operation in the net-positive dispersion regime, the all-bulk spectral broadening approach typically yields single-stage compression factors of 4-8, where both a high spatial beam quality and a good compression can be achieved [77, 78]. Higher spectral broadening factors of up to 22 have further been realized by cascading multiple broadening stages with intermediate re-compression [81, 82]. While the concept is reportedly capable of generating spectra supporting a FTL of below 15 fs, the experimentally achieved pulse durations have so far been limited to 18 fs and 22 fs. In both cases the compression quality is only sub-optimal, leading to significant satellite pulses and an undesirably low fraction of 45 % and 57 % of the total energy being contained in the main peak. Closer evaluation of the results published in references [81] and [82] reveals that in both systems, the net-dispersion of the multipass-cells was adjusted close to zero in order to maximize the amount of spectral broadening. In the first part of the following section, the potential improvement in compression quality and the corresponding spectral broadening factors of Herriott-type multipass-cells with a positive net-dispersion are hence investigated in further detail. The second part introduces a dual-stage nonlinear pulse compression setup which serves as the basis for the post-compression techniques and the subsequent experiments on frequency-conversion to the mid-IR which are presented in chapter 4 and chapter 5.

3.1.1 Dispersion-controlled spectral broadening parameters

To experimentally assess how the spectral broadening factor and the compression quality of the multipass-cell spectral-broadening scheme can be optimized for operation in the positive dispersion environment, the Herriott-cell that was introduced in the previous section was re-built with slightly differing parameters. A schematic depiction of the experimental setup is given in Fig. 3.1. While the inital radius of curvature of 300 mm of the multipass-cell mirrors was preserved, the new configuration features a Gouy-parameter of $\psi_E = 2\pi\cdot(16/17)$ corresponding to a mirror separation distance of $d \approx 580$ mm and a total number of 34 passes through the 6.35 mm thick fused silica plate that is used as a nonlinear medium. Adequate mode-matching is again achieved by using a variable zoom-beam expander in conjunction with a plano-concave focusing mirror. However, due to the reduced angular advance when compared to the configuration in the self-compression experiment, a single mirror with 1000 mm radius of curvature can be used for both focusing the beam into the Herriott-cell and collimating the vertically offset output beam. To achieve a reasonable collimation, the focusing mirror is positioned at approximately the distance corresponding to its focal length of 500 mm to the center plane of the Herriott-cell. The spectrally broadened output is then sent towards a water-cooled thermal power sensor using two plane turning mirrors. Alternatively, the beam can be coupled to a chirped-mirror compressor which will be described in further detail in a later paragraph. The surface reflection off of an uncoated fused silica wedge in the collimated beam close to the power sensor is used to provide a low power copy of the full output for beam diagnostics.

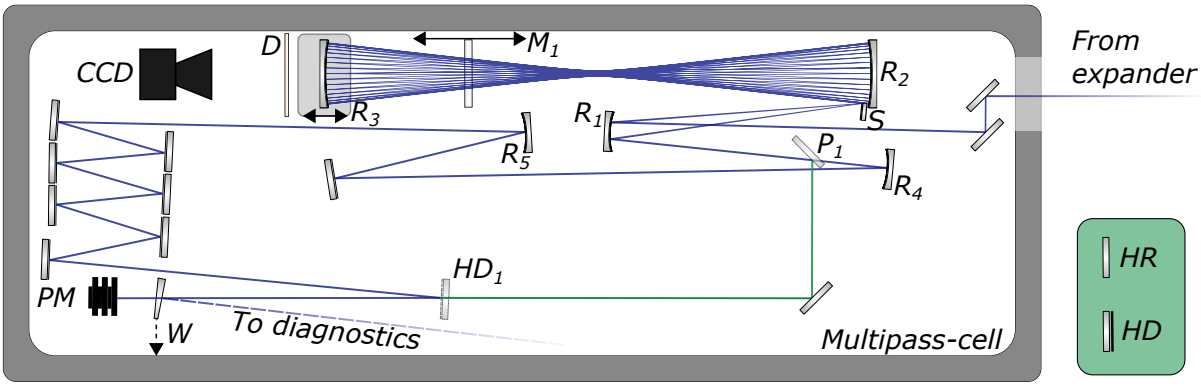

Fig. 3.1: Schematic of the experimental setup for spectral broadening in the positive-dispersion regime. R_1, concave mirror with a radius of curvature of 1000 mm; S, scraper mirror; R_2, R_3, multipass-cell mirrors with a radius of curvature of 300 mm; M_1, 6.35 mm-thick fused silica plate; D, ground-glass diffuser screen; P_1, plane folding mirror; R_4, R_5, concave mirrors with a radius of curvature of 1000 mm forming a folded 4-f-imaging arrangement; HD_1, dispersive mirror; W, removeable fused-silica wedge. The green line indicated the beam path used for power and OSA measurements. By removing the folding mirror P_1 and inserting the dispersive mirror HD_1 the beam can be guided to a chirped-mirror compressor before arriving at the power meter (PM).

To ensure that the spectral broadening takes place in a net-positive dispersion environment, the dispersive coating of the Herriott-cell mirrors was changed fundamentally. The new target curve (dashed black line in Fig. 3.2) is designed to exactly compensate the third-order chromatic dispersion of the 6.35 mm thick fused silica medium but undercompensates its second order dispersion by 10 fs^2 over the entire spectral range. In an effort to improve the mirror reflectivity and to reduce the residual dispersion oscillations, the coating bandwidth was limited to a wavelength range of 940 nm to 1100 nm. The supported pulse durations is on the order of around 50 fs for the strongly modulated spectra obtained from SPM-based spectral broadening. Furthermore, the narrower wavelength range decreases the total GD the mirror needs to compensate. Therefore, the coating can be realized without imposing the need for a complementary dispersive design. While the measured GDD of the multipass-cell mirrors still exhibits significant dispersion ripple (cf. green curve in Fig. 3.2), the reflectivity could be slightly improved resulting in a single pass transmission through the Herriott-cell of $T_S > 99.85\,\%$ and a total optical efficiency of $\eta_{total} = 94\,\%$. Unfortunately, however, the beginning degradation of the beam expander coatings and re-designed optical path with additional turning mirrors caused the available average input power to drop from the previous 136 W to 114 W.

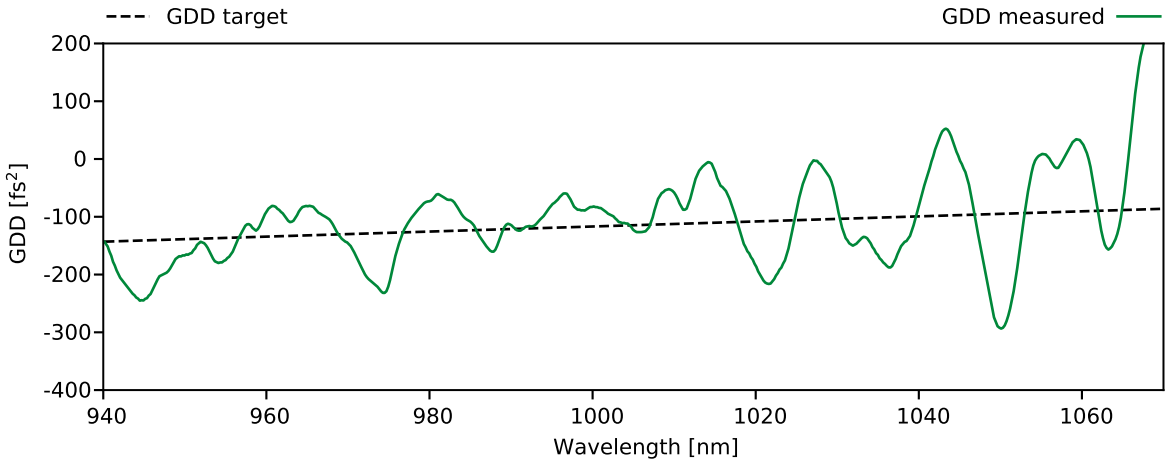

Fig. 3.2: Group delay dispersion (GDD) measurement of the utilized multipass cell mirrors with coating PC1841. The measurement was performed on a reference pair of flat 1-inch mirrors. The solid green line shows the measured GDD curve with its residual oscillations. The dashed black line displays the requested target GDD curve with a GDD of $-104\,fs^2$ and a third-order dispersion of $-234\,fs^3$ at 1030 nm wavelength.

Nonlinearity scan

As introduced in section 2.2.2, nonlinearities in quasi-waveguide assemblies such as the Herriott-type multipass-cells utilized here can generally broaden the spectrum of an in-

cident pulse homogeneously over its entire beam profile. As a prerequiste for a good homogeneity of the output beam, the total accumulated nonlinear phase $\Sigma\phi_{NL}$ needs to be distributed over a sufficient number of passes through a nonlinear medium. In section 2.3.3, a critical value of 0.3 rad for the maximum nonlinear phase shift per pass through the nonlinear medium has been introduced which was based on the numerical simulations presented in reference [81]. However, the result of the previously performed experiments on self-compression in an all-bulk multipass geometry suggest that per-pass phase shifts exceeding the aforementioned critical value might be tolerated without severely affecting the overall beam quality as long as the excessive per-pass phase shifts are only reached in a small number of passes. As shown in Fig. 2.13, for spectral broadening in the net-positive dispersion regime ($\beta_2^{eff} > 0$), the per-pass nonlinear phase shift is highest in the first pass through the broadening medium.

To investigate, for the Herriott-cell parameters given above ($\beta_2^{eff} \approx 2.6\,\mathrm{fs}^2/\mathrm{mm}$), which nonlinear phase shifts can still provide a good beam quality, the multipass-cell's output spectrum and beam profile were recorded for different distances of the broadening medium to the center plane of the cell. The initial nonlinear phase shifts corresponding to the respective nonlinear medium positions were then calculated numerically using equations 1.20 and 1.102 under the assumption that the propagating beam matches the eigenmode of the Herriott-cell and can be described by equation 2.10.

For an initial nonlinear phase in the range $\phi_{NL}^i = 0.05\,\mathrm{rad} - 0.3\,\mathrm{rad}$, the spectral bandwidth increases linearly without apparent deterioration of the beam profile (cf. Fig. 3.3). In contrast, the spectral broadening starts to saturate quickly for initial nonlinear phases exceeding 0.3 rad. At the same time, the appearance of weak distortions in the output beam profile in the characteristic shape of a ring-shaped pedestal around the central lobe can be observed. As a result of the accumulated self-focusing, the eccentricity of the initially slightly elliptic beam profile is likewise reduced at higher nonlinear phase shifts. It should be noted that the measurement for the value $\phi_{NL}^i = 0.35\,\mathrm{rad}$ had to be repeated thrice, since during the first two attempts, the fused silica plate which is utilized as a nonlinear medium was damaged while ramping the input power. Both, the degradation of the beam profile and the increased susceptibility to damage could be attributed to the excessive nonlinear phase shifts. The correspondingly increased spatio-temporal coupling and self-focusing yield an increase of the local peak intensities, which is potentially enhanced further by minor deviations from the ideal mode-matching due to the experimental accuracy. The experimental results for the maximum acceptable nonlinear phase shifts are found to be in good agreement with the numerical predictions from reference [81]. For the net-positive dispersion environment with $\beta_2^{eff} \approx 2.6\,\mathrm{fs}^2/\mathrm{mm}$, an initial phase shift of 0.25 rad is identified as a good trade-off between providing a substantial amount of spectral broadening while reliably preventing dominance of spatio-temporal coupling effects, and is consequently used for further experiments.

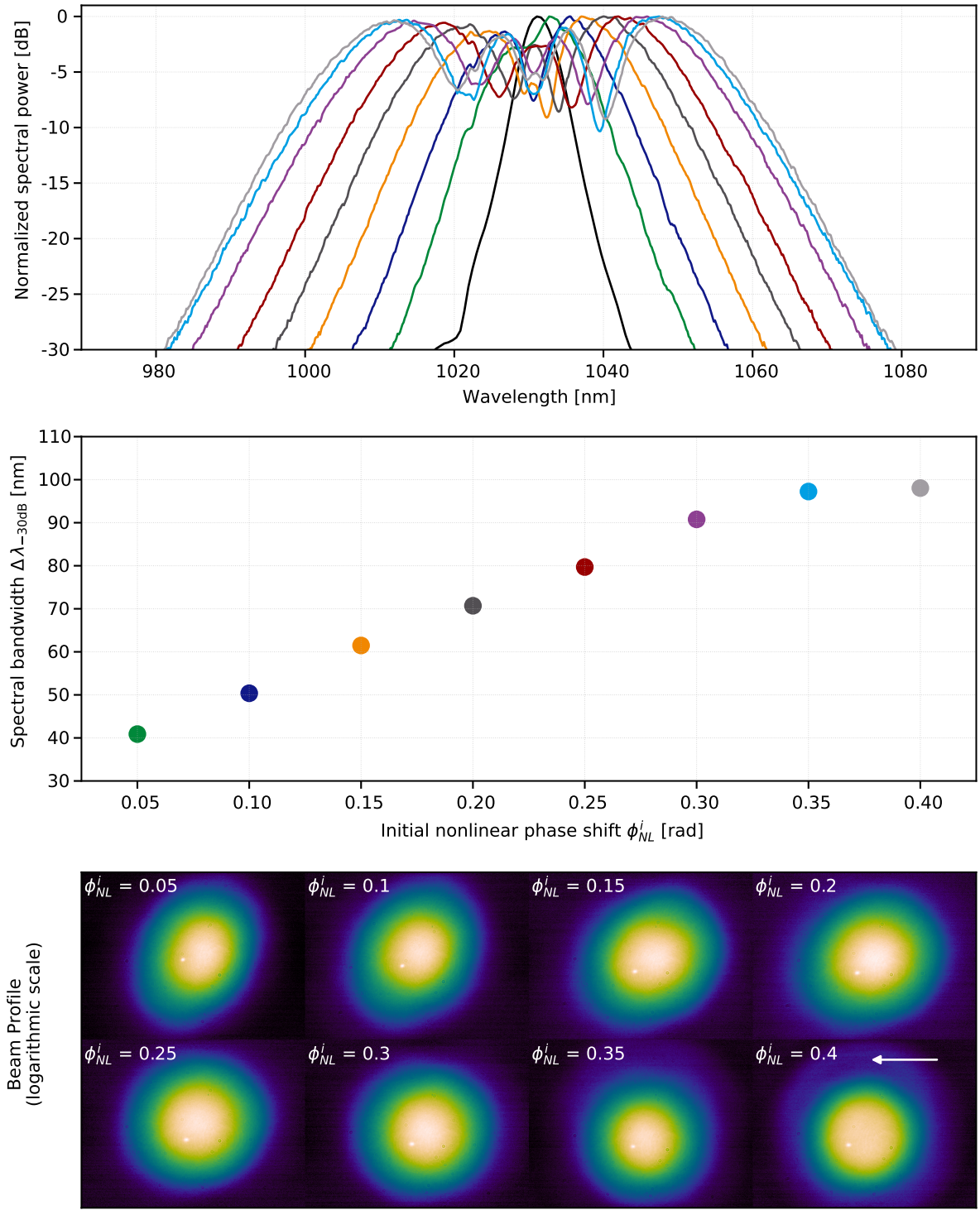

Fig. 3.3: Measurement of the spectral bandwidth and beam profile dependence on the initial nonlinear phase shift ϕ^i_{NL}. **Top:** Spectra for different initial phase shifts recorded with an OSA. **Center:** Spectral bandwidth (at −30 dB-level) vs. initial phase shifts. The black curve shows the oscillator spectrum which serves as input to the multipass-cell. The color coding of the top and center subfigures are identical to allow identification of the initial nonlinear phase shift for the curves in the subfigure at the top. **Bottom:** Beam profile corresponding to the different initial phase shifts. The beam profile plots are logarithmic in order to enhance the deterioration of the beam profile to make it visible more clearly. The white arrow in the beam profile corresponding to $\phi^i_{NL} = 0.4$ indicates the area where a ring shaped pedestal appears around the main beam.

3.1.2 Compression quality in the positive dispersion regime

To experimentally evaluate whether the transition to the net-positive dispersion regime positively affects the compression quality of the spectrally broadened pulses, the output of the multipass-cell was sent to a chirped-mirror compressor consisting of a folded symmetric 4-f-imaging arrangement and multiple highly dispersive mirrors (cf. Fig. 3.1). The total dispersion in the compressor amounts to GDD $\approx -2360\,\mathrm{fs}^2$ and TOD $\approx -720\,\mathrm{fs}^3$ specified at a center wavelength of 1030 nm.

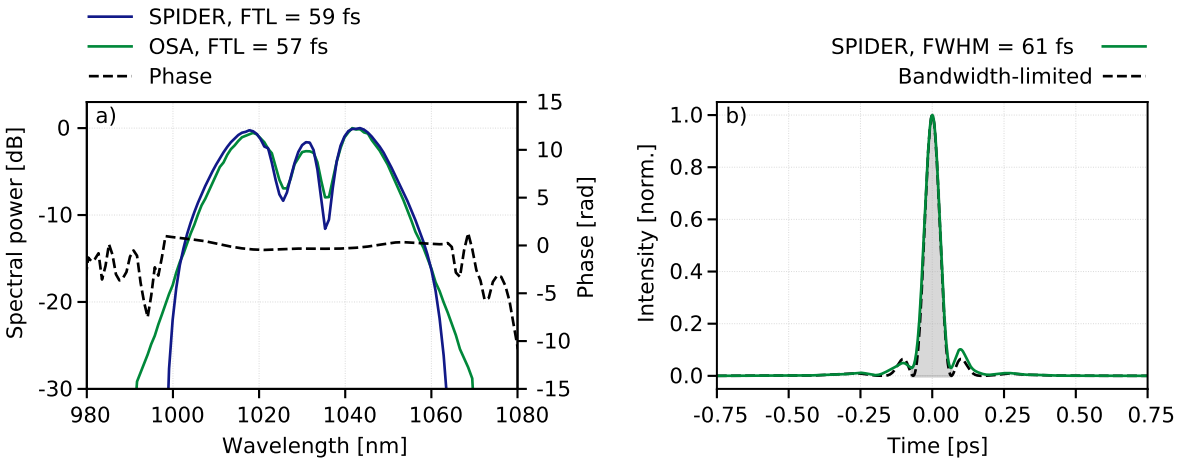

Fig. 3.4: Characterization of the compressed multipass-cell output for spectral broadening in the positive dispersion regime measured using OSA and spectral phase interferometry for direct electric field reconstruction (SPIDER). **a)** Spectral phase and intensity from SPIDER compared to reference measurement with an OSA; the Fourier-transform limit (FTL) is given in the legend. **b)** Retrieved intensity profile compared to the bandwidth-limited pulse shape. The area under the main peak is shaded in grey; 84 % of the pulse energy is contained within it.

The spectrum and pulse duration of the compressed pulse were measured using a commercial SPIDER (APE - FC Spider IR) and are shown in Fig. 3.4. Interestingly, the spectral bandwidth of the SPIDER measurement with a corresponding Fourier-transform limit of 59 fs is slightly narrower than the spectrum measured by the OSA (FTL = 57 fs, Fig. 3.4 a). Since the OSA measurement was taken before the chirped-mirror compressor, the difference most likely stems from irregularities in the bandwidth of reflectivity of the compressor-mirrors. The measured pulse duration is $\tau_{FWHM} = 61\,\mathrm{fs}$, which is already reasonably close to the bandwidth limited pulse duration. Closer inspection of the spectral phase reveals the presence of a residual positive chirp of the pulse which would require an additional GDD of approximately $-800\,\mathrm{fs}^2$ for optimal compression.

Most importantly, however, the overall compression quality is vastly improved compared to the results of the self-compression experiment (cf. section 2.3.1). With an obtained temporal compression factor of five, the output peak power is increased by a factor of 4.3

compared to the input pulses which corresponds to a compression efficiency of $\eta_{comp} = 91\,\%$ with more than 84 % of the power in the main peak. Numerical subtraction of the residual linear chirp further indicates that for an optimized compression, even higher peak powers reaching factors close to 4.7 can be obtained.

3.1.3 Optimization of the accumulated nonlinear phase

While the transition to spectral broadening in the net-positive dispersion regime facilitates a significant improvement of the attainable pulse compression quality, the corresponding single-stage compression factors are considerably lower than those achieved with self-compression. It is therefore instructive to take a closer look, if and how the nonlinear spectral broadening factors in the net-positive dispersion regime can be further optimized.

In analogy to equation 2.26, the accumulated nonlinear phase $\Sigma\phi_{NL}$, which determines the total amount of spectral broadening within the multipass-cell, can for arbitrary dispersion environments be generalized to

$$\Sigma\phi_{NL} = \phi_{NL}^{i} + \phi_{NL}^{2} + ... + \phi_{NL}^{N} = \sum_{k=1}^{N} \phi_{NL}^{k}, \tag{3.1}$$

where ϕ_{NL}^{k} denotes the nonlinear phase shift in the k-th pass and N denotes the total number of passes through the broadening medium. As shown in the previous section, in the positive dispersion regime, the maximum per-pass nonlinear phase-shift is accumulated in the first pass through the broadening medium and cannot be increased beyond approximately 0.3 rad due to the occurrence of spatio-temporal effects resulting in an a deterioration of the beam quality. Further scaling of the total nonlinear phase can therefore only be realized by increasing the number of passes N through the nonlinear medium or by reducing the variance of the individual per-pass nonlinear phase shifts ϕ_{NL}^{k}. While $\Sigma\phi_{NL}$ can in principle be increased indefinitely by simply scaling the number of passes, it does not constitute a suitable parameter for further optimization since the number of passes that can be realized in an actual experiment is typically restricted by the geometry of the optical components. As a consequence, the spectral broadening rate η_s is introduced as

$$\eta_s = \frac{1}{N} \sum_{k=1}^{N} \frac{\phi_{NL}^{k}}{\phi_{NL}^{i}}, \tag{3.2}$$

which normalizes the total nonlinear phase shift to the maximum nonlinear phase $\Sigma\phi_{NL}^{max} = N \cdot \phi_{NL}^{i}$ that can be accumulated in N passes through a broadening medium in the absence of temporal self-compression. Using this definition of the spectral broadening rate, equation 3.1 can be rewritten as

$$\Sigma\phi_{NL} = N \cdot \phi_{NL}^{i} \cdot \eta_s. \tag{3.3}$$

The spectral broadening rate η_s can therefore be interpreted as a measure for the efficiency of the spectral broadening process which should preferably be maximized.

Unfortunately, the exact calculation of η_s still requires knowledge over the evolution of the individual per-pass phase shifts. As no closed-form analytic expression for ϕ_{NL}^k as a function of the number of propagated passes has been found until today, the dependence of the spectral broadening rate on the effective GVD coefficient is instead analyzed numerically using the model presented in section 2.2.2. The simulation parameters are chosen such that the initial nonlinear phase shift ϕ_{NL}^i takes a value of approximately 0.25 rad for the nonlinear propagation of a sech^2-shaped pulse with an input pulse duration of 300 fs. The nonlinear medium is modelled to represent a 6.35 mm long fused silica plate with the material parameters given in section 2.3.2. For the multipass-cell mirror coating, a fixed TOD value of $-235\,\text{fs}^3$ at a central wavelength of 1030 nm is assumed to compensate for the TOD of fused silica. To discern the influence of dispersion on the pulse evolution more easily, self-steepening and the time-delayed Raman-response as well as linear losses are neglected in the simulations.

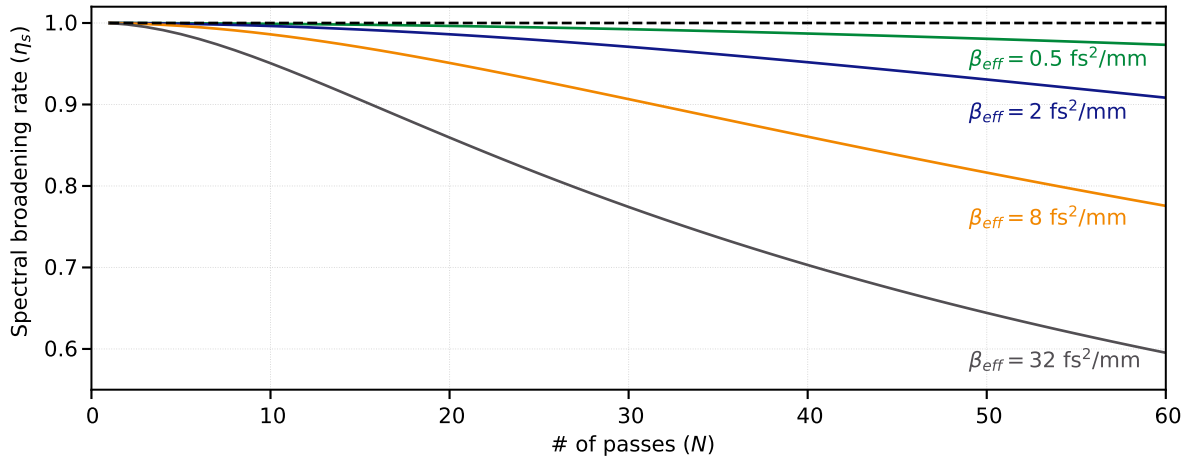

Fig. 3.5: Simulated spectral broadening rate η_s as defined in equation 3.2 vs. number of passes the pulse propagates through the multipass-cell for different values of the effective GVD coefficient β_{eff}. The effective GVD coefficient was adjusted numerically by varying the mean-GDD of the utilized multipass-cell mirrors. The simulations are based on an input pulse duration of 300 fs and an initial nonlinear phase shift of approximately 0.25 rad. The dashed black lines indicates the spectral broadening rate for a non-dispersive system which is always unity.

The effective GVD coefficient is varied by numerically adjusting the GDD-value of the utilized multipass-cell mirror pair (cf. equation 2.34). Fig. 3.5 shows the resulting spectral broadening rates η_s versus the propagated number of passes N for various β_2^{eff} in the range from $0.5\,\text{fs}^2/\text{mm}$ to $32\,\text{fs}^2/\text{mm}$. It is easily seen that, for all N, the broadening rate is reduced for increasing values of the effective GVD coefficient, where the highest level of η_s is maintained for β_2^{eff} close to zero.

According to equation 2.34, the value of β_2^{eff} can, for a given nonlinear material, be adjusted by varying the thickness of the broadening medium or the arithmetic mean group

delay dispersion of the utilized multipass-cell mirror pair $\overline{GDD_M}$. In practice, approaching effective GVD values close to zero by using bulk plates with appropriate thickness as nonlinear media is often inhibited by their commercial availability. While in principle fused silica can be custom polished to the exact required thickness, the process is costly and the typical manufacturing tolerances remain on the order of $\pm 0.2\,\mathrm{mm}$ for fused silica plates of 2 mm to 8 mm thickness [103]. Further fine-tuning of the total propagation length in material could potentially be achieved by combining multiple thin AR-coated plates to average out the individual manufacturing deviations. However, the distribution of the nonlinear interaction over multiple separated media will likely cause an enhancement of the Fresnel-losses, even with good quality AR-coating, due to the increased number of air-glass interfaces in the multipass-cell.

In the scope of this thesis, the thickness of the fused silica plates which are used as nonlinear media was therefore fixed to 6.35 mm and the effective GVD was optimized via adapting the GDD curve of the utilized multipass-cell mirrors just as it has been realized in the numerical simulations. To account for the aforementioned manufacturing tolerances of the fused silica plates as well as small deviations in the coating process, the target GDD curves of the multipass-cell mirrors are typically designed for an effective GVD coefficient on the order of $2\,\mathrm{fs}^2/\mathrm{mm}$ to $3\,\mathrm{fs}^2/\mathrm{mm}$. By doing so, excessive temporal broadening due to accumulated dispersion can still be kept on a low level while operation in the net-positive dispersion regime can be ensured even for the eventuality of an unfavorable combination of plate thickness on the lower end of the tolerances as well as small deviations from the target coating specification . Only in cases where a more precise dispersion control is absolutely required, extra efforts of further reducing β_2^{eff} were made by selecting the fused silica plates with best matching thickness from a larger batch.

3.2 Cascaded nonlinear pulse-compression stages

As shown in the previous sections, all-bulk multipass spectral broadening in Herriott-cells can provide a valuable tool for the temporal compression of laser pulses facilitating a high compression quality combined with excellent beam quality. This renders the approach especially suitable for being used in front-ends designed for highly nonlinear applications such as IPDFG, where short transients and high peak powers are required [20]. Although temporal compression up to a factor of 8 can readily be achieved in single-stage, high-power thin-disk oscillator driven multipass-cells in the positive dispersion regime, this is still not sufficient to reach the desired pulse durations below 20 fs. As a result, the cascading of multiple nonlinear compression stages is typically required. Since earlier realization of the cascaded multipass-cell concept have been subject to suboptimal compression quality, a dual-stage pulse compression setup was developed in the frame of this thesis, with the goal of reproducing the spectral broadening factors of ≈ 20 which were previously demonstrated in references [81, 82], but with superior compression quality owing to an improved dispersion management.

3.2.1 Re-characterization of the driving oscillator

Since the long-term goal for the laser system under development is to perform time-domain spectroscopy on medical samples using mid-IR radiation generated by IPDFG similar to reference [6], the laser front-end had to be assembled in a laboratory with bio-medical certification. Owing to the altered environmental conditions, the driving laser introduced in section 2.3.1 was modified after being moved to the new laboratory, as described below.

While the laboratory is equipped with a reliable temperature stabilization to 20 °C, the relative humidity of the ambient air fluctuates between 15 % - 40 % rH depending on the weather conditions. Consequently, the laser output power can vary by up to 10 W. This variation is also visible during continuous wave operation and is likely due to the modified thermal conductivity of the ambient air which causes a change of the thermal-lens inside the laser cavity, shifting the optimal operation point of the laser oscillator. To minimize day-to-day fluctuations of the driving laser power, the relative humidity was therefore stabilized to an equilibrium value of 28 % rH by introducing a constant stream of air with controlled humidity into the housing containing the laser oscillator. Since the laser had previously been operated at 40 % rH, its performance was re-optimized by scanning the stability parameter and the position of the Kerr-medium inside the laser oscillator to maximize the output power and spectral bandwidth.

Furthermore, the new arrangement of the experimental chambers on the optical table after the move necessitated a re-design of the beam path between the oscillator and the first broadening stage, including the setup for polarization- and spatial mode-cleaning. As a consequence, the oscillator length had to be reduced by approximately 3 cm by changing the position of the output coupler to free a sufficient amount of space for the additionally required turning mirrors. Since the relative change is only of the order of 0.2 % of the total length, the effect on the pulse energy and pulse repetition frequency can be considered negligible.

To evaluate, whether the aforementioned modifications adversely affect the performance of the state-of-the-art oscillator introduced in section 2.3.1, a full characterization of the decisive laser parameters was undertaken. In the new configuration, the oscillator emits an average power of 145 W of p-polarized light measured using a thermal power sensor after linearizing the polarization with an AR-coated TFP. The output power still compares well to the original output power of 149 W. The continuously mode-locked pulse train with 10.6 MHz pulse repetition frequency consists of individual pulses with a spectral bandwidth of 17 nm centered around a wavelength of 1030 nm. A FWHM-pulse duration of 288 fs was measured using an SHG-FROG (Fig. 3.6 b). The pulses are compressed close to the bandwidth-limited pulse duration of 283 fs (cf. Fig. 3.6 b) with a minor residual up-chirp that has been previously observed in references [23, 104].

While the faint circular pattern surrounding the main Gaussian beam (cf. section 2.3.1) remains unimproved by the modifications made to the oscillator, the divergence of the emitted laser beam is slightly reduced. Narrowing the diameter of the external water-cooled copper aperture to 3.2 mm is found to result in an excellent quality of the transmitted beam, characterized by an M^2 factor of 1.03 in the tangential- and 1.02 in the sagittal plane. The

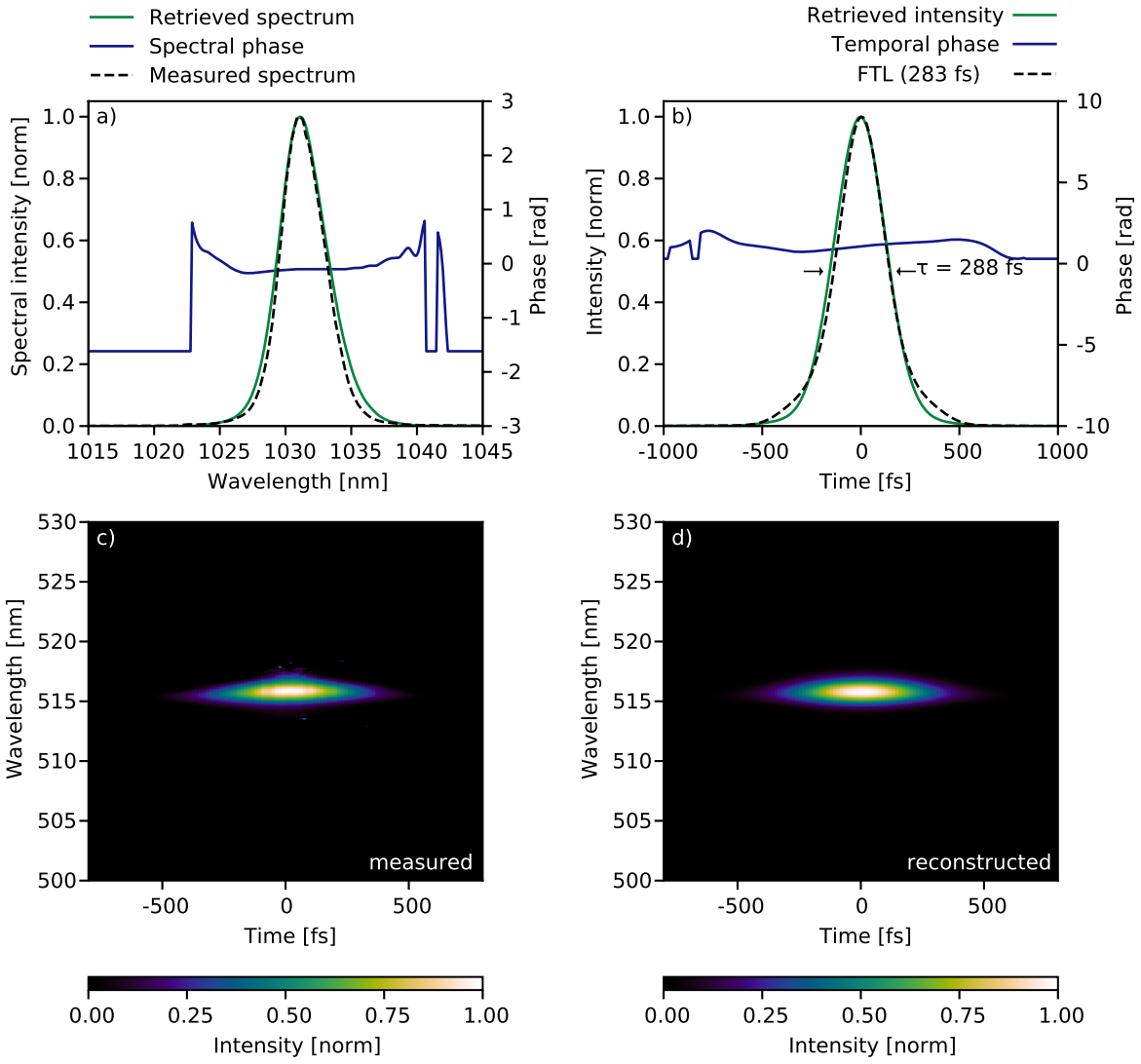

Fig. 3.6: Temporal characterization of the modified driving oscillator. **a)** Spectral phase and intensity, compared to reference measurement with an OSA. **b)** Temporal phase and intensity compared with the FTL of the spectrum. **c)** Measured SHG-FROG trace, and **d)** reconstructed FROG trace with < 0.0045 error on a 512×512 grid. For the temporal characterization measurement a small fraction of the full power beam was extracted using an uncoated fused silica wedge.

measurement of the M^2 factor and the beam profile, both measured behind the copper aperture, are shown in Fig. 3.7.

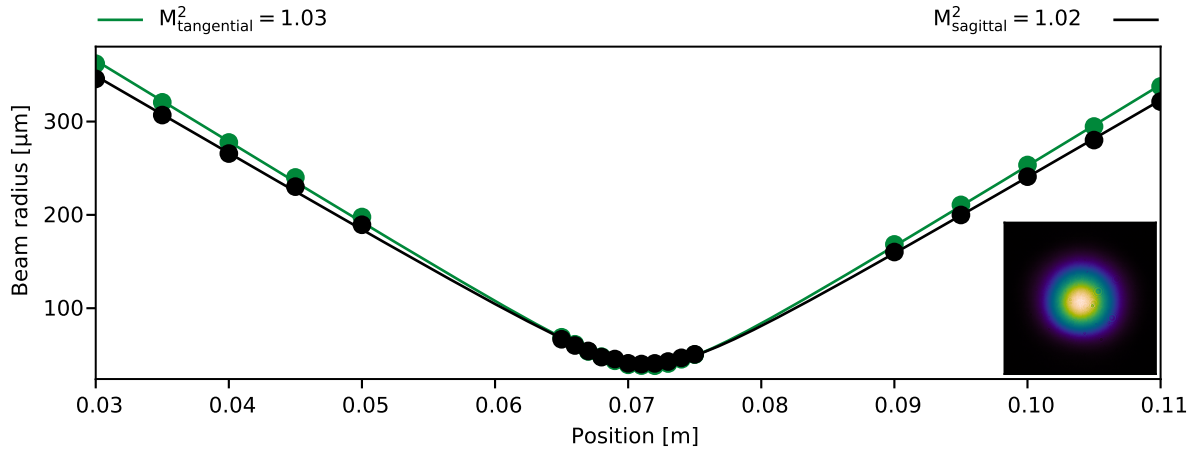

Fig. 3.7: M^2-measurement of the modified oscillator for the tangential and sagittal plane according to ISO norm [31]. Inset: beam profile of the collimated beam. Both measurements were taken after spatial cleaning of the oscillator output using a water-cooled copper aperture with a diameter of 3.2 mm that is placed in the collimated beam. The data was recorded using a Cinogy CinCam CMOS-1203 beam profiler.

The slightly divergent output of the oscillator is collimated using a plano-concave mirror with a radius of curvature of 6000 mm placed at a distance of approximately 3000 mm to the output coupler. With a still reasonable transmission of $T = 85\,\%$ through the copper aperture and turning mirrors, pulses with 11.3 µJ pulse energy and 34.6 MW peak power, corresponding to an average power of 120 W, are available as input for the subsequent spectral broadening stages. A full schematic of the experimental setup, including the two nonlinear compression stages which are described in further detail in the following paragraphs, is shown in Fig. 3.8.

3.2.2 First compression stage

As a direct consequence of the promising results obtained for spectral broadening in the net-positive dispersion regime presented in the previous section, the dispersive coating of the multipass-cell mirrors forming the first spectral broadening stage is chosen identical to the curve shown in Fig. 3.2. The configuration of the multipass-cell is modified to feature a Gouy-parameter of $\psi_E = 2\pi \cdot (12/17)$, corresponding to a mirror separation distance of $d \approx 480$ mm for a pair of multipass-cell mirrors with a radius of curvature of 300 mm. Consequently, the beam propagates a total number of 34 passes through the 6.35 mm-thick fused silica nonlinear medium before being extracted from the multipass-cell using a small scraper mirror. By placing the nonlinear medium off-centered at a distance of 174 mm to

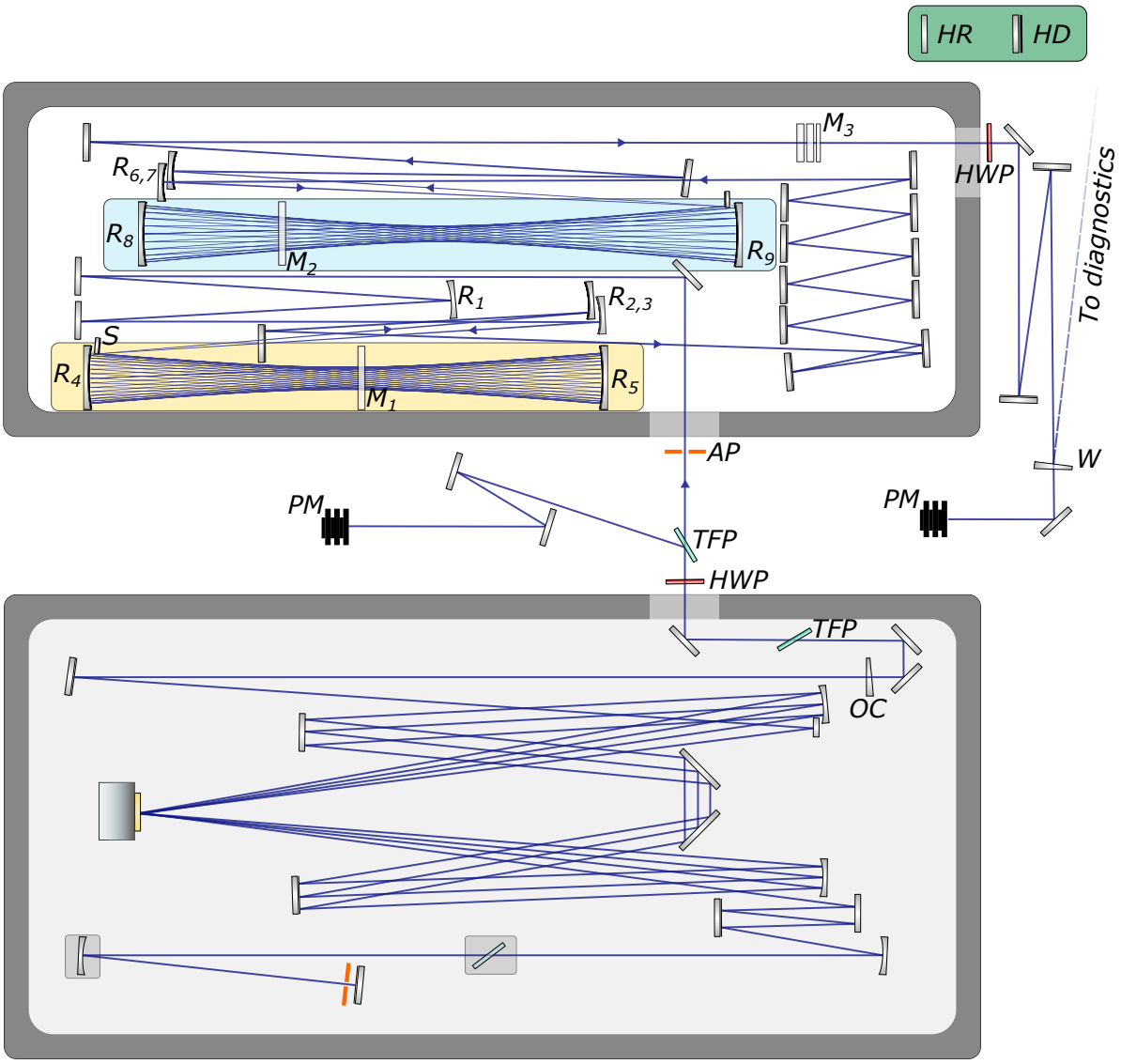

Fig. 3.8: Schematic of the dual-stage multipass-cell spectral broadening setup. The oscillator contains the same elements as in Fig. 2.6 but its output coupler (OC)is moved to slightly shorten the cavity, leaving enough space for an additional beam folding stage inside the oscillator chamber. The oscillator is followed by a dual-stage multipass-cell spectral broadening setup described in the text. The abbreviations are: *TFP*, thin-film polarizer; *HWP*, half-wave plate; *PM*, power meter; R_1, collimating mirror with a radius of curvature of 6000 mm; $R_{2,3}$, first-stage focusing- and collimation mirrors with radius of curvature of 1500 mm (PC1841); S, scraper mirror; R_4, R_5, first-stage multipass-cell mirrors (PC1841); M_1, 6.35 mm-thick fused silica plate; $R_{6,7}$, second-stage focusing- and collimation mirrors with radius of curvature of 1500 mm (PC1711); R_8, R_9, second-stage multipass-cell mirrors (PC1711); M_2, 6.23 mm-thick fused silica plate; M_3, variable amount of additional fused silica plates for dispersion compensation; W, removeable, uncoated fused-silica wedge. The area of the first- and second multipass-cell are shaded in yellow and light blue, respectively.

one of the multipass-cell mirrors, the nonlinear phase shift in the first pass is adjusted to a value of $\phi^i_{NL} \approx 0.2\,\mathrm{rad}$. The initial nonlinear phase-shift is deliberately set to an even lower value here than the 0.25 rad used in the experiments presented in section 3.1.2 to further reduce potential beam degradation due to spatio-temporal couplings.

Due to the different eigenparameters of the Herriott-cell utilized in this experiment, the collimated output of the driving oscillator can be mode-matched to the eigenmode of the Herriott-cell by a simple plano-concave focusing mirror with 1500 mm radius of curvature placed at a distance of 750 mm to the center plane of the multipass-cell. Importantly, the necessity of using transmissive optical elements such as the degrading zoom beam expander for the mode-matching can thus be avoided. Due to the large angular advance within the Herriott-cell, an additional, vertically offset plano-concave mirror with identical radius of curvature is used for collimating the output of the multipass-cell.

Sending an average power of 120 W into the multipass-cell, an output power of 109 W was measured after a small fraction of the power had been split-off for diagnostics using an uncoated fused silica wedge. Retrospectively correcting the output power for the uncoated fused silica wedge by considering two reflections with a transmission of 96.8 % yields an effective output power of 116 W and a resulting total optical efficiency of 96.7 % for the first multipass-cell.

To qualitatively assess the effectiveness of the spatio-temporal homogenization within the multipass-cell, the ouput beam profiles for the collimated beam were recorded at low and high output power ($\approx$ 1 W and 109 W, Fig. 3.9 a and b, respectively). Owing to the low per-pass nonlinear phase shifts within the multipass-cell the beam profile shows no discernible deterioration. When focused down, the Gaussian shape of the beam is maintained and no ring structure can be observed (Fig. 3.9 c). The measured M^2 factor is 1.04 in the tangential- and 1.00 in the sagittal plane (cf. Fig. 3.9 d) which is in excellent agreement with the oscillator M^2 factor. The deviation towards lower values for the M^2 factor in the sagittal plane is attributed to the experimental uncertainty and was not investigated further.

The spectrum at the multipass-cell output was measured using an OSA and is shown in Fig. 3.10 a. The output spectrum is symmetrically broadened with respect to the input spectrum and features a bandwidth of approximately 70 nm at -30 dB level, supporting a Fourier-transform limited pulse duration of 67 fs (cf. Fig. 3.10 b).

To assess whether the multipass-cell indeed operates in a net-positive dispersion environment, the temporal shape of the uncompressed output was characterized using an SHG-FROG. The measured trace was reconstructed by the retrieval algorithm (Fig. 3.10 c and d) with a residual error < 0.0077 on a 1024×1024 grid. A high quality of the retrieval is further indicated by the excellent agreement between the fundamental and the retrieved spectrum (Fig. 3.10 a) which supports a bandwidth-limited pulse duration of 67 fs. It should be noted that an additional GDD of $-350\,\mathrm{fs}^2$ — which is added to the pulse by the utilized turning mirrors — was not accounted for during the analysis of the uncompressed pulse duration. Nevertheless, the retrieved FWHM pulse duration of 325 fs clearly shows that the pulse has been subject to a small amount of temporal broadening during the propagation through the multipass-cell which ultimately confirms the operation

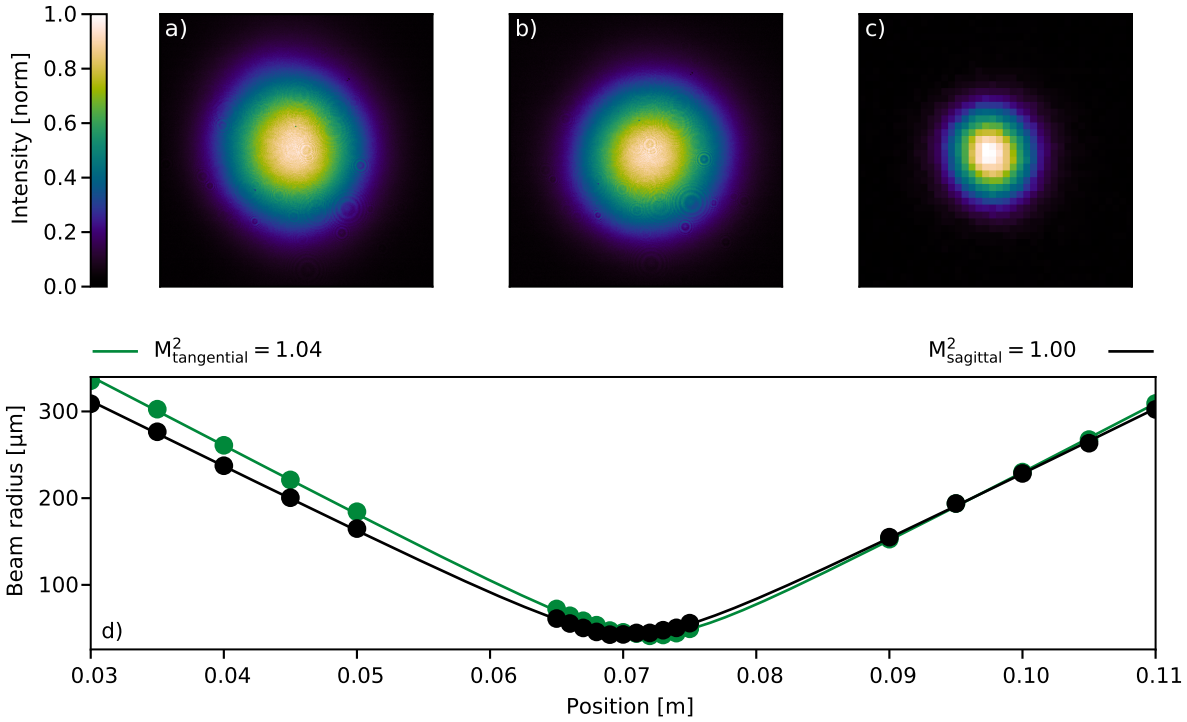

Fig. 3.9: Spatial characterization of the first spectral broadening stage. Beam profile of collimated beam at **a)** $\approx 1\,\mathrm{W}$ average output power and **b)** 109 W average output power. **c)** Beam profile of a focus created by an achromatic lens with $f = 200\,\mathrm{mm}$ focal length at full power. The $1/e^2$ beam diameter in the focus is 75 µm. **d)** M^2-measurement according to ISO norm [31].The data was recorded using a Cinogy CinCam CMOS-1203 beam profiler.

in the net-positive dispersion regime.

The spectrally broadened pulses are subsequently compressed using a chirped-mirror compressor with a total GDD of approximately $-4000\,\mathrm{fs}^2$ added via 15 reflections off of highly dispersive mirrors (type PC162). Fig. 3.11 a and b displays the results of the SPIDER measurement of the compressed pulses which shows that the pulses exhibit a clean pulse shape with a FWHM pulse duration of 71 fs corresponding to a temporal compression factor of 4. The compression efficiency of the pulses at the output of the first compression stage is 89 %. The observed slight asymmetry of the compressed pulse can likely be attributed to imperfect TOD compensation of the utilized multipass-cell mirror pair. A small residual GDD of approximately $500\,\mathrm{fs}^2$ is intentionally left uncompressed to avoid spectral narrowing induced by negatively pre-chirped input pulses for the spectral broadening in a second stage.

Due to Fresnel losses at the compressor mirrors, the average output power and the total optical efficiency after the chirped-mirror compressor are further reduced to 107 W and 89 %, respectively. The compressed pulses have a peak power of 117.6 MW, which is

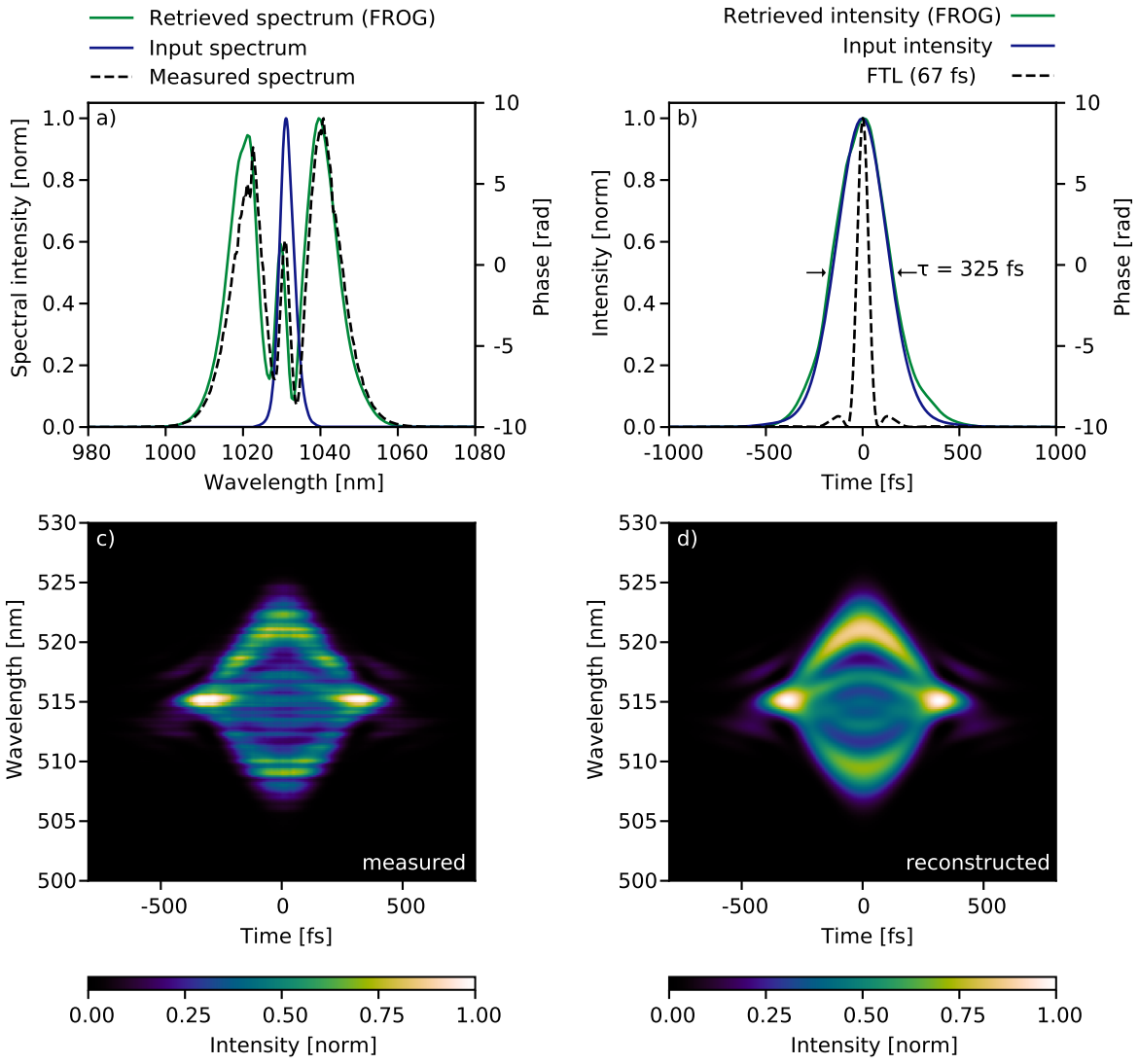

Fig. 3.10: FROG measurement of the uncompressed output of the first spectral broadening stage confirming operation in the net-positive dispersion regime. **a)** Spectral phase and intensity, compared to reference measurement with an OSA. **b)** Temporal phase and intensity compared with the FTL of the spectrum. The area under the main peak is shaded in light grey. **c)** measured SHG-FROG trace, and **d)** reconstructed FROG trace with < 0.0078 error on a 1024×1024 grid. The fringes in the measured trace are a measurement artefact originating from imperfect coupling of the generated SHG radiation to a multimode-fiber attached to the FROG spectrometer.

approximately a factor of 3.4 higher than the peak power of the input pulses.

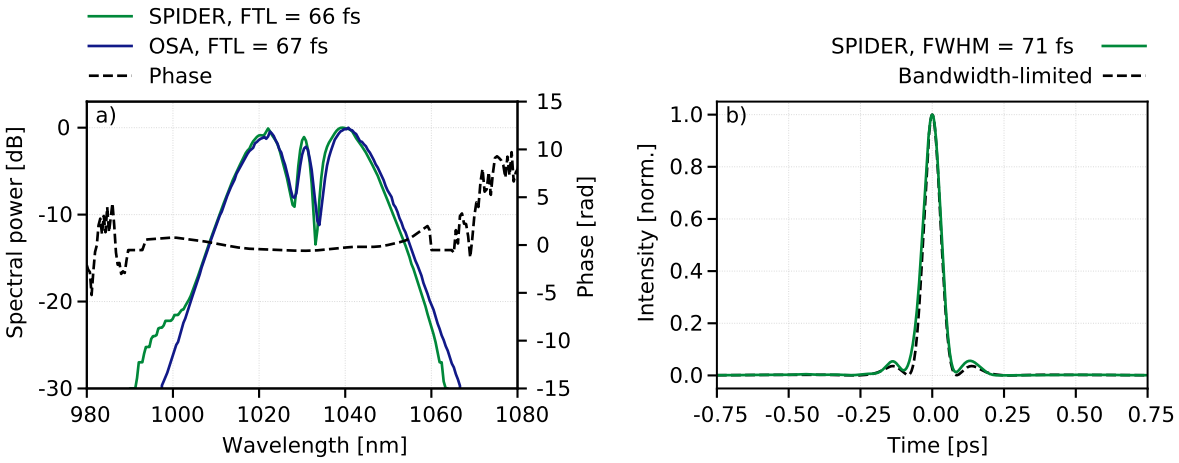

Fig. 3.11: Characterization of the first spectral broadening stage after temporal compression. **a)** Retrieved spectral phase and intensity from the SPIDER measurement compared to reference measurement from an OSA. **b)** Measured intensity profile compared with the bandwidth-limited pulse shape determined by Fourier-transformation of the spectrum.

3.2.3 Second compression stage

In order to further compress the output pulses of the first nonlinear pulse compression stage, a second Herriott-type multipass-cell was assembled. Since the input pulse duration of the second broadening stage is more than a factor of 4 shorter than in the first stage, the effect of accumulated dispersion, which causes temporal broadening of the propagating pulses, increases significantly (cf. section 3.1.3). Since strong temporal broadening is expected to result in a reduced spectral broadening rate, the number of passes through the nonlinear medium is reduced to $N = 22$ by choosing a Herriott-cell configuration with a Gouy-parameter of $\psi_E = 2\pi \cdot (9/11)$. This corresponds to a mirror separation distance of $d \approx 553\,\mathrm{mm}$ for multipass-cell mirrors with a radius of curvature of 300 mm. The output of the previous compression stage is matched to the eigenmode of the multipass-cell by focusing the collimated output of the chirped-mirror compressor using a plano-concave mirror with a radius of curvature of 1500 mm at a distance of approximately 750 mm to the center plane of the second Herriott-cell.

The multipass-cell mirrors are different to those used for the first multipass-cell and feature a dispersive coating with a target mean GDD and TOD of $-119\,\mathrm{fs}^2$ and $-240\,\mathrm{fs}^3$ at a center wavelength of 1030 nm, respectively. Due to the high demands on the mirror bandwidth (850 nm - 1400 nm) and to reduce residual GDD oscillations, the coating is realized as a complementary dispersive pair. A measurement of the GDD curves in the spectral

range spanning 850 nm - 1070 nm is shown in Fig. 3.12, and it shows good agreement between the realized mean- and target GDD. The strong oscillations in the GDD-curve of the second mirror (dashed black line in Fig. 3.12) at around 1020 nm wavelength are likely an artefact of dispersion measurement which were found to not affect the spectral broadening in the experiment.

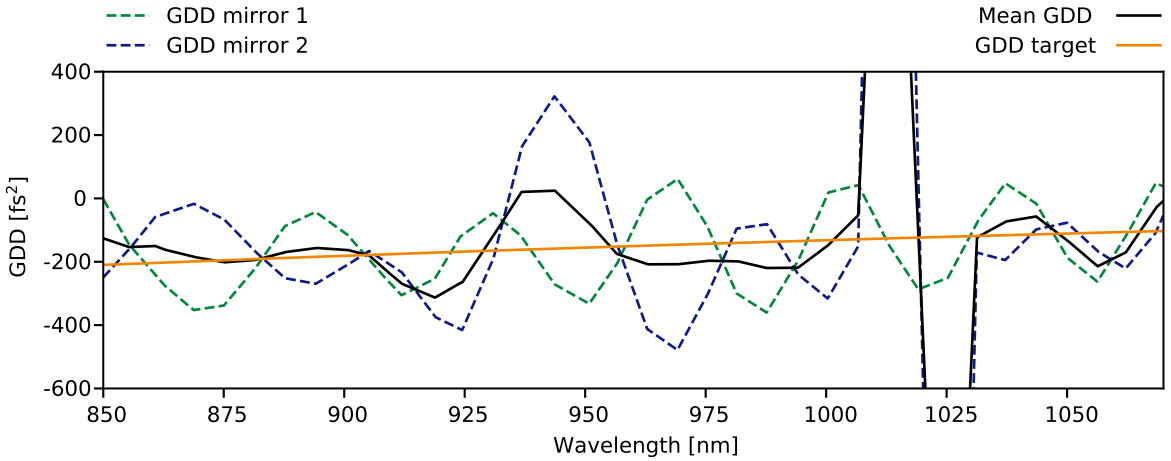

Fig. 3.12: Group delay dispersion (GDD) measurements of the multipass cell mirrors with PC1711 coating utilized in the second broadening stage. The measurements were performed on a reference pair of flat 1-inch mirrors. The dashed green and blue lines display the GDD of the two individual sample mirrors. The solid black line displays the arithmetic mean GDD of the two measured complementary curves with a resulting GDD of $-119\,\mathrm{fs}^2$ and TOD of $-240\,\mathrm{fs}^3$ at 1030 nm wavelength. The yellow line shows the target curve of the coating. The strong oscillations in the GDD-curve of the second mirror at around 1020 nm are likely an artefact of dispersion measurement which were found to not affect the spectral broadening in the experiment.

In an effort to further reduce the influence of dispersion on the pulse propagation, multiple fused silica plates with slightly varying length were tested as nonlinear medium. A 6.23 mm thick fused silica plate was experimentally found to maximize the spectral broadening while maintaining operation in the net-positive dispersion regime. To compensate for the reduced number of passes when compared to the first broadening stage, the initial nonlinear phase shift needs to be substantially increased to achieve a similar total accumulated phase $\Sigma\phi_{NL}$. By placing the fused silica plate at a distance of 137 mm to one of the multipass-cell mirrors, the initial nonlinear phase shift is adjusted to $\phi^i_{NL} = 0.35\,\mathrm{rad}$, which is expected to provide a trade-off between high nonlinearity and already slightly degrading beam quality (cf. Fig. 3.3).

Unfortunately, no low-GDD turning mirrors that support the full bandwidth of the spectrally broadened pulses for reflection under small angles were available at the time of the experiment. Consequently, the pulses were directly sent into a chirped-mirror compressor, which at the same time serves as the beam delivery setup for subsequent experiments.

The chirped-mirror compressor comprises several broadband, dispersive mirrors with a total GDD of $-690\,\mathrm{fs}^2$ and a TOD of $-480\,\mathrm{fs}^3$, an air-spaced achromatic half-wave retarder plate for rotating the polarization by 90° and a variable number of fused silica plates for fine-tuning of the residual dispersion (cf. Fig 3.8).

At full input power, an average output power of 95 W is recorded for second nonlinear compression stage. Equivalent to the characterization of the first spectral broadening stage, a small fraction of the beam has been split off for diagnostics using an uncoated fused silica wedge. The output power corrected for the wedge's Fresnel losses (see first compression stage for details) is 101 W which corresponds to an excellent optical efficiency of 94 % and a total combined efficiency of 84 % of the first- and second stage. While the stability of the system was not evaluated systematically at this point it should be highlighted that the spectral broadening arrangement could be operated for several hours continuously over multiple days without the need for any daily re-alignment. A more detailed analysis of the system stability and noise after post-compression is provided in section 4.3.2.

The broadened spectrum was measured using an OSA and is shown in Fig. 3.13 a. At the output of the second compression stage, the spectrum spans from 885 nm to 1155 nm at −30 dB level, corresponding to a bandwidth of 270 nm and a bandwidth-limited pulse duration of 14.6 fs. The spectral broadening in the second multipass-cell exhibits a slight asymmetry that enhances the spectral content in the shorter wavelengths which is likely caused by residual uncompressed TOD during propagation in the quasi-waveguide [35, p. 120 f.]. In addition to the asymmetrical broadening, a small spectral side-lobe appears in the wavelength range from 875 nm to 885 nm which presumably originates from optical wave breaking during the nonlinear propagation [42].

The temporal shape of the compressed pulses was characterized using the SPIDER technique and is shown in Fig. 3.13 b. Compression to a FWHM pulse duration of 15.6 fs is achieved with three additional fused silica plates placed behind the multipass-cell with a total length of 15.7 mm, corresponding to approximately $300\,\mathrm{fs}^2$ of GDD and approximately $600\,\mathrm{fs}^3$ of TOD. To the author's knowledge, these are the shortest pulse durations that have so far been realized using an all-bulk multipass spectral-broadening approach. The pulses are compressed close to the bandwidth-limited pulse determined from the SPIDER measurement of the fundamental spectrum which is 15.2 fs. Slight differences in the Fourier-transform limits of the OSA- and SPIDER measurement are attributed to the presence of additional dielectric turning mirrors (HR 1707) with a reduced reflectivity towards the edges of the measured spectrum in the SPIDER measurement. The temporal compression factor of the second stage is 4.6, which is on the same order as the compression factor in the first stage. The total temporal compression factor of 18.5 is well comparable to the highest compression rate of ≈ 22 that has to date been realized using all-bulk multipass spectral broadening (cf. reference [82]), but with better temporal pulse quality.

By comparing the area under the main peak (grey shaded area Fig. 3.13) to the total area under the curve, the main pulse is found to contain $> 78\,\%$ of the pulse energy which constitutes a significant improvement over the previously achieved values of 45 % for the 18 fs long pulses in reference [81] and 57 % for the 22 fs long pulses reported in reference [82]. The excellent compression efficiency of 87 % that is achieved with the presented dual-

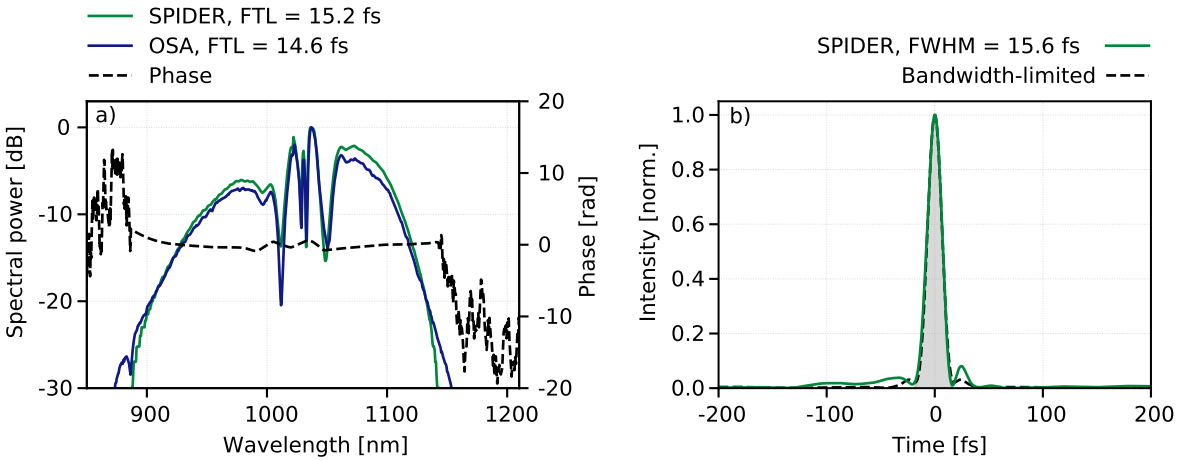

Fig. 3.13: Characterization of the second spectral broadening stage after temporal compression. **a)** Retrieved spectral phase and intensity from the SPIDER measurement compared to reference measurement from an OSA. **b)** Measured intensity profile compared with the bandwidth-limited pulse shape determined by Fourier-transformation of the spectrum.The grey shaded area denotes the main part of the beam. 78 % of the total energy is contained within it.

stage nonlinear compression scheme is made possible by the precise balancing of effective multipass-cell dispersion and nonlinear propagation length in the second broadening stage. Due to the high compression quality, a peak power of 463 MW is reached which is more than a factor of 13 higher than the input peak power. To the author's knowledge, this is the highest peak power that has to date been realized in an amplifier-free thin-disk laser system.

In contrast to the excellent temporal properties, the high initial nonlinear phase shift causes the onset of degradation of the beam quality which manifests in a slight deterioration of the collimated beam profile at the output of the second multipass-cell (Fig. 3.14 inset). The onset of spatio-temporal couplings affecting the overall beam quality is further supported by measurement of the M^2 factor which is 1.11 in the tangential- and 1.07 in the sagittal plane when evaluated for a center wavelength of 1030 nm (cf. Fig. 3.14).

While the observed beam quality is still on par with other implementations of thin-disk oscillator driven multipass spectral broadening (reported values are for example $M^2 < 1.15$ for 88 fs pulses in reference [105] or $M^2 < 1.15$ for 18 fs pulses in reference [81]), the significant change when compared to the output of the first broadening stage calls for a more detailed analysis of the spatio-temporal properties of the output beam. It should be noted that while a reduction of the beam homogeneity will inevitably induce an worsening of the beam quality, an increased value of the M^2 factor does not necessarily imply a low beam homogeneity. Especially in complex optical setups which contain a multitude of reflective and transmissive optical elements, the beam quality is likely to also degrade due to linear spatial aberrations caused by for example thermal lensing, accumulated spherical

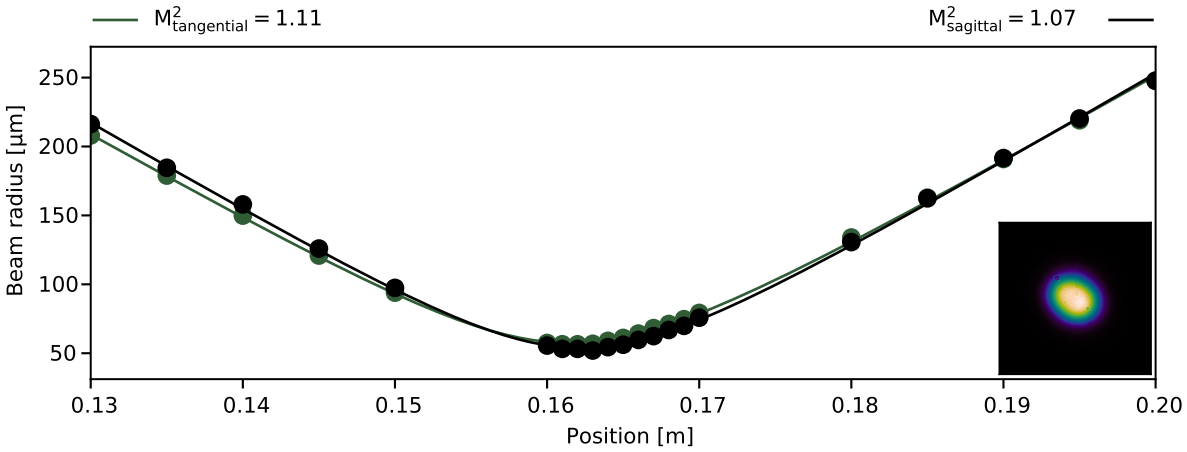

Fig. 3.14: M^2-measurement of the modified oscillator for the tangential and sagittal plane according to ISO norm [31]. The measurement was performed using a scanning slit beam profiler (Ophir NanoScan 2s Pyro/9/5 µm). Inset: beam profile of the collimated beam showing first signs of beam degradation. The beam profile was recorded using a Cinogy CinCam CMOS-1203 beam profiler.

aberrations or even minor beam clipping due to tight geometrical constraints.

To assess whether the degradation of the beam quality factor can be correlated to spatio-temporal coupling, the output beam homogeneity was analyzed in more detail following the approach described in reference [100]. For the homogeneity measurement, 2×45 spectra were recorded scanning both the x- and y-axis of the collimated beam in 0.2 mm steps using a multi-mode fiber (400 µm core diameter) with FC/PC tip coupled to an OSA (Fig. 3.15, left panel).

For each recorded spectrum $I(\lambda)$, the overlap V with the spectrum on the beam axis $I_0(\lambda)$ is calculated using [100]

$$V = \frac{\left[\int \sqrt{I(\lambda) \cdot I_0(\lambda)} \mathrm{d}\lambda\right]^2}{[\int I(\lambda)\mathrm{d}\lambda \cdot \int I_0(\lambda)\mathrm{d}\lambda]} \tag{3.4}$$

where the overlap V serves as a quantitative measure for the beam homogeneity. The position dependant spectral overlap (blue curves) and normalized integrated spectral intensities (green curves) for the x- and y-axis of the beam are shown in the right panel of Fig. 3.15. The retrieved overlap is $V_x > 94\,\%$ and $V_y > 92\,\%$ within the $1/e^2$ intensity of the integrated spectrum (represented by the dashed black lines in Fig. 3.15) indicating a good homogeneity of the central part of the spectrally broadened beam. The decrease of the calculated overlap towards the edges of the beam likely originates from inhomogeneous broadening in the second multipass-cell. Unfortunately, a more detailed, quantitative evaluation is hampered by the insufficient signal-to-noise ratio of the OSA

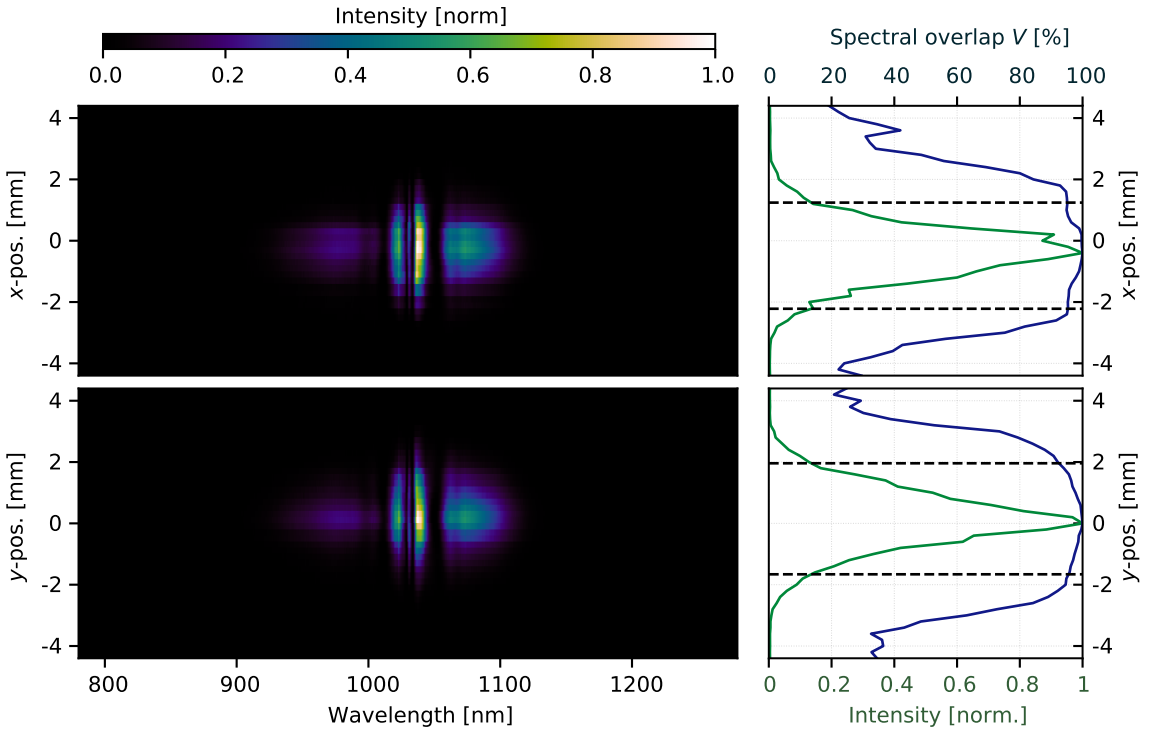

Fig. 3.15: Homogeneity measurement of the second spectral broadening stage. **Left panel:** recorded spectra vs. position. The spectra were recorded using a multi-mode fiber (400 µm core diameter) with FC/PC tip coupled to an OSA **Right panel:** calculated position dependent spectral overlap V (blue curves) and integrated spectral density (green curves). The dashed black lines indicate the $1/e^2$ level of the integrated spectral densities beyond which the accuracy of the measurement degrades due to the reduction in signal-to-noise ratio.

at low intensities. Calculation of the intensity weighted overlap factor yields an effective overlap of $\overline{V}_{eff} > 97.5\,\%$ for both the x- and y-axis of the beam which is lower than the typical effective overlap for single-stage broadening ($\overline{V}_{eff} > 99.2\,\%$ for 115 fs long pulses in reference [100]) but still excellent compared to alternative spectral broadening schemes such as the multi-plate approach ($\overline{V}_{eff} > 96.0\,\%$ for 27 fs long pulses in reference [105]). It should be noted that a deterioration of the beam homogeneity can likewise result in a reduction of the claimed peak power level [105]. However, the determination of the exact peak power would require a spatially resolved measurement of the pulse duration which is extremely difficult to achieve with high reliability. A further evaluation of the spatial dependence of the peak power is therefore beyond the scope of this thesis.

3.2.4 Conclusion

Table 3.1 provides a summarized overview over the evolution of the decisive laser parameters throughout the dual-stage pulse compression setup developed in this thesis. By cascading two nonlinear pulse-compression stages, a total temporal compression factor of 18.5 was achieved. The output pulses are compressed to a FWHM pulse duration of 15.6 fs which is the shortest pulse duration that has to date been realized using an all-bulk multipass spectral broadening scheme. The energy content of the compressed pulses' main feature is as high as 78 %, made possible by the careful tuning of the multipass-cell dispersion and the nonlinear interaction length. Despite the high per-pass nonlinear phase shifts in the second broadening stage, a good beam quality characterized by an M^2 factor ≤ 1.11 is achieved and a reasonable effective beam overlap of $\overline{V}_{eff} > 97.5\,\%$ can be preserved throughout the spectral broadening process. With a peak power exceeding 460 MW, the laser system constitutes an ideal, state-of-the-art front-end for the further investigation of post-compression techniques for reaching the regime of gigawatt-class few-cycle laser pulses at unprecedented high pulse repetition frequencies.

Laser parameter	Input	First compression stage	Second compression stage
P_{avg} [W]	120	107	101
FTL [fs]	283	67	15.2
τ_{FWHM} [fs]	288	71	15.6
Compression factor	N.A.	4	18.5
η_{comp} [%]	98	89	87
P_{peak} [MW]	34.6	117.6	463
M^2-parameter	<1.03	<1.04	<1.11

Table 3.1: Summarized overview over the evolution of the decisive laser parameters throughout the dual-stage pulse compression setup including average power (P_{avg}), the Fourier-transform limit (FTL), pulse duration (τ_{FWHM}), compression factor, compression efficiency (η_{comp}), peak power (P_{peak}), and the M^2-parameter.

3.3 Limitations of all-bulk multipass-cell-based spectral broadening

In the previous section, a nonlinear pulse compression scheme based on two cascaded multipass-cell spectral broadening stages has been introduced. By optimizing the dispersion environment and nonlinear interaction length inside the multiass-cells, the generation of cleanly compressed sub-20 fs pulses has been achieved. The realized 15.6 fs long pulses represent the current state-of-the art of all-bulk multipass-cell based pulse compression where the pulse duration corresponds to only ≈ 4.5 optical cycles for a center wavelength of 1030 nm. Nontheless, even shorter pulses with 1 - 3 optical cycles (3.4 fs - 10.3 fs at 1030 nm wavelength would be highly beneficial, for example, for the efficient generation of short wavelength mid-IR radiation via IPDFG, It should therefore be evaluated, whether even shorter pulse durations can be obtained using the presented all-bulk multipass-cell spectral broadening approach.

In principle, the reduction to even shorter pulse duration should be feasible by further increasing the total nonlinear phase shift $\Sigma\phi_{NL}$ accumulated during the nonlinear interaction in the multipass-cell assembly. In the experiment, the individual per-pass nonlinear phase shifts were however restricted to values ≤ 0.35 rad due to the rapid decrease of the output beam quality caused by strong spatio-temporal coupling which can be observed for larger values of ϕ^i_{NL}. Furthermore, in experiments where the number of passes was increased beyond $N = 22$ in the second multipass stage did not yield significant additional spectral broadening but typically resulted in damages of the utilized fused silica plate.

These damages are likely caused by a combination of slight mode-mismatching of the input beam with respect to the eigenmode of the second Heriott-cell as well as accumulated self-focusing that ultimately leads to beam collapse within the nonlinear medium. The origin of the corresponding excessive accumulated nonlinear phase shift is of a twofold nature. Firstly, the SPM-based spectral broadening induces a change in spectral shape which, even for Herriott-cells operated close to the zero-dispersion regime as used in this thesis, is transferred into a re-shaping of the temporal pulse profile during propagation through the multipass-cell. Secondly, uncompensated higher order dispersion components can accumulate during propagation in the quasi-waveguide and ultimately distort the temporal shape of the pulse. A similar effect has been observed in a numerical study on multipass-cell-based compression of radially and azimuthally polarized pulses conducted by H. Cao et al in 2019 [106]. The proposed remedy of transitioning to significantly shorter nonlinear media (a length of 500 µm was used for the fused silica window for the simulations in reference [106]) might help alleviate the influence of higher order dispersion components. However, achieving an effective GVD close to zero for such short nonlinear media would require a precision in the dispersive coating process of $\approx 1\,\text{fs}^2$ which can hardly be realized today for the required wide bandwidths and high reflectivities.

To date, compression to the few-cycle regime using the multipass-cell spectral broadening approach has therefore only been realized in gas-filled geometries where the accumulated dispersion naturally is much lower than in the all-bulk case [83, 84]. However,

the nonlinear refractive index of most gases is significantly lower when compared to bulk media. Consequently, the efficient pulse compression using gas-filled geometries typically requires pulse energies of at least several hundred microjoules, which makes the approach unsuitable for being driven directly by a thin-disk oscillator.

In the presented all-bulk case, pulse durations in the few-cycle regime can potentially be realized by adding a third Herriott-type spectral-broadening stage to the already existing ones. However, the low initial pulse durations of below 20 fs after the second compression stage will make the pulse propagation in a third stage even more susceptible to the detrimental dispersive effects described in the previous paragraphs. Additionally, temporal broadening of the pulse during propagation through the multipass-cell will be strongly enhanced as a result of the reduced input pulse duration (cf. section 1.1.3). When combined with the currently achievable precision of the dispersion control, this would likely cause the spectral broadening efficiency to deteriorate within only a few passes. Due to the high initial alignment complexity and the low remaining compression factor required to reach the few-cycle regime, this approach was not pursued any further in the scope of this thesis. Instead, two alternative post-compression techniques which mitigate the high requirements on the precision of the dispersion control were investigated and are presented in chapter 4.

3.4 Chapter summary

The results presented in this chapter underpin the importance of a rigorous dispersion control for all-bulk spectral broadening in Herriott-type multipass-cells. By meticulously tuning the mean GDD of the utilized multipass-cell mirrors as well as the per-pass nonlinear phase shifts of the nonlinear interaction, the efficient pulse compression in Herriott-cells driven by a high power thin-disk laser at around 1030 nm wavelength could be achieved.

By shifting the spectral broadening within the multipass-cells into the net-positive dispersion regime, significantly higher compression qualities could be realized when compared to the self-compression experiments presented in chapter 2. However, despite the improvement in compression quality, the attainable single-stage temporal compression factors are reduced by dispersion induced temporal broadening of the pulses during propagation in the quasi-waveguide — a limitation which can be overcome by cascading multiple spectral broadening stages with intermediate re-compression. Following this approach, a dual-stage compression setup based on multipass spectral broadening was developed. The presented front-end facilitates a temporal compression by a factor of 18.5 reaching a state-of-the-art FWHM output pulse duration of 15.6 fs. Due to the precise engineering of dispersion and nonlinear interaction length, a compression quality as high as 87 % could be achieved. The corresponding peak power of 463 MW is unprecedented for an amplifier-free thin-disk laser system. An excellent total power throughput of 84 % as well as a good beam quality characterized by an M^2 factor of < 1.11 were measured. A low spatio-spectral dependence of the output beam was verified by measuring the intensity weighted spectral overlap which is $\overline{V}_{eff} > 97.5\,\%$ for two perpendicular axes.

Ultimately, the achievable precision of the dispersion control was determined to be

the limiting factor for realizing even shorter pulse durations towards the few-cycle regime using an all-bulk multipass-cell based approach and alternatives are investigated in the next chapter.

4

Nonlinear pulse compression towards the few-cycle regime

4.1 Alternative all-bulk spectral broadening techniques

In the preceding two chapters, the investigations on spectral broadening of short laser pulses in Herriott-type multipass-cells have been presented in detail. In particular, the focus was placed on the dispersion management of multipass-cells containing a bulk nonlinear medium. Unfortunately, as discussed in section 3.3, the nonlinear pulse compression using this method is currently limited to pulse durations on the order of 15 fs. This limitation is mainly due to the available precision of the dispersive multipass-cell mirror coatings. More specifically the residual uncompensated positive GDD of the nonlinear medium causes a continuous temporal broadening of the laser pulse upon propagation through the quasi-waveguide operated in a net-positive dispersion environment. As a result, the peak power of the pulse steadily decreases with growing number of passes. In a properly mode-matched Herriott-cell, the effective beam size is the same for each pass through the nonlinear medium (cf. equation 2.31). Consequently, the peak intensity, which is directly related to the nonlinear phase via equation 2.26, decreases with each pass through the nonlinear medium. This ultimately results in a saturation of the spectral broadening process. Since the influence of dispersion on the temporal pulse profile grows with decreasing pulse duration (cf. section 1.1.3), this effect is even further enhanced for very short ($\tau_{FWHM} \leq 20$ fs) input pulse durations where the saturation of the spectral broadening is expected to set in after only a few passes through the nonlinear medium.

As described in the Herriott-cell spectral broadening fundamentals (section 2.2), a homogeneous spectral broadening over the entire beam profile merely requires the accu-

mulated nonlinear phase shift to be distributed over a sufficient amount of passes through a nonlinear medium with intermediate refocusing of the beam. Herriott-cells can facilitate this and allow many passes to be folded in a compact manner However, if only low temporal-compression factors — on the order of two to three — are targeted, the spectral broadening can already be realized in only a few (< 5) passes through a nonlinear medium, even if the per-pass nonlinear phase shift is required to stay below < 0.35 rad (cf. equation 1.110). For such a small number of passes, the effort and complexity of setting up a Herriott-type multipass-cell appears disproportionate. Furthermore, the limited flexibility in fine-tuning the per-pass dispersion and nonlinearity within the multipass-cell and the, correspondingly, induced saturation of the spectral broadening already in the first few passes through the nonlinear medium renders the multipass-cell approach inefffective for reaching even shorter pulse durations than 15 fs.

Fortunately, various alternative techniques for all-bulk spectral broadening are available, which could help further reduce the pulse duration of the dual-stage multipass-cell output. A few of these techniques will be presented and discussed in the following sections. A more comprehensive review of pulse-compression techniques can for example be found in reference [107] and references therein.

Single-plate spectral broadening

Already in the first publication on SPM-based all-bulk spectral broadening in the year 1987, C. Rolland and P. Corkum showed that spectral broadening towards sub-20 fs pulse durations can be realized by simply focusing a short laser pulse into a single optically transparent dielectric medium such as a fused silica plate [75]. However, for the rather high temporal compression factor of approximately five which was realized in reference [75], the large magnitude of spectral broadening was accompanied by a significant amount of conical emission and strong spatio-spectral inhomogeneity which is caused by the intensity variation across the beam profile (see sections 1.2.3 and 2.2.2). More specifically, the authors of reference [75] state that only a fractional amount on the order of 4 % of the total pulse energy, corresponding to the very central part of the initially Gaussian beam profile, was effectively compressed without large residual phase modulations after spatial filtering using a pinhole. It should be emphasized that the experimental conditions in reference [75] were chosen such that self-focusing of the laser beam inside the nonlinear material was considered negligible by choosing a nonlinear medium much shorter than the critical length for self-focusing.

In a more recent study on thin-disk oscillator driven spectral broadening by M. Seidel et al. [76], the influence of self-focusing on the spectral broadening process was analysed in further detail. By simulating the evolution of the beam caustic of laser pulses with a peak power beyond the critical power for self focusing P_{cr}, the authors of reference [76] found that significantly higher broadening efficiencies can be obtained if the nonlinear medium is placed in the divergent beam such that beam diffraction and self-focusing act together to maintain a small beam diameter throughout the nonlinear medium. When compared to reference [75], the homogeneously broadened fraction of the incident pulse energy could

also be vastly improved to around 60 % in the experiment where an initially 250 fs long pulse from an Yb:YAG thin-disk oscillator was compressed to 43 fs in a single crystal quartz plate. A similar approach has been used in reference [108] to compress the 17 fs long pulses of a fiber-broadened Yb:YAG thin-disk oscillator to the few cycle regime (< 10 fs) in a single crystal quartz plate. However, the efficiency in reference [108] was likewise limited to < 60 % by the emergence of spatio-temporal couplings, resulting in additional conical emission which was subsequently filtered by inserting a circular aperture into the beam.

Cascaded thin-plate spectral broadening

A different method for the temporal compression of laser pulses into the few-cycle regime which has gained a significant amount of interest over the recent years is based on the successive cascading of nonlinearities in thin bulk media. The approach, which was originally proposed and demonstrated in the context of continuum generation by C.-H. Lu et al. [109], is based on the following working principle: An intense laser pulse with a peak power several times higher than the critical power for self-focusing is focused into a thin (typically 50 µm to 2 mm) bulk medium. Due to the nonlinear interaction inside the dielectric medium, the beam is subject to strong spectral broadening and self-focusing. If the intensity and the length of the nonlinear medium are properly matched, self-focussing can overcome the natural beam diffraction and a new focus is created closely behind the nonlinear medium. By placing an additional nonlinear medium in the thus created focus, the process can continuously be repeated until the spectral broadening starts to saturate due to accumulated dispersion [109]. It should be noted that extremely high intensities are required in the bulk media in order to generate a sufficient amount of self-focusing to overcome the natural beam diffraction. Consequently, the nonlinear interaction becomes very complex and the resulting spectral phase can be difficult to compensate for. Specifically, for continuum generation, the formation of a weak but wide pedestal in the shorter wavelength part of the spectrum is commonly observed [109, 110]. While continuum generation can be used to rapidly broaden the pulse spectrum (see reference [107]), equivalently to the previously introduced single-plate spectral broadening techniques, the associated spectral broadening typically exhibits a strong spatial dependence in the form of conical emission which impairs the compression quality as a result of strong space-time couplings [110]. Therefore, the output of cascaded thin-plate broadening schemes often requires appropriate filtering of the central part of the beam using a pinhole before further use [109]. A more comprehensive introduction to the cascaded thin-plate technique can e.g. be found in reference [111], which also provides basic criteria for optimum plate thickness, peak intensity of the input pulse and position of the individual thin plates for the case of broadband continuum generation which are based on numerical simulations.

To date, the cascaded thin-plate spectral broadening approach has successfully been used for continuum generation and subsequent temporal compression with a variety of different input pulse durations, peak power levels and pulse repetition rates [109, 112–117]. While cascaded thin-plate spectral broadening in two stages has been shown to facilitate pulse compression to the few-cycle regime [115–117], large compression factors —

when realized using only few plates — commonly introduce strong space-time couplings and conical emission which can reduce the efficiency to below 60 % [109]. Furthermore, the compression quality is often sub-par with a significant amount of the pulse energy being contained in satellite pulse [115]. Only recently, an in-depth investigation of the spatio-temporal coupling effects in a cascaded thin-plate spectral broadening has been presented by S. Zhang et al. in reference [118]. In their publication, pulse compression down to 22 fs was achieved with high spatio-spectral homogeneity by distributing the nonlinearity over 15 individual fused silica plates forming a periodically-layered Kerr-medium.

It should be noted that, while the cascading of thin plates is a very active field of research, the focus has so far almost exclusively been placed on the spectral broadening of pulses with high pulse energy (typically hundreds of microjoules) and kilohertz repetition rates. Only recently it has been shown by C.-L. Tsai et al. that the concept is likewise applicable for spectral broadening at megahertz repetition rates with pulse energies in the range of few tens of microjoules [105]. In reference [105], the output of a high-power thin-disk oscillator was first compressed to a pulse duration of 88 fs using a Herriott-type multipass-cell. The pre-compressed output was subsequently sent into a sequence of four thin fused silica plates (1 to 3 mm thickness) which spectrally broaden the pulse to a bandwidth limited pulse duration of 27 fs. While a good compression quality with pulse duration close to the transform-limit is reported, the beam shows first signs of the typical conical emission reducing the available peak power of the pulses. Nevertheless, since the amount of conical emission is still well controlled, a high spatio-temporal homogeneity of the beam is reported. In reference [105] it is further shown that spectral broadening towards a bandwidth-limited pulse duration of 5 fs can be achieved by adding one more spectral broadening stage consisting of five additional fused silica plates. However, no spatio-spectral analysis or compression results are reported to this point [105].

In a recent collaboration headed by G. Barbiero [119] it could be shown that spectral broadening in cascaded thin sapphire plates can be used to efficiently generate pulses as short as 8.5 fs when driving the multi-plate scheme with microjoule pulse energy and sub-20 fs pulse durations — parameters, which are closely comparable to the output of the dual-stage multipass-cell arrangement presented in chapter 3. Despite the already realized high quality pulse compression with more than 64 % of the energy in the main peak, a high homogeneity of the thin-plate broadening scheme output has yet to be confirmed experimentally. Furthermore, since the method relies on nonlinearly induced self-focusing for creating the individual successive focii, high peak intensities and a precise positioning of the individual plates are indispensable. This makes the approach susceptible to damages as a result of catastrophic self-focusing caused by fluctuations in laser power. Moreover, it complicates the systematic optimization and daily reproducibility of the system. In the frame of this thesis it was therefore investigated whether the inherent limitations of the multi-plate scheme can be overcome by utilizing a different approach named the *distributed quasi-waveguide (DQWG)*, which is presented in detail in the following sections.

4.2 The distributed quasi-waveguide concept

The distributed quasi-waveguide (DQWG) concept is derived from the working principle of Herriott-cells and is based on a simple re-focusing geometry constructed from concave mirrors with individual nonlinear media placed in between them and i schematically dpeicted in Fig. 4.1. In detail, the DQWG is based on the following design principle: In analogy to spectral broadening in Herriott-type multipass-cells, a concave mirror with large radius of curvature is used to create a loose focus of an initially collimated input beam. In comparison to the Herriott-type multipass-cell, this process can be identified as the mode-matching mechanism for the DQWG. By positioning a nonlinear medium in the focused beam, the propagating pulses experience a nonlinear phase shift due to SPM which results in spectral broadening of the input pulse. Similar to in a Herriott-cell, the nonlinear phase shift is kept low to avoid spatial degradation due to self-focusing and aberrations of the induced Kerr-lens [120]. In the experiment, the nonlinear phase shift can easily be adjusted, for example by varying the length of the nonlinear material or its axial position along the beam caustic (cf. equation 2.26). It is furthermore considered preferable to place the nonlinear medium in the divergent beam after the beam waist (cf. Fig. 4.1), where the residual effect of Kerr-lensing is counteracted by the natural beam diffraction, helping to reduce the risk of beam collapse due to critical self-focusing [76].

Since a nonlinear phase shift that does not cause strong self-focusing will also be too weak for significant spectral broadening, the process needs to be repeated multiple times to reach the desired bandwidth. In analogy to spectral broadening in Herriott-cells, a spatio-spectral homogenization is expected to occur during this process, if the beam is allowed to intermittently propagate without being influenced by nonlinear spatial effects before being refocused into an additional nonlinear medium by a focusing element [29]. In the DQWG, in contrast to the thin-plate approach, this focusing element is realized in the form of a second concave mirror that reflects the beam at a small horizontal angle to the incident beam. The distance between focus and refocusing mirror for which a self-similar nature of the beam caustic over many passes through the DQWG is obtained can be determined by solving equation 2.10 for d. As a result, the propagating beam matches the eigenmode of a stable resonantor if the second mirror is placed at exactly a distance d_f to the initially created focus given by

$$d_f = \frac{1}{2}\left(R + \sqrt{R^2 - \left(\frac{2\pi w_{0,in}^2}{\lambda}\right)^2}\right) \tag{4.1}$$

where R is the radius of curvature of the second focusing mirror, $w_{0,in}$ is the beam size in the first focus and λ is the central wavelength of the spectrum, a second focus with identical waist as the first focus is generated at, again, a distance d_f to the second focusing mirror. By placing additional refocusing mirrors at a relative separation distance of $2d_f$ to each other, this process can be repeated for an arbitrary amount of passes. When placing a separate nonlinear medium in each of these passes, a high total nonlinear phase $\Sigma\phi_{NL}$ can be accumulated while a low per-pass phase shift in the individual passes is maintained.

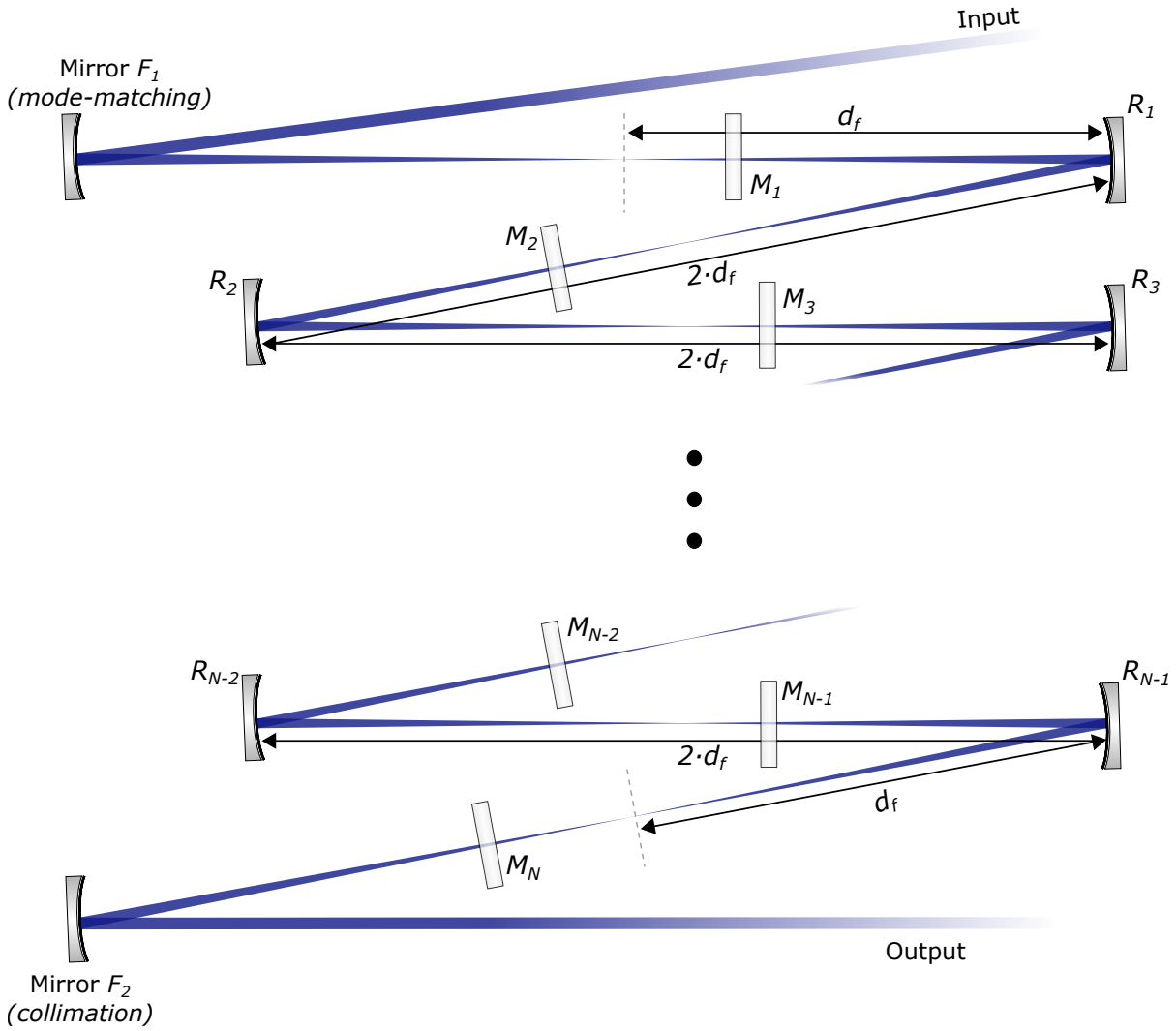

Fig. 4.1: Schematic depiction of the distributed quasi-waveguide (DQWG) concept. A collimated input beam is focused by a concave mirror F_1, which serves as the mode-matching element of the DQWG. To spectrally broaden the pulse, a nonlinear medium M_1 is placed in the divergent beam in close vicinity to the created focus. The beam is subsequently refocused to the same waist size by placing an additional concave mirror R_1 with smaller radius of curvature than F_1 at a distance of d_f, which is given by equation 4.1, to the initial focus. The process can be repeated multiple times by inserting additional focusing mirrors (R_2 – R_{N-1}) with identical radius of curvature spaced at a distance of $2 \cdot d_f$ to each other. Ultimately, the beam is collimated using a final concave mirror F_2. Since the position, material and thickness can be varied for each of the individual nonlinear media M_1 – M_N, both nonlinearity and dispersion can be separately optimized for each pass in the DQWG.

After the spectrum has been broadened to the desired bandwidth, the beam can easily be collimated to a suitable beam size with a collimation mirror.

A DQWG which is designed following the above principle therefore exhibits a modal structure which is equivalent to that of a perfectly mode-matched Herriott-type multipass cell consisting of two mirrors of radius of curvature R which are placed at a separation distance of $2d_f$. Consequently, the spatio-spectral homogenization is expected to work similarly for DQWGs and multipass-cells. This claim is further supported by early investigations on spectral broadening in quasi-waveguide assemblies which were performed by J. Brons in the frame of his dissertation, where an efficient compression of initially 140 fs pulses to a pulse duration of 30 fs was achieved with high spatio-spectral homogeneity. In this experiment, two individual DQWGs consisting of 9 passes distributed over 5 seprate fused silica plates were cascaded with an intermediate re-collimation and temporal re-compression between the first and second DQWG [121].

Since the DQWG is derived from the Herriott-cell concept, it can likewise be tuned to operate in the different dispersion regimes introduced in section 2.2.2 by adjusting the dispersion parameters of the utilized focusing mirrors. More specifically, the operation of a DQWG in the net-positive dispersion regime is expected to yield the same linearization of the accumulated positive chirp which has previously been shown to facilitate a high temporal compression quality [40]. However, since the beam does not trace a closed path between two mirrors but continuously propagates in a forward direction, the position of the nonlinear medium can be optimized individually for each pass through the DQWG. In contrast to Herriott-type multipass cell spectral broadening, the nonlinear phase shift can therefore likewise be tailored in each individual pass through the separate nonlinear media. This way, any reduction of peak power caused by temporal broadening during the extended propagation can be counteracted by decreasing the beam size in the nonlinear medium such that a fixed nonlinear phase shift is maintained during the propagation in the DQWG — even for the dispersion-sensitive short input pulses.

4.3 Proof-of-concept experiment

4.3.1 Distributed quasi-waveguide parameters

In order to confirm the applicability of the DQWG approach to short input pulse durations and operation in the net-positive dispersion regime, a proof-of-concept experiment was conceived. The experiment is aimed at further compressing the approximately 15 fs long pulses generated by the dual-stage Herriott-type multipass-cell spectral broadening experiment presented in chapter 3 to pulse durations on the order of 10 fs without introducing a significant degradation of the spatial beam quality or spatio-temporal homogeneity.

The experimental setup of the DQWG is shown in Fig. 4.2. Before the input of the DQWG, a 3 mm thick fused silica plate is inserted into the collimated beam at the compressed output of the second broadening stage. This additional material is required to introduce a slight positive pre-chirp to the incident pulse in order to avoid spectral nar-

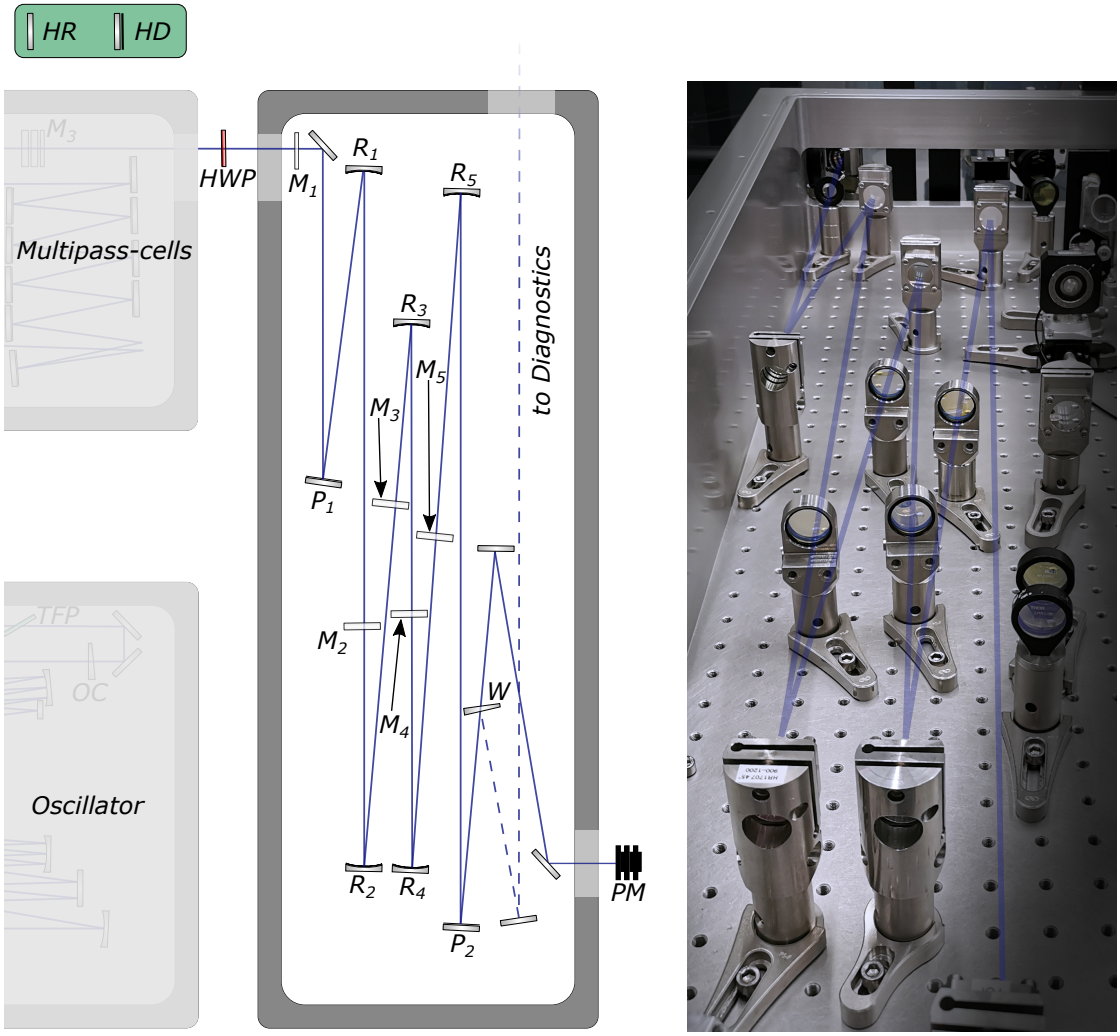

Fig. 4.2: Left: Schematic of the DQWG spectral broadening setup. The beam enters the experimental chamber from the output of the dual-stage multipass-cell system described in section 3.2 where the dispersive mirror P_1 is the last components in the chirped-mirror compressor after the second-stage. The DQWG follows the design principle described in section 4.2 and is described in further detail in the text. The abbreviations are: M_1, 3 mm-thick fused silica plate for additional dispersion compensation; R_1, focusing mirror with a radius of curvature of 1000 mm (PC1711) for creating the initial focus of the DQWG; R_1-R_4, re-focusing mirrors with a radius of curvature of 300 mm (PC1711), R_5, collimating mirror with a radius of curvature of 900 mm (PC1711), P_2, highly-dispersive plane compressor mirror (PC1611); M_2-M_5, 6.35 mm-thick, broadband AR-coated fused silica plates; W, removable, uncoated fused-silica wedge; PM, power meter. **Right:** Picture of the DQWG assembly. The beam bath is schematically depicted in blue. All components were implemented in the most rugged way available to facilitate a high stability of the setup.

rowing in the first pass in the DQWG. The initial pass in the DQWG is then formed by placing a concave mirror with 1000 mm radius of curvature into the collimated beam. The subsequent concave focusing mirrors have a radius of curvature of 300 mm and are equipped with the same broadband dispersive mirror coating which has previously been used for the second Herriott-cell broadening stage and which was introduced in Fig. 3.12. For determining the separation distance of the subsequent DQWG mirrors according to equation 4.1, knowledge over the waist size of the initial pass through the DQWG is required. Consequently, the beam caustic around the focus was measured using a scanning-slit beam profiler (Ophir NanoScan 2s Pyro/9/5 µm). For the measurement, one of the second-stage compressor mirrors was temporarily replaced with an uncoated fused silica wedge to avoid damage to the beam profiler while maintaining the propagation direction of the incident beam. The measured $D4\sigma$ beam width in the focus is 267 mm (averaged over two orthogonal axes) which yields a waist size of 128 µm of the embedded Gaussian beam (compare section 1.1.2) for an average M^2 value of 1.09 (cf. Fig. 3.14). Consequently, the first focusing mirror is placed at a distance of 291 mm to the initial focus while the subsequent mirrors are positioned at a relative separation distance of 583 mm to each other (the values were determined using equation 4.1). Ultimately, the beam is re-collimated using another concave mirror with 900 mm radius of curvature placed at a distance of 450 mm to the last focus. In total, four passes are thus realized in the DQWG.

Spectral broadening inside the DQWG is realized by inserting fused silica plates as nonlinear media into each pass of the DQWG (cf. Fig 4.2). The individual plates have a thickness of 6.35 ± 0.2 mm [103], corresponding to a GDD of 120 fs^2 specified at a central wavelength of 1030 nm. It is easily seen that for the 6.35 mm long fused silica plates, equation 2.29 does not hold for the short input pulse durations of approximately 15 fs. Consequently, the pulses are expected to be temporally broadened even during a single transition through a nonlinear medium. The comparatively long nonlinear interaction length was purposefully chosen to maximize the linearisation of the accumulated chirp during spectral broadening, since the nonlinear interaction thus takes place in a positive dispersion environment similar to the propagation of pulses in single-mode silica fibers [40].

4.3.2 Spectral broadening in a distributed quasi-waveguide

Since, for short pulses, dispersive effects cannot be neglected even during the propagation through one plate, the calculation of the per-pass nonlinear phase shift requires precise knowledge over both the beam caustic and evolution of the temporal profile within the nonlinear medium in order to solve equation 2.26. However, since the beam is at the same time subject to diffraction, residual self-focusing effects and temporal broadening, this knowledge can only be obtained by properly modelling the propagation and numerically solving a spatially resolved version of the GNLSE given in equation 1.117. Unfortunately, no suitable framework for performing these simulations was available at the time of the experiment. Consequently, the a-priori calculation of the spectral broadening factor according to equation 1.110 was omitted and the spectral broadening was optimized based on an empirical experiment, instead.

Spatio-spectral evolution

To achieve an even distribution of the spectral broadening over the four passes formed by the DQWG, a reduction of the Fourier-transform limit of 10 % is targeted for each pass. After inserting the first fused silica plate, its position was optimized by gradually reducing its distance to the beam waist position while monitoring the spectrum in a low power beam using an OSA. The low power beam was obtained by temporarily replacing the first re-focusing mirror with 300 mm radius of curvature by a plano-concave mirror with 600 mm radius of curvature which approximately collimates the divergent beam after the first focus. This collimating mirror is placed under a slightly different incident angle which allows the beam to be coupled out of the DQWG. A small fraction of the power can thus be split-off the main beam for diagnostics using the surface reflection off of an uncoated fused silica wedge.

For the first pass, the corresponding amount of spectral broadening is reached when the fused silica nonlinear medium is positioned at a distance of approximately 105 mm to the waist position (cf. Fig. 4.3 a). The peak intensity incident on the fused silica plate is approximately 270 GW cm^{-2}. To obtain a first assessment of whether the spectral broadening in the first plate adversely affects the beam quality, the M^2 value was measured. It takes an average value of 1.13, measured over two orthogonal axes. The slight decrease in beam quality when compared to the output of the dual-stage Herriott-cell spectral broadening ($M^2 = 1.09$) can be attributed to the non-uniformity of the accumulated nonlinear-phase across the beam profile [120].

The optimization process was repeated for the subsequent three passes where the optimum distances from the beam waist to the fused silica plate was determined to be 80 mm for both the second and third pass and 50 mm in the fourth pass through the DQWG. The reduced optimum distances from beam waist to nonlinear medium when compared to the first pass in the DQWG can be explained as follows: During each pass through one of the nonlinear media, the pulse accumulates a positive chirp as a result of the nonlinear interaction and material dispersion which causes a temporal broadening of the pulse. After a subsequent propagation through air, the beam is refocused by a concave mirror. However, the dispersive mirror coating is designed such that the positive chirp which is accumulated during the previous propagation through the fused silica plate is only partially removed (cf. section 3.1). As a result of the residual temporal broadening, the pulse duration in the next pass of the DQWG is slightly longer and the peak power is slightly lower, correspondingly. To maintain a fixed peak intensity, the reduction in peak power therefore needs to be counteracted by reducing the effective area inside the nonlinear medium which, in the experiment, is realized by moving the subsequent fused silica plate slightly closer to the focus than the previous one. It is interesting to note that in contrast to the expected linear reduction of the distance, the position of the second and third medium with respect to the corresponding beam waists is almost identical. While no further investigations were undertaken to verify the exact cause, this behaviour is assumed to be due to the dispersive focusing mirror after the second pass having a slightly larger negative GDD than the other mirrors. This results in a peak power which is approximately similar in the second and

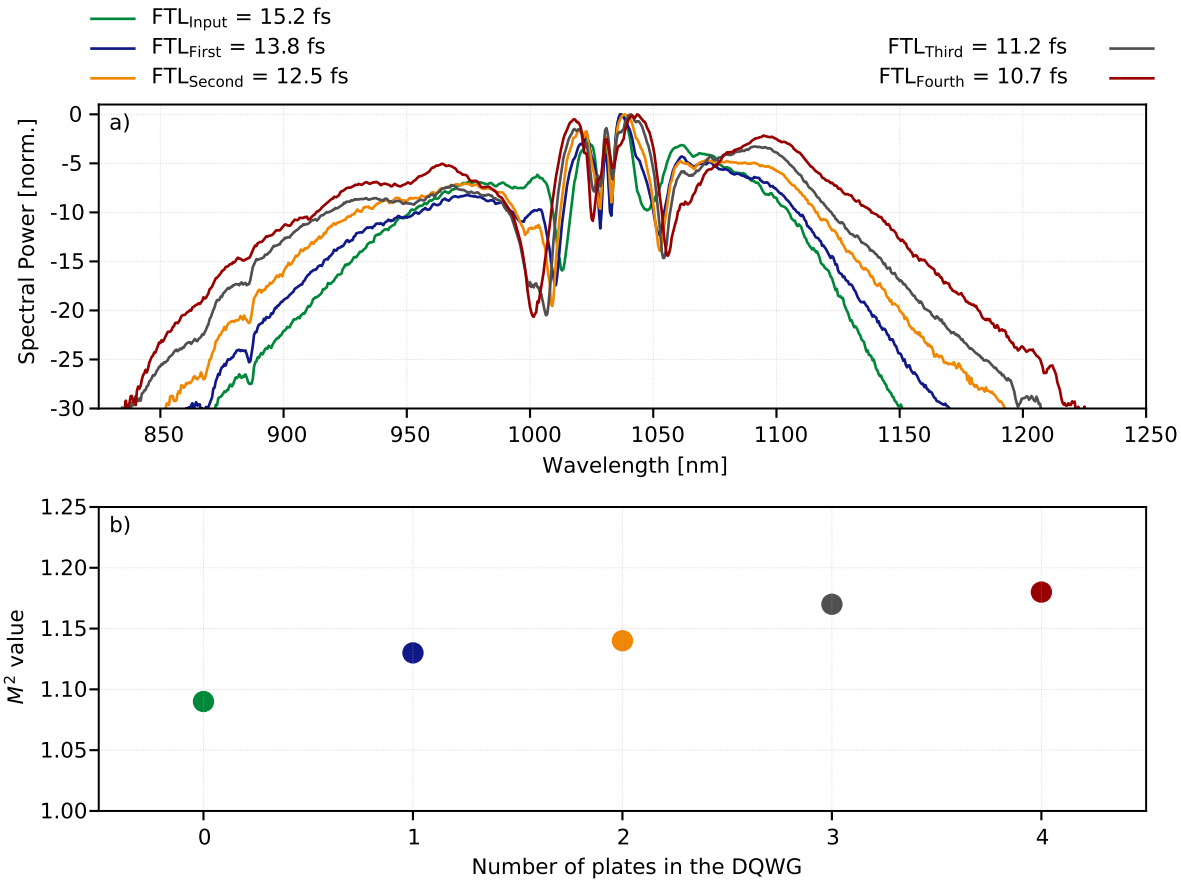

Fig. 4.3: Spatio-spectral evolution in the distributed quasi-waveguide. **a)** Spectral measurement at the DQWG output using an OSA for varying number of fused-silica plates. **b)** Corresponding M^2 value. The measurements were performed using a scanning slit beam profiler (Ophir NanoScan 2s Pyro/9/5 µm). The data sets in subfigures a) and b) follow the same color coding for easy mapping of spectrum and M^2 value.

third pass in the DQWG.

The corresponding spectra for the collimated output after two, three and four passes are shown in Fig. 4.3 a. For the second and third pass, the spectral broadening inside each fused silica plate reduces the Fourier-transform limited pulse duration by 1.3 fs. At the same time, the M^2 factor increases slightly further to 1.14 and 1.17 after the second and third pass, respectively. After four plates, a bandwidth limited pulse duration of 10.7 fs is reached with a final M^2 factor of 1.17. It should be noted that the fourth pass of the DQWG only reduces the Fourier-transform limited pulse duration by 0.5 fs which is significantly less than the target 10 % of the FTL. Shifting the fourth plate even closer towards the beam waist did not yield a further enhancement of the broadening factor but resulted in damage to the fused silica plate. A potential cause for the saturation of the spectral broadening might lie in the dispersion environment of the DQWG. In the preceding discussion, the accumulated effect of dispersion and nonlinear interaction was assumed to cause a temporal broadening of the pulse which results in a reduction of the peak power. However, as introduced in section 1.1.3, for a non-Gaussian temporal pulse shape the effect of dispersion will not only affect the pulse duration but also the temporal shape of the pulse. Especially in the case of strongly modulated spectra as they are generated by SPM-based spectral broadening, the pulse shape can quickly deteriorate under the influence of accumulated dispersion — forming strong temporal oscillations once a sufficient amount of chirp is accumulated. This, in turn, can lead to a rapid reduction of the peak power and, consequently, the amount of spectral broadening.

In the DQWG, the pulse accumulates a certain amount of positive dispersion during the propagation through the first three plates, each followed by an incomplete chirp removal by the subsequent focusing mirrors. Consequently, the pulses entering the fourth plate are already positively pre-chirped. It is therefore likely that in the fourth fused silica plate, only a small fraction of the total length of the material contributes to the spectral broadening since the pulse shape is excessively distorted already within a short propagation through the medium. As a result, the nonlinear phase shift which in the first plate is distributed over the entire length of a 6.35 mm long fused silica plate, needs to be accumulated in only a small fraction of the propagation distance. When compensating the reduced effective interaction length by increasing the peak intensity (for example by moving the medium closer to the focus), self-focusing becomes more pronounced as well, which correspondingly reduces the focal length of the generated Kerr-lens. Once the focal length becomes too short, the generated focus will lie within the fused silica plate and the beam can collapse which ultimately causes damage of the nonlinear medium.

The suspected reason for the saturation of spectral broadening mentioned above could potentially be verified by measuring the temporal shape of the pulse after each individual pass in the DQWG or by simulating the evolution of the temporal pulse shape and beam profile using a suitable numerical approach. If the saturation can be confirmed to originate from the accumulated positive dispersion, countermeasures could include the optimization of the mirror coating to suppress excessive distortions of the temporal beam shape. If the mirror coating cannot be optimized further, an intermediate re-compression of the pulse could help in removing the residual accumulated chirp to increase the effective interaction

length in sbusequent nonlinear media. For lowering the susceptibility to damage, the use of thinner nonlinear media could be advantageous since shorter focal-lengths of the generated Kerr-lens could be tolerated without resulting in self-collapse of the beam.

4.3.3 Output characterization and compression results

To conclusively evaluate the performance of the presented DQWG, the spectrally broadened output beam was thoroughly characterized. To do so, the beam is collimated by the previously mentioned concave mirror with 900 mm radius of curvature which features the same coating as the other focusing mirrors inside the DQWG. The pulses are subsequently compressed using a plane dispersive mirror with a GDD of $-150\,\mathrm{fs}^2$ (PC 1611, see P_2 in Fig. 4.2).

At a full input power of 101 W (measured after the compressor of the second broadening stage, see section 3.2.3), an output power of 100.4 W could be measured at the output of the DQWG, corresponding to a remarkable optical efficiency of $> 99\,\%$. The superb efficiency of the DQWG can be attributed to the high quality AR-coating on the fused silica plates as well as the low reflections losses of the focusing mirrors. The long-term stability of the average power of the full setup was measured over one hour with a resolution of 10 Hz and is shown in Fig. 4.4. A normalized RMS deviation of 0.134 % was recorded which is equivalent to the stability of the driving oscillator itself. It should be emphasized that the spectral broadening in the DQWG could equivalently be maintained over much longer time-scales of up to several hours at a time. Additionally, a similar performance of the DQWG was achieved for multiple successive days without any re-alignments except for the daily optimization of the driving oscillator during its thermalization period.

By placing an uncoated fused silica wedge in the collimated beam, a small fraction of the full beam power can be split off for further characterization. The relative intensity noise (RIN) of the spectrally broadened DQWG was measured using a similar method as described in reference [95, p. 49]. An integrated root-mean-square intensity noise of 0.092 % was measured in the range from 10 Hz to 1.25 MHz, which is about three times higher than the RIN of the driving oscillator. Closer evaluation of the recorded noise traces revealed, that the additional noise is mostly added in the acoustic frequency range between 10 Hz to 20 kHz as well as in a sharp noise peak centred at around 22 kHz which is already visible in the noise spectrum of the driving oscillator. The additional noise likely stems from an enhancement of the incident noise during the nonlinear interaction in the three cascaded compression stages such as it has previously been observed for continuum generation in fibers [122]. It should be emphasized that while the RIN of the broadened spectrum is significantly higher than that of the driving oscillator, the absolute noise value is still well comparable to other ultrafast systems [24, 72]. Further reduction of the RIN can potentially be achieved by utilizing active noise suppression techniques such as presented in reference [24] or by meticulously optimizing the noise-properties of the driving oscillator e.g. via mechanical de-coupling from the ambient environment.

The spectral and temporal shape of the compressed pulses was characterized using the SPIDER technique and is shown in Fig. 4.5. Both the spectral shape and Fourier-

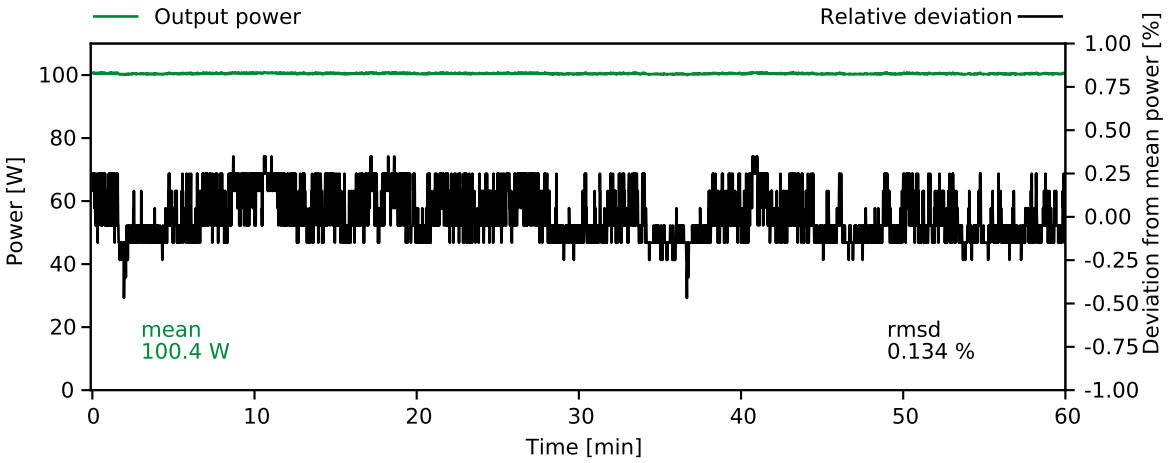

Fig. 4.4: Output average-power stability of the distributed quasi-waveguide and its root-mean-square-deviation (rmsd) measured over one hour with 10 Hz sampling frequency. The measurements was taken after a thermalization period of approximately 30 minutes.

transform limit of 10.7 fs retrieved from the SPIDER measurement are in good agreement with an additional spectral measurement performed using an OSA. The spectrum exhibits a similar shape to those obtained using the Heriott-type multipass-cell spectral-broadening approach, indicating that the spectral broadening is governed mostly by the effect of SPM. For the DQWG, compression to a pulse duration of 10.8 fs is achieved which is close to the bandwidth-limited pulse duration of 10.7 fs. The temporal compression factor of the DQWG is 1.44, which is slightly below the targeted factor of 1.5. Nevertheless, the DQWG approach shown here facilitated compression of laser pulses into the few-cycle regime; the output pulse duration of 10.8 fs corresponds to approximately 3.2 optical cycles at a center wavelength of 1030 nm. Most importantly, however, the compression quality is not significantly impaired when compared to the results of the dual-stage Herriott-cell broadening scheme (compare Fig. 3.13). By comparing the area under the main peak (grey shaded area in Fig. 4.5 b) to the total area under the curve, the main pulse is found to contain more than 75 % of the pulse energy which is well comparable to the input energy fraction of 78 %. As a result of the high compression quality, a peak power of 0.64 GW is reached, which is a factor of 1.38 higher than at the input of the DQWG. To the author's knowledge, this is the highest peak power that has to date been realized in any amplifier-free thin-disk system and constitutes the first demonstration that thin-disk oscillators can be compressed to gigawatt-scale peak powers without additional amplification. The compression quality, which is calculated as the ratio of the calculated peak power to the peak power of a bandwidth-limited pulse according to equation 2.27 is 87 %. This value is identical to the compression quality of the dual-stage multipass-cell output and further indicates a low amount of uncompensated spectral phase components — verifying the high quality of the additional temporal compression.

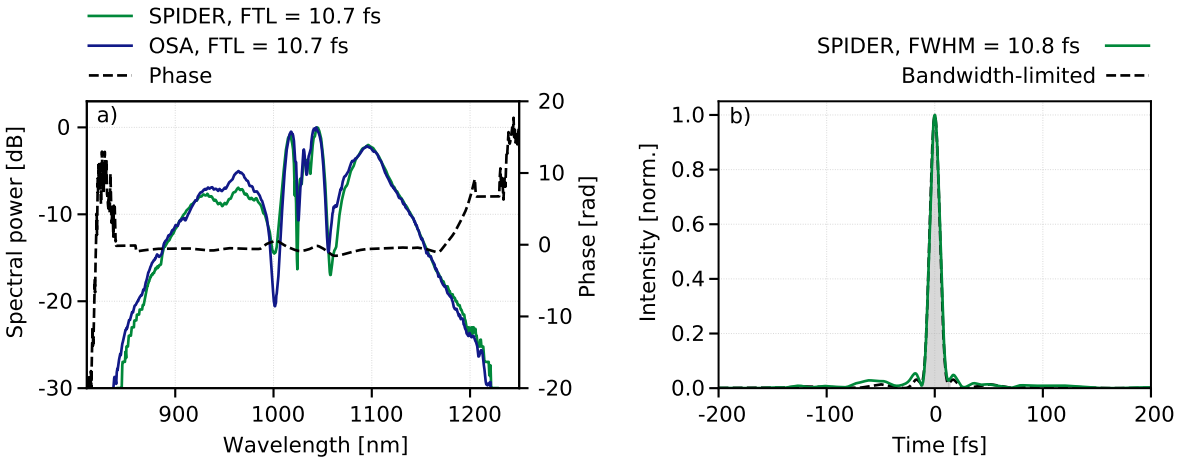

Fig. 4.5: Spectral and temporal characterization of the distributed quasi-waveguide output. **a)** Retrieved spectral phase and intensity from the SPIDER measurement compared to reference measurement from an OSA. **b)** Measured intensity profile compared with the bandwidth-limited pulse shape determined by Fourier-transformation of the spectrum. The grey shaded area denotes the main part of the beam; 75 % of the total energy are contained within it.

In the previous section, the spatial quality of a beam propagating through the DQWG was observed to steadily decrease with the number of passes in the DQWG (see Fig. 4.3). The M^2 measurement of the final compressed DQWG-output is shown in Fig. 4.6. The M^2 factor of the beam is 1.16 in the transversal and 1.18 in the sagittal plane, respectively. As indicated in the previous section, the decrease of beam quality is expected to originate from aberrations of the Kerr-lens, which are imprinted on the incident beam during the extended propagation through the nonlinear media [120]. Nevertheless, the overall beam quality is still on a comparable level to the typical M^2 factor of approximately 1.15 obtained for thin-disk oscillator spectral broadening in Herriott-type multipass cells [81, 105]. The good quality of the output beam is further supported by the measurement of the beam-profile in the collimated beam (inset in Fig. 4.6). Importantly, it shows no strong signs of conical emission as often observed for bulk-spectral broadening with excessive per-pass nonlinear phase shift. Consequently, this already indicated a high spatio-spectral homogeneity [76, 108].

To further assess whether the observed degradation of the beam quality factor is translated into spatio-spectral couplings, the beam homogeneity was measured using the method described in section 2.3.2. However, in order to increase the resolution of the measurement, the step-size of the homogeneity scan was reduced to 0.1 mm. Furthermore, the scanning range was slightly extended to 15 mm per axis (corresponding to 2×150 spectra) to ensure that no spectral components in the far wings of the beam remain undetected. The recorded spectra as a function of the axial position for two orthogonal axes are shown in the left panel of Fig. 4.7. In analogy to section 2.3.2, the overlap V with the spectrum on the

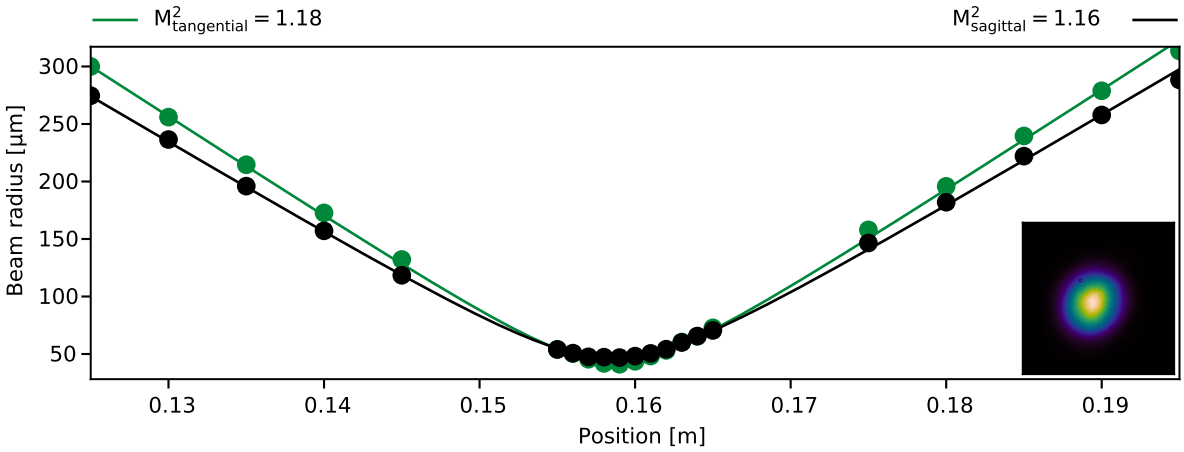

Fig. 4.6: M^2-measurement of the distributed quasi-waveguide output according to ISO 11146-1 [31]. The measurement was performed using a scanning slit beam profiler (Ophir NanoScan 2s Pyro/9/5 µm). Inset: beam profile of the collimated beam showing no strong signs of additional conical emission (compare to last frame in Fig. 3.5). The beam profile was recorded using a Cinogy CinCam CMOS-1203 beam profiler.

beam axis was calculated for each spectrum using equation 3.4. It is shown in the right panel of Fig. 4.7 (blue curves) together with the normalized integrated spectral intensities (green curves) for both the x- and y-axis of the beam. The retrieved overlap is $V_x > 90\,\%$ and $V_y > 92\,\%$ within the $1/e^2$ intensity of the integrated spectrum as indicated by the dashed black lines. The measured spectral overlap is very comparable to the result after the dual-stage Herriott-type multipass-cell ($V_x > 94\,\%$ and $V_y > 92\,\%$) and proofs that the DQWG concept facilitates a good homogenization of the spectral broadening if the nonlinear phase shift is distributed over a sufficient amount of passes through a nonlinear medium. The intensity weighted overlap factor of the DQWG output is $\overline{V}_{eff} > 98.4\,\%$ for both the x- and y-axis of the beam, which is slightly higher than that of the input beam. While the reason for this was not systematically investigated further, the difference in the intensity weighted overlap factor could originate from a re-shaping of the spatial beam profile from a Gaussian-shape towards a Townes-like profile, as a result of accumulated self-focusing in the DQWG as previously discussed for bulk media and hollow-waveguides in reference [123]. Since the Townes-profile exhibits a steeper roll-off of the intensity towards the wings of the beam, the homogeneously broadened central section of the beam would gain a stronger impact for the calculation of the intensity-weighted overlap factor.

It should be emphasized that the DQWG approach is best suited if only low compression factors smaller than two to three are required, since the number of focusing optics continuously grows with the necessary amount of spectral broadening, which in turn increases the system size and complexity. Pulse compression using a DQWG consequently provides a suitable means of reaching the few-cycle regime with pulses that have previously

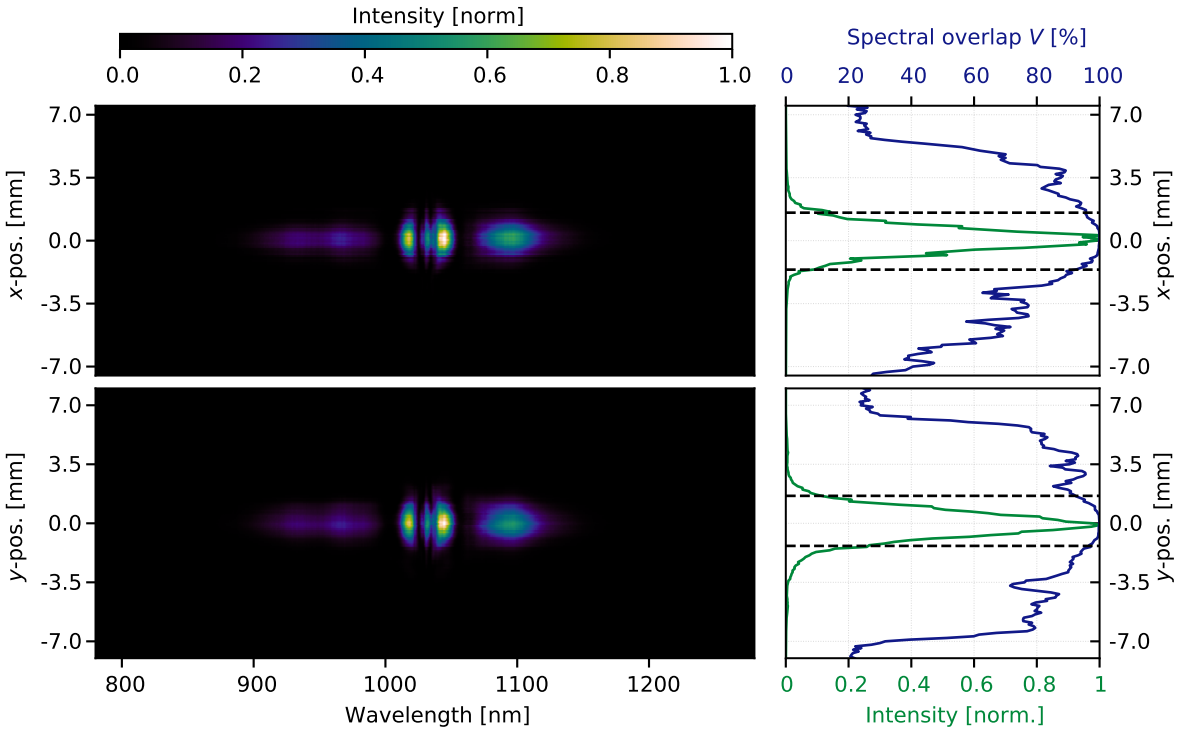

Fig. 4.7: Homogeneity measurement of the distributed quasi-waveguide output. **Left panel:** recorded spectra vs. position. The spectra were recorded using a multi-mode fiber (400 µm core diameter) with FC/PC tip coupled to an OSA. **Right panel:** calculated position dependent spectral overlap V (blue curves) and integrated spectral density (green curves). The dashed black lines indicate the $1/e^2$ level of the integrated spectral densities beyond which the accuracy of the measurement degrades due to the reduction in signal-to-noise ratio. The spectral overlap is $> 90\,\%$ within the $1/e^2$ intensity of the integrated spectra.

been compressed to ≈ 20 fs, by, for example, using multipass-cell- or fiber-based spectral broadening. Further compression to pulse duration close to the single-cycle regime appears feasible by implementing additional DQWG stages.

4.4 Chapter summary

In this chapter, the concept of spectral broadening in distributed quasi-waveguides (DQWGs) has been introduced. The DQWG represents a method for homogeneously broadening the spectrum of a laser pulse over its entire beam profile by distributing the underlying effect of SPM over a sufficient amount of passes through a nonlinear medium and with intermediate re-focusing of the beam. By designing the DQWG to mimic a stable resonant structure, a comparable homogenization to spectral broadening in Herriott-type multi-pass cells is facilitated. However, in contrast to multipass-cell based spectral broadening, the use of individual nonlinear media for each pass in the DQWG permits an optimization of the individual per-pass nonlinear phase shifts. This property of DQWGs can be used to mitigate the stringent requirements on dispersion control which constitute a key limitation for reaching the few-cycle regime in multipass-cell based spectral broadening techniques.

In a proof-of-concept experiment, spectral broadening in a DQWG has been utilized to spectrally broaden the 15.6 fs long output pulses of the previously introduced dual-stage multi-pass system (cf. chapter 3) to a Fourier-transform limit of 10.7 fs in a sequence of four individual fused silica plates. Pulse compression to the few-cycle regime was achieved with a chirped mirror compressor yielding an output pulse duration of 10.8 fs. By operating the DQWG deep in the positive dispersion regime, an excellent compression quality is maintained with more than 75 % of the pulse energy being contained in the main peak and a calculated compression efficiency of 87.6 % (cf. equation 2.27). Owing to an excellent optical efficiency exceeding 99 % as well as the high compression quality, a peak power of 0.64 GW is reached at the output of the DQWG. To the author's knowledge, this first demonstration of gigawatt-scale peak power constitutes the highest peak power that has so far been realized in any amplifier-free thin-disk laser. By performing a thorough characterization, the DQWG approach could further be shown to preserve the spatio-spectral homogeneity of the beam while only marginally reducing the beam quality.

In the experiment, a saturation of the spectral broadening in the last pass of the DQWG was observed, which inhibited the compression to even shorter pulse durations. While the saturation is assumed to stem from accumulated dispersion causing a re-shaping of the temporal pulse shape in the DQWG, further investigation of the exact reason remains to be conducted. Pulse compression to shorter pulse durations approaching the single-cycle regime appears feasible by cascading additional DQWG stages at the compressed output or by resorting to single-plate or cascaded thin-plate spectral broadening techniques.

The availability of few-cycle laser pulses with gigawatt-scale peak powers represents a milestone in the development of ultrafast thin-disk lasers. By utilizing frequency conversion mechanisms such as IPDFG, these laser pulses are expected to facilitate the generation of broadband mid-IR radiation with extended frequency cut-off at unprecedented power levels.

A proof-of-principle study on the frequency conversion to the mid-IR using IPDFG as well as a discussion of the benefits of an extended frequency cut-off for time-domain spectroscopy applications is presented in the next chapter 5. In this thesis, only the frequency conversion into the mid-IR spectral range was further investigated. However, the availability of few-cycle laser pulses with gigawatt-scale peak powers is furthermore expected to facilitate the realization of compact high photon-flux XUV-sources at megahertz repetition rates [124]. When combined with a suitable method of stabilizing the CEP of the pulses as further described in chapter 6, even attosecond pulse generation at megahertz repetition rates can be envisioned.

5

Generation of broadband mid-infrared radiation

5.1 Waveform-stable mid-IR generation

As briefly stated in the introduction, most biologically relevant molecules exhibit fundamental vibrational modes in the spectral range between 2 µm and 20 µm. As a result, mid-IR spectroscopy can, for example, be used for a wide variety of medical applications [12]. For many of these applications, a broad spectral bandwidth of the utilized radiation source is highly beneficial since it enables the simultaneous detection of resonances from a multitude of different molecules. Until now, the most commonly utilized devices for investigating the mid-IR spectral response of biological samples are Fourier-transform infrared (FTIR) spectrometers employing thermal- or laser-based- radiation sources (cf. references [6] and [125] and references therein). While these spectrometers can readily cover the entire mid-IR spectral range, the detection of weak molecular responses is, due the limited dynamic range of the measurement instruments, typically restricted to concentrations above a few micrograms per millilitre [126, 127]. Only recently, a novel type of spectrometers based on the field-resolved detection of IR transients has been proposed and demonstrated to enable the vibrational spectroscopy of biological samples with unprecedented sub-microgram per millilitre sensitivity [6, 128, 129]. However, in contrast to FTIR spectroscopy, field-resolving measurement techniques further require a high temporal coherence of the utilized mid-IR radiation, prohibiting the use of thermal radiation sources.

As an alternative, frequency down-conversion in nonlinear crystals driven by NIR lasers has been shown an excellent method for generating the required broadband coherent mid-IR radiation as it facilitates octave spanning spectra from table-top sized setups at brightness levels exceeding those of synchrotron facilities by orders of magnitude [20, 130]. Specifi-

cally, the generation of mid-IR radiation via IPDFG in a suitable crystal exhibits several advantages when compared to alternative techniques such as optical parametric amplification (OPA) [131] or Raman-induced soliton self-frecuency shifting [132]: Since both frequency components which participate in the generation of the mid-IR radiation are contained within the same driver pulse, spatial as well as temporal overlap of the individual frequency components can inherently be ensured. The result are much simpler and compact setups then typically required for OPA-based approaches. Furthermore, the CEP of the resulting pulse is inherently stabilized in the IPDFG process [133]. Therefore, the stable waveform of the mid-IR pulses can directly be measured using methods like electro-optical sampling (EOS). This is a pre-requisite for time-resolved spectroscopic applications such as the field-resolved spectroscopy (FRS) of biological tissues, which promises significant improvements in measurement sensitivity and dynamic range when compared to existing techniques based on FTIR spectrometers (cf. introductory chapter) [6].

While the technique of IPDFG can provide many advantages for the generation of coherent mid-IR radiation, the low efficiency of the frequency conversion when driven by laser pulses in the NIR dictates the use of driving lasers with high peak powers (see equation 1.90). Additionally, the upper frequency cut-off of the conversion process scales linearly with the bandwidth of the incident pulse spectrum (cf. equation 1.88). Consequently, the generation of short-wavelength mid-IR radiation via IPDFG requires the availability of broadband, ultra-short input pulses and is thus increasingly difficult to achieve. It should be emphasized that the spectral responses of various of important functional groups are located in the spectral region below 6.5 µm [134]. Importantly, it contains the amide I and amid II bands ($\approx$ 5.8 to 6.6 µm) which are the two major bands of protein IR spectra as well as the spectral response of several molecular stretching vibrations found in various lipids ($\approx$ 3.1 to 3.6 µm) [125] — both of which are important biological markers. As a result of the scarcity of ultra-short laser pulses at sufficiently high peak power levels, IPDFG driven by NIR laser pulses has so far mostly been limited to the generation of mid-IR radiation in the spectral range above 6 µm [6, 20, 135]. To date, the field-resolved spectroscopy of biological tissues has hence only been demonstrated within the molecular fingerprint region ($\approx$ 6.5 to 20 µm). However, it would be highly desirable to further extend the applicability range of field-resolved spectrometers by increasing the bandwidth of the utilized mid-IR spectra generated via IPDFG towards even shorter wavelengths. To evaluate whether the high power few-cycle laser pulses at the output of the DQWG described in chapter 4 can benefit the generation of short-wavelength mid-IR radiation via IPDFG, a simple proof-of-principle frequency conversion experiment was conducted which will be described in the following sections.

5.2 Few-cycle-laser based intra-pulse difference-frequency generation

5.2.1 Generation of tunable mid-infrared radiation below 6.5 µm

For the experiment, $LiGaS_2$ was chosen as a nonlinear crystal for the frequency conversion. LGS is a non-centrosymmetric bi-axial crystal that features a high second-order nonlinearity and allows for broadband phase matching of the DFG process. Furthermore, LGS offers a wide transparency range up to 11.6 µm and exhibits a high laser-induced damage threshold of approximately 1 TW/cm^2 for femtosecond pulse durations [20]. The crystal which was used in the experiment has a length of 0.75 mm, which provides a good trade-off between broadband phase matching and conversion efficiency. It is uncoated and cut at $\phi = 0°$ and $\theta = 48°$ to facilitate broadband type I phase-matching (see reference [25, p. 1030] for further details on phase-matching types).

The experimental setup for the mid-IR generation experiment is schematically depicted in Fig. 5.1. As previously stated in section 3.2.3, no non-dispersive dielectric mirrors with a high reflectivity over the entire spectral bandwidth of the DQWG output are currently available. The compressed pulses from the output of the DQWG are hence reflected from a dispersive mirror and subsequently focused using a likewise dispersive concave mirror with 600 mm radius of curvature. The coating for these two mirrors is the same as utilized for the mirrors in the DQWG shown in Fig. 3.12. Two fused silica plates with a thickness of 6.35 mm each are placed in the collimated beam before the focusing mirror to compensate the dispersion introduced by the additional mirrors. A small radius of curvature of the focusing mirror was deliberately chosen to be able to avoid the need for adding additional dispersive folding mirrors to the beam path. However, the peak intensity of the incident laser pulses in the thus created waist exceeds the aforementioned damage threshold of the LGS crystal. Consequently, the nonlinear crystal had to be placed in the divergent beam where the intensity is reduced enough to avoid crystal damage (cf. Fig. 5.1).

In the experiment, the crystal was placed at a distance of 510 mm to the focusing mirror. The peak power on the uncoated front surface of the LGS crystal was calculated to be on the order of 100 GW/cm^2, which is a factor of ten below the expected damage threshold. Whilst higher peak-intensities are expected to facilitate a significant enhancement of the conversion efficiency, the low value was deliberately chosen here to minimize crystal degradation and facilitate long-term operation. To be able to optimize the phase-matching for different spectral components, the crystal was mounted such that the orientation of ϕ and θ as well as the tilt of the crystal with respect to the vertical axis could be smoothly adjusted. The crystal is initially rotated such that the incident power is distributed evenly among the ordinary and extraordinary axis of the LGS crystal.

After IPDFG, the NIR-beam is separated from the newly created mid-IR radiation using a dichroic mirror. The mirrors is based on a ZnSe-substrate with a highly reflective coating for the NIR on the front surface and an AR-coating for the mid-IR radiation on the back surface. Since the residual NIR transmission through the dichroic mirror is

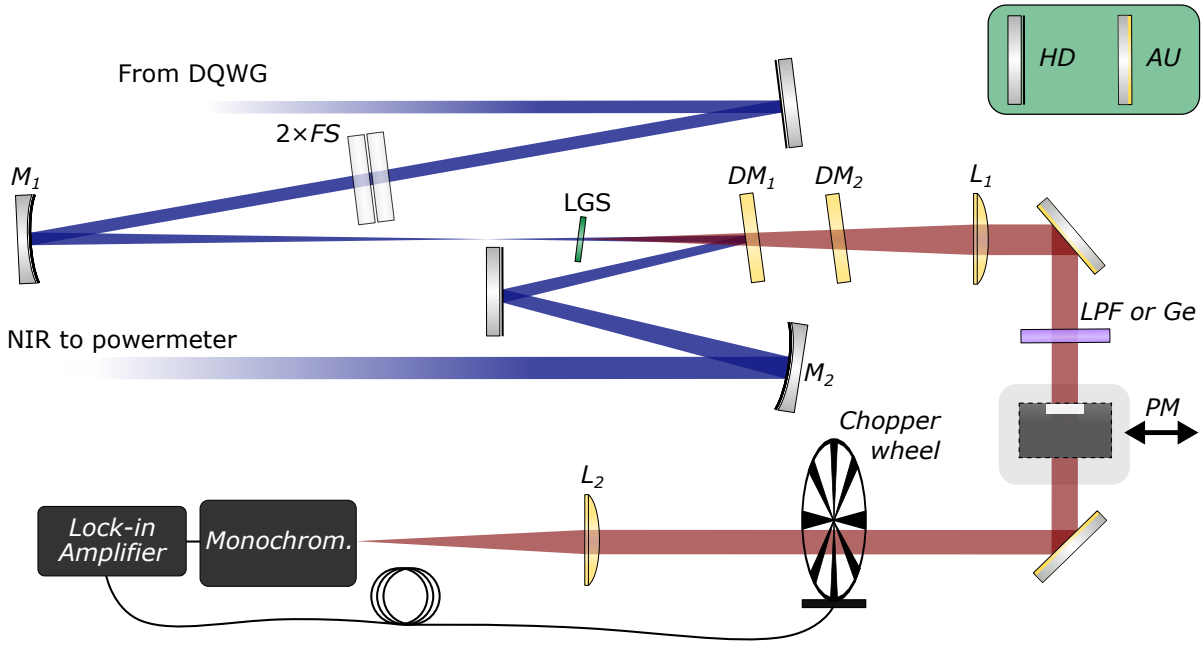

Fig. 5.1: Schematic of the mid-IR generation setup. The DQWG output is focused into the *LGS* crystal using a highly dispersive (*HD*) concave mirror M_1 with a radius of curvature of 600 mm. Two additional fused-ilica plates (*FS*) are placed in the input beam for dispersion compensation. The beam path for the NIR and mid-IR spectral components are described in detail in the text. The abbreviations are: M_2, NIR collimating mirror; *DM*, dichroic mirror on zinc selenide (ZnSe) substrate; L_1, ZnSe mid-IR collimating lens with a focal length of 500 mm; *AU*, bare gold folding mirrors; *LPF*, long-pass filter that can be replaced by a germanium plate (*Ge*) for the measurement of spectral components below 4.5 µm; *PM*, power meter, L_2, focusing lens with a focal length of 200 mm.

still on the order of several hundreds of milliwatts for the 100 W-level incident beam, a second dichroic mirror is added. The mid-IR radiation is subsequently collimated using a broadband AR-coated spherical ZnSe lens with 500 mm focal length (Thorlabs LA7270-E4). It should be noted that using a spherical lens for the collimation worked well in the proof-of-principle experiment where only the spectrum of the generated mid-IR radiation was further analysed. However, collimation of the broadband radiation should ideally be performed with optical elements that do not exhibit chromatic aberrations. Doing so reduces space-time coupling and minimizes spectral inhomogeneity across the beam profile, and thus ensures a good compression of the pulse for subsequent experiments [136, 137].

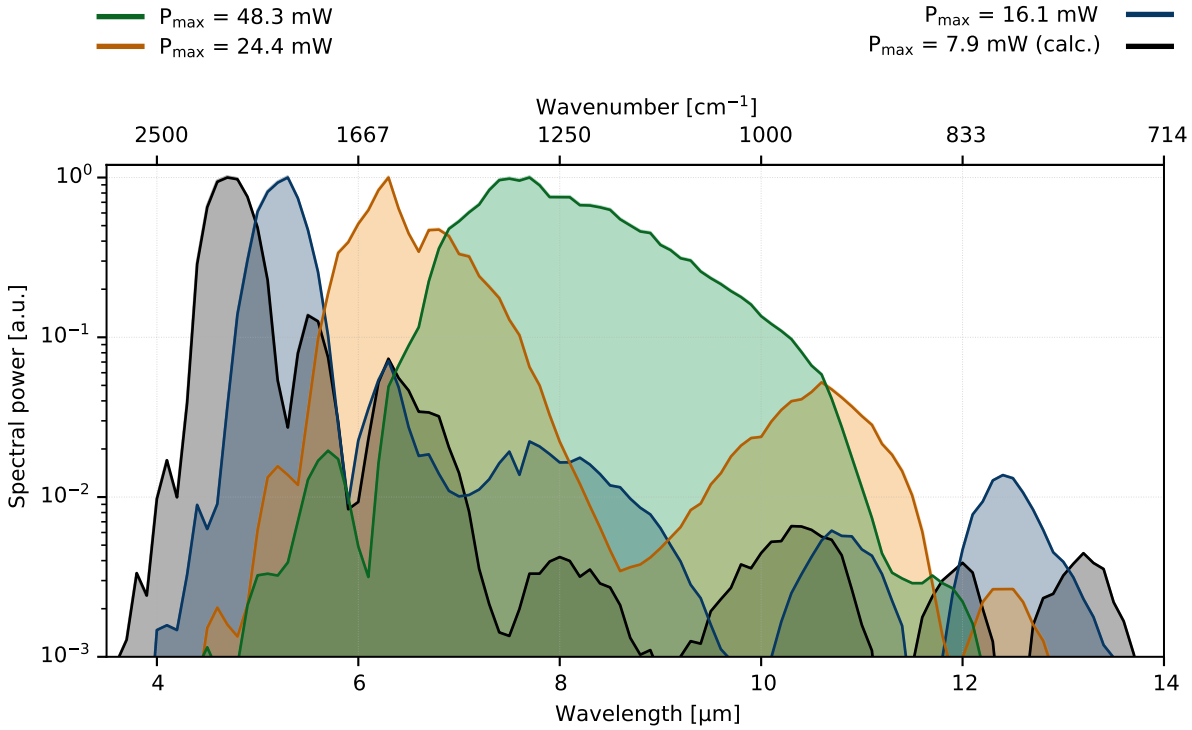

Fig. 5.2: Generated mid-IR for different phase-matching tuning angles. The spectra were measured using a Czerny-Turner monochromator (Newport, Cornerstone 260) equipped with multiple diffraction gratings. Each spectrum is stitched together from three individual measurements at wavelengths of 5.1 µm and 7.6 µm without additional amplitude normalization. The corresponding average power levels for each spectrum are given in the legend.

Once collimated, the mid-IR beam is guided towards a Czerny-Turner monochromator (Newport, Cornerstone 260) equipped with multiple diffraction gratings for characterization of the generated spectrum. The collimated mid-IR beam is modulated using a chopper wheel to enable lock-in detection of the signal at the monochromator output (cf. Fig 5.1). To match the input numerical aperture of the monochromator and further enhance the signal-to-noise ratio of the spectral measurement, the mid-IR is loosely focused onto the

entrance slit of the monochromator using another AR-coated ZnSe lens with a focal length of 200 mm (Thorlabs LA7228-E4). The resulting spectra for different phase-matching angles of the LGS crystal are shown in Fig. 5.2. Each spectrum is stitched together from three individual measurements corresponding to a different combination of longpass filter (to filter out second-order diffraction peaks) and gratings. The measurements were stitched at wavelengths of 5.1 µm and 7.6 µm without additional amplitude normalization.

For each crystal angle, the resultant average power of the generated mid-IR radiation was measured using a low-noise thermal power sensor. The average power for each phase-matching configuration are given in the legend of Fig. 5.2. Since a significant amount (several tens of milliwatts) of second-harmonic radiation was generated inside the LGS crystal which was mostly transmitted through the dichroic mirrors (see Fig. 5.3), a long-pass filter with a cut-on wavelength of 4.5 µm was placed in front of the power sensor for the average power measurements. As the mid-IR spectrum corresponding to the black curve in Fig. 5.2 contains a significant amount of spectral components below 4.5 µm, the long-pass filter was replaced for this measurement by an uncoated 5 mm long germanium plate which only transmits spectral components beyond 1.7 µm. The corresponding average output power was retrospectively corrected for the transmission T of the utilized germanium plate, which is approximately $T = 48\,\%$ and mostly flat over the range of the measured spectrum.

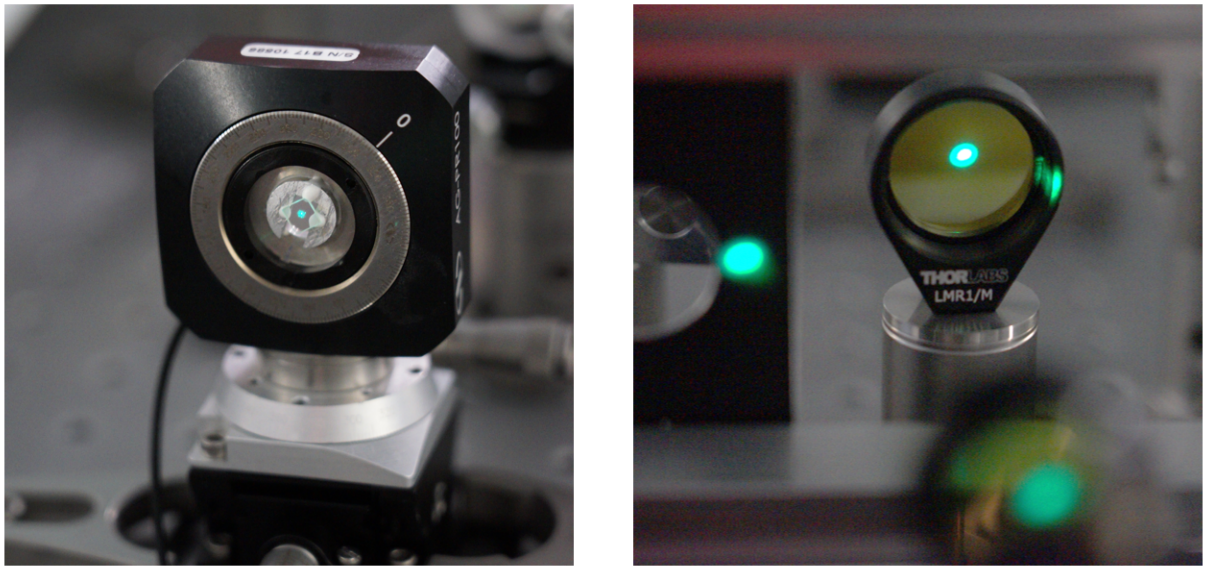

Fig. 5.3: Left: Second-harmonic radiation generated inside the LGS crystal, which is placed in a electrically controlled rotation mount. **Right:** Picture of the emitted green light impinging on the dichroic mirror used for separation of NIR and mid-IR radiation. The green light of the second-harmonic is partially transmitted through the dichroic mirror and the transmitted fraction is visible as a faint green glow at the bottom of the image.

The highest conversion efficiency was found for the phase-matching condition resulting

in the green spectrum shown in Fig. 5.2, which is centred at around a wavelength of 8.5 µm and where a maximum average power of the mid-IR radiation of 48.3 mW was measured on the thermal power sensor. This corresponds to an optical-to-optical efficiency of just below 0.05 %. Despite the high peak power of the input pulses exceeding 0.6 GW, the power level of the generated mid-IR radiation is slightly below that of previous implementations of IPDFG in LGS (reported values are for example 0.21 % in reference [20] or 0.13 % in reference [138]). The main reasons for the rather low achieved conversion efficiency are the conservative choice of the peak intensity of the NIR pulse on the incident surface of the LGS crystal, which is about a factor of two to three lower than in references [20] and [138], as well as the short length of the LGS crystal of only 0.75 mm chosen to facilitate broader band phase-matching of the IPDFG process. A significant improvement in the mid-IR power is expected to be achievable by optimizing the incident pulses peak intensity. This could for example be realized by carefully translating the LGS crystal along the optical axis towards the beam waist.

As stated in the previous paragraphs, the spectrum and power level of the generated mid-IR radiation can be adjusted by varying the orientation of the ϕ and θ angle of the nonlinear crystal. Some of the possible spectra for different phase-matching configurations of the LGS crystal are shown in Fig. 5.2. It is easily seen that for the few-cycle input pulses from the output of the DQWG presented in chapter 4, the cut-off wavelength of the generated mid-IR spectrum can be extended to wavelengths significantly below 6 µm. More specifically, it is possible to adjust the crystal angle such that the output spectrum covers the entire amide band spectral range (5.8 to 6.6 µm) at the −10 dB level (orange spectrum in Fig. 5.2), which validates the advantage of using few-cycle laser pulses for IPDFG-based mid-IR generation for spectroscopic applications beyond the molecular fingerprint region. By optimizing the phase-matching for the generation of spectral components with even shorter wavelengths, a cut-off wavelength of 3.6 µm was achieved at −30 dB level (black curve in Fig. 5.2). While the IPDFG-based generation of mid-IR radiation spanning the wavelength range below 3.6 µm appears feasible, it would require the further broadening of the spectral bandwidth of the driving NIR pulses (cf. equation 1.88), which is equivalent to compressing the pulse to even shorter pulse durations. This could be carried out using one of the methods presented in chapter 4.

It should be noted that the average power of the generated mid-IR radiation is continuously reduced when optimizing the phase-matching configuration for the generation of spectral components with ever shorter wavelength — reaching an average power of 7.6 mW for the phase-matching condition corresponding to the black curve in Fig. 5.2. This reduction in average power can be understood by taking a closer look at the spectral shape of the pulse at the DQWG output. It is easily seen in Fig. 4.5 that for the SPM-broadened pulses at the output of the DQWG, the spectral power density drops rapidly near the spectral wings which are responsible for the generation of short-wavelength components in the frequency mixing process (cf. equation 1.88). A further spectral broadening of the incident NIR laser pulses could therefore not only facilitate the generation of radiation containing even shorter wavelength components but additionally enhance the available energy content in the already demonstrated short-wavelength mid-IR spectral ranges due to

a further redistribution of energy into the wings of the NIR spectrum.

5.2.2 Optimized broadband operation

In the previous section, the generation of tunable mid-IR radiation with a low-wavelength cut-off below 6.5 µm was presented. For the resulting spectra presented in Fig. 5.3, the phase-matching inside the LGS crystal had deliberately been chosen to maximize the energy content in narrow spectral ranges around a peak-wavelength which was continuously tuned towards ever shorter wavelengths. By doing so, a spectrum that covers the entire amide band spectral region (5.8 to 6.6 µm) at −10 dB-level could be generated (orange curve in Fig. 5.3). It is, however, important to emphasize that especially for medical applications the generated mid-IR spectrum should preferably allow the *simultaneous* coverage of both the functional group- and molecular fingerprint spectral regions — corresponding to the wavelength range of 3.5 to 20 µm — to facilitate monitoring and characterization of as many molecules as possible concurrently.

Time-domain spectroscopic applications such as FRS of biological tissues further depend not only on the spectral range of the mid-IR radiation to cover the molecular excitation frequency, but require the radiation to be delivered in a coherent short pulse to enhance the signal-to-noise ratios beyond those of classical FTIR-spectroscopy [6]. More specifically, in reference [6] it is pointed out that further improvement of the detection limit depends critically on the availability of a steeper decay of the exciting mid-IR radiation — corresponding to a tight temporal confinement of the generated mid-IR radiation into a short pulse. According to Fourier-transform, the generation of short pulses likewise requires broadband spectra with a well controlled spectral phase over the entire spectral bandwidth (c.f. section 1.1.3). In the frame of this thesis it was hence briefly investigated, whether the generation of broadband mid-IR spectra is feasible via IPDFG within the same optical arrangement and LGS crystal described in the previous section 5.2.1.

The resultant bandwidth optimized spectrum which was achieved by optimizing the orientation of the ϕ and θ angles of the LGS crystal as well as the crystal tilt is shown in Fig. 5.4. To facilitate the measurement of spectral components up to 16 µm, four individual monochromator measurements with different combinations of diffraction grating and long-pass filter were stitched together during post-processing at wavelengths of 5.1 µm, 8.6 µm and 12.2 µm without additional amplitude normalization. The broadband spectrum extends from approximately 5 to 12 µm at the −20 dB level (indicated by the dashed blue line in Fig. 5.4) covering both the spectral region of the amide bands as well as a significant fraction of the molecular fingerprint region at the same time. The Fourier-transform limited pulse duration corresponding to the measured spectrum is 33 fs — or merely 1.2 optical cycles at a center wavelength of 8.5 µm. A detailed measurement of the temporal profile of the generated mid-IR waveform via EOS as well as further temporal compression by tailored chirped mirrors will lead to the desired short excitation pulses for FRS.

The achieved spectral coverage is already well comparable to the latest generation of FRS measurement instruments [138]. In contrast to reference [138], the lower wavelength extension of the generated mid-IR spectrum in the broadband experiment presented here

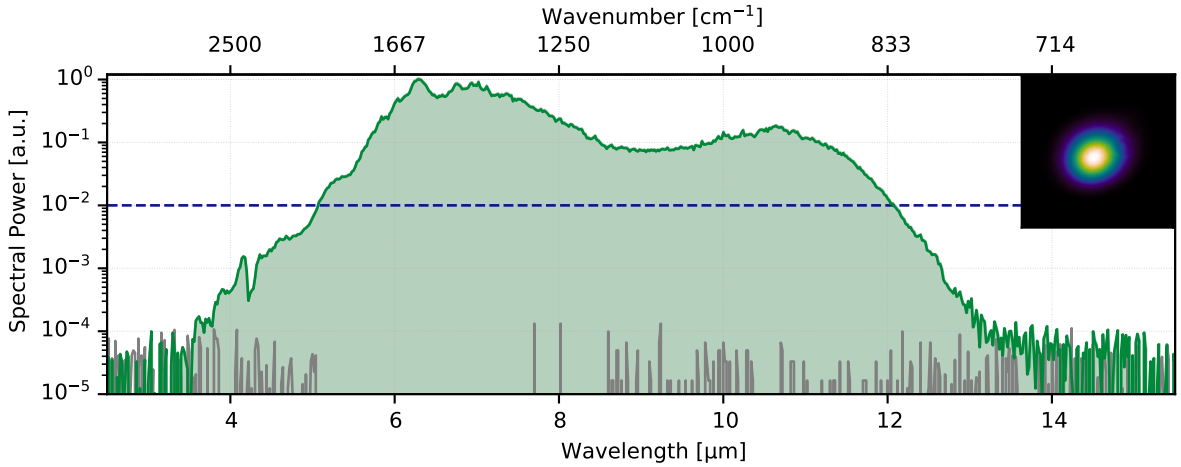

Fig. 5.4: Generated mid-IR spectrum when optimized for broadband operation (green). The measurement noise floor is depicted by the grey line. The dashed blue line marks the −20 dB-level. For both measurements, four individual monochromator traces were stitched together during post-processing at wavelengths of 5.1 µm, 8.6 µm and 12.2 µm without additional amplitude normalization. **Inset:** Beam profile of the collimated mid-IR radiation.

is so far not limited by the bandwidth of the few-cycle driving NIR laser pulse and can thus likely be extended further to at least 3.6 µm by utilizing a thinner LGS crystal with larger phase-matching bandwidth at the expense of a reduced conversion efficiency. For the proof-of-principle experiment presented in this section, the average output power of the generated mid-IR radiation is on the order of 26 mW (measured after two dichroic beamsplitters and a 4.5 µm longpass filter). Further enhancement of the output power appears to be feasible by utilizing the methods discussed in the previous section 5.2.1. It should further be pointed out that the generated mid-IR radiation is emitted in a clean spatial profile which appears to be of Gaussian shape (cf. inset to Fig. 5.4) and was characterized to be linearly polarized with a polarization extinction ratio exceeding 100:1.

5.3 Chapter summary

In this chapter, the results of a proof-of-principle frequency conversion experiment driven by the high-power few-cycle laser pulses generated using the spectral broadening methods described in chapters 3 and 4 have been presented. The frequency conversion experiment aimed at investigating whether the increased bandwidth of the aforementioned few-cycle laser pulses, when compared to previous implementations, can benefit the generation of broadband, coherent mid-IR radiation via IPDFG in a nonlinear crystal. More specifically, it was evaluated whether the extended bandwidth of the NIR driver pulses can help in extending the lower cut-off wavelength of the generated mid-IR radiation to below 6.5 µm

— a pre-requisite for enabling mid-IR spectroscopy on for example amides and lipids, which feature various important resonances in this spectral region [125].

By focusing the few-cycle NIR laser pulses into a thin (0.75 mm) LGS crystal, the generation of narrow-band mid-IR radiation was achieved. The peak wavelength of the mid-IR radiation is tunable from approximately 8.5 to 4.7 µm by adjusting the phase-matching conditions inside the nonlinear crystal. For the case optimized for the generation of short-wavelength components, the spectrum extends down to 3.6 µm at −30 dB-level at an average output power of 7.6 mW. Further optimization of the mid-IR power can potentially be achieved by utilizing a dichroic half-wave plate for selectively adjusting the input polarization of the short wavelength components of the incident NIR pulses with respect to the polarization of the long wavelength components to enhance the efficiency of the type I phase matching process. Importantly, however, the experiment already confirms that the cut-off wavelength of the generated mid-IR radiation can be significantly reduced if sufficiently short (and thus broadband) NIR driver pulses are used for the frequency conversion.

For the efficient implementation of time-domain spectroscopic applications such as FRS, the generated mid-IR radiation should preferably be broadband to allow the simultaneous coverage of a multitude of resonances from various biologically important molecules. The frequency conversion inside the LGS crystal was therefore additionally optimized for the generation of broadband coherent mid-IR radiation — spanning from approximately 5 to 12 µm at the −20 dB level with an average output power of 26 mW. The achieved spectral coverage of this first demonstration is already on par with the latest generation of FRS measurement instruments (compare references [6, 138]), with ample room for further improvement. Importantly, the results from the narrow-bandwidth tuning experiment suggest that the low-wavelength cut-off of the generated broadband radiation is not yet limited by the bandwidth of the NIR driver pulse and can thus be extended further by utilizing thinner nonlinear crystals allowing for a more wide-band phase-matching of the IPDFG process. Alternatively, a dielectric notch-filter with a stopband at around the center wavelength of the incident NIR pulses could be used to enhance the relative power density of their spectral wings. Doing so while maintaining the peak intensity inside the LGS crystal can result in a strong enhancement of the short-wavelength components of the generated mid-IR spectrum, and a significantly increase in usable bandwidth, correspondingly. The extension of the mid-IR spectrum towards shorter wavelength is expected to result in even shorter compressed mid-IR pulses, facilitating a significant improvement in the effective dynamic range of the targeted FRS of biological tissues and unprecedentedly low detection limits of the chemical compounds under investigation [6].

6

Waveform control of high-power thin-disk lasers

6.1 Frequency comb spectroscopy in the extreme ultraviolet

In the preceding chapter 5, it has briefly been introduced how spectroscopic applications in the mid-IR spectral range, such as the laser-based FRS of biological tissues, can benefit from the availability of high-power few-cycle laser pulses for driving the required frequency down-conversion process with high photon flux. However, the same pulses, especially at megahertz repetition rates, similarly open up new perspectives for the frequency up-conversion of the NIR laser radiation. The generation of coherent, high-brightness and CEO-stable radiation in the XUV spectral range is of special importance for the further development of precision spectroscopy techniques such as photoemission spectroscopy or XUV frequency comb spectroscopy [5, 7, 8, 139]. As an example, XUV frequency comb spectroscopy could facilitate the direct detection of the 1S–2S atomic transition in singly ionized helium ions using coherent radiation at around a wavelength of 61 nm, which is expected to provide valuable insights into the higher-order corrections of bound-state quantum electro-dynamics (QED) [11]. A slightly more mundane example for the utility of XUV frequency comb spectroscopy is the development of novel, optical clocks based on nuclear transitions in Thorium atoms, which are expected to provide an unprecedented fractional inaccuracy on the order of 1×10^{-19} [10]. The feasibility of performing time measurements with such low error will benefit a manifold of applications, including the improvement in accuracy of satellite-based navigation, or even setting a new primary standard in the definition of the second [9].

To date, the required coherent radiation in the XUV spectral range is commonly gen-

erated via HHG in noble gases driven by laser pulses in the NIR spectral range [140, 141]. However, the effectiveness of this approach is often impaired by the inherently low efficiency of the frequency conversion process (typically $< 10^{-6}$), even if the conversion is driven by pulses as short as 20 fs [142, 143]. While the conversion efficiency into single harmonic peaks can in principle be increased, for example, by improving the phase-matching of the conversion process using hollow capillary tubes [144], the low conversion efficiencies are more commonly counteracted by enhancing the average- and peak power of the driver laser. Since laser oscillators with sufficiently high power to directly drive the HHG process are hardly available, extra-cavity amplification or passive enhancement cavities are usually employed for these purposes (cf. reference [145] and references therein). Unfortunately, such systems are typically bulky and complex in design. Furthermore, specifically fiber amplifier-based systems can suffer from significant high frequency (> 100 kHz) intensity noise [146]. Owing to amplitude-to-phase coupling in nonlinear media, this intensity noise can be coupled to the noise of the CEO frequency [147], which is expected to be further enhanced during the frequency conversion process [148] — constituting an additional limitation to high-precision spectroscopic applications in the XUV spectral range.

The aforementioned limitation of excessive high-frequency noise can be mitigated by utilizing femtosecond thin-disk lasers for driving the nonlinear frequency conversion into the XUV spectral range [19]. This class of lasers has previously been demonstrated to exhibit excellent noise characteristics where shot-noise limited performance can easily be obtained at frequencies above ≈ 100 kHz [24]. The recent advances in high-power, few-cycle thin-disk laser sources with megahertz repetition rates, such as developed in the frame of this thesis, are expected to allow for efficient frequency conversion even in single-pass geometries such as presented in reference [124] — significantly reducing the complexity of the required frequency conversion setup when compared to passive enhancement cavities.

It is important to note that in contrast to IPDFG, the waveform of the generated XUV radiation is not inherently stabilized in the HHG process. Consequently, the generation of XUV frequency combs by means of laser-based HHG requires the utilized NIR driver laser to itself form a frequency comb. Since Kerr-lens mode-locked oscillators commonly emit a train of short pulses, the associated spectrum already consists of a discrete set of equally spaced lines with frequencies f_n (see red lines in Fig. 6.1), given by [5]

$$f_n = n \cdot f_{rep} + f_{CEO} \tag{6.1}$$

where n is a large integer number corresponding to the longitudinal mode order of the oscillator cavity, f_{rep} is the pulse repetition rate of the laser and f_{CEO} is the CEO frequency. This offset frequency f_{CEO} is directly connected to the change in CEP ($\Delta\phi_{CEP}$, cf. section 1.1.3) the pulse experiences during one roundtrip through the oscillator and can be written as [34, p. 350]

$$f_{CEO} = \frac{\Delta\phi_{CEP}}{2\pi} f_{rep}\,. \tag{6.2}$$

It is instructive to first take a closer look at the physical origin of the CEO frequency. In section 1.1.3, the change in CEP has been introduced as the result of a discrepancy between

phase- and group velocity of a light pulse propagating through a dispersive medium. In an ideal laser oscillator in steady-state operation, the roundtrip dispersion is invariant over time resulting in a constant change in CEP and hence, also a constant CEO frequency. However, in real world laser oscillators, both the repetition rate and the CEO frequency often fluctuate significantly as a result of variations in the optical path length and intra-cavity dispersion — caused by, for example, nonlinearly induced refractive index changes, thermal effects or even mechanical vibrations. Consequently, to form a stable frequency comb, the pulse repetition rate as well as the CEO frequency of the driving oscillator typically need to be actively stabilized [149].

Since the repetition rate of most thin-disk lasers lies in the range from 1 to 100 MHz it can be measured directly using sufficiently fast photodetectors. Fluctuations of the repetition rate can then be reduced for example by mounting one of the intra-cavity mirrors to a piezo-transducer that stabilizes the optical length of the laser resonator [149]. As the CEO frequency is directly related to the optical phase fluctuations of the carrier wave (cf. equation 6.2) it is significantly more complicated to be assessed directly. To date, the CEO frequency is most commonly measured utilizing interferometric f-$2f$ self-referencing schemes [150, 151]. In such schemes, an octave-spanning spectrum is first generated from the driver laser by means of SPM-based spectral broadening or continuum-generation. After frequency doubling the octave-spanning spectrum, the residual, unconverted fundamental spectrum is interfered with the newly generated second-harmonic components on a sufficiently fast photodetector. As a result, a beating between adjacent lines of the fundamental- and second-harmonic spectrum can be observed (cf. Fig 6.1) [152].

Since the SHG is driven by the initial frequency spectrum, the frequency of the resulting beat note is given by

$$f_n^{SHG} - f_{2n}^{fund} = 2 \cdot (n \cdot f_{rep} + f_{CEO}) - (2n \cdot f_{rep} + f_{CEO}) = f_{CEO} \tag{6.3}$$

which is the CEO frequency. This beat note can subsequently be mixed with a stable radio frequency (RF)-reference to generate an error signal. The reference could be derived from a frequency generator or even from the laser itself. Importantly, the error signal can subsequently be minimized via controlling the CEO frequency of the laser oscillator for example by providing negative feedback in a phase-locked loop (PLL).

The following section 6.2 provides a brief overview over the various commonly employed techniques for controlling the CEO frequency of laser pulses in high-power laser systems. Furthermore, a novel method for stabilizing the CEO frequency of Kerr-lens mode-locked laser oscillators is introduced. It is based on intra-cavity loss modulation using an AOM which at the same time serves as the nonlinear medium inside the laser oscillator. This novel concept is applied to a high-power Kerr-lens mode-locked thin-disk oscillator, resulting in a stabilization of the CEO frequency with a residual in-loop phase noise below 90 mrad measured from 1 Hz to 500 kHz at an unprecedented average power of more than 105 W and intra-cavity peak power exceeding 200 MW.

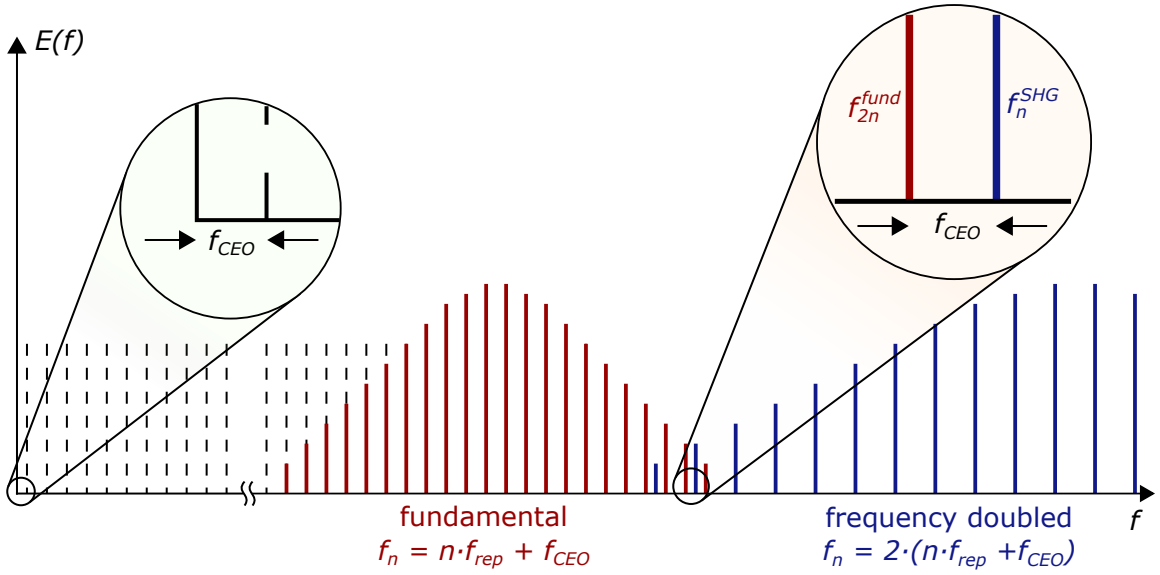

Fig. 6.1: Schematic depiction of the CEO-frequency beating. A fundamental line spectrum (red columns), corresponding to a regular pulse train, is shown. The individual lines are equally spaced by the repetition rate f_{rep} and the entire line spectrum is offset from zero by the carrier-envelope offset (CEO)-frequency f_{CEO} (green inset, cf. equation 6.1). The frequency doubled line spectrum (blue columns) consists of individual lines which are spaced by $2 \cdot f_{rep}$ and is offset by $2 \cdot f_{CEO}$. If the fundamental line spectrum is octave spanning it overlaps with the second-harmonic spectrum and a beating between adjacent lines of the two spectra can be observed at the CEO-frequency (orange inset).

6.2 Carrier-envelope offset frequency stabilization

6.2.1 State-of-the-art stabilization techniques

The most commonly employed techniques for stabilizing the CEO frequency of high-power laser systems can be separated into two groups: feed-forward stabilization methods which are used to directly stabilize the CEO frequency at the output of a free-running oscillator, and feedback schemes in which the CEO frequency stabilization is achieved inside the laser oscillator by modifying the intra-cavity dispersion or nonlinearity.

Feed-forward CEO frequency stabilization

In feed-forward stabilization schemes, the CEO frequency of the free-running mode-locked laser oscillator output is retroactively stabilized by utilizing the diffraction of the laser beam from an acousto-optic frequency shifter (AOFS) [153]. To date, the feed-forward approach has successfully been demonstrated for low-power seed lasers (e.g. based on Ti:sapphire or Yb:CYA gain materials) which can be followed by extra-cavity amplification chains to obtain higher powers [153, 154]. The direct application of the feed-forward stabilization approach to high-power lasers remains challenging due to multiple reasons: The concept typically introduces significant linear losses since it relies on using the first diffraction order beam from the AOFS where efficiencies are typically below 80 % [155]. In addition to power losses, utilization of the first diffraction order can introduce beam-pointing instabilities as well as angular and spatial chirp of the laser pulses that subsequently need to be corrected. This can significantly increase the system complexity [155–157]. For high-power driving lasers, the beam size incident on the AOFS furthermore needs to be large, and the propagation length inside the AOFS crystal should be restricted to only a few millimeters. This is to avoid excessive nonlinear phase shifts and therefore self-focusing and uncontrolled spectral broadening, cf. section 1.1.3, and thermal lensing inside the AOFS material. These requirements in turn impose severe constraints on the achievable diffraction efficiency as well as the accessible modulation bandwidth of the AOFS — critically impairing the applicability of this approach for high power thin-disk lasers.

Stabilization schemes based on negative feedback

The aforementioned limitations of feed-forward stabilization approaches can mostly be mitigated by utilizing stabilization schemes where the CEO frequency is stabilized directly inside the oscillator cavity. Over the past decades, a manifold of techniques for directly manipulating the CEO frequency of mode-locked oscillators has been developed. In the early days of frequency combs, the CEO frequency was often controlled via translating transmissive intra-cavity wedges or tilting of the resonator end mirror close to an intra-cavity prism in order to vary the group delay accumulated by the circulating laser pulse during one resonator round-trip [151, 158, 159]. However, these approaches are hardly applicable to modern-day high power thin-disk oscillators which almost exclusively rely

on chirped mirror technology for controlling the intra-cavity dispersion. Furthermore, the achievable control bandwidths of such approaches are often insufficiently small for achieving CEO frequency stabilization with low residual phase noise levels.

Significantly wider control bandwidths can be obtained by modulating the intensity of the laser pulse circulating inside the cavity which induces a variation of the CEO frequency as a result of refractive index changes and amplitude-to-phase coupling inside nonlinear media by the optical Kerr-effect [147]. Typical approaches for manipulating the intra-cavity pulse intensity previously used with high power thin-disk oscillators include the modulation of the pump power, gain depletion, or intra-cavity loss. In the first type of CEO frequency control schemes, the pump power of the thin-disk oscillator is modulated directly by controlling the current of the utilized pump laser diode [19, 65, 160]. Alternatively, a dual-wavelength pumping scheme has been presented in reference [161] where a second, low-power pump diode at a different wavelength was utilized to facilitate a fast modulation of the laser gain without requiring direct modulation of the high power pump diode at high frequencies. Unfortunately, for the case of Yb:based thin-disk oscillators, the achievable bandwidth of the pump control stabilization schemes is commonly restricted to several kilohertz by the cavity dynamics of the laser oscillator [19]. Specifically, the millisecond-scale upper-state lifetime of the Yb:doped gain material significantly dampens the oscillator's sensitivity to externally applied power modulations with frequency beyond the inverse upper-state lifetime. While wider control bandwidths could be achieved by utilizing phase lead filters in the PLL [161, 162], tight CEO frequency locking of a thin-disk oscillator with a residual phase noise $< 100\,\mathrm{mrad}$ using pump power control schemes remains to be demonstrated to this day. Additionally, no further improvement of the achievable modulation bandwidth could so far be realized by directly modulating the gain depletion of the thin-disk gain medium [163].

The bandwidth limitation of the aforementioned pump control schemes can for example be overcome by modulating the intra-cavity loss of the thin-disk oscillator using an AOM, which likewise enables control over the CEO frequency via amplitude-to-phase coupling as a result of the Kerr-nonlinearity. This has previously been reported to facilitate a promising stabilization with a residual phase noise down to 180 mrad [108]. In contrast to the aforementioned feed-forward schemes using the first order diffraction from an AOFS, the zero-order transmission from the AOM is used in the loss-modulation approach. This results in a high transmission efficiency through the AOM and no additionally added beam-pointing instabilities. As a result, the can readily be used even in high-average-power laser oscillators. In the implementation in reference [108], the AOM was placed in the collimated arm of a Kerr-lens mode-locked oscillator with an intra-cavity peak power below 30 MW. The specific placement of the AOM into a region of the laser resonator where the peak intensity of the beam is low is required to avoid self-focusing inside the AOM material since the occurrence of additional Kerr-lensing is expected to detrimentally impact the mode-locking performance of the laser oscillator. The additional nonlinear interaction inside the AOM material consequently constitutes the key limitation to the power scalability of the approach presented in reference [108]. More specifically, adapting the concept to thin-disk oscillators with significantly higher peak-power levels would necessitate an increase

of the beam size inside the AOM in order to maintain a low nonlinear response from the AOM material. However, increasing the beam size inside the AOM is expected to result in a significant reduction of the attainable modulation bandwidth and compromise the achievable phase stability [164].

Acousto-optic modulator as Kerr-medium

It is easily seen that none of the aforementioned techniques for controlling the CEO frequency can provide the desirable features; namely a large control bandwidth facilitating sub-100 mrad phase noise levels, and simultaneously being power scalable to the intra-cavity peak powers of several hundred megawatts commonly observed in the latest generation of Kerr-lens mode-locked thin-disk oscillators [22]. Consequently, a novel, power-scalable stabilization scheme which addresses these limitations was developed.

It should be emphasized that for Kerr-lens mode-locked oscillators, the key limitation to power scalability of the previously described intra-cavity loss-modulation approach originates from a potential unfavourable distribution of the nonlinear contributions inside the laser oscillator. More specifically, the AOM required to modulate the intensity of the intra-cavity laser pulses can introduce non-negligible self-focusing if the peak intensity of the laser pulses passing through the AOM material is sufficiently large (cf. section 1.2.3). Depending on the position of the AOM inside the resonator, the generated Kerr-lens can in turn detrimentally affect the resonator beam caustic, which can significantly weaken the self-amplitude modulation (SAM) required for forming and stabilizing the pulse train during Kerr-lens mode-locking [165].

In Kerr-lens mode-locked oscillators based on thin-disk gain materials, the required nonlinearity for achieving a sufficient amount of SAM for initiating and stabilizing pulsed operation is commonly provided by placing a *Kerr-medium* (typically a bulk dielectric medium such as a thin sapphire or quartz plate) into a focal region of the laser resonator (see Fig. 2.6 or references [21–23]). Since AOMs effectively consist of a bulk dielectric medium, a suitable AOM can equivalently be used as the Kerr-medium when placed in the focal region of the oscillator, while still serving its other role of loss-modulation. Importantly, in this case, the self-focusing inside the AOM material due to high peak-intensities is explicitly desired since it facilitates mode-locked operation of the oscillator via introducing a sufficient amount of SAM. Furthermore, the achievable control bandwidth when positioning the AOM in a focal region is expected to be significantly improved when compared to placing the AOM in the collimated arm of the oscillator, since the modulation bandwidth of AOMs is known to scale inversely with the beam diameter [164]. Most importantly, however, using the AOM as the Kerr-medium inside the thin-disk oscillator resolves the power-scaling limitation of the intra-cavity loss-modulation approach presented in reference [108], since the laser oscillator can be designed to contain only a single nonlinear medium — inherently circumventing the unfavourable interplay between multiple nonlinear contributions in the laser resonator.

6.2.2 Stabilization results of a 100 W-level femtosecond thin-disk oscillator

The performance of the novel CEO frequency control scheme introduced in the previous section was experimentally assessed. For testing the scalability of the approach to high intra-cavity peak power levels, the experiment was based on a state-of-the-art high power Kerr-lens mode-locked thin-disk oscillator developed and built by Jonathan Brons, and described in further detail in reference [22]. For the stabilization experiment, the thin-disk oscillator was configured to emit a continuous pulse train with an average output power of 105 W at a pulse duration of 190 fs and a pulse repetition rate of 15.6 MHz. Since the thin-disk oscillator is operated with an output coupler with only 15 % transmission, the intra-cavity peak power is estimated to be approximately 210 MW. The output power of the oscillator was intendedly reduced when compared to reference [22] to optimize the passive stability of the CEO frequency. A schematic of the oscillator and the experimental setup is shown in Fig. 6.2.

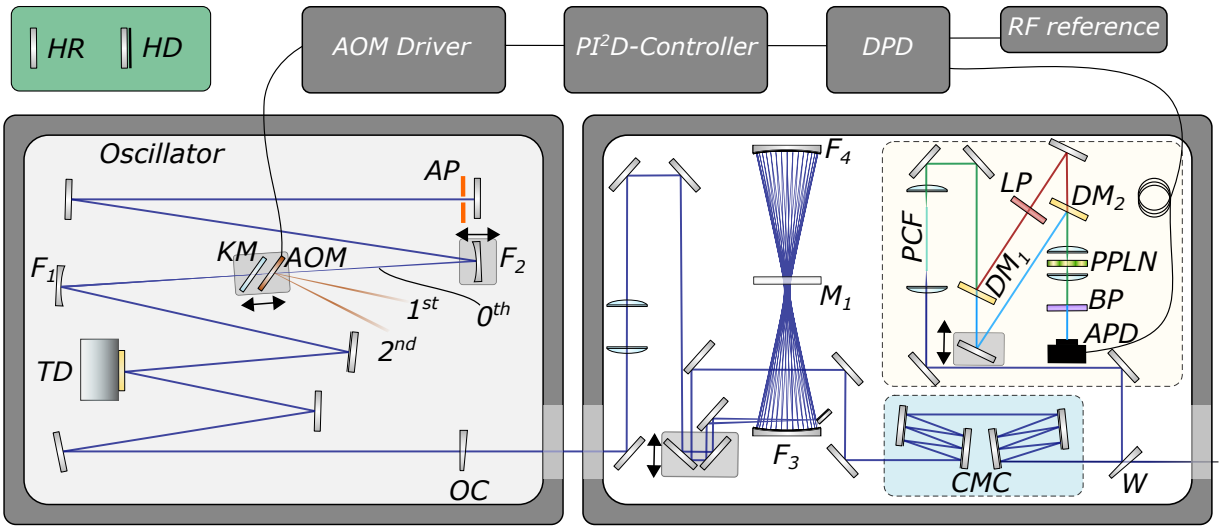

Fig. 6.2: Schematic of the CEO-frequency stabilization setup. The AOM is placed inside the focusing telescope as additional Kerr-medium. *AP*, hard aperture; *KM*, Kerr-medium; F_1-F_4, focusing mirrors; *HD*, highly dispersive mirror; *TD*, thin-disk; *OC* output coupler; M_1, fused silica plate, *CMC*, chirped-mirror compressor. At the output of the chirped-mirror compressor, a small fraction of the power is extracted using an uncoated ZnSe wedge *W* and sent into a photonic crystal fiber (*PCF*) followed by a f-2f-interferometer. The interferometer components are: $DM_{1,2}$, dichroic mirrors; *LP*, longpass filter at 1250 nm; *PPLN*, periodically poled lithium niobate crystal (Covesion SHG1375-1455-1); *BP*, bandpass filter (Thorlabs FP 690-10) and *APD*, avalanche photodetector (MenloSystems APD210).

Originally, the required Kerr-nonlinearity for mode-locking the thin-disk oscillator was provided by a 5 mm thick sapphire plate positioned at Brewster's angle inside the focusing

telescope of the resonator cavity [22]. This sapphire plate is replaced by a 3 mm long AOM (Gooch & Housego MQS080-6C10R10-3) made of crystal quartz. The utilized AOM operates in the Raman-Nath diffraction regime and features a diffraction efficiency into the higher orders of approximately 0.9 %. To match the total amount of Kerr-nonlinearity of the original configuration, an additional 3 mm thick crystal quartz plate is placed in the same focus in close vicinity (≈ 1.5 cm) to the AOM (cf. Fig. 6.2). It is important to note that due to the high intra-cavity peak power of the oscillator, the beam is only loosely focussed to a waist diameter of approximately 600 µm inside the AOM and the additional quartz plate. Since the associated Rayleigh-length is on the order of tens of centimetres, the exact distance between the AOM and the additional crystal quartz plate was found to be uncritical in the experiment. Due to the small distance between the AOM and the crystal quartz plate, and the large Rayleigh-length of the incident beam, the combination of the two individual optical elements can essentially be treated as a compound Kerr-medium assembly with similar properties to those of a single Kerr-medium.

To facilitate measurement of the CEO frequency, about 80 W of the oscillator output are coupled into a nonlinear compression stage which was likewise designed and built by Jonathan Brons. The compression stage is based on a Herriott-type multipass-cell for SPM-based spectral broadening and subsequent chirp removal using a chirped-mirror compressor. It reduces the pulse duration to around 40 fs while increasing the peak power to 67 MW. The limitation in input power of the Herriott-cell to around 80 W was due to imperfections in the mode-matching (cf. section 2.2.2). Using higher input powers led to white-light generation and damage inside the 6.35 mm thick fused silica plate serving as the nonlinear medium in the multipass-cell. The achieved spectral coverage of approximately 100 nm around a center wavelength of 1030 nm (at -20 dB, see blue curve in Fig. 6.3) is still significantly too narrow to facilitate detection of the CEO frequency using the self-referencing method described in section 6.1. However, the compressed laser pulses can now be used to drive continuum generation in a highly nonlinear fiber, where a loss of temporal coherence has previously been observed during the generation of octave-spanning spectra driven by >100 fs long pulses owing to the high required soliton orders for sufficient spectral broadening [92].

In order to generate an octave spanning spectrum, a small fraction of the main beam (approximately 130 mW) is split off at the compressor output using an uncoated ZnSe wedge and coupled into a highly nonlinear photonic crystal fiber (NKT Photonics SC-3.7-975) with a core diameter of 3.7 µm for continuum generation. After re-collimation of the fiber output, the laser pulses with an octave-spanning spectrum are sent into a home-built f-$2f$-interferometer (see schematic in Fig. 6.2). For the interferometer, a Mach-Zehnder layout was chosen over a common path geometry despite the slightly higher susceptibility to parasitic noise contributions. As a key advantage, the Mach-Zehnder interferometer geometry facilitates the filtering of specific frequency components inside the individual interferometer arms, providing an additional degree of freedom for optimizing the SNR in the subsequent detection of the beat signal. In the f-$2f$-interferometer, the red part of the octave spanning spectrum (cf. Fig. 6.3) is separated from the main beam using a dichroic mirror and is longpass-filtered at 1250 nm before being recombined with the blue

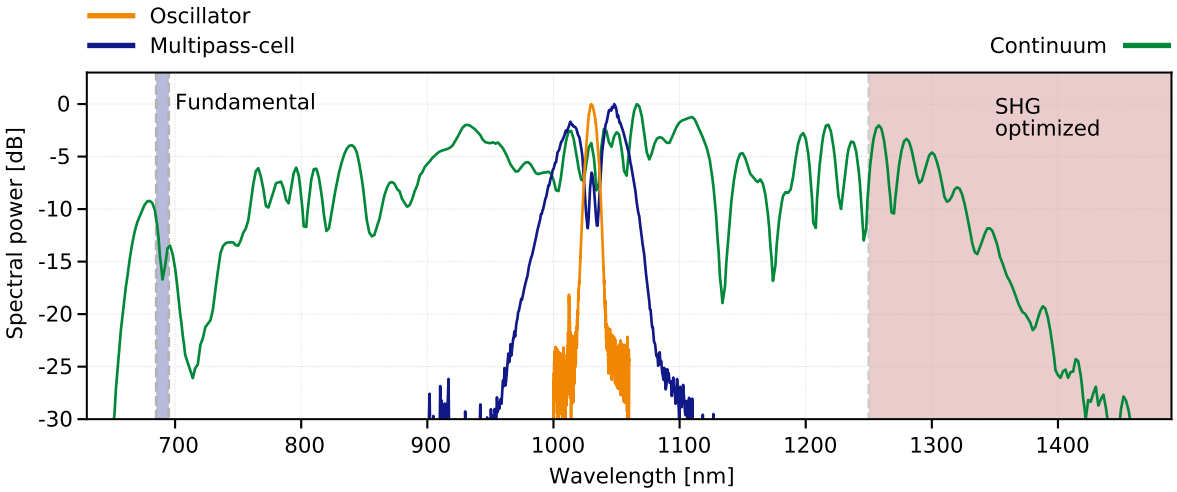

Fig. 6.3: Spectral evolution in the CEO-frequency stabilization setup showing the oscillator spectrum, the SPM-broadened spectrum after the multipass-cell and the continuum after the highly nonlinear photonic crystal fiber, from which the CEO beat signal was obtained. The red shaded area indicates the wavelength range for which the second-harmonic generation inside the periodically-poled lithium niobate crystal was optimized. The shaded blue area at around a wavelength of 690 nm indicates the passband of the utilized spectral filter for which an optimum signal-to-noise ratio of the generated beat signal could be observed.

part using a second dichroic mirror. While the additional longpass filter is not strictly required for the stabilization scheme, it greatly helps in optimizing the phase-matching of the subsequent SHG-stage for the correct input spectral range. The beam path for the blue part of the spectrum contains a variable delay that can be adjusted to achieve a temporal overlap of the f and $2f$ frequency components at the position of the photodetector. The collinearly propagating red and blue spectral components after recombination are focused into a periodically-poled lithium niobate crystal which enables an efficient frequency doubling of the red part of the spectrum. Ultimately, a beat signal at the CEO frequency can be detected using an avalanche photodetector (APD) after spectral filtering of the fundamental and second harmonic beams using a narrow ($\Delta\lambda_{FWHM} = 10\,\text{nm}$) bandpass filter centered at 690 nm (cf. blue shaded area in Fig. 6.3) for an optimal SNR.

Characterization of the modulation bandwidth

To assess its potential for achieving a tight lock of the CEO frequency to an externally applied RF reference, the control bandwidth of the CEO frequency stabilization scheme where the AOM is used as the Kerr-medium of the mode-locked oscillator was quantified empirically. For this, a RF-power of approximately1.6 W was applied to the AOM-driver. The phase- and amplitude response of the oscillator output power with respect to the AOM-induced intra-cavity loss modulation was subsequently measured using a photode-

tector coupled to a commercially available lock-in amplifier (Zurich Instruments UHF). The resulting transfer function is shown in Fig. 6.4 a. A phase lag of 90° is reached at a corner frequency of approximately 230 kHz. This constitutes a significant improvement when compared to pump modulation schemes (a cutoff frequency of 10 kHz has been reported in reference [161]) and allows for control of the CEO frequency over a wide frequency range. The weak, wideband phase-shift of 25° centred at around a frequency of 2 kHz (see blue curve in Fig. 6.4 a) presumably originates from resonance close to the relaxation oscillation frequency of the laser.

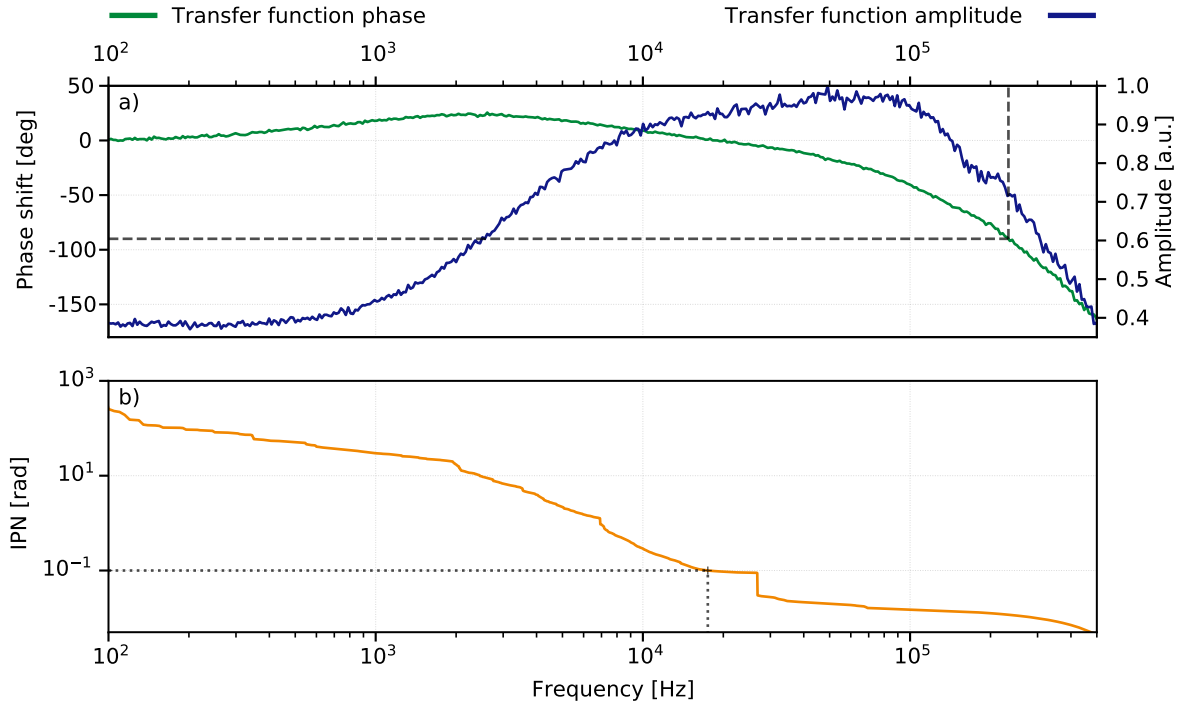

Fig. 6.4: a) Phase- and amplitude transfer function of the oscillator output power in response to the AOM modulation measured with a Zurich Instruments UHF lock-in amplifier. The dashed black line indicates the frequency at which a phase shift of 90° is accumulated. b) integrated phase noise (IPN) of the free-running CEO beat signal. The dotted black line indicates the frequency at which an IPN of 100 mrad is reached.

In contrast to the nearly flat phase response, the amplitude transfer function of the oscillator (green curve in Fig. 6.4 a) has a significantly more complex shape and exhibits a strong high-pass filtering effect. The specific shape of the amplitude transfer function is likely due to a dynamic gain-saturation of the laser medium: At frequencies below the inverse upper-state lifetime of the gain medium ($\approx$ 1 kHz for an upper-state lifetime of approximately 1 ms in Yb:YAG), the slow modulation of the cavity loss is partially negated by the laser gain which reduces the effective modulation amplitude [166]. At frequencies

exceeding 1 kHz, the power oscillations caused by the loss-modulator are too fast to be followed by the upper-state population of the gain medium. Consequently, the modulation amplitude at frequencies > 1 kHz is only slightly reduced. It should be emphasized that the observed reduction of the modulation amplitude at low frequencies only corresponds to a dampening of about -7 dB. This can easily be compensated for by adjusting the frequency-dependent electronic gain of the feedback in the servo loop.

Measurement and stabilization of the CEO frequency

To evaluate the passive CEO frequency stability of the mode-locked high-power thin-disk oscillator, the noise characteristics of the free-running beat signal — obtained at the output of the previously described f-$2f$ interferometer — was analysed using the numerical method described in reference [161]. The integrated phase noise (IPN) of the free-running beat signal is shown in Fig. 6.4 b. A closer evaluation reveals that the major contribution to the IPN comes from noise components in the acoustic frequency band (< 20 kHz). This observation is in good agreement with previous studies which indicate a strong coupling of amplitude-to-phase noise in Kerr-lens mode-locked oscillators at frequencies below the inverse upper state lifetime [167]. A sharp increase of the IPN at 26.4 kHz presumably stems from the oscillator dynamics and was not investigated in further detail. The analysis of the free-running IPN indicates that a residual phase noise of below 100 mrad can be reached if the bandwidth of the CEO-frequency control mechanism extends from the low frequencies to 17 kHz at least, which is readily provided by the utilized AOM.

To stabilize the CEO frequency of the mode-locked thin-disk oscillator, the free-running CEO beat signal was shifted to the intended locking frequency by adjusting the current of the utilized pump diodes. A locking frequency of 10.7 MHz was chosen for this experiment to maximize the difference between the beat signals and the fundamental repetition frequency since of 15.6 MHz. Furthermore, high quality and sufficiently narrow electronic bandpass filters with 10.7 MHz center frequency are readily available. The beat signal obtained from the APD in the f-$2f$ interferometer was subsequently bandpass-filtered to remove the much stronger RF-signal at the pulse repetition frequency and amplified by 60 dB before being compared to an externally applied RF signal (10.7 MHz, from a Marconi 2022D Signal Generator) in a home built $\pm 16\pi$ digital phase detector (DPD). The error signal obtained from the DPD was subsequently split, sending half of the power towards a commercially available proportional–integral–derivative (PID) controller (Vescent-Photonics D2-125) while using the other half for monitoring the locking performance on a digital oscilloscope. To close the phase-locked loop, the servo signal which is generated inside the PID controller is applied to the modulation input of the AOM driver.

The locking performance of the CEO frequency stabilization scheme was optimized by iteratively varying the corner frequencies of the integral- and derivative parts and the proportional gain of the PID controller. A tight lock of the CEO frequency could be achieved by setting the corner frequency of the first integrator to 50 kHz, the second integrator to 5 kHz and the derivative part to 20 kHz. The single-sided power spectral density (PSD) and corresponding IPN of the detected error signal are shown in Fig. 6.5. A minimum

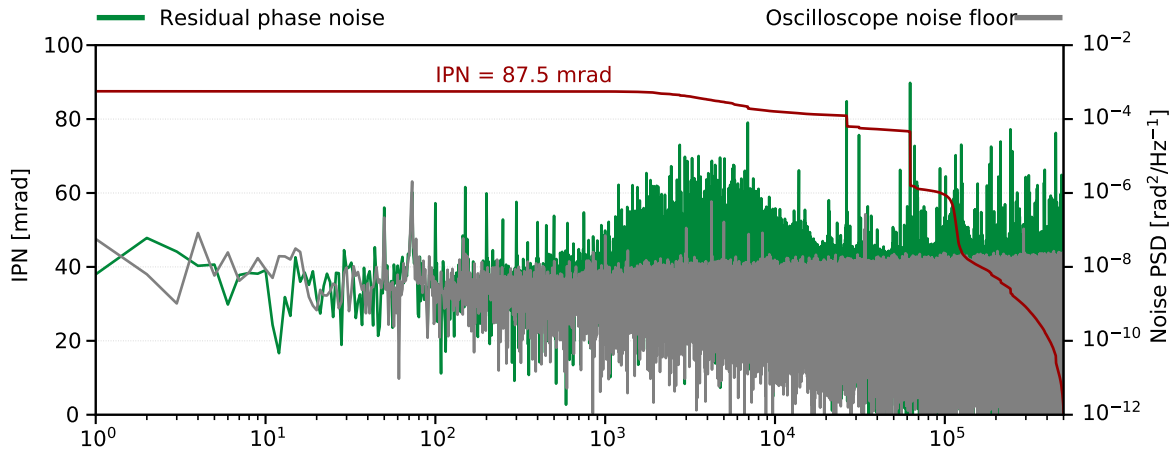

Fig. 6.5: Residual phase noise of the detected error signal. The green curve shows the phase noise power spectral density (PSD) of the CEO-beat assessed from the recorded error signal. The integrated phase noise (IPN) from 500 kHz to 1 Hz is displayed in red. The noise floor power spectral density of the oscilloscope (without digital phase detector) is shown in grey.

residual in-loop phase noise of 87.5 mrad was determined by integrating the PSD in the range from 500 kHz to 1 Hz. The PSD exhibits a distinctive spike at 26.4 kHz which is already visible in the noise spectrum of the free-running beat note (cf. Fig. 6.4 b) and presumably stems from the oscillator dynamics. A second, narrow spike at a frequency of 62.5 kHz as well as excessive high frequency noise (> 100 kHz), which is responsible for approximately half of the residual IPN, could be identified to originate from the utilized DPD. This noise could potentially be reduced by optimizing the DPD electronics or using a different phase detector with intrinsically lower noise floor.

Limitations of the stabilization method and outlook

It should be emphasized that the noise levels specified above were only measured in-loop due to the lack of a second f-$2f$ interferometer and are therefore not identical to the noise level at the thin-disk oscillator output. Out-of-loop noise measurements were performed for example in reference [108] where a comparable interferometer type had been used for the detection of the CEO frequency. The results presented in reference [108] suggest that the out-of-loop noise of the stabilization scheme presented here can be expected to be a factor of two to three higher than the measured in-loop noise. The additional noise in the out-of-loop measurement has previously been observed to originate mainly from beam pointing fluctuations which are converted to phase noise by amplitude-to-phase coupling in the highly nonlinear fiber, as well as a general amplification of the noise during the continuum generation process [122].

It should further be noted that in the presented experiment, thermal drifts inside the

oscillator were observed when applying the required 1.6 W of RF-power to the piezoelectric transducer of the AOM. The associated variation in beam pointing of the oscillator output caused a reduction in the coupling efficiency into the photonic crystal fiber which ultimately prohibited the lock from being maintained for more than a few minutes at a time. The observed drift originated from the warming up of the AOM due to absorption of the applied RF-power where a thermal equilibrium was reached after approximately 1 h of operation. An extended duration of the lock could likely be achieved by allowing the AOM to fully thermalize before closing the PLL. Unfortunately, the source of the thermal drift inside the oscillator only became known after the f-$2f$ interferometer had been disassembled, prohibiting further quantitative studies on the long-term locking potential of the presented stabilization scheme. In an alternative approach, the photonic crystal fiber would be omitted and the octave spanning spectrum could directly be generated using SPM-based all-bulk spectral broadening schemes. This approach would circumvent the general alignment sensitivity of small core fibers and at the same time facilitate a more realistic estimate of the residual phase noise of the compressed output since it avoids the erroneous inclusion of additional noise contributions from the continuum generation process. In this thesis, all-bulk spectral broadening using cascaded multipass-cells and a DQWG has already been demonstrated to facilitate the generation of few-cycle laser pulses with a spectral coverage of more than 350 nm at a central wavelength of 1030 nm (measured at −30 dB level, cf. Fig 4.5). Further spectral broadening using the techniques outlined in chapter 4 is expected to enable the generation of octave-spanning spectra from an all-bulk laser system within the near future.

6.3 Chapter summary

In this chapter, a novel technique for stabilizing the CEO frequency of high power Kerr-lens mode-locked thin-disk oscillators has been introduced and characterized for the first time. In the presented approach, an AOM is intentionally positioned in the focal region of the oscillator, significantly enhancing the nonlinear response inside the AOM material. As a result, the AOM can be used to modulate the intra-cavity loss of the oscillator in a wide frequency band, while at the same time serving as a nonlinear Kerr-medium which enables the initiation and stabilization of mode-locked operation. This design is in stark contrast to previously demonstrated intra-cavity loss-modulation schemes where the nonlinear phase shift from inside the AOM is minimized to avoid a potential unfavourable distribution of the nonlinear contributions inside the laser oscillator. The novel approach enables CEO frequency stabilization with a large control bandwidth of 230 kHz which is comparable to the bandwidths achievable in state-of-the art feed-forward schemes commonly used in the phase-stabilization of Ti:sapphire-based laser systems [153]. Importantly, the control bandwidth is increased by about a factor of ten when compared to the previously demonstrated CEO frequency control schemes for thin-disk oscillators based on pump power modulation which are inherently limited by the gain dynamics in the thin-disk oscillator [19].

Using the novel control mechanism, CEO frequency stabilization with a residual in-loop

phase noise of below 90 mrad was achieved at an unprecedented intra-cavity peak power exceeding 200 MW and an average output power of 105 W. The achieved results constitute an improvement of the CEO frequency stabilized intra-cavity peak power by more than a factor of seven when compared to previous state-of-the-art demonstrations [108]. To the authors knowledge, the presented oscillator further represents the highest average power CEO frequency-stable laser available today. At the same time, the residual in-loop phase noise was improved by a factor of two, demonstrating that even high-power thin-disk oscillators can be stabilized to the sub-100 mrad level.

As briefly discussed in section 6.1, CEO-frequency-stabilized high-power Kerr-lens mode-locked thin-disk oscillators are expected to play a key role in the development of compact, coherent XUV sources for precision spectroscopy applications. In reference [124], it has been shown that the achievable photon flux in the XUV can tremendously benefit from the availability of high-power ultrashort (< 30 fs) laser pulses at megahertz repetition rates. By implementing a Herriott-type multipass-cell pulse compression scheme with, CEO frequency-stable pulses with a pulse duration of 40 fs and peak power of 67 MW was already demonstrated at a pulse repetition rate of 15.6 MHz — output parameters approaching those reported in reference [124] (30 fs and 140 MW). A significant further improvement of the available pulse parameters is expected from the combination of the novel CEO frequency stabilization scheme presented here with the all-bulk spectral broadening techniques presented earlier in this thesis (chapter 3 and 4). The Yb:YAG thin-disk oscillator used for the spectral broadening experiments in this thesis (cf. section 2.3.1) has an intra-cavity peak power of around 80 MW and uses a 3 mm long sapphire crystal as Kerr-medium [23]. Based on the results presented in this chapter, the replacement of the sapphire Kerr-medium by an appropriate AOM should be feasible without necessitating further changes to the oscillator. The reduced waist size of around 150 µm in the Kerr-medium of the oscillator even indicates a potential for the further extension of the available control bandwidth to higher frequencies, allowing for a similar or even lower residual phase noise level when compared to the first experimental demonstration presented in this chapter. Importantly, however, a successful stabilization of the oscillator presented in section 2.3.1 would facilitate the generation of CEO-frequency-stable few-cycle laser pulses with gigawatt-scale peak powers and megahertz repetition rates. These steps are expected to pave the way for the development of a new generation of compact, low noise XUV frequency combs with high photon flux that can be utilized for XUV frequency comb spectroscopy and the investigation of various other phase-sensitive effects in the XUV spectral range.

The results of the CEO-frequency-stabilization experiment presented in this chapter were published in a peer-reviewed journal article [168]. A patent application for simultaneously using an intra-cavity loss-modulator as the Kerr-medium of a laser oscillator has been filed [169].

Conclusions

The availability of high-brightness, broadband and waveform-controlled radiation sources is of vital importance to a variety of state-of-the-art precision spectroscopy techniques such as field-resolved infrared spectroscopy and direct frequency comb spectroscopy. These techniques find numerous applications ranging from basic research to medical sciences, which promise to enhance our understanding of fundamental correlations in physics as well as providing deeper insights into the human physiology when applied in medical settings. Specifically, sources in the XUV or mid-IR spectral region can be used to perform spectroscopy on atoms and molecules by exploiting their electronic transitions or their vibrational and rotational modes. Lacking suitable direct sources in these regions, high-power near-IR lasers are often employed to drive nonlinear frequency conversion into the aforementioned spectral ranges. However, the output properties of even one of the most promising near-IR laser sources — Kerr-lens mode-locked Yb:YAG lasers — are still sub-optimal for the conversion processes.

The research presented in this thesis was driven by the goal of extending the boundaries of thin-disk oscillator-based laser technology. The focus is on generating waveform-controlled ultra-short pulses with unprecedented peak and average power levels — pulse parameters that enable the efficient generation of ultra-broadband, coherent and waveform controlled radiation in the mid-IR and XUV spectral ranges.

Summary and Outlook

In *chapter 2*, the fundamentals of spectral broadening in all-bulk Herriott-type multipass-cells were reviewed, and the influence of various parameters such as the dispersion environment were discussed. Experimentally, spectral broadening in a Herriott-type multipass-cell tuned to operate in the net-negative dispersion regime and driven at around 1 µm wavelength has been demonstrated for the first time. Specifically, a state-of-the-art Kerr-lens mode-locked Yb:YAG thin-disk oscillator delivering 290 fs long pulses at a repetition rate of 15.6 MHz with 150 W-scale average power was used for the experiments. As a result of the negative dispersion, the output pulses were self-compressed to a FWHM pulse duration of 31 fs, which corresponds to a temporal compression factor of almost ten — unprecedented for a multipass-cell featuring a single nonlinear medium. However, the soliton dynamics underlying the nonlinear pulse propagation caused an energy transfer of $> 55\,\%$ into satellite pulse structures. Thus, despite the high transmission of 88 %, the peak power was only

increased by approximately a factor of three, reaching a maximum value of 140 MW at the output of the Herriott-cell.

Significantly higher peak powers were achieved by utilizing Herriott-cells with net-positive dispersion, the results of which were discussed in *chapter 3*. By cascading two Herriott-cells with chirp-compensation in between, an output pulse duration of 15.6 fs was realized at an average output power of 101 W. This corresponds to an excellent optical efficiency of 84 % for the entire system. The high temporal compression factor of 18.5 for the two-cell system, combined with a substantial reduction in temporal pedestal, yielded an output peak power of 463 MW. Importantly, the short pulse duration and high peak power were achieved with minimal spatio-temporal couplings — confirmed by a low M^2 value of 1.11 and an intensity-weighted spectral overlap exceeding 97.5 % for two perpendicular axes. The near-diffraction-limited focusability and superb spectral homogeneity distinguishes this compression method from other techniques. These pulses are also amongst the shortest that have so far been generated using all-bulk multipass-cell-based spectral broadening [119], but with more than two times higher peak power. The maximum temporal compression factor from the dual-stage system was found to be limited ultimately by the achievable precision in the dispersion control within the multipass-cell.

An alternative method for generating even shorter pulses down to only a few optical cycles was presented in *chapter 4*. It introduced the distributed quasi-waveguide (DQWG) concept, which is a simple and robust way for realizing homogeneous spectral broadening in multiple passes through a dielectric bulk medium. Importantly, the use of a dedicated nonlinear medium for each pass of the DQWG permits a flexible optimization of the individual passes. In a proof-of-concept experiment, the 15.6 fs pulses from the output of the previously presented dual-stage multipass-cell system were compressed to a pulse duration of 10.8 fs — equivalent to 3.2 optical cycles. Operation of the DQWG deep in the positive dispersion regime facilitated a high compression quality which, in combination with the excellent optical efficiency of 99 %, resulted in an output peak of 0.64 GW. To the author's knowledge, this gigawatt-level of peak power is the highest so far realized in an amplifier-free ultrafast laser system. At few-cycle pulse duration and at megahertz repetition rate, the output represents an important milestone for thin-disk technology and is expected to facilitate a significant enhancement of the efficiency for broadband frequency conversion into the mid-IR and XUV spectral ranges. By constructing additional DQWG stages, further pulse compression towards the single-cycle regime could also be realized.

Chapter 5 investigated whether the increased bandwidth of the aforementioned few-cycle laser pulses can indeed benefit frequency conversion, specifically the generation of waveform-stable mid-IR radiation via intra-pulse difference-frequency generation (IPDFG) with wavelengths below 6.5 µm. This spectral range contains the vibrational resonances of various important functional groups such as amides in lipids, and has previously been inaccessible to thin-disk-oscillator-driven nonlinear conversion. By focusing the few-cycle NIR-pulses into a thin $LiGaS_2$ (LGS) crystal, and optimizing the phase-matching condition generating short-wavelength components, the resulting spectrum extended down to 3.6 µm (at −30 dB level) at an average output power of 7.6 mW. This showcased the tremendous advantage of using few-cycle laser pulses for IPDFG. Adjusting the phase-matching con-

ditions for the broadest simultaneous coverage, a super-octave mid-IR radiation spanning from 5 to 12 µm at the −20 dB level was generated with an average output power of 26 mW. Even broader mid-IR spectra are expected if thinner LGS crystals are used, or if the driver laser spectrum is pre-shaped to enhance the relative contribution of the spectral wings in the IPDFG process.

The advantages of using low-noise, ultrashort NIR laser pulses with high peak- and average powers are not restricted to frequency conversion into the mid-IR region. If combined with active waveform stabilization, such pulses will open the door for the development of a new generation of compact, low-noise sources of XUV frequency combs at megahertz repetition rates. In *chapter 6*, a novel method for controlling the carrier-envelope offset (CEO) frequency of high power Kerr-lens mode-locked oscillators was introduced. The peak- and average-power-scalable approach is based on intra-cavity loss modulation using an AOM which at the same time serves as the nonlinear Kerr-medium inside the laser resonator. The concept was successfully implemented in a high-power Kerr-lens mode-locked thin-disk oscillator, yielding CEO frequency stabilization with a residual in-loop phase noise of below 90 mrad. Crucially, this is achieved at an unprecedented intra-cavity peak power exceeding 200 MW and an average output power of 105 W. To the author's knowledge, the presented oscillator is the highest average power CEO-frequency-stable laser demonstrated to date. Subsequent pulse compression of the stabilized oscillator output based on a Herriott-type multipass-cell scheme further generated CEO-frequency-stable pulses with a pulse duration of 40 fs and peak power of 67 MW, at a repetition rate of 15.6 MHz. The combination of the novel approach for CEO frequency stabilization with the improved spectral broadening techniques presented in the earlier chapters will further facilitate the generation of waveform-controlled, gigawatt-scale and few-cycle laser pulses from a compact, amplifier-free laser system in the near future.

In conclusion, the results presented here constitute a notable progress in the ongoing development of high-power ultrafast laser sources, showcasing pulses with unparalleled qualities whether in terms of pulse duration, peak and average power, spatio-temporal homogeneity or waveform-control. These unique parameters will open up new perspectives for, amongst others, the generation of coherent radiation in the mid-IR and XUV spectral ranges. These will extend the boundaries of the latest high-precision spectroscopy techniques, providing valuable new insights into fundamental physics and the human physiology.

Data archiving

The experimental raw data, the corresponding evaluation files and the resulting figures are saved on the data archive server of the Laboratory for Attosecond Physics at the Max Planck Institute of Quantum Optics and can be found in the following directory:

/afs/ipp-garching.mpg.de/mpq/lap/publication_ archive/Theses/2021/Groebmeyer, Sebastian (PhD)

The files are organized in accordance with the structure of the thesis. For each figure, there is a separate folder that contains the associated data. If necessary, a *readme.txt* file provides further explanations and instructions about the folder's contents. The modified python module used for the simulation in the thesis is likewise archived in a separated folder in the same path.

Bibliography

[1] Cavalieri, A. L., Müller, N., Uphues, T., Yakovlev, V. S., Baltuška, A., Horvath, B., Schmidt, B., Blümel, L., Holzwarth, R., Hendel, S., Drescher, M., Kleineberg, U., Echenique, P. M., Kienberger, R., Krausz, F., and Heinzmann, U., "Attosecond spectroscopy in condensed matter", *Nature* **449**, 1029–1032 (2007).

[2] Goulielmakis, E., Loh, Z.-H., Wirth, A., Santra, R., Rohringer, N., Yakovlev, V. S., Zherebtsov, S., Pfeifer, T., Azzeer, A. M., Kling, M. F., Leone, S. R., and Krausz, F., "Real-time observation of valence electron motion", *Nature* **466**, 739–743 (2010).

[3] Eisele, M., Cocker, T. L., Huber, M. A., Plankl, M., Viti, L., Ercolani, D., Sorba, L., Vitiello, M. S., and Huber, R., "Ultrafast multi-terahertz nano-spectroscopy with sub-cycle temporal resolution", *Nature Photonics* **8**, 841–845 (2014).

[4] Hashimoto, K., Badarla, V. R., Kawai, A., and Ideguchi, T., "Complementary vibrational spectroscopy", *Nature Communications* **10**, 4411 (2019).

[5] Picqué, N. and Hänsch, T. W., "Frequency comb spectroscopy", *Nature Photonics* **13**, 146–157 (2019).

[6] Pupeza, I., Huber, M., Trubetskov, M., Schweinberger, W., Hussain, S. A., Hofer, C., Fritsch, K., Poetzlberger, M., Vamos, L., Fill, E., Amotchkina, T., Kepesidis, K. V., Apolonski, A., Karpowicz, N., Pervak, V., Pronin, O., Fleischmann, F., Azzeer, A., Žigman, M., and Krausz, F., "Field-resolved infrared spectroscopy of biological systems", *Nature* **577**, 52–59 (2020).

[7] Gohle, C., Udem, T., Herrmann, M., Rauschenberger, J., Holzwarth, R., Schuessler, H. A., Krausz, F., and Hänsch, T. W., "A frequency comb in the extreme ultraviolet", *Nature* **436**, 234–237 (2005).

[8] Cingöz, A., Yost, D. C., Allison, T. K., Ruehl, A., Fermann, M. E., Hartl, I., and Ye, J., "Direct frequency comb spectroscopy in the extreme ultraviolet", *Nature* **482**, 68–71 (2012).

[9] Wense, L. von der and Seiferle, B., "The ^{229}Th isomer: prospects for a nuclear optical clock", *The European Physical Journal A* **56**, 277 (2020).

[10] Campbell, C. J., Radnaev, A. G., Kuzmich, A., Dzuba, V. A., Flambaum, V. V., and Derevianko, A., "Single-Ion Nuclear Clock for Metrology at the 19th Decimal Place", *Physical Review Letters* **108**, 120802 (2012).

[11] Herrmann, M., Haas, M., Jentschura, U. D., Kottmann, F., Leibfried, D., Saathoff, G., Gohle, C., Ozawa, A., Batteiger, V., Knünz, S., Kolachevsky, N., Schüssler, H. A., Hänsch, T. W., and Udem, T., "Feasibility of coherent xuv spectroscopy on the 1S-2S transition in singly ionized helium", *Physical Review A* **79**, 052505 (2009).

[12] Lasch, P. and Kneipp, J., *Biomedical Vibrational Spectroscopy*. 1st edition. Hoboken, NJ, USA: Wiley & Sons Ltd, 2008.

[13] Baker, M. J., Hussain, S. R., Lovergne, L., Untereiner, V., Hughes, C., Lukaszewski, R. A., Thiéfin, G., and Sockalingum, G. D., "Developing and understanding biofluid vibrational spectroscopy: a critical review", *Chemical Society Reviews* **45**, 1803–1818 (2016).

[14] Byrne, H. J., Bonnier, F., McIntyre, J., and Parachalil, D. R., "Quantitative analysis of human blood serum using vibrational spectroscopy", *Clinical Spectroscopy* **2**, 100004 (2020).

[15] Psychogios, N., Hau, D. D., Peng, J., Guo, A. C., Mandal, R., Bouatra, S., Sinelnikov, I., Krishnamurthy, R., Eisner, R., Gautam, B., Young, N., Xia, J., Knox, C., Dong, E., Huang, P., Hollander, Z., Pedersen, T. L., Smith, S. R., Bamforth, F., Greiner, R., McManus, B., Newman, J. W., Goodfriend, T., and Wishart, D. S., "The Human Serum Metabolome", *PLOS ONE* **6**, e16957 (2011).

[16] Huber, M., Kepesidis, K. V., Voronina, L., Fleischmann, F., Fill, E., Hermann, J., Koch, I., Milger-Kneidinger, K., Kolben, T., Schulz, G. B., Jokisch, F., Behr, J., Harbeck, N., Reiser, M., Stief, C., Krausz, F., and Zigman, M., "Infrared molecular fingerprinting of blood-based liquid biopsies for the detection of cancer", *eLife* **10**, e68758 (2021).

[17] Chalmers, J. M., Diem, M., and Griffiths, P. R., *Vibrational spectroscopy for medical diagnosis*. 1st edition. Hoboken, NJ, USA: Wiley & Sons Inc, 2008.

[18] Anderson, N. L. and Anderson, N. G., "The Human Plasma Proteome: History, Character, and Diagnostic Prospects", *Molecular & Cellular Proteomics* **1**, 845–867 (2002).

[19] Emaury, F., Diebold, A., Klenner, A., Saraceno, C. J., Schilt, S., Südmeyer, T., and Keller, U., "Frequency comb offset dynamics of SESAM modelocked thin disk lasers", *Optics Express* **23**, 21836–21856 (2015).

[20] Pupeza, I., Sanchez, D., Zhang, J., Lilienfein, N., Seidel, M., Karpowicz, N., Paasch-Colberg, T., Znakovskaya, I., Pescher, M., Schweinberger, W., Pervak, V., Fill, E., Pronin, O., Wei, Z., Krausz, F., Apolonski, A., and Biegert, J., "High-power sub-two-cycle mid-infrared pulses at 100 MHz repetition rate", *Nature Photonics* **9**, 721–724 (2015).

[21] Brons, J., Pervak, V., Fedulova, E., Bauer, D., Sutter, D., Kalashnikov, V., Apolonskiy, A., Pronin, O., and Krausz, F., "Energy scaling of Kerr-lens mode-locked thin-disk oscillators", *Optics Letters* **39**, 6442–6445 (2014).

[22] Brons, J., Pervak, V., Bauer, D., Sutter, D., Pronin, O., and Krausz, F., "Powerful 100-fs-scale Kerr-lens mode-locked thin-disk oscillator", *Optics Letters* **41**, 3567–70 (2016).

[23] Poetzlberger, M., Zhang, J., Gröbmeyer, S., Bauer, D., Sutter, D., Brons, J., and Pronin, O., "Kerr-lens mode-locked thin-disk oscillator with 50% output coupling rate", *Optics Letters* **44**, 4227–4230 (2019).

[24] Huber, M., Schweinberger, W., Stutzki, F., Limpert, J., Pupeza, I., and Pronin, O., "Active intensity noise suppression for a broadband mid-infrared laser source", *Optics Express* **25**, 22499–22509 (2017).

[25] Saleh, B. and Teich, M., *Fundamentals of Photonics*. 3rd edition. Hoboken, NJ, USA: Wiley & Sons Ltd, 2019.

[26] Akturk, S., Gu, X., Bowlan, P., and Trebino, R., "Spatio-temporal couplings in ultrashort laser pulses", *Journal of Optics* **12**, 093001 (2010).

[27] Boyd, R. W., "Intuitive explanation of the phase anomaly of focused light beams", *Journal of the Optical Society of America* **70**, 877–880 (1980).

[28] Feng, S. and Winful, H. G., "Physical origin of the Gouy phase shift", *Optics Letters* **26**, 485–487 (2001).

[29] Weitenberg, J., "Transversale Moden in optischen Resonatoren für Anwendungen hoher Laserintensität; 1. Auflage". PhD thesis, RWTH Aachen University, 2017.

[30] Siegman, A. E., "New developments in laser resonators". OE/LASE '90 **1224** (1990).

[31] International Organization for Standardization, *Lasers and laser-related equipment — Test methods for laser beam widths, divergence angles and beam propagation ratios — Part 1: Stigmatic and simple astigmatic beams*. ISO 11146-1:2005. (2005).

[32] Siegman, A. E., "How to (Maybe) Measure Laser Beam Quality", in: *DPSS (Diode Pumped Solid State) Lasers: Applications and Issues*. Edited by M. Dowley. Volume 17. OSA Trends in Optics and Photonics. Optical Society of America, MQ1.

[33] Vaveliuk, P. and Martinez-Matos, O., "Effect of ABCD transformations on beam paraxiality", *Optics Express* **19**, 25944–25953 (2011).

[34] Weiner, A., *Ultrafast optics. Wiley series in pure and applied optics.* 1st edition. Hoboken, NJ, USA: Wiley & Sons Ltd, 2009.

[35] Agrawal, G., *Nonlinear Fiber Optics*. 3rd Edition. London and San Diego, CA, USA: Elsevier Science, 2001.

[36] Polyanskiy, M. N., *Refractive index database,* `https://refractiveindex.info`. Accessed on 2021-11-11.

[37] Pervak, V., Razskazovskaya, O., Angelov, I. B., Vodopyanov, K. L., and Trubetskov, M., "Dispersive mirror technology for ultrafast lasers in the range 220–4500 nm", *Advanced Optical Technologies* **3**, 55–63 (2014).

[38] Boyd, R. W., *Nonlinear Optics*. 4th edition. London, UK: Elsevier Science, 2020.

[39] Boyd, R. W., "Order-of-magnitude estimates of the nonlinear optical susceptibility", *Journal of Modern Optics* **46**, 367–378 (1999).

[40] Tomlinson, W. J., Stolen, R. H., and Shank, C. V., "Compression of optical pulses chirped by self-phase modulation in fibers", *Journal of the Optical Society of America B* **1**, 139–149 (1984).

[41] Grischkowsky, D. and Balant, A. C., "Optical pulse compression based on enhanced frequency chirping", *Applied Physics Letters* **41**, 1–3 (1982).

[42] Tomlinson, W. J., Stolen, R. H., and Johnson, A. M., "Optical wave breaking of pulses in nonlinear optical fibers", *Optics Letters* **10**, 457–459 (1985).

[43] Anderson, D., Desaix, M., Lisak, M., and Quiroga–Teixeiro, M. L., "Wave breaking in nonlinear-optical fibers", *Journal of the Optical Society of America B* **9**, 1358–1361 (1992).

[44] Diels, J., Rudolph, W., Liao, P., and Kelley, P., *Ultrashort Laser Pulse Phenomena*. 2nd edition. Burlington, MA, USA: Elsevier Science, 2006.

[45] Milosevic, N., Tempea, G., and Brabec, T., "Optical pulse compression: bulk media versus hollow waveguides", *Optics Letters* **25**, 672–674 (2000).

[46] Chiao, R. Y., Garmire, E., and Townes, C. H., "Self-Trapping of Optical Beams", *Physical Review Letters* **13**, 479–482 (1964).

[47] Moll, K. D., Gaeta, A. L., and Fibich, G., "Self-Similar Optical Wave Collapse: Observation of the Townes Profile", *Physical Review Letters* **90**, 203902 (2003).

[48] Hult, J., "A Fourth-Order Runge–Kutta in the Interaction Picture Method for Simulating Supercontinuum Generation in Optical Fibers", *Journal of Lightwave Technology* **25**, 3770–3775 (2007).

[49] Stolen, R. H., Gordon, J. P., Tomlinson, W. J., and Haus, H. A., "Raman response function of silica-core fibers", *Journal of the Optical Society of America B* **6**, 1159–1166 (1989).

[50] Tünnermann, H., Hickstein, D., and Ycas, G., *PyNLO,* `https://github.com/pyNLO/PyNLO`. (2020).

[51] Spence, D. E., Kean, P. N., and Sibbett, W., "60-fsec pulse generation from a self-mode-locked Ti:sapphire laser", *Optics Letters* **16**, 42–44 (1991).

[52] Ell, R., Morgner, U., Kärtner, F. X., Fujimoto, J. G., Ippen, E. P., Scheuer, V., Angelow, G., Tschudi, T., Lederer, M. J., Boiko, A., and Luther-Davies, B., "Generation of 5-fs pulses and octave-spanning spectra directly from a Ti:sapphire laser", *Optics Letters* **26**, 373–375 (2001).

[53] Danson, C. N., Haefner, C., Bromage, J., Butcher, T., Chanteloup, J.-C. F., Chowdhury, E. A., Galvanauskas, A., Gizzi, L. A., Hein, J., Hillier, D. I., Hopps, N. W., Kato, Y., Khazanov, E. A., Kodama, R., Korn, G., Li, R., Li, Y., Limpert, J., Ma, J., Nam, C. H., Neely, D., Papadopoulos, D., Penman, R. R., Qian, L., Rocca, J. J., Shaykin, A. A., Siders, C. W., Spindloe, C., Szatmári, S., Trines, R. M. G. M., Zhu, J., Zhu, P., and Zuegel, J. D., "Petawatt and exawatt class lasers worldwide", *High Power Laser Science and Engineering* **7**, e54 (2019).

[54] Matsushima, I., Yashiro, H., and Tomie, T., "10 kHz 40 W Ti:sapphire regenerative ring amplifier", *Optics Letters* **31**, 2066–2068 (2006).

[55] Jauregui, C., Limpert, J., and Tünnermann, A., "High-power fibre lasers", *Nature Photonics* **7**, 861–867 (2013).

[56] Russbueldt, P., Hoffmann, D., Höfer, M., Löhring, J., Luttmann, J., Meissner, A., Weitenberg, J., Traub, M., Sartorius, T., Esser, D., Wester, R., Loosen, P., and Poprawe, R., "Innoslab Amplifiers", *IEEE Journal of Selected Topics in Quantum Electronics* **21**, 447–463 (2015).

[57] Negel, J.-P., Loescher, A., Voss, A., Bauer, D., Sutter, D., Killi, A., Ahmed, M. A., and Graf, T., "Ultrafast thin-disk multipass laser amplifier delivering 1.4 kW (4.7 mJ, 1030 nm) average power converted to 820 W at 515 nm and 234 W at 343 nm", *Optics Express* **23**, 21064–21077 (2015).

[58] Giesen, A., Hügel, H., Voss, A., Wittig, K., Brauch, U., and Opower, H., "Scalable concept for diode-pumped high-power solid-state lasers", *Applied Physics B* **58**, 365–372 (1994).

[59] Keller, U., Weingarten, K. J., Kartner, F. X., Kopf, D., Braun, B., Jung, I. D., Fluck, R., Honninger, C., Matuschek, N., and Au, J. A. d., "Semiconductor saturable absorber mirrors (SESAM's) for femtosecond to nanosecond pulse generation in solid-state lasers", *IEEE Journal of Selected Topics in Quantum Electronics* **2**, 435–453 (1996).

[60] Aus der Au, J., Spühler, G. J., Südmeyer, T., Paschotta, R., Hövel, R., Moser, M., Erhard, S., Karszewski, M., Giesen, A., and Keller, U., "16.2-W average power from a diode-pumped femtosecond Yb:YAG thin disk laser", *Optics Letters* **25**, 859–861 (2000).

[61] Pronin, O., Brons, J., Grasse, C., Pervak, V., Boehm, G., Amann, M. C., Kalashnikov, V. L., Apolonski, A., and Krausz, F., "High-power 200 fs Kerr-lens mode-locked Yb:YAG thin-disk oscillator", *Optics Letters* **36**, 4746–4748 (2011).

[62] Saraceno, C. J., Emaury, F., Schriber, C., Hoffmann, M., Golling, M., Südmeyer, T., and Keller, U., "Ultrafast thin-disk laser with 80 µJ pulse energy and 242 W of average power", *Optics Letters* **39**, 9–12 (2014).

[63] Saltarelli, F., Graumann, I. J., Lang, L., Bauer, D., Phillips, C. R., and Keller, U., "Power scaling of ultrafast oscillators: 350-W average-power sub-picosecond thin-disk laser", *Optics Express* **27**, 31465–31474 (2019).

[64] Zhang, J., Brons, J., Seidel, M., Bauer, D., Sutter, D., Pervak, V., Kalashnikov, V., Wei, Z., Apolonski, A., Krausz, F., and Pronin, O., "Generation of 49-fs pulses directly from distributed Kerr-lens mode-locked Yb:YAG thin-disk oscillator", in: *Advanced Solid State Lasers*. OSA Technical Digest (online). Optical Society of America, ATh4A.7.

[65] Modsching, N., Paradis, C., Labaye, F., Gaponenko, M., Graumann, I. J., Diebold, A., Emaury, F., Wittwer, V. J., and Südmeyer, T., "Kerr lens mode-locked Yb:CALGO thin-disk laser", *Optics Letters* **43**, 879–882 (2018).

[66] Diebold, A., Emaury, F., Schriber, C., Golling, M., Saraceno, C. J., Südmeyer, T., and Keller, U., "SESAM mode-locked Yb:CaGdAlO4 thin disk laser with 62 fs pulse generation", *Optics Letters* **38**, 3842–3845 (2013).

[67] Erhard, S., Gao, J., Giesen, A., Contag, K., Lagatsky, A. A., Abdolvand, A., Kuleshov, N. V., Au, J. A. d., Spuhler, G. J., Brunner, F., Paschotta, R., and Keller, U., "High power Yb:KGW and Yb:KYW thin disk laser operation", in: *Technical Digest. Summaries of papers presented at the Conference on Lasers and Electro-Optics. Postconference Technical Digest (IEEE Cat. No.01CH37170)*. (2001), 333–334.

[68] Travers, J. C., Chang, W., Nold, J., Joly, N. Y., and St. J. Russell, P., "Ultrafast nonlinear optics in gas-filled hollow-core photonic crystal fibers [Invited]", *Journal of the Optical Society of America B* **28**, A11–A26 (2011).

[69] Emaury, F., Saraceno, C. J., Debord, B., Ghosh, D., Diebold, A., Gèrôme, F., Südmeyer, T., Benabid, F., and Keller, U., "Efficient spectral broadening in the 100-W average power regime using gas-filled kagome HC-PCF and pulse compression", *Optics Letters* **39**, 6843–6846 (2014).

[70] Mak, K. F., Travers, J. C., Joly, N. Y., Abdolvand, A., and Russell, P. S. J., "Two techniques for temporal pulse compression in gas-filled hollow-core kagomé photonic crystal fiber", *Optics Letters* **38**, 3592–3595 (2013).

[71] Mak, K. F., Seidel, M., Pronin, O., Frosz, M. H., Abdolvand, A., Pervak, V., Apolonski, A., Krausz, F., Travers, J. C., and Russell, P. S. J., "Compressing µJ-level pulses from 250 fs to sub-10 fs at 38-MHz repetition rate using two gas-filled hollow-core photonic crystal fiber stages", *Optics Letters* **40**, 1238–1241 (2015).

[72] Köttig, F., Schade, D., Koehler, J. R., Russell, P. S. J., and Tani, F., "Efficient single-cycle pulse compression of an ytterbium fiber laser at 10 MHz repetition rate", *Optics Express* **28**, 9099–9110 (2020).

[73] Koehler, J. R., Köttig, F., Trabold, B. M., Tani, F., and Russell, P. S. J., "Long-Lived Refractive-Index Changes Induced by Femtosecond Ionization in Gas-Filled Single-Ring Photonic-Crystal Fibers", *Physical Review Applied* **10**, 064020 (2018).

[74] Trabold, B. M., Suresh, M. I., Koehler, J. R., Frosz, M. H., Tani, F., and Russell, P. S. J., "Spatio-temporal measurement of ionization-induced modal index changes in gas-filled PCF by prism-assisted side-coupling", *Optics Express* **27**, 14392–14399 (2019).

[75] Rolland, C. and Corkum, P. B., "Compression of high-power optical pulses", *Journal of the Optical Society of America B* **5**, 641–647 (1988).

[76] Seidel, M., Arisholm, G., Brons, J., Pervak, V., and Pronin, O., "All solid-state spectral broadening: an average and peak power scalable method for compression of ultrashort pulses", *Optics Express* **24**, 9412–9428 (2016).

[77] Schulte, J., Sartorius, T., Weitenberg, J., Vernaleken, A., and Russbueldt, P., "Nonlinear pulse compression in a multi-pass cell", *Optics Letters* **41**, 4511–4514 (2016).

[78] Weitenberg, J., Saule, T., Schulte, J., and Rußbüldt, P., "Nonlinear Pulse Compression to Sub-40 fs at 4.5 µJ Pulse Energy by Multi-Pass-Cell Spectral Broadening", *IEEE Journal of Quantum Electronics* **53**, 1–4 (2017).

[79] Vlasov, S. N., Koposova, E. V., and Yashin, V. E., "Spectral broadening and compression of high-intensity laser pulses in quasi-periodic systems with Kerr nonlinearity", *Quantum Electronics* **42**, 989–995 (2012).

[80] Herriott, D., Kogelnik, H., and Kompfner, R., "Off-Axis Paths in Spherical Mirror Interferometers", *Applied Optics* **3**, 523–526 (1964).

[81] Fritsch, K., Poetzlberger, M., Pervak, V., Brons, J., and Pronin, O., "All-solid-state multipass spectral broadening to sub-20 fs", *Optics Letters* **43**, 4643–4646 (2018).

[82] Vicentini, E., Wang, Y., Gatti, D., Gambetta, A., Laporta, P., Galzerano, G., Curtis, K., McEwan, K., Howle, C. R., and Coluccelli, N., "Nonlinear pulse compression to 22 fs at 15.6 µJ by an all-solid-state multipass approach", *Optics Express* **28**, 4541–4549 (2020).

[83] Balla, P., Bin Wahid, A., Sytcevich, I., Guo, C., Viotti, A.-L., Silletti, L., Cartella, A., Alisauskas, S., Tavakol, H., Grosse-Wortmann, U., Schönberg, A., Seidel, M., Trabattoni, A., Manschwetus, B., Lang, T., Calegari, F., Couairon, A., L'Huillier, A., Arnold, C. L., Hartl, I., and Heyl, C. M., "Postcompression of picosecond pulses into the few-cycle regime", *Optics Letters* **45**, 2572–2575 (2020).

[84] Müller, M., Buldt, J., Stark, H., Grebing, C., and Limpert, J., "Multipass cell for high-power few-cycle compression", *Optics Letters* **46**, 2678–2681 (2021).

[85] Kogelnik, H. and Li, T., "Laser Beams and Resonators", *Applied Optics* **5**, 1550–1567 (1966).

[86] Tovar, A. A. and Casperson, L. W., "Generalized Sylvester theorems for periodic applications in matrix optics", *Journal of the Optical Society of America A* **12**, 578–590 (1995).

[87] Sennaroglu, A. and Fujimoto, J. G., "Design criteria for Herriott-type multi-pass cavities for ultrashort pulse lasers", *Optics Express* **11**, 1106–1113 (2003).

[88] Tovar, A. A. and Casperson, L. W., "Generalized beam matrices: Gaussian beam propagation in misaligned complex optical systems", *Journal of the Optical Society of America A* **12**, 1522–1533 (1995).

[89] Milam, D., "Review and assessment of measured values of the nonlinear refractive-index coefficient of fused silica", *Applied Optics* **37**, 546–550 (1998).

[90] Major, A., Yoshino, F., Nikolakakos, I., Aitchison, J. S., and Smith, P. W. E., "Dispersion of the nonlinear refractive index in sapphire", *Optics Letters* **29**, 602–604 (2004).

[91] Fritsch, K., "Nonlinear pulse compression of state-of-the-art femtosecond Yb-doped lasers". PhD thesis, Ludwig-Maximilians-University, Munich, Germany, *in preparation*.

[92] Dudley, J. M., Genty, G., and Coen, S., "Supercontinuum generation in photonic crystal fiber", *Reviews of Modern Physics* **78**, 1135–1184 (2006).

[93] Mitschke, F. M. and Mollenauer, L. F., "Discovery of the soliton self-frequency shift", *Optics Letters* **11**, 659–661 (1986).

[94] Jargot, G., Daher, N., Lavenu, L., Delen, X., Forget, N., Hanna, M., and Georges, P., "Self-compression in a multipass cell", *Optics Letters* **43**, 5643–5646 (2018).

[95] Pötzlberger, M., "High-power femtosecond laser sources for mid-infrared generation". PhD thesis, Ludwig-Maximilians-University, Munich, Germany, 2021.

[96] Neuhaus, J., Kleinbauer, J., Killi, A., Weiler, S., Sutter, D., and Dekorsy, T., "Passively mode-locked Yb:YAG thin-disk laser with pulse energies exceeding 13 µJ by use of an active multipass geometry", *Optics Letters* **33**, 726–728 (2008).

[97] Adair, R., Chase, L. L., and Payne, S. A., "Nonlinear refractive index of optical crystals", *Physical Review B* **39**, 3337–3350 (1989).

[98] Chen, C.-M. and Kelley, P. L., "Nonlinear pulse compression in optical fibers: scaling laws and numerical analysis", *Journal of the Optical Society of America B* **19**, 1961–1967 (2002).

[99] Malitson, I. H., "Interspecimen Comparison of the Refractive Index of Fused Silica", *Journal of the Optical Society of America* **55**, 1205–1209 (1965).

[100] Weitenberg, J., Vernaleken, A., Schulte, J., Ozawa, A., Sartorius, T., Pervak, V., Hoffmann, H.-D., Udem, T., Russbüldt, P., and Hänsch, T. W., "Multi-pass-cell-based nonlinear pulse compression to 115 fs at 7.5 µJ pulse energy and 300 W average power", *Optics Express* **25**, 20502–20510 (2017).

[101] A.F.Systems, *Compact 100 W femtosecond laser,* `http://www.afs-jena.de/#compact`. Accessed on 2021-11-11.

[102] Gröbmeyer, S., Fritsch, K., Schneider, B., Poetzlberger, M., Pervak, V., Brons, J., and Pronin, O., "Self-compression at 1 µm wavelength in all-bulk multi-pass geometry", *Applied Physics B* **126**, 159 (2020).

[103] Optics, E., *Precision Round Windows Brochure,* `https://eksmaoptics.com/out/media/EKSMA_Optics_Precision_Round_Windows_18.pdf`. Accessed on 2021-11-11.

[104] Neuhaus, J., Bauer, D., Kleinbauer, J., Killi, A., Sutter, D. H., and Dekorsy, T., "Numerical analysis of a sub-picosecond thin-disk laser oscillator with active multi-pass geometry showing a variation of pulse duration within one round trip", *Journal of the Optical Society of America B* **27**, 65–71 (2010).

[105] Tsai, C.-L., Meyer, F., Omar, A., Wang, Y., Liang, A.-Y., Lu, C.-H., Hoffmann, M., Yang, S.-D., and Saraceno, C. J., "Efficient nonlinear compression of a mode-locked thin-disk oscillator to 27 fs at 98 W average power", *Optics Letters* **44**, 4115–4118 (2019).

[106] Cao, H., Nagymihaly, R. S., Chvykov, V., Khodakovskiy, N., and Kalashnikov, M., "Multipass-cell-based post-compression of radially and azimuthally polarized pulses to the sub-two-cycle regime", *Journal of the Optical Society of America B* **36**, 2517–2525 (2019).

[107] Nagy, T., Simon, P., and Veisz, L., "High-energy few-cycle pulses: post-compression techniques", *Advances in Physics: X* **6**, 1845795 (2021).

[108] Pronin, O., Seidel, M., Lucking, F., Brons, J., Fedulova, E., Trubetskov, M., Pervak, V., Apolonski, A., Udem, T., and Krausz, F., "High-power multi-megahertz source of waveform-stabilized few-cycle light", *Nature Communications* **6**, 6988 (2015).

[109] Lu, C.-H., Tsou, Y.-J., Chen, H.-Y., Chen, B.-H., Cheng, Y.-C., Yang, S.-D., Chen, M.-C., Hsu, C.-C., and Kung, A. H., "Generation of intense supercontinuum in condensed media", *Optica* **1**, 400–406 (2014).

[110] Dubietis, A., Tamošauskas, G., Šuminas, R., Jukna, V., and Couairon, A., "Ultrafast supercontinuum generation in bulk condensed media (Invited Review)", *Lithuanian Journal of Physics* **57**, 113–157 (2017).

[111] Cheng, Y.-C., Lu, C.-H., Lin, Y.-Y., and Kung, A. H., "Supercontinuum generation in a multi-plate medium", *Optics Express* **24**, 7224–7231 (2016).

[112] Budriūnas, R., Kučinskas, D., and Varanavičius, A., "High-energy continuum generation in an array of thin plates pumped by tunable femtosecond IR pulses", *Applied Physics B* **123**, 1–9 (2017).

[113] He, P., Liu, Y., Zhao, K., Teng, H., He, X., Huang, P., Huang, H., Zhong, S., Jiang, Y., Fang, S., Hou, X., and Wei, Z., "High-efficiency supercontinuum generation in solid thin plates at 0.1 TW level", *Optics Letters* **42**, 474–477 (2017).

[114] Lu, C.-H., Witting, T., Husakou, A., Vrakking, M. J. J., Kung, A. H., and Furch, F. J., "Sub-4 fs laser pulses at high average power and high repetition rate from an all-solid-state setup", *Optics Express* **26**, 8941–8956 (2018).

[115] Lu, C.-H., Wu, W.-H., Kuo, S.-H., Guo, J.-Y., Chen, M.-C., Yang, S.-D., and Kung, A. H., "Greater than 50 times compression of 1030 nm Yb:KGW laser pulses to single-cycle duration", *Optics Express* **27**, 15638–15648 (2019).

[116] Ishii, N., Xia, P., Kanai, T., and Itatani, J., "Optical parametric amplification of carrier-envelope phase-stabilized mid-infrared pulses generated by intra-pulse difference frequency generation", *Optics Express* **27**, 11447–11454 (2019).

[117] Seo, M., Tsendsuren, K., Mitra, S., Kling, M., and Kim, D., "High-contrast, intense single-cycle pulses from an all thin-solid-plate setup", *Optics Letters* **45**, 367–370 (2020).

[118] Zhang, S., Fu, Z., Zhu, B., Fan, G., Chen, Y., Wang, S., Liu, Y., Baltuska, A., Jin, C., Tian, C., and Tao, Z., "Solitary beam propagation in periodic layered Kerr media enables high-efficiency pulse compression and mode self-cleaning", *Light: Science & Applications* **10**, 53 (2021).

[119] Barbiero, G., Wang, H., Graßl, M., Gröbmeyer, S., Kimbaras, D., Neuhaus, M., Pervak, V., Nubbemeyer, T., Fattahi, H., and Kling, M. F., "Efficient nonlinear compression of a thin-disk oscillator to 8.5 fs at 55 W average power", *Optics Letters* **46**, 5304–5307 (2021).

[120] Mokhov, S., Glebov, L., and Zeldovich, B., "Quality deterioration of self-phase modulated Gaussian beams", *Laser Physics Letters* **12**, 015004 (2014).

[121] Brons, J., "High-power femtosecond laser-oscillators for applications in high-field physics". PhD thesis, Ludwig-Maximilians-University, Munich, Germany, 2017.

[122] Newbury, N. R., Washburn, B. R., Corwin, K. L., and Windeler, R. S., "Noise amplification during supercontinuum generation in microstructure fiber", *Optics Letters* **28**, 944–946 (2003).

[123] Fibich, G. and Gaeta, A. L., "Critical power for self-focusing in bulk media and in hollow waveguides", *Optics Letters* **25**, 335–337 (2000).

[124] Hädrich, S., Krebs, M., Hoffmann, A., Klenke, A., Rothhardt, J., Limpert, J., and Tünnermann, A., "Exploring new avenues in high repetition rate table-top coherent extreme ultraviolet sources", *Light: Science & Applications* **4**, e320 (2015).

[125] Baker, M. J., Trevisan, J., Bassan, P., Bhargava, R., Butler, H. J., Dorling, K. M., Fielden, P. R., Fogarty, S. W., Fullwood, N. J., Heys, K. A., Hughes, C., Lasch, P., Martin-Hirsch, P. L., Obinaju, B., Sockalingum, G. D., Sulé-Suso, J., Strong, R. J., Walsh, M. J., Wood, B. R., Gardner, P., and Martin, F. L., "Using Fourier transform IR spectroscopy to analyze biological materials", *Nature Protocols* **9**, 1771–1791 (2014).

[126] Newbury, N. R., Coddington, I., and Swann, W., "Sensitivity of coherent dual-comb spectroscopy", *Optics Express* **18**, 7929–7945 (2010).

[127] Schwaighofer, A., Montemurro, M., Freitag, S., Kristament, C., Culzoni, M. J., and Lendl, B., "Beyond Fourier Transform Infrared Spectroscopy: External Cavity Quantum Cascade Laser-Based Mid-infrared Transmission Spectroscopy of Proteins in the Amide I and Amide II Region", *Analytical Chemistry* **90**, 7072–7079 (2018).

[128] Sell, A., Scheu, R., Leitenstorfer, A., and Huber, R., "Field-resolved detection of phase-locked infrared transients from a compact Er:fiber system tunable between 55 and 107 THz", *Applied Physics Letters* **93**, 251107 (2008).

[129] Kowligy, A. S., Timmers, H., Lind, A. J., Elu, U., Cruz, F. C., Schunemann, P. G., Biegert, J., and Diddams, S. A., "Infrared electric field sampled frequency comb spectroscopy", *Science Advances* **5**, eaaw8794 (2019).

[130] Gaida, C., Gebhardt, M., Heuermann, T., Stutzki, F., Jauregui, C., Antonio-Lopez, J., Schülzgen, A., Amezcua-Correa, R., Tünnermann, A., Pupeza, I., and Limpert, J., "Watt-scale super-octave mid-infrared intrapulse difference frequency generation", *Light: Science & Applications* **7**, 94 (2018).

[131] Seidel, M., Xiao, X., Hussain, S. A., Arisholm, G., Hartung, A., Zawilski, K. T., Schunemann, P. G., Habel, F., Trubetskov, M., Pervak, V., Pronin, O., and Krausz, F., "Multi-watt, multi-octave, mid-infrared femtosecond source", *Science Advances* **4**, eaaq1526 (2018).

[132] Nagl, N., Mak, K. F., Wang, Q., Pervak, V., Krausz, F., and Pronin, O., "Efficient femtosecond mid-infrared generation based on a Cr:ZnS oscillator and step-index fluoride fibers", *Optics Letters* **44**, 2390–2393 (2019).

[133] Schliesser, A., Picqué, N., and Hänsch, T. W., "Mid-infrared frequency combs", *Nature Photonics* **6**, 440–449 (2012).

[134] Movasaghi, Z., Rehman, S., and Rehman, I. U., "Fourier Transform Infrared (FTIR) Spectroscopy of Biological Tissues", *Applied Spectroscopy Reviews* **43**, 134–179 (2008).

[135] Chen, B. H., Nagy, T., and Baum, P., "Efficient middle-infrared generation in LiGaS2 by simultaneous spectral broadening and difference-frequency generation", *Optics Letters* **43**, 1742–1745 (2018).

[136] Bor, Z., "Distortion of femtosecond laser pulses in lenses", *Optics Letters* **14**, 119–121 (1989).

[137] Kempe, M., Stamm, U., Wilhelmi, B., and Rudolph, W., "Spatial and temporal transformation of femtosecond laser pulses by lenses and lens systems", *Journal of the Optical Society of America B* **9**, 1158–1165 (1992).

[138] Buberl, T., "Towards next-generation molecular fingerprinting - Advancing mid-infrared spectroscopy for biomedical applications". PhD thesis, Ludwig-Maximilians-University, Munich, Germany, 2021.

[139] Ozawa, A., Rauschenberger, J., Gohle, C., Herrmann, M., Walker, D. R., Pervak, V., Fernandez, A., Graf, R., Apolonski, A., Holzwarth, R., Krausz, F., Hänsch, T. W., and Udem, T., "High Harmonic Frequency Combs for High Resolution Spectroscopy", *Physical Review Letters* **100**, 253901 (2008).

[140] Ferray, M., L'Huillier, A., Li, X. F., Lompre, L. A., Mainfray, G., and Manus, C., "Multiple-harmonic conversion of 1064 nm radiation in rare gases", *Journal of Physics B: Atomic, Molecular and Optical Physics* **21**, L31–L35 (1988).

[141] Li, X. F., L'Huillier, A., Ferray, M., Lompré, L. A., and Mainfray, G., "Multiple-harmonic generation in rare gases at high laser intensity", *Physical Review A* **39**, 5751–5761 (1989).

[142] Hädrich, S., Jan, R., Krebs, M., Demmler, S., Klenke, A., Tünnermann, A., and Limpert, J., "Single-pass high harmonic generation at high repetition rate and photon flux", *Journal of Physics B: Atomic, Molecular and Optical Physics* **49**, 172002 (2016).

[143] Heyl, C. M., Arnold, C. L., Couairon, A., and L'Huillier, A., "Introduction to macroscopic power scaling principles for high-order harmonic generation", *Journal of Physics B: Atomic, Molecular and Optical Physics* **50**, 013001 (2017).

[144] Rundquist, A., Durfee Iii, C. G., Chang, Z., Heme, C., Backus, S., Murnane, M. M., and Kapteyn, H. C., "Phase Matched Generation of Coherent Soft-X-rays", *Optics and Photonics News* **9**, 54–55 (1998).

[145] Pupeza, I., Zhang, C., Högner, M., and Ye, J., "Extreme-ultraviolet frequency combs for precision metrology and attosecond science", *Nature Photonics* **15**, 175–186 (2021).

[146] Wunram, M., Storz, P., Brida, D., and Leitenstorfer, A., "Ultrastable fiber amplifier delivering 145-fs pulses with 6-μJ energy at 10-MHz repetition rate", *Optics Letters* **40**, 823–826 (2015).

[147] Paschotta, R., Schlatter, A., Zeller, S. C., Telle, H. R., and Keller, U., "Optical phase noise and carrier-envelope offset noise of mode-locked lasers", *Applied Physics B* **82**, 265–273 (2006).

[148] Benko, C., Allison, T. K., Cingöz, A., Hua, L., Labaye, F., Yost, D. C., and Ye, J., "Extreme ultraviolet radiation with coherence time greater than 1 s", *Nature Photonics* **8**, 530–536 (2014).

[149] Fortier, T. and Baumann, E., "20 years of developments in optical frequency comb technology and applications", *Communications Physics* **2**, 153 (2019).

[150] Holzwarth, R., Udem, T., Hänsch, T. W., Knight, J. C., Wadsworth, W. J., and Russell, P. S. J., "Optical Frequency Synthesizer for Precision Spectroscopy", *Physical Review Letters* **85**, 2264–2267 (2000).

[151] Jones, D. J., Diddams, S. A., Ranka, J. K., Stentz, A., Windeler, R. S., Hall, J. L., and Cundiff, S. T., "Carrier-Envelope Phase Control of Femtosecond Mode-Locked Lasers and Direct Optical Frequency Synthesis", *Science* **288**, 635–639 (2000).

[152] Telle, H. R., Steinmeyer, G., Dunlop, A. E., Stenger, J., Sutter, D. H., and Keller, U., "Carrier-envelope offset phase control: A novel concept for absolute optical frequency measurement and ultrashort pulse generation", *Applied Physics B* **69**, 327–332 (1999).

[153] Koke, S., Grebing, C., Frei, H., Anderson, A., Assion, A., and Steinmeyer, G., "Direct frequency comb synthesis with arbitrary offset and shot-noise-limited phase noise", *Nature Photonics* **4**, 462–465 (2010).

[154] Zhang, Z., Han, H., Wang, H., Shao, X., Fang, S., and Wei, Z., "Ultra-low-noise carrier-envelope phase stabilization of a Kerr-lens mode-locked Yb:CYA laser frequency comb with a feed-forward method", *Optics Letters* **44**, 5489–5492 (2019).

[155] Lücking, F., "Carrier-envelope phase control for the advancement of attosecond pulse generation". PhD thesis, Ludwig-Maximilians-University, Munich, Germany, 2014.

[156] Borchers, B., Koke, S., Husakou, A., Herrmann, J., and Steinmeyer, G., "Carrier-envelope phase stabilization with sub-10 as residual timing jitter", *Optics Letters* **36**, 4146–4148 (2011).

[157] Borchers, B., Anderson, A., and Steinmeyer, G., "On the role of shot noise in carrier-envelope phase stabilization", *Laser & Photonics Reviews* **8**, 303–315 (2014).

[158] Apolonski, A., Poppe, A., Tempea, G., Spielmann, C., Udem, T., Holzwarth, R., Hänsch, T. W., and Krausz, F., "Controlling the Phase Evolution of Few-Cycle Light Pulses", *Physical Review Letters* **85**, 740–743 (2000).

[159] Udem, T., Reichert, J., Holzwarth, R., and Hänsch, T. W., "Absolute Optical Frequency Measurement of the Cesium D_1 Line with a Mode-Locked Laser", *Physical Review Letters* **82**, 3568–3571 (1999).

[160] Klenner, A., Emaury, F., Schriber, C., Diebold, A., Saraceno, C. J., Schilt, S., Keller, U., and Südmeyer, T., "Phase-stabilization of the carrier-envelope-offset frequency of a SESAM modelocked thin disk laser", *Optics Express* **21**, 24770–24780 (2013).

[161] Seidel, M., Brons, J., Lucking, F., Pervak, V., Apolonski, A., Udem, T., and Pronin, O., "Carrier-envelope-phase stabilization via dual wavelength pumping", *Optics Letters* **41**, 1853–1856 (2016).

[162] Balčiūnas, T., Mücke, O. D., Mišeikis, P., Andriukaitis, G., Pugžlys, A., Giniūnas, L., Danielius, R., Holzwarth, R., and Baltuška, A., "Carrier envelope phase stabilization of a Yb:KGW laser amplifier", *Optics Letters* **36**, 3242–3244 (2011).

[163] Andrade, J. R. C., Modsching, N., Tajalli, A., Dietrich, C. M., Kleinert, S., Placzek, F., Kreipe, B., Schilt, S., Wittwer, V. J., Südmeyer, T., and Morgner, U., "Carrier-Envelope Offset Frequency Stabilization of a Thin-Disk Laser Oscillator via Depletion Modulation", *IEEE Photonics Journal* **12**, 1–9 (2020).

[164] Boyd, J., Young, E., and Yao, S., "Design Procedure for Wide Bandwidth Acousto-Optic Modulator", *Optical Engineering* **16**, 165452 (1977).

[165] Brabec, T., Spielmann, C., Curley, P. F., and Krausz, F., "Kerr lens mode locking", *Optics Letters* **17**, 1292–1294 (1992).

[166] Lee, C. C., Mohr, C., Bethge, J., Suzuki, S., Fermann, M. E., Hartl, I., and Schibli, T. R., "Frequency comb stabilization with bandwidth beyond the limit of gain lifetime by an intracavity graphene electro-optic modulator", *Optics Letters* **37**, 3084–3086 (2012).

[167] Raabe, N., Feng, T., Mero, M., Tian, H., Song, Y., Hänsel, W., Holzwarth, R., Sell, A., Zach, A., and Steinmeyer, G., "Excess carrier-envelope phase noise generation in saturable absorbers", *Optics Letters* **42**, 1068–1071 (2017).

[168] Gröbmeyer, S., Brons, J., Seidel, M., and Pronin, O., "Carrier-Envelope-Offset Frequency Stable 100 W-Level Femtosecond Thin-Disk Oscillator", *Laser & Photonics Reviews* **13**, 1800256 (2019).

[169] Pronin, O., Krausz, F., Gröbmeyer, S., and Brons, J., *Device and method for generating laser pulses by Kerr lens based mode locking with a loss-modulation device as a Kerr medium*. Patent Application PCT/EP2019/051560. (2019).

List of publications

Peer reviewed journal articles

- **Sebastian Gröbmeyer**, Jonathan Brons, Marcus Seidel and Oleg Pronin, "Carrier-Envelope-Offset Frequency Stable 100 W-Level Femtosecond Thin-Disk Oscillator", Laser & Photonics Reviews 13, 1800256 (2019).
- Nathalie Nagl, **Sebastian Gröbmeyer**, Vladimir Pervak, Ferenc Krausz, Oleg Pronin, and Ka Fai Mak, "Directly diode-pumped, Kerr-lens mode-locked, few-cycle Cr:ZnSe oscillator," Optics Express 27, 24445-24454 (2019)
- Markus Poetzlberger, Jinwei Zhang, **Sebastian Gröbmeyer**, Dominik Bauer, Dirk Sutter, Jonathan Brons and Oleg Pronin, "Kerr-lens mode-locked thin-disk oscillator with 50 % output coupling rate", Optics Letters 44, 4227-4230 (2019).
- **Sebastian Gröbmeyer**, Kilian Fritsch, Benedikt Schneider, Markus Poetzlberger, Vladimir Pervak, Jonathan Brons and Oleg Pronin, "Self-compression at 1 µm wavelength in all-bulk multi-pass geometry", Applied Physics B 126, 159 (2020)
- Gaia Barbiero, Haochuan Wang, Martin Grassl, **Sebastian Gröbmeyer**, Dziugas Kimbaras, Marcel Neuhaus, Thomas Nubbemeyer, Hanieh Fattahi and Matthias F. Kling, "Efficient nonlinear compression of a thin-disk oscillator to 8.5 fs at 55 W average power", Optics Letters 46, 5304-5307 (2021).
- *In preparation:*
  Sebastian Gröbmeyer, Kilian Fritsch, Vladimir Pervak, Kafai Mak and Ferenc Krausz, "High fidelity, GW-scale few-cycle pulse generation via a distributed quasi-waveguide".

Selected conference contributions

- **Sebastian Gröbmeyer**, Jonathan Brons, Marcus Seidel and Oleg Pronin, "CEP stabilization of a 100 W-level femtosecond thin-disk oscillator", in XXI International Conference on Ultrafast Phenomena, Hamburg (Germany, 2018).

- **Sebastian Gröbmeyer**, Kilian Fritsch, Benedikt Schneider, Markus Poetzlberger, Vladimir Pervak, Jonathan Brons and Oleg Pronin, "Energy scalable soliton self-compression in all-bulk multi-pass geometry", in 8th EPS-QEOD Europhoton Conference 2018, PD.Tue-2 (2018).

Patent applications

- Oleg Pronin, Ferenc Krausz, **Sebastian Gröbmeyer** and Jonathan Brons, "Device and method for generating laser pulses by Kerr lens based mode locking with a loss-modulation device as a Kerr medium", Patent Application No. PCT/EP2019/051560 (2019).

Acknowledgements

Finally, I would like to thank everyone who contributed to this PhD thesis and who supported me during the last five years.

At first, I would like to express my deep gratitude to Prof. Dr. Ferenc Krausz for supervising this thesis and for providing such an excellent and productive research atmosphere. The experiments presented here have only been made possible by the generous funding, outstanding laboratory infrastructure and knowledgeable team of people he has assembled over the years, and I feel honoured, for having been given the chance to be part of his group for such a long time. Furthermore, I would like to thank Prof. Dr. Franz Kärtner for, without hesitation, agreeing to take over the important role as the second referee of this thesis. Additionally, I would like to cordially thank the professors Dr. Ivo Sachs, Dr. Joachim Rädler and Dr. Armin Scrinzi as well as Dr. Theobald Lohmüller for generously spending their time as being part of the examination committee.

My biggest thank you goes to Dr. Ka Fai Mak for all his guidance and the great deal of motivational energy throughout the past years. I could not imagine a better group leader than him and I want to specifically thank him for his patience and unconditional support even in situations where I was completely clueless or had lost the confidence in myself. Many thanks also to Prof. Dr. Oleg Pronin who initially introduced me to the group already as a HiWi-student during my undergraduate studies and continued to be a capable supervisor during the first two years of my PhD thesis.

Next I would like to thank all the former and current members of the HFS-team, many of which are not merely colleagues but have become close friends. In particular, I would like to thank Jonathan, Marcus and Jinwei who introduced me to the world of high-power lasers and taught me all about the laser fundamentals and lab essentials: how to clean mirrors, connect chillers, and importantly, how to not give up if the laser would not mode-lock — again. My office mates and fellow PhD students: Kilian, who always helped me with my rudimentary attempts at writing Python code, Markus, for providing and maintaining his beautifully engineered oscillator and Nathalie for the helpful discussions on noise measurements and mode-locking concepts. I will also never forget the great fun we had off work, be it during our trips to various conferences or simply while sitting together in the evening watching the "Nockherberg". A big thank you also to the more recent members of our team Aleksandar, Philipp, Shizhen and Maciej for the great teamwork throughout the last two years and also the valuable feedback they have given me for my thesis!

I also would like to thank all the other wonderful members of the Krausz-group who

always had an open ear and a helping hand. Specifically, I would like to thank Theresa, Ali, Martin and Gaia for the enlightening discussions on how to solve the issues related to multipass-cell spectral broadening. Furthermore I would like to thank Wolfgang, Daniel, Alex, Philip and Christina for sharing their knowledge on mid-IR generation techniques and for often helping out last minute and at late hours in the lab, especially when I was struggling to find a first mid-IR signal. I am also grateful that Hadil took over the system to develop it into a state-of-the-art real-world measurement system. I also would like to thank Vladimir and his team for coating all those excellent mirrors — often at last-minute requests — and for taking the time to explaining the fundamentals and considerations in coating design to always ensure the best possible results.

Beside the scientific team, my PhD would not have been successful without the indispensable help from our administrative and technical teams. Here I would like to particularly thank Klaus for his endless efforts to manage our daily administrative problems and making sure that we could focus our time on scientific problems. Furthermore I would like to thank Katharina and Martin for their support during ordering and making sure that all necessary purchases could be made as efficiently as possible. A special thanks also goes to Florian and Hans for their assistance when moving chambers or preparing the lab for construction work as well as Herr Bär from Caverion for his fast response times after power cuts and all other building related problems. I also would like to express my gratitude to Herr Oehm and his entire team from the mechanical workshop for always helping us out quickly with their knowledge and production capabilities — despite the often amateurish quality of technical drawings.

Zu guter Letzt möchte ich noch einige nichtwissenschaftliche Dankesworte in meiner Muttersprache abfassen: Mein ganz besonderer Dank geht an Laura, dafür, dass Sie immer für mich da war und mich über die letzten fünf Jahre jederzeit bedingungslos und von ganzem Herzen unterstützt hat. Vielen Dank auch an meine Freunde in und um München, die mich über die letzten Jahre begleitet haben und immer wieder ermutigt haben weiterzumachen und meine Doktorarbeit zu Ende zu bringen. Zum Schluss danke ich meiner Familie, insbesondere meinen Eltern Birgit und Georg sowie meiner Schwester Marion, dafür, dass Sie immer an mich geglaubt haben und mich auf meinem Weg unterstützen.